

THREE-DIMENSIONAL MODEL-BASED
ANALYSIS OF VASCULAR AND CARDIAC
IMAGES

ALEJANDRO F. FRANGI

Colophon

This book was typeset by the author using L^AT_EX2_ε. The main body of the text was set using a 10-points Computer Modern Roman font. All graphics and images were included formatted as Encapsulated PostScript (TM Adobe Systems Incorporated). The final PostScript output was converted to Portable Document Format (PDF) and transferred to film for printing.

Copyright © 2001 by Alejandro F Frangi. All rights reserved. No part of this publication may be reproduced or transmitted in any form or by any means, electronic or mechanical, including photocopy, recording, or any information storage and retrieval system, without permission in writing from the author.

ISBN 90-393-2647-9

This thesis was printed with financial support from PHILIPS Medical Systems Nederland B.V. (EasyVision Advanced Development).

Printed by Ponsen & Looijen, Wageningen, The Netherlands.

Three-Dimensional Model-Based Analysis of Vascular and Cardiac Images

Driedimensionale Modelgestuurde Analyse
van Vaat- en Hartbeelden
(met een samenvatting in het Nederlands)

PROEFSCHRIFT

TER VERKRIJGING VAN DE GRAAD VAN DOCTOR AAN DE UNIVERSITEIT UTRECHT
OP GEZAG VAN DE RECTOR MAGNIFICUS, PROF. DR. W. H. GISPEN, INGEVOLGE
HET BESLUIT VAN HET COLLEGE VOOR PROMOTIES IN HET OPENBAAR TE
VERDEDIGEN OP MAANDAG 2 APRIL 2001 DES OCHTENDS TE 10:30 UUR

DOOR

Alejandro Federico Frangi

geboren op 15 november 1972 te La Plata, Argentinië.

Promotor: **Prof. Dr. Ir. M. A. Viergever**
University Medical Center Utrecht

Co-promotor: **Dr. W. J. Niessen**
University Medical Center Utrecht

Reading Committee: Dr. Ir. F. A. Gerritsen
Philips Medical Systems, Best, The Netherlands

Prof. Dr. D. J. Hawkes
Kings' College London, London, United Kingdom

Prof. Dr. B. Hillen
University Medical Center, Utrecht, The Netherlands

Prof. Dr. Ir. J. J. W. Lagendijk
University Medical Center, Utrecht, The Netherlands

Prof. Dr. Ir. A. W. M. Smeulders
University of Amsterdam, Amsterdam, The Netherlands



Image Sciences Institute

The research described in this thesis was carried out at the Image Sciences Institute, University Medical Center Utrecht, The Netherlands, under the auspices of ImagO, the Utrecht Graduate School for Biomedical Image Sciences. The project was financially supported by The Netherlands Ministry of Economic Affairs, within the framework of the Innovation Oriented Research Programme (IOP Beeldverwerking, project number IBV97009), and sponsored by Philips Medical Systems, EasyVision Advanced Development.

TO SILVIA

Endowed with intellect and free will, each man is responsible for his self-fulfillment even as he is for his salvation. He is helped, and sometimes hindered, by his teachers and those around him; yet whatever be the outside influences exerted on him, he is the chief architect of his own success or failure. Utilizing only his talent and will-power, each man can grow in humanity, enhance his personal worth, and perfect himself.

– Paul VI, *Populorum Progressio*, 15.

Preface

This thesis summarizes the work carried out during my Ph.D. studies at the Image Sciences Institute (ISI) of the University Medical Center Utrecht, The Netherlands. The ISI is a multidisciplinary group comprising both technical and medical research communities. Both disciplines have left their imprint on this thesis. The chapters report on the development and evaluation of model-based algorithms for medical image analysis.

Writing a thesis is a titanic enterprise, the result of which reflects by no means only the author's efforts and dedication. Perhaps more than anyone else, I am aware of how much help I have received during the last three and a half years. First off, I would like to thank my promotor Prof. Max Viergever for offering me the opportunity to do this research within his group, and for providing the required financial support. I am greatly indebted to my daily supervisor Wiro Niessen. Wiro, you were the one who explained to me how to carry out research, and you bore most of my inexperience in all matters. Looking back I think we made an excellent team ;-).

This work was done in collaboration with Philips Medical Systems, Department of EasyVision Advanced Development. I would like to thank Frans Gerritsen, Steven Lobregt, Marcel Breeuwer and Bert Verdonck (Philips Medical Systems, Best), Cristian Lorenz and Jürgen Weese (Philips Research, Hamburg), and Sherif Makram-Ebeid (Philips Research, Paris) for their input and critiques at several stages of my work. Reconciling the interests of a company with those of a university is a challenging task. I believe that this collaboration has assisted in shaping my personality, and has instilled a particular flavor into my Ph.D.

A number of people have been involved in the completion of this thesis: Jeanette Bakker, Michael Egmont-Petersen, Otto Elgersma, Romhild Hoogeveen, Paul Nederkoorn, Prof. Johan Reiber, Daniel Rueckert, Jolanda Scheffers, Julia Schnabel, Koen Vincken, Theo van Walsum and Onno Wink. Several people have provided me with data sets or with interesting applications. Prof. Mali (Department of Radiology) from the University Medical Center Utrecht provided me with the carotid data sets for the evaluation in Chapter 4. The Department of Psychiatry of the University Medical Center Utrecht kindly provided me with the caudate nucleus data sets and manual segmentations for Chapter 6. The radius data sets and segmentations used in the same chapter were provided by Maarten Hoogbergen. Finally, the cardiac functional MR data used in Chapter 7 was kindly provided by Warren J. Manning, co-director of the Cardiac MR Center at the Beth Israel Deaconess Medical Center in Boston, US.

Others have helped me in solving the many technical and administrative problems in the materialization of this thesis. I should mention Gerard van Hoorn, for

his patience and assistance with computers; Rene Mandl and Hugo Schnack, for providing assistance in many practical issues; Sandra Boeijink, for easing the economical matters, and Margo Agterberg for her help in all kinds of secretarial work.

It is difficult not to mention all my colleagues and friends that have given support and enthusiasm during the years of my Ph.D.: Arjan, Astrid, Bart, Bram, Carolien, Caroline, Clemens, Chris B, Chris K, Erik and Greetje, Evert-Jan, Estia, Freek, Herke Jan, Hugo, Ingrid, Josien, Manon and Edward, Marco, Marleen, Marloes, Miriam, Nelly, Remko and Adri, Robert, Shirley, Stiliyan, Tanja, Theo and Paula, and Wilbert. In particular I would like to mention Thijs and Joes since we started our Ph.D. on the same day and we have been through many things together. Thanks to both for agreeing to be “paranimf” during the public defense of my thesis. Also particular thanks to Kees, Wiro and Wilbert who helped with the Nederlandse Samenvatting.

I also would like to express my gratitude to the people I have lived with during my stay in The Netherlands, Mr Theo and Mrs Johnny Matton, and Pisit Suwannachot. Thanks for making me feel “at home” in The Netherlands. I would like to thank Mrs Ann Kearns who took care of me as if I were her own grandson during my stay in London. A special word of thanks goes to Spain where I have so many friends that have helped me during the last few years. Their friendship has stimulated me to carry on through difficult periods. In particular I would like to thank Pere Talavera and Javier López for their visits to The Netherlands and their support.

The work described in the last two chapters of this thesis was carried out partly in London, UK, during a combined three-month stay at the Visual Information Processing Group, Department of Computing, Imperial College, and at the Computational Imaging Science Group at Guy’s Hospital, King’s College London. I am very thankful to Daniel Rueckert and Julia Schnabel for their help and enthusiasm in the last phase of my project. I would also like to express my gratitude to Prof. David Hawkes for his interest in my work and for agreeing to be an external examiner for my thesis.

I am particularly indebted to my parents, Jorge and Ana, and to my siblings: Pablo, Leandro, Andrés, Mariano, Luciana and Santiago. You have supported me during all these years of my undergraduate and graduate studies. Although far away, you know that you are close in my heart. Very special thanks to my girlfriend, Silvia, thankyou for always helping me to put things into the right perspective. Without your support this thesis would not have been completed. It is impossible not to conclude by giving thanks to God for all the good things I received during my Ph.D. studies. Beyond the influences exerted by any human or environmental factor, only within Him may we find the deepest explanation to fully comprehend the trajectory of our lives.

Alejandro F. Frangi
London/Utrecht, December 2000

Contents

Colophon	ii
Preface	vii
Abbreviations	xiii
1 Introduction and Summary	1
2 Multiscale vessel enhancement filtering	7
2.1 Introduction	7
2.2 Method	8
2.3 Results	12
2.3.1 2-D Digital Subtraction Angiography images	12
2.3.2 3-D Magnetic Resonance Angiography images	13
2.4 Discussion	15
3 Model-based quantitation of	
3-D Magnetic Resonance angiographic images	17
3.1 Introduction	17
3.2 Model-based vessel segmentation	20
3.2.1 Central vessel axis model	20
3.2.2 Diameter criterion for MRA	25
3.2.3 Vessel wall model	26
3.3 Implementation issues	27
3.3.1 Image resampling	27
3.3.2 Scenario for 3-D interaction	27
3.3.3 Model optimization	29
3.3.4 Geometric modeling	30
3.4 In vitro evaluation	31
3.4.1 Phantom and image acquisition	31
3.4.2 Performance assessment	32
3.5 Results	33
3.5.1 Carotid bifurcation phantom	33
3.5.2 Illustration of the algorithm on patient data	34
3.6 Discussion	35

3.A	Appendix: Analytical model of a toroidal vessel	38
3.B	Appendix: Analytical expression for the gradient of Equation (3.16) . .	39
3.C	Appendix: Segmental vessel wall deformation	42
4	Quantitative analysis of vascular morphology from 3-D MR angiograms: <i>in vitro</i> and <i>in vivo</i> results	47
4.1	Introduction	47
4.2	Algorithm overview	49
4.3	Materials and methods	51
4.3.1	Phantoms	51
4.3.2	Image acquisition	53
4.3.3	Geometric modeling	54
4.4	<i>In vitro</i> results	54
4.4.1	Linear and carotid bifurcation phantoms	55
4.4.2	Cerebral vasculature phantom	58
4.5	<i>In vivo</i> results	61
4.6	Discussion and conclusion	63
4.A	Appendix: Central vessel axis image feature	66
5	Three-dimensional modeling for functional analysis of cardiac images – A review	71
5.1	Introduction	71
5.2	Imaging techniques for cardiac examination	73
5.2.1	Angiocardiology	73
5.2.2	Cardiac ultrasound	74
5.2.3	Isotope imaging	75
5.2.4	Cardiac Computed Tomography	75
5.2.5	Magnetic Resonance Imaging	75
5.3	Classical descriptors of cardiac function	76
5.3.1	Global functional analysis	76
5.3.2	Motion and deformation analysis	78
5.4	Overview of modeling techniques	80
5.4.1	Surface models	81
5.4.2	Volumetric models	89
5.4.3	Deformation models	90
5.5	Discussion	95
5.5.1	Validation	95
5.5.2	Performance criteria	96
5.6	Conclusions and suggested future research	100
5.A	Appendix: Non-traditional shape and motion descriptors	102
5.B	Appendix: MR tag localization techniques	105
6	Automatic 3-D statistical shape model construction via atlas-based landmarking and volumetric elastic registration	107
6.1	Introduction	107
6.2	Active Shape Models	109

6.2.1	Modeling shape variation	109
6.2.2	Choice of the number of modes	111
6.3	Method	111
6.3.1	Overview	111
6.3.2	Atlas building	111
6.3.3	Atlas landmarking	113
6.3.4	Landmark propagation	114
6.4	Results	114
6.4.1	Data sets	114
6.4.2	Atlas construction	115
6.4.3	Automatically built statistical shape models	116
6.4.4	Reconstruction error	116
6.5	Discussion and conclusion	118
6.A	Appendix: Elastic registration with FFDs	123
6.A.1	Global transformation	123
6.A.2	Local transformation	123
6.A.3	Speed-up of the elastic registration	124
6.A.4	Registration measure	124
6.A.5	Optimization	125
6.B	Appendix: On the statistical analysis of spatial transformation parameters	126
7	Automatic construction of multiple-object three-dimensional statistical shape models: Application to cardiac modeling	129
7.1	Introduction	129
7.2	Methods	130
7.2.1	Overview	130
7.2.2	Preprocessing	131
7.2.3	Atlas construction	132
7.2.4	Landmark extraction	135
7.2.5	Landmark propagation	135
7.3	Results	137
7.3.1	Data sets and pre-processing	137
7.3.2	Comparison of label images	137
7.3.3	Atlas construction	138
7.3.4	Statistical shape models	140
7.4	Discussion and conclusions	145
7.A	Appendix: Elastic registration with multi-level FFDs	146
7.A.1	Transformation model	146
7.A.2	Global transformation	146
7.A.3	Local transformation	147
7.A.4	Hierarchical FFD optimization	149
	Bibliography	151
	Samenvatting	169

Publications	173
Curriculum Vitae	175

Abbreviations

<i>n</i> -D	<i>n</i> -dimensional, $n \in \{2, 3, 4\}$.
<i>n</i> DE	<i>n</i> -dimensional echocardiography.
ASM	Active shape model.
BA	Biplane angiography.
CAD	Computer-aided design.
CDT	Continuous distance transform.
CE	Contrast-enhanced.
CFM	Color flow (Doppler) mapping.
CI	Cardiac index.
CNR	Contrast-to-noise ratio.
CO	Cardiac output.
CSG	Constructive solid geometry.
CT	Computed tomography.
CTA	Computed tomography angiography.
CVD	Cardiovascular disease.
CVP	Closest vessel projection.
DOF	Degrees of freedom.
DSA	Digital subtraction angiography.
DSR	Dynamic spatial reconstructor.
EBCT	Electron beam computed tomography.
EDV	End diastolic volume.
EF	Ejection fraction.
ESV	End systolic volume.
FE	Finite element.
FFD	Free-form deformation.
FOV	Field of view.
FWHM	Full-width-half-maximum.
FWTM	Full-width-10%-maximum.
GCG	Geometric cardiogram.
Gd-DTPA	Gadopentetate dimeglumine.
GDT	Geometrically deformable template.
HARP	Harmonic phase.
HR	Heart rate.
ICP	Iterative closest point (algorithm).
KLT	Karhunen-Loeve transform.

LV	Left ventricle.
LVM	Left ventricular mass.
LVV	Left ventricular volume.
MF	Wall/tissue motion field.
MIP	Maximum intensity projection.
MPR	Multi-planar reformatting.
MRA	Magnetic resonance angiography.
MRI	Magnetic resonance imaging.
MTI	Model tag intersections.
NN	Neural network.
NURBS	Non uniform rational B-spline.
PCA	Phase-contrast angiography.
PCA	Principal component analysis (Chap. 7).
RV	Right ventricle.
RVV	Right ventricular volume.
SA	Strain analysis.
SPAMM	Spatial modulation of magnetization.
SPECT	Single photon emission computed tomography.
SSP	Similar shape patches.
SV	Stroke volume.
SVI	Stroke volume index.
TE	Echo time.
TR	Repetition time.
TOF	Time-of-flight.
US	Ultrasound (imaging).
WT	Wall thickening.

If we begin with certainties, we shall end in doubts; but if we begin with doubts, and are patient in them, we shall end in certainties.

— F. Bacon, 1561-1626

Chapter 1

Introduction and Summary

Volumetric medical imaging techniques, such as Computed Tomography (CT), Magnetic Resonance Imaging (MRI), Positron Emission Tomography (PET), Single Photon Emission Computed Tomography (SPECT) and Ultrasound imaging (US), provide a large amount of anatomical and functional information to clinicians and researchers. As a consequence, the demand for processing tools to optimally benefit from the wealth of information available has increased dramatically, which has made computerized medical image analysis a vivid field of research.

Over the years, medical image analysis has enlarged its area of applications. Typical problems tackled by this discipline have been, amongst others, image registration, quantification, visualization of volumetric data sets, rigid and non-rigid motion analysis, image segmentation and pattern recognition. More recently, the introduction of computer-assisted techniques in surgery and treatment planning has inspired new research areas, such as the development of image analysis tools for surgical planning and simulation, and intra-operative navigation.

Initially, many medical image analysis tasks were tackled by low-level mathematical operators followed by some sort of grouping strategy. For instance, in the area of image segmentation, techniques like thresholding, region growing, statistical pixel clustering and relaxation labeling are amongst the most popular techniques. These *bottom-up* approaches were meant to be fully automatic. Although fully automatic procedures seem to be ideal from an operator's standpoint, their efficacy has been limited to applications where the structures of interest have a good contrast with respect to the background. The local nature of these techniques makes them vulnerable to the imperfections of real clinical data where image quality is limited by safety considerations, constrained time windows and patient movement.

In the last two decades many *top-down* approaches have emerged in the medical image analysis literature. In these approaches the key concept is the introduction of *prior knowledge* in the form of a *model* that aids the image analysis task. A model, referring to a simplification of the physical world, is often used in science to reduce a problem to manageable proportions. However, in medical image analysis, model-based strategies are usually more sophisticated than model-free approaches. The use of generic or prior contextual knowledge is particularly attractive in medical

applications where the structure (tissue or organ) to be analyzed is usually known beforehand as well as the imaging modality and the acquisition protocol.

Several arguments can be provided in favor of model-based medical image analysis. In some cases, the use of prior models arises by necessity. This is typically the case in images of poor quality where the solution space of a given processing task has to be constrained with prior knowledge in order to reach a sensible solution. Another advantage is that a higher level of abstraction in solving an analysis task can be achieved. A few examples will clarify this. A shape model may be expressed in terms of a few parameters that directly offer diagnostic information. Also a geometric model can be used to support user-friendly interaction, *e.g.* manipulating curves or surfaces rather than interacting with the data at voxel level. A spatio-temporal model can provide a compact description of the motion in an image sequence which can be more robust to outlier frames and can incorporate prior constraints like motion periodicity. A further reason to opt for a model-based approach is computational complexity. Usually, the use of a model reduces the number of degrees of freedom with respect to a model-free analysis. This is typically the case in shape models where a suitable geometric representation can reduce the number of required parameters to describe shape.

Frequently, model-based approaches deal with prior shape knowledge, *i.e.* the prior is a geometric model. However, there are other sources of prior knowledge that can be considered. In medical image analysis, at least three types of modeling can be distinguished:

1. *Modeling image acquisition.* There are many factors that contribute to the image formation process. The underlying physical imaging principle for image contrast, the sampling strategy, the presence of possible image artifacts, the imaging device, and environmental noise all affect the eventual image data. Modeling this information can aid in deciding how to interpret the image data or in improving the accuracy of algorithms.
2. *Modeling the subject being imaged.* Prior knowledge concerning the anatomy, function, physiology and/or pathology of the structure of interest can be incorporated in the procedure.

Anatomical knowledge is probably one of the most common types of prior knowledge. Incorporating this knowledge allows one to apply constraints that help to regularize the image analysis task. For instance, shape knowledge can be introduced by selecting a suitable model parameterization or by performing a statistical shape analysis leading to a description of the average shape and its variability over a population of subjects.

Modeling the subject being imaged is not necessarily restricted to shape modeling. Sometimes the task is to relate the information present in the image data to a model describing the underlying (patho)physiology of the subject under investigation.

3. *Modeling the human observer.* This type of knowledge models the effect of user interaction in clinical decision making. In clinical practice, manual image

analysis procedures sometimes follow written protocols in order to maximize the reproducibility of the results. A careful study of the protocol can provide hints on which steps can be automated.

Another related issue is efficient user interaction. Currently, in most image analysis approaches, the user is kept outside the loop of the algorithm. Interaction is restricted, in many cases, to editing the results of a more or less automatic algorithm. An efficient interaction mechanism should allow the user to guide the process in an intuitive manner; ideally small user actions should have a large impact on the final result thus avoiding fully manual editing. At the same time the results of the interaction should be intuitive and reproducible.

This thesis explores the potential of using the above mentioned types of knowledge in 3-D model-based image analysis with the focus on vascular and cardiac MRI.

Chapters 2 to 4 present different aspects of a model-based technique for semi-automated quantification of linear vessel segments from 3-D Magnetic Resonance Angiography (MRA).

Chapter 2 is concerned with a multiscale filter for the enhancement of vessels in 2-D and 3-D angiograms. Here, the prior knowledge is expressed in the form of a local discriminant function that enhances tubular structures. This discriminant is based on a suitable combination of the eigenvalues of the Hessian matrix of an image. In the presence of a tubular structure, the eigenvalues of the Hessian matrix satisfy certain relationships, which are used to discriminate between 3-D tubular patterns and patterns corresponding to plate- or blob-like structures. The developed filter has proven useful as a preprocessing algorithm to highlight the vasculature from other surrounding structures. This can be particularly appropriate for visualization purposes. However, as this preprocessing step tends to introduce vessel narrowing, a more accurate method for quantitative analysis of vessel morphology was developed in the next chapter.

Chapter 3 applies the filter developed in Chapter 2 to determine the central vessel axis in 3-D MRA images. This procedure is initialized using an efficient user interaction technique that naturally incorporates the knowledge of the operator about the vessel of interest. Also in this chapter, a linear vessel model is used to recover the position of the vessel wall in order to carry out an accurate quantitative analysis of vascular morphology. Prior knowledge is provided in two main forms: a cylindrical model introduces a shape prior while prior knowledge on the image acquisition (type of MRA technique) is used to define an appropriate vessel boundary criterion. Preliminary *in vivo* and *in vitro* results illustrate that both geometric and acquisition related knowledge can effectively be incorporated into the framework of deformable models.

In order to gain clinical acceptance, evaluation of medical image analysis algorithms is an important prerequisite. Accordingly, in Chapter 4 an extensive *in vitro* and *in vivo* evaluation of the algorithm introduced in Chapter 3 is described. *In vitro* experiments have the advantage that true dimensions (*e.g.* vessel radii) are known and can be objectively compared to those obtained by other methods. On the other hand, *in vivo* experiments represent a realistic clinical test case. In order to evaluate the results, measurements carried out with the model-based technique have been

compared to measurements obtained by means of expert readers. The *in vitro* experiments show that the proposed method can achieve similar accuracy to manual quantification of vessel dimensions in the three major MR angiographic techniques (time-of-flight, phase contrast, and contrast-enhanced MRA). However, the boundary criterion used for phase contrast angiography can be inaccurate in regions with large flow variations (stenotic regions). The preliminary *in vivo* experiments carried out using time-of-flight MRA in Chapter 3 indicated that in highly stenotic vessels the presence of flow artifacts can hamper the applicability of the model-based technique. Chapter 4 provides results on state-of-the-art contrast-enhanced MRA of the carotid arteries where the model-based technique can provide estimates of the degree of stenosis with an accuracy similar to that of manual operators. Additionally, where this technique can be applied, a number of 3-D morphological parameters are readily available.

Chapters 5 to 7 change the focus to cardiac image analysis, an area where the use of model knowledge has been extensively explored.

Spatio-temporal cardiac images are currently acquired using various imaging modalities like CT, MRI and US. Images are usually acquired in a small temporal window which limits the achievable image quality. Moreover, a typical functional cardiac study involves a large amount of (4-D) data which requires laborious manual post-processing before the relevant information is obtained. Over the last two decades, a rich bibliography has appeared in the area of 3-D cardiac modeling but no critical review was available. Chapter 5 presents an extensive survey, a categorization and a critical review of the field. The most important observation from this review is that although many algorithms to model and recover cardiac shape and motion have been presented in the literature, none of them has been able to completely achieve these goals in an automatic fashion. From this survey it can also be noted that most of the current approaches to cardiac modeling use standard geometrical primitives like superquadrics, B-splines or polygonal meshes to recover the shape of the ventricles of the heart. Shape recovery is usually achieved by solving an optimization problem that balances image-guided terms (*e.g.* intensity- or gradient-based information) with shape regularization terms that limit the flexibility of the selected geometrical representation. Whereas these shape constraints are usually rather general, a promising methodology to limit the geometrical representations to plausible cardiac shapes are statistical shape models. These models can describe the average shape and its variability over a population of sample shapes. However, this approach has not been used for 3-D cardiac modeling. One possible explanation for this is the inherent difficulty in building 3-D statistical shape models which requires the extraction of a set of corresponding 3-D landmarks in a set of sample shapes. This problem is the main topic addressed in the last two chapters.

Chapter 6 introduces a new algorithm to build 3-D statistical shape models from a set of sample shapes. Existing approaches first landmark all shapes, and subsequently determine landmark correspondences. In our approach, all shapes in the training set inherit the landmarks from an atlas via volumetric elastic registration. This approach presents some advantages over previously published methods: it can handle multiple-part structures and requires less restrictive assumptions on the structure's topology.

The applicability of the method has been illustrated by the construction of statistical shape models of two anatomical structures: the radius, a bone of the wrist, and the caudate nucleus, a deep structure of the brain.

In Chapter 7, the method as introduced in Chapter 6 is extended to build statistical shape models from cardiac MRI data, containing both the endo- and epicardial wall of the left ventricle and the endocardial wall of the right ventricle. Since anatomical variability of the heart is quite large, the volumetric elastic registration algorithm had to be modified; a hierarchical approach was used to determine the deformation field in a coarse-to-fine manner. Additionally, whereas maximization of the normalized mutual information was the registration measure employed in Chapter 6, a new similarity measure coined label consistency has been introduced in this chapter. This new measure is more suitable for images containing multiple objects. The combination of the hierarchical representation of the deformation field and the new registration measure could successfully cope with the large shape variability present among the cardiac chambers of several subjects. The results presented in Chapter 7 pave the way for 3-D cardiac MR image segmentation using statistical shape models.

A journey of a thousand miles begins with a single step.

— Confucius, 551-479 B.C.

Chapter 2

Multiscale vessel enhancement filtering

Abstract — The multiscale second order local structure of an image (Hessian) is examined with the purpose of developing a vessel enhancement filter. A measure of vessel-likeness is obtained on the basis of all eigenvalues of the Hessian. This measure is tested on two-dimensional Digital Subtraction Angiography (DSA) and three-dimensional aortoiliac and cerebral Magnetic Resonance Angiographic (MRA) data. Its clinical utility is shown by the simultaneous noise and background suppression and vessel enhancement in maximum intensity projections and volumetric displays.

Adapted from: A.F. Frangi, W.J. Niessen, K.L. Vincken, and M.A. Viergever (1998). *Multiscale vessel enhancement filtering*. *Medical Image Computing & Computer Assisted Interventions, MICCAI98 (Boston, USA)*, vol 1496 of *Lecture Notes in Computer Science*, pp. 130–7.

2.1 Introduction

The development of accurate visualization and quantification techniques for the human vasculature is an important prerequisite for a number of clinical procedures. Grading of stenoses is important in the diagnosis of the severity of vascular disease since it determines the treatment therapy. Interventional procedures such as the placement of a prosthesis in order to prevent aneurysm rupture or a bypass operation require an accurate insight into the three dimensional vessel architecture.

Both two-dimensional projection techniques, such as Digital Subtraction Angiography (DSA), and three-dimensional modalities as X-ray rotational angiography, Computed Tomography Angiography (CTA) and Magnetic Resonance Angiography (MRA) are employed in clinical practice. Although CTA and MRA provide volumetric data, the common way of interpreting these images is by using a maximum intensity projection.

The main drawbacks of maximum intensity projections are the overlap of non-vascular structures and the fact that small vessels with low contrast are hardly visible. This has been a main limitation in time-of-flight MRA [84]. In contrast enhanced

MRA [243] the delineation of these vessels is considerably improved, but other organs can be still projected over the arteries.

The purpose of this chapter is to present a method to enhance vessel structures with the eventual goal of vessel segmentation. A vessel enhancement procedure as a preprocessing step for maximum intensity projection display will improve small vessel delineation and reduce organ overprojection. Segmentation of the vascular tree will facilitate volumetric display and will enable quantitative measurements of vascular morphology.

There are several approaches to vessel enhancement. Some of them work at a fixed scale and use (nonlinear) combinations of finite difference operators applied in a set of orientations [50, 83, 84]. Orkisz *et al.* [221] presents a method that applies a median filter in the direction of the vessel. All these methods have shown problems to detect vessels over a large size range since they perform a fixed scale analysis. Moreover, to handle voxel anisotropy, these methods usually need to resample the dataset or to resource to $2\frac{1}{2}D$ processing [221]. Multi-scale approaches to vessel enhancement include “cores” [13], steerable filters [162, 163], and assessment of local orientation via eigenvalue analysis of the Hessian matrix [184, 260].

The multiscale approach we discuss in this chapter is inspired by the work of Sato *et al.* [260] and Lorenz *et al.* [184] who use the eigenvalues of the Hessian to determine locally the likelihood that a vessel is present. We modify their approach by considering all eigenvalues and giving the vessel likeliness measure an intuitive, geometric interpretation. Examples on medical image data are included.

2.2 Method

In our approach we conceive vessel enhancement as a filtering process that searches for geometrical structures which can be regarded as tubular. Since vessels appear in different sizes it is important to introduce a measurement scale which varies within a certain range.

A common approach to analyze the local behavior of an image, $I(\mathbf{x})$, is to consider its Taylor expansion in the neighborhood of a point \mathbf{x}_o ,

$$I(\mathbf{x}_o + \delta\mathbf{x}_o, \sigma) \approx I(\mathbf{x}_o, \sigma) + \delta\mathbf{x}_o^T \nabla_{o,\sigma} + \delta\mathbf{x}_o^T \mathcal{H}_{o,\sigma} \delta\mathbf{x}_o \quad (2.1)$$

This expansion approximates the structure of the image up to second order. $\nabla_{o,\sigma}$ and $\mathcal{H}_{o,\sigma}$ are the gradient vector and Hessian matrix of the image computed in \mathbf{x}_o at scale σ . To calculate these differential operators of $I(\mathbf{x})$ in a well-posed fashion we use concepts of linear scale-space theory [102, 160]. In this framework differentiation is defined as a convolution with derivatives of Gaussians:

$$\frac{\partial}{\partial x} I(\mathbf{x}, \sigma) = \sigma^\gamma I(\mathbf{x}) * \frac{\partial}{\partial x} G(\mathbf{x}, \sigma) \quad (2.2)$$

where the D-dimensional Gaussian is defined as:

$$G(\mathbf{x}, \sigma) = \frac{1}{(2\pi\sigma^2)^{D/2}} e^{-\frac{\|\mathbf{x}\|^2}{2\sigma^2}} \quad (2.3)$$

The parameter γ was introduced by Lindeberg [181] to define a family of normalized derivatives. This normalization is particularly important for a fair comparison of the response of differential operators at multiple scales. When no scale is preferred γ should be set to unity.

Analyzing the second order information (Hessian) has an intuitive justification in the context of vessel detection. The second derivative of a Gaussian kernel at scale σ generates a probe kernel that measures the contrast between the regions inside and outside the range $(-\sigma, \sigma)$ in the direction of the derivative (Figure 2.1(a)). This approach is the one followed in this work.

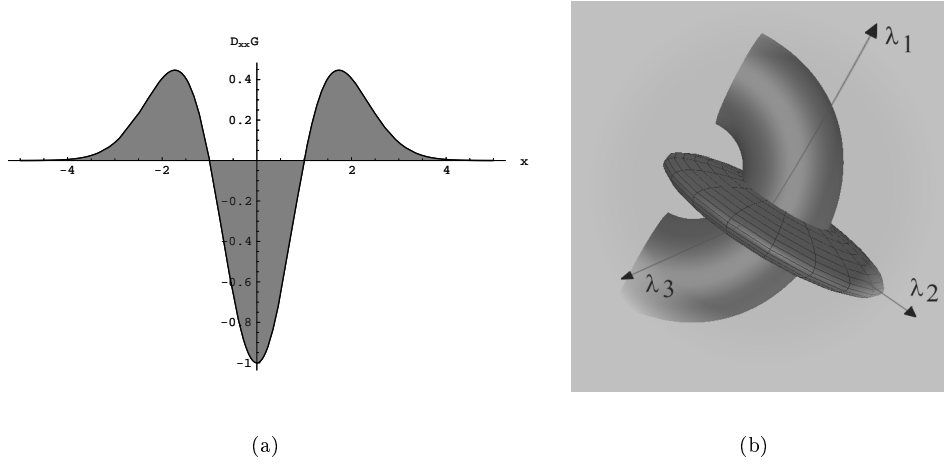


Figure 2.1. a) The second order derivative of a Gaussian kernel probes inside/outside contrast of the range $(-\sigma, \sigma)$. In this example $\sigma = 1$. b) The second order ellipsoid describes the local principal directions of curvature.

The third term in Equation (2.1) gives the second order directional derivative,

$$\delta \mathbf{x}_o^T \mathcal{H}_{o,\sigma} \delta \mathbf{x}_o = \left(\frac{\partial}{\partial \delta \mathbf{x}_o} \right) \left(\frac{\partial}{\partial \delta \mathbf{x}_o} \right) I(\mathbf{x}_o, \sigma) \quad (2.4)$$

The idea behind eigenvalue analysis of the Hessian is to extract the principal directions in which the local second order structure of the image can be decomposed. Since this directly gives the direction of smallest curvature (along the vessel) application of several filters in multiple orientations is avoided. This latter approach is computationally more expensive and requires a discretization of the orientation space.

Let $\lambda_{\sigma,k}$ denote the eigenvalue corresponding to the k -th normalized eigenvector $\hat{\mathbf{u}}_{\sigma,k}$ of the Hessian $\mathcal{H}_{o,\sigma}$, all computed at scale σ . From the definition of eigenvalues:

$$\mathcal{H}_{o,\sigma} \hat{\mathbf{u}}_{\sigma,k} = \lambda_{\sigma,k} \hat{\mathbf{u}}_{\sigma,k} \quad (2.5)$$

and it follows that

$$\hat{\mathbf{u}}_{\sigma,k}^T \mathcal{H}_{o,\sigma} \hat{\mathbf{u}}_{\sigma,k} = \lambda_{\sigma,k} \quad (2.6)$$

By analyzing Equations (2.4)-(2.6) a nice geometric interpretation arises. The eigenvalue decomposition extracts three orthonormal directions which are invariant up to a scaling factor when mapped by the Hessian matrix. In particular, a spherical neighborhood centered at \mathbf{x}_o with radius 1, $\mathcal{N}_{\mathbf{x}_o}$, will be mapped by \mathcal{H}_o onto an ellipsoid whose axes are along the directions given by the eigenvectors of the Hessian and the corresponding axis' semi-lengths are the magnitudes of the respective eigenvalues.

This ellipsoid locally describes the second order structure of the image (thus we coin it *second order ellipsoid* –Figure 2.1(b)-) and can be used as an intuitive construct for the design of geometric similarity measures.

In the remainder of the chapter λ_k will be the eigenvalue with the k -th smallest magnitude ($|\lambda_1| \leq |\lambda_2| \leq |\lambda_3|$). Under this assumption Table 2.1 summarizes the relations that must hold between the eigenvalues of the Hessian for the detection of different structures. In particular, a pixel belonging to a vessel region will be signaled by λ_1 being small (ideally zero), and λ_2 and λ_3 of a large magnitude and equal sign (the sign is an indicator of brightness/darkness). The respective eigenvectors point out singular directions: $\hat{\mathbf{u}}_1$ indicates the direction along the vessel (minimum intensity variation) and $\hat{\mathbf{u}}_2$ and $\hat{\mathbf{u}}_3$ form a base for the orthogonal plane. We are interested in vessel likeliness measures suited for medical images. In MRA and CTA, vessels emerge as bright tubular structures in a darker environment. This *a priori* information related to the imaging modality can be used as a consistency check to discard structures present in the dataset with a polarity different than the one sought. Accordingly, we shall look for structures whose λ_2 and λ_3 are both simultaneously negative.

To summarize, for an ideal tubular structure in a 3-D image:

$$|\lambda_1| \approx 0 \quad (2.7)$$

$$|\lambda_1| \ll |\lambda_2| \quad (2.8)$$

$$\lambda_2 \approx \lambda_3 \quad (2.9)$$

and the sign of λ_2 and λ_3 indicate its polarity.

We emphasize that all three eigenvalues play an important role in the discrimination of the local orientation pattern. This will yield expressions that differ from

2-D		3-D			orientation pattern
λ_1	λ_2	λ_1	λ_2	λ_3	
N	N	N	N	N	noisy, no preferred direction
		L	L	H-	plate-like structure (bright)
		L	L	H+	plate-like structure (dark)
L	H-	L	H-	H-	tubular structure (bright)
L	H+	L	H+	H+	tubular structure (dark)
H-	H-	H-	H-	H-	blob-like structure (bright)
H+	H+	H+	H+	H+	blob-like structure (dark)

Table 2.1. Possible patterns in 2-D and 3-D, depending on the value of the eigenvalues λ_k (H=high, L=low, N=noisy, usually small, +/- indicate the sign of the eigenvalue). The eigenvalues are ordered: $|\lambda_1| \leq |\lambda_2| \leq |\lambda_3|$.

the similarity measures proposed by Sato *et al.* [260] and Lorenz *et al.* [184] who only make use of two eigenvalues in their respective 3-D line filters. In particular, Sato’s approach [260] uses a different eigenvalue ordering scheme: they are sorted in increasing *value* (not magnitude), and only the two largest are considered in the line filter. This implies that dark and bright lines are not treated in a similar manner.

Our dissimilarity measure takes into account two geometric ratios based on the second order ellipsoid. The first ratio accounts for the deviation from a blob-like structure but cannot distinguish between a line- and a plate-like pattern:

$$\mathcal{R}_B = \frac{\text{Volume}/(4\pi/3)}{(\text{Largest Cross-Section Area}/\pi)^{3/2}} = \frac{|\lambda_1|}{\sqrt{|\lambda_2\lambda_3|}} \quad (2.10)$$

This ratio attains its maximum for a blob-like structure and is zero whenever $\lambda_1 \approx 0$, or λ_1 and λ_2 tend to vanish (notice that λ_1/λ_2 remains bounded even when the second eigenvalue is very small since its magnitude is always larger than the first).

The second ratio refers to the largest area cross-section of the ellipsoid (in the plane orthogonal to $\hat{\mathbf{u}}_1$) and accounts for the aspect ratio of the two largest second order derivatives. This ratio is essential for distinguishing between plate-like and line-like structures since only in the latter case it will be zero,

$$\mathcal{R}_A = \frac{(\text{Largest Cross-Section Area})/\pi}{(\text{Largest Axis Semi-length})^2} = \frac{|\lambda_2|}{|\lambda_3|} \quad (2.11)$$

The two geometric ratios we introduced so far are grey-level invariant (*i.e.*, they remain constant under intensity re-scalings). This ensures that our measures only capture the geometric information of the image. However, in MRA and CTA images there is additional knowledge available: vessel structures are brighter than the background and occupy a (relatively) small volume of the whole dataset. If this information is not incorporated background pixels would produce an unpredictable filter response due to random noise fluctuations. However, a distinguishing property of background pixels is that the magnitude of the derivatives (and thus the eigenvalues) is small, at least for typical signal-to-noise ratios present in acquired data sets. To quantify this we propose the use of the norm of the Hessian. We use the Frobenius matrix norm since it has a simple expression in terms of the eigenvalues when the matrix is real and symmetric. Hence we define the following measure of “second order structureness”,

$$\mathcal{S} = \|\mathcal{H}\|_F = \sqrt{\sum_{j \leq D} \lambda_j^2} \quad (2.12)$$

where D is the dimension of the image.

This measure will be low in the background where no structure is present and the eigenvalues are small owing to the lack of contrast. In regions with high contrast compared to the background, the norm will become larger since at least one of the eigenvalues will be large. We therefore propose the following combination of the

components to define a vessel likeliness function,

$$\mathcal{V}_o(s) = \begin{cases} 0 & \text{if } \lambda_2 > 0 \text{ or } \lambda_3 > 0, \\ (1 - \exp(-\frac{\mathcal{R}_A^2}{2\alpha^2})) \exp(-\frac{\mathcal{R}_B^2}{2\beta^2}) (1 - \exp(-\frac{\mathcal{S}^2}{2c^2})) & \end{cases} \quad (2.13)$$

where α , β and c are thresholds which control the sensitivity of the line filter to the measures \mathcal{R}_A , \mathcal{R}_B and \mathcal{S} . The idea behind this expression is to map the features in Equations (2.10)-(2.12) into probability-like estimates of vessel likeliness according to different criteria. We combine the different criteria using their product to ensure that the response of the filter is maximal only if all three criteria are fulfilled. In all the results presented in this work α and β were fixed to 0.5. The value of the threshold c depends on the grey-scale range of the image and a quarter of the value of the maximum intensity at the vessels of interest has proven to work in most cases. However, the results are fairly insensitive to this threshold and, for a standard imaging protocol, it can be fixed.

The vessel likeliness measure in Equation (2.13) is analyzed at different scales, σ . The response of the line filter will be maximum at a scale that approximately matches the size of the vessel to detect. We integrate the vessel likeliness measure provided by the filter response at different scales to obtain a final estimate of vessel likeliness:

$$\mathcal{V}_o(\gamma) = \max_{\sigma_{min} \leq \sigma \leq \sigma_{max}} \mathcal{V}_o(\sigma, \gamma) \quad (2.14)$$

where σ_{min} and σ_{max} are the maximum and minimum scales at which relevant structures are expected to be found. They can be chosen so that they will cover the range of vessel widths.

For 2-D images we propose the following vessel likeliness measure which follows from the same reasoning as in 3-D,

$$\mathcal{V}_o(s) = \begin{cases} 0 & \text{if } \lambda_2 > 0, \\ \exp(-\frac{\mathcal{R}_B^2}{2\beta^2}) (1 - \exp(-\frac{\mathcal{S}^2}{2c^2})) & \end{cases} \quad (2.15)$$

Here, $\mathcal{R}_B = \lambda_1/\lambda_2$ is the blobness measure in 2-D and accounts for the eccentricity of the second order ellipse.

Equations (2.13) and (2.15) are given for bright curvilinear structures (MRA and CTA). For dark objects (as in DSA) the conditions (or the images) should be reversed.

2.3 Results

2.3.1 2-D Digital Subtraction Angiography images

In this section we show some results of vessel enhancement filtering in 2-D DSA images. These images are obtained by acquiring an X-ray projection when intra-arterial contrast material is injected. A reference image is first acquired without contrast, which is subtracted from the image with contrast for background suppression. If no motion artifacts are present the subtracted images are of such good quality, that further processing is not desirable. We therefore only apply our enhancement filter to

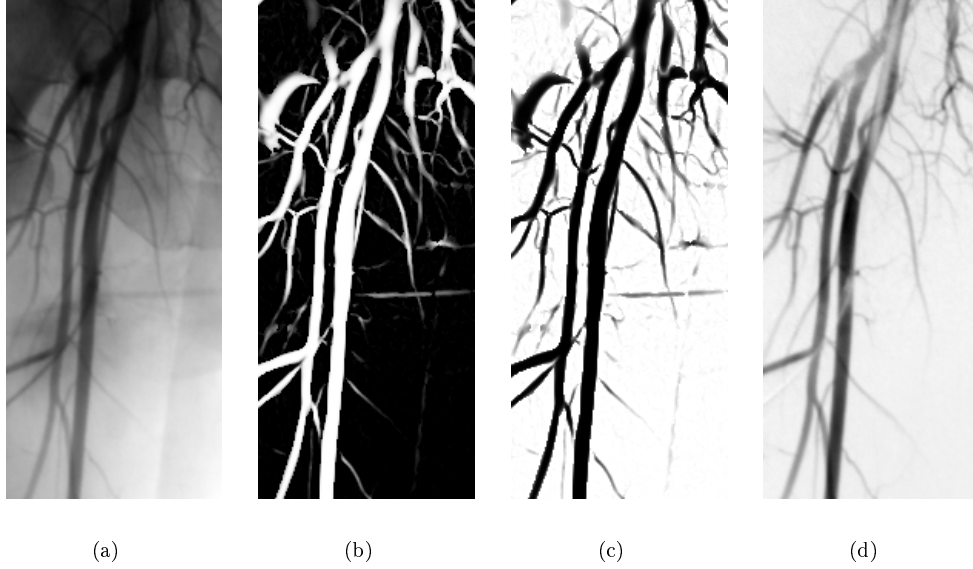


Figure 2.2. *a)* Part of a contrast X-ray image of the peripheral vasculature. *b)* Calculated vessel likeliness of the left image. *c)* Calculated vessel likeliness after inversion of the grey-scale map. *d)* Image obtained by subtracting reference (without contrast) image from left image; shown here to facilitate visual inspection of the results of the filtering procedure.

the contrast images directly, and use the subtracted images to be able to judge the performance of the vessel enhancement filter.

In Figure 2.2, a part of an image of the peripheral vasculature is shown, where performance of subtraction is usually quite good. Although contrast is not very high in the contrast images, the method detects most vessels, over a large size range. Notice however that some artifacts were introduced in regions where background fluctuations have line patterns.

2.3.2 3-D Magnetic Resonance Angiography images

We have applied our method to three-dimensional aortoiliac and cerebral MRA datasets, to show the potential of enhancement filtering to improve visualization of the vasculature. In Figure 2.3 (left) we show a maximum intensity projection which is applied directly to the grey-scale data of an MRA dataset of the aortoiliac arteries.

By determining the vessel likeliness of the MRA image at multiple scales we obtain separate images depicting vessels of various widths. This is shown in Figure 2.4. Here we plotted maximum intensity projections of the vessel likeliness at four scales. The rightmost image shows how we can combine these multiscale measurements by using a scale selection procedure (recall that we work with normalized derivatives), eventually

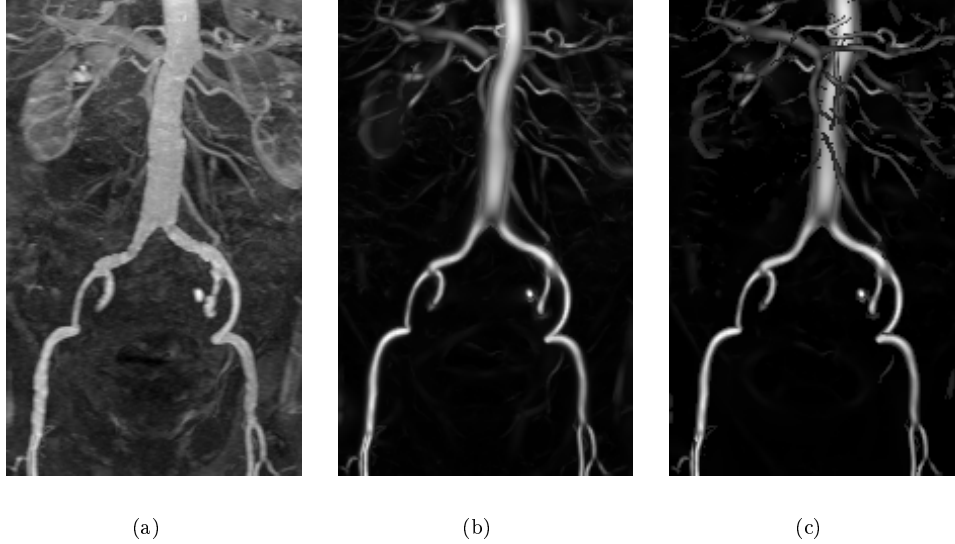


Figure 2.3. *a)* Original maximum intensity projection of a contrast (Gd-DTPA) MRA image. *b)* Maximum intensity projection of vessel enhanced image where good background suppression has been achieved. *c)* Closest vessel projection, facilitated by the filter's ability to suppress background structures.

yielding a display of both the small and large vessels. Since the enhancement filtering does not give a high output at other structures, additional information can more easily be visualized. In the middle frame of Figure 2.3 we show the maximum intensity projection which is obtained after vessel enhancement filtering. In the right frame a closest vessel projection is shown. In this case, it is possible to determine the order in depth of various vascular structures. The excellent noise and background suppression provided by the vessel likelihood measure greatly facilitates the use of a closest vessel projection. In order to compare the results of the vessel enhancement procedure with renderings obtained using a threshold on the original image, we show both renderings in Figure 2.5. We see that the original image has more background disturbance. However, the vessels tend to be narrower in the vessel enhancement image compared to the original dataset. This is due to the fact that at the boundaries of vessels the vessel likelihood is not very high. The vessel enhancement filtering should be used in a subsequent segmentation procedure for obtaining quantitative measurements on the vasculature.

As a last example of the utility of vessel enhancement filtering we applied the procedure to the MRA dataset of the cerebral vasculature of Figure 2.6(a). In order to show the vessel enhancement with accompanying noise suppression, we both scaled the original MRA dataset and the vessel likelihood measure between 0 and 1, and window-leveled the image between 0 and 0.1. Figure 2.6(b) shows that the vessel

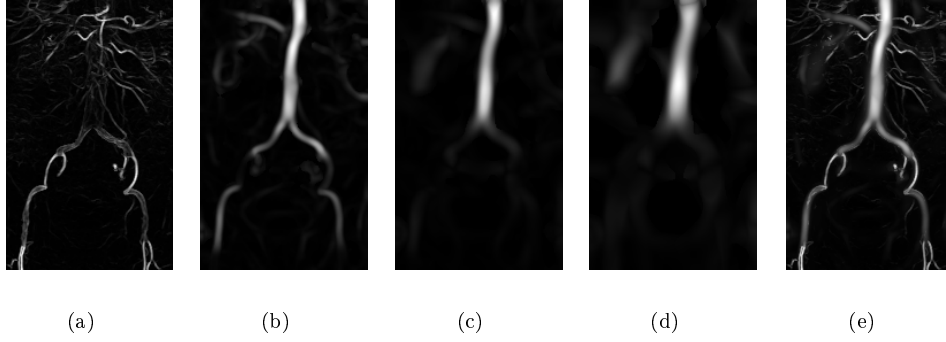


Figure 2.4. *a-d)* Vessel likeliness obtained at increasing four increasing scales ($\sigma = 1, 2, 4$ and 8 pixels). *e)* Result after scale selection.

enhancement procedure keeps the vascular structure while removing noise.

2.4 Discussion

We have presented a method for vessel enhancement filtering which is based on local structure. To this end we examined the local second order ellipsoid. Since we use information about all axes of the second order ellipsoid (all eigenvalues), the approach is a generalization of other existing approaches on the use of second order information for line detection. Recently, Sato *et al.* [260] and Lorenz *et al.* [184] used eigenvalue analysis of the Hessian for vessel enhancement, but they did not use all eigenvalues simultaneously. We have shown the excellent noise and background suppression in a two clinical imaging modalities, underlying the potential of the approach.

It is important to realize that we do not obtain a segmentation of the vasculature. Only if an accurate model of the typical luminance in the perpendicular direction of the vessel is known, an estimate of the size of the vessel can be made based on the response of the filter over scales. However this is often not the case. For example, in MRI it is common to reduce the reconstruction time by restricting the number of lines in k -space (scan percentage) which accounts for a reduction of the effective Fourier spectrum of the measured signal. This technique can lead to ringing artifacts (overshoot) in high transition steps (for example, in vessels boundaries) thus violating simplified profile models (Gaussian/bar-like [163,184]). The vessel likeliness measure can serve as a preprocessing step for visualization and segmentation of this type of images.

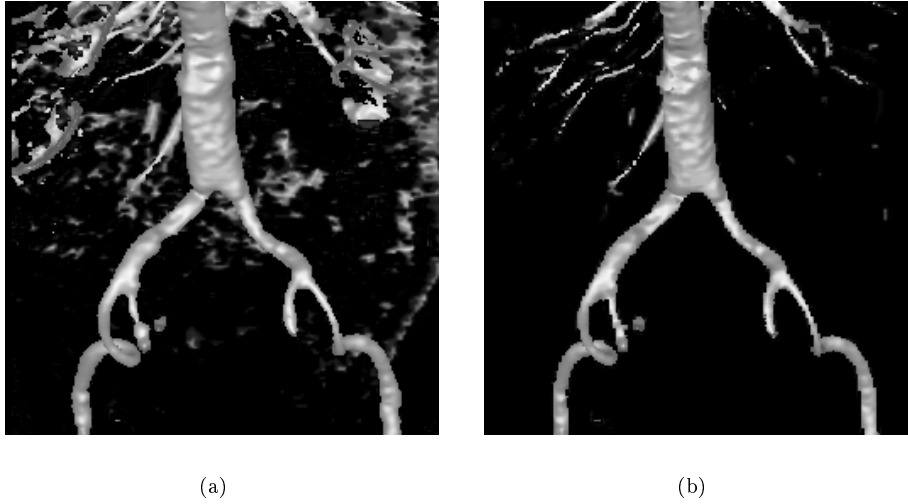


Figure 2.5. *a)* Volume rendering based on threshold of the original dataset. *b)* Volume rendering based on threshold of the vessel likelihood image.

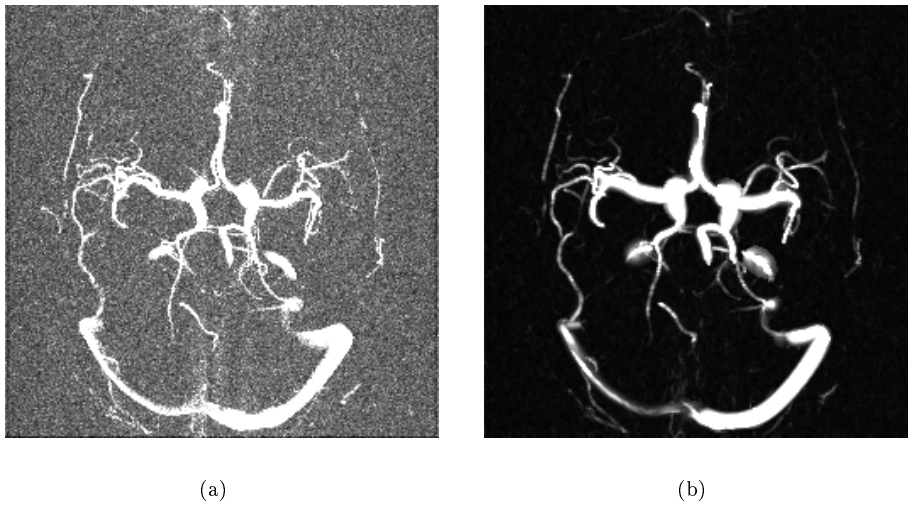


Figure 2.6. *a)* Original maximum intensity projection of a contrast-enhanced MRA dataset of the cerebral vasculature. The image is window-leveled to ten percent of the grey-value range to visualize the noise. *b)* Maximum intensity projection of the vessel likelihood measure with the same window-level settings. Noise is suppressed while largely maintaining the vasculature.

*People seldom improve when they have no other model
but themselves to copy after.*

— O. Goldsmith, 1730-1774

Chapter 3

Model-based quantitation of 3-D Magnetic Resonance angiographic images

Abstract — Quantification of the degree of stenosis or vessel dimensions is important for diagnosis of vascular diseases and planning vascular interventions. Although diagnosis from 3-D Magnetic Resonance Angiograms (MRA) is mainly performed on 2-D maximum intensity projections, automated quantification of vascular segments directly from the 3-D dataset is desirable to provide accurate and objective measurements of the 3-D anatomy.

A model-based method for quantitative 3-D MRA is proposed. Linear vessel segments are modeled with a central vessel axis curve coupled to a vessel wall surface. A novel image feature to guide the deformation of the central vessel axis is introduced. Subsequently, concepts of deformable models are combined with knowledge of the physics of the acquisition technique to accurately segment the vessel wall and compute the vessel diameter and other geometrical properties.

The method is illustrated and validated on a carotid bifurcation phantom, with ground truth and medical experts as comparisons. Also, results on 3-D Time-Of-Flight (TOF) MRA images of the carotids are shown. The approach is a promising technique to assess several geometrical vascular parameters, directly on the source 3-D images, providing an objective mechanism for stenosis grading.

Adapted from: A.F. Frangi, W.J. Niessen, R.M. Hoogeveen, Th. van Walsum, and M.A. Viergever (1999). *Model-based quantitation of 3D magnetic resonance angiographic images*. IEEE Trans Med Imaging, 18(10):946–56, October 1999.

3.1 Introduction

Accurate determination of vessel width is important in grading vascular stenosis. Stenosis quantification in the carotid arteries, for instance, determines the choice of stroke treatment. Studies have revealed that a patient with a severe ($> 70\%$) symptomatic stenosis in the carotids should be operated while patients with stenoses smaller than 30% should not undergo surgical treatment [92, 216]. The benefit of surgery in cases of stenosis with severity between 30% and 70% is still under

investigation [91, 92]. These findings support the relevance of accurate measurement techniques of vascular segments.

Magnetic Resonance Angiography (MRA) is a technique which can supply 3-D information of the vasculature. Although evaluation by radiologists is mainly performed on 2-D Maximum Intensity Projections (MIP) [53], it is known that these lead to vessel width underestimation and decreased Contrast-to-Noise Ratio (CNR) [7, 53, 263].

In order to improve grading of stenoses it would be desirable to obtain quantitative morphological information directly from the original 3-D images, and not only from their projections [6, 67, 134]. To this end, accurate 3-D segmentation tools are required.

Vessel enhancement and segmentation of 3-D images has been investigated by many researchers (Table 3.1). A number of approaches analyze the images at a *single scale* [49, 83, 84, 171, 221, 282, 314], which limits their applicability to images in which the range of vessel widths is small. This is probably the reason of the observation made [49, 83, 84] that small vessels are better enhanced than large vessels. A number of papers have acknowledged the importance of *multi-scale* algorithms that can cope with vessel width variability [13, 106, 163, 167, 168, 184, 239, 260, 261, 286].

The majority of approaches for vessel enhancement and segmentation [13, 106, 163, 167, 168, 184, 261] rely on purely morphological criteria.¹ This has the advantage that the method is applicable to a wide variety of imaging modalities. However, the physics of the image formation influences the eventual depiction of the vessels and not taking this into account may lead to important structural measurement errors. Consider, for instance, the multi-scale approaches that estimate vessel width on the basis of the scale of maximum response of some differential operator [13, 106, 163, 167, 168, 184, 239, 260, 261] as suggested in the seminal work on scale selection by Lindeberg [182]. In these approaches, a number of assumptions are made: the vessel is circular with radius equal to some empirical function of scale [13, 167, 168, 184, 260, 261]. This leads to the fact that the discretization of the scale parameter *a priori* determines the possible vessel diameters. This is specially problematic when one considers that the number of scales is in general small to reduce the computational burden involved in multi-scale methods. However, multi-scale vessel enhancement methods have proven to be very useful for reconstructing the vessel tree in order to provide a 3-D visualization. This can be highly valuable for surgical planning where the relative location of the vessels, rather than their precise width, is the important issue. However accurate quantification in these approaches is limited since the underlying assumptions are often not valid, especially in pathological conditions [90, 227]. The fact that very few quantitative evaluation results have been reported in the literature reveals, to some extent, the difficulty of obtaining accurate measurements with purely geometry guided algorithms. To our knowledge, a few schemes have been proposed for automated quantitative angiography which focus on *quantitative coronary angiography* (QCA) [158, 250] from 2-D X-ray DSA images. Little work has been reported, however, on automated quantitative MR angiography directly from the 3-D data. So, whereas the area of vessel enhancement and segmentation has received considerable attention, there is still progress to be made in

¹Summers *et al.* [286], however, used phase-contrast MR images and, therefore, could also incorporate flow directionality information. Note that in this chapter our main concern is to obtain accurate vessel dimensions and not flow information.

Table 3.1. Summary of literature on vessel enhancement and segmentation.

Reference	D	Multi scale	Method	Application
Aylward [13]	3-D	Y	segmentation of tubular objects based on medial representation and cores [238]	Generic (MRA and CT)
Chen [50]	3-D	N	analysis of the dispersion range of directional filters	(TOF) MRA
Du [83]	3-D	N	non linear combination of second order finite difference filter	TOF MRA
Du [84]	3-D	N	long range correlation filter based on local orientation coherence	TOF MRA
Frangi [106]	2/3-D	Y	eigenanalysis of Hessian matrix	Generic (MRA and DSA)
Koller [163]	2/3-D	Y	non linear combination of linear filters	Generic (MRA, aerial imagery)
Krissian [167]	3-D	Y	filtering algorithm based on eigenanalysis of the Hessian matrix and integration of the gradient field	3-D X-ray angiography
Lorenz [184]	2/3-D	Y	eigenanalysis of Hessian matrix	Generic (MRA and DSA)
Orkisz [221]	$2\frac{1}{2}$ -D	N	non linear anisotropic filter	CE MRA
Poli [239]	2-D	Y	filters steered to vessel width and orientation	coronary angiograms
Sato [260, 261]	3-D	Y	eigenanalysis of Hessian matrix	Generic (MRA and CT)
Summers [286]	3-D	Y	recursive decision making based on occupancy rules and flow features	PC MRA
Wilson [314]	3-D	N	model based statistical classifier	TOF MRA

automated quantitative 3-D MRA.

In this chapter we suggest a novel scheme for quantitative vessel analysis from MRA that uses knowledge of the image formation process to accurately define vessel boundaries. The procedure operates on the 3-D source images (not their projections) using a 3-D deformable model. The model consists of a representation of a central vessel axis coupled to a vessel wall surface. The use of a B-spline representation for the curve and surface models enables the use of already existing, powerful interaction mechanisms inherited from Computer Assisted Design (CAD). For initialization, which is an important step in segmentation schemes based on deformable models, we introduce a technique based on an iso-surface rendering of the vasculature which allows for intuitive and efficient interaction in a 3-D setting.

The chapter is organized as follows. In Section 3.2 we introduce a model-based approach to estimate the central axis and width of a vessel. Section 3.3 discusses some implementation details. Section 3.4 describes the materials and methods involved in the validation of our algorithm with phantom experiments and clinical MRA datasets. After the results of the validation are presented in Section 3.5, the chapter is concluded with a discussion (Section 3.6).

3.2 Model-based vessel segmentation

In this section, a two-step vessel segmentation procedure is proposed. First, a representation of the central vessel axis is obtained. This axis is subsequently used as a reference for extracting the boundaries of the vessel.

3.2.1 Central vessel axis model

The central vessel axis, $\mathbf{C}(v)$, is modeled using a B-spline curve of degree n with $s + 1$ control points. This representation enforces the lumen line to be connected

$$\mathbf{C}(v) = \sum_{i=0}^s N_{in}(v) \mathbf{P}_i \quad (3.1)$$

Here \mathbf{P}_i are the control points, $N_{in}(v)$ is the i -th B-spline basis function of order n [97] and $v \in [0, 1]$. The model (sometimes referred to as *snake*) deforms towards the center of the vessel by minimizing an energy functional, \mathcal{E}^C , containing terms associated with the shape of the spline and the image contents [149, 292]

$$\mathcal{E}^C = \mathcal{E}_{external}^C + \gamma_s^C \mathcal{E}_{stretching}^C + \gamma_b^C \mathcal{E}_{bending}^C \quad (3.2)$$

where

$$\mathcal{E}_{stretching}^C = \frac{1}{\ell} \int_0^1 \|\mathbf{C}_v(v)\|^2 \|\mathbf{C}_v(v)\| dv \quad (3.3)$$

$$\mathcal{E}_{bending}^C = \frac{1}{\ell} \int_0^1 \|\mathbf{C}_{vv}(v)\|^2 \|\mathbf{C}_v(v)\| dv \quad (3.4)$$

$$\ell = \int_0^1 \|\mathbf{C}_v(v)\| dv \quad (3.5)$$

provide the internal constraints over the first and second order parametric derivatives. If we consider the central vessel axis as a physical string, these constraints are associated with simple approximations [313] to its stretch and bending energies respectively. The constants γ_s^C and γ_b^C regulate the contribution of the internal forces with respect to that of the external (or image driven) force. In the physical analogy, the optimization process is interpreted as the evolution of the model towards a state of minimal energy.

The external energy is used to attract the curve towards points which have a high likelihood of lying along the central vessel axis. For this purpose, a new filter has been developed in Chapter 2 that has the following properties: *i*) filters out non line-like structures, *ii*) is maximum at the center of the vessel, and *iii*) is sensitive to vessels of different sizes.

The filter computes the eigenvalues and eigenvectors of the Hessian matrix at multiple scales, σ . The eigenvalues are then combined into a discriminant function that has maximum response for structures behaving as a tube at scale σ .

We shall now formalize these ideas. Let $\mathcal{H}_\sigma(\mathbf{x})$ be the Hessian matrix at a given voxel \mathbf{x}

$$\mathcal{H}_\sigma(\mathbf{x}) = \begin{bmatrix} \mathcal{I}_{xx}(\mathbf{x}) & \mathcal{I}_{xy}(\mathbf{x}) & \mathcal{I}_{xz}(\mathbf{x}) \\ \mathcal{I}_{yx}(\mathbf{x}) & \mathcal{I}_{yy}(\mathbf{x}) & \mathcal{I}_{yz}(\mathbf{x}) \\ \mathcal{I}_{zx}(\mathbf{x}) & \mathcal{I}_{zy}(\mathbf{x}) & \mathcal{I}_{zz}(\mathbf{x}) \end{bmatrix} \quad (3.6)$$

where $\mathcal{I}_{uv}(\mathbf{x})$ denote regularized derivatives of the image $I(\mathbf{x})$, which are obtained by convolving the image with the derivatives of the Gaussian kernel at scale σ [102,160]

$$\mathcal{I}_{uv}(\mathbf{x}) \triangleq \sigma^2 \frac{\partial^2 G(\mathbf{x}, \sigma)}{\partial u \partial v} * I(\mathbf{x}) \quad (3.7)$$

$$G(\mathbf{x}, \sigma) \triangleq \frac{1}{\sqrt{(2\pi\sigma^2)^3}} e^{-\frac{\|\mathbf{x}\|^2}{2\sigma^2}} \quad (3.8)$$

In the remainder of the chapter λ_k will denote the eigenvalue with the k -th smallest magnitude ($|\lambda_1| \leq |\lambda_2| \leq |\lambda_3|$). Under this assumption Table 3.2 summarizes the relations that must hold between the eigenvalues of the Hessian for the detection of different structures. In particular, a pixel belonging to a vessel region will be signaled by λ_1 being small (ideally zero), and λ_2 and λ_3 being large and of equal sign (the sign is an indicator of brightness/darkness). The respective eigenvectors correspond to

Table 3.2. Possible patterns in 3-D based on Hessian eigenanalysis ⁸

λ_1	λ_2	λ_3	orientation pattern
N	N	N	noisy, no preferred direction
L	L	H-	plate-like structure (bright)
L	L	H+	plate-like structure (dark)
L	H-	H-	tubular structure (bright)
L	H+	H+	tubular structure (dark)
H-	H-	H-	blob-like structure (bright)
H+	H+	H+	blob-like structure (dark)

⁸ H=high, L=low, N=noisy and usually small, \pm indicates the sign of the eigenvalue.

Note that $|\lambda_1| \leq |\lambda_2| \leq |\lambda_3|$.

particular directions: $\hat{\mathbf{u}}_1$ indicates the direction along the vessel (minimum intensity variation) and $\hat{\mathbf{u}}_2$ and $\hat{\mathbf{u}}_3$ form a basis for the orthogonal plane.

Based on these observations we developed a discriminant function in Chapter 2 that enhances tubular structures while reducing the effect of other morphologies. The discriminant function can be expressed as

$$\mathcal{V}(\mathbf{x}, \sigma) \triangleq \begin{cases} 0 & \text{if } \lambda_2 > 0 \text{ or } \lambda_3 > 0, \\ \left[1 - \exp\left(-\frac{\mathcal{R}_A^2}{2\alpha^2}\right)\right] \exp\left(-\frac{\mathcal{R}_B^2}{2\beta^2}\right) \left[1 - \exp\left(-\frac{\mathcal{S}^2}{2c^2}\right)\right] & \text{otherwise} \end{cases} \quad (3.9)$$

$$\mathcal{R}_A \triangleq \frac{|\lambda_2|}{|\lambda_3|}, \quad \mathcal{R}_B \triangleq \frac{|\lambda_1|}{\sqrt{|\lambda_2\lambda_3|}} \quad (3.10)$$

$$\mathcal{S} \triangleq \|\mathcal{H}_\sigma\|_F = \sqrt{\sum_j \lambda_j^2} \quad (3.11)$$

where \mathcal{R}_A , \mathcal{R}_B and \mathcal{S} correspond to local measures of cross-sectional asymmetry, blobness and degree of image structure [106]. The parameters α , β and c tune the sensitivity of the filter to deviations in \mathcal{R}_A , \mathcal{R}_B and \mathcal{S} relative to the ideal behavior for a line structure.

In Figure 3.1, a typical filter output for a straight vessel model with Gaussian luminance cross-section is shown. The maximum is achieved at the center, while the signal decays smoothly towards the boundaries. This behavior is desirable since it implies that a long range potential will attract the spline towards the center. Similar results can be derived for other symmetric luminance models which is consistent with results reported on previously published filters [184, 260, 261].

Equation (3.9) explicitly states that the filter response is a function of the scale at which the Gaussian derivatives are computed. The filter is applied at multiple scales that span the range of expected vessel widths according to the imaged anatomy. In order to provide a unique filter output for each pixel, the multiple scale outputs

undergo a *scale selection* procedure [182]. This amounts to computing the maximum filter response across scales

$$V(\mathbf{x}) = \max_{\sigma_{min} \leq \sigma \leq \sigma_{max}} \mathcal{V}(\mathbf{x}, \sigma) \quad (3.12)$$

In this way, vessels of different size will be detected at their corresponding scales and both small and large vessels will be captured with the same scheme. In order to deform the vessel central axis, we chose for the following external energy formulation

$$\mathcal{E}_{external}^C = -\frac{1}{\ell} \int_0^1 V(\mathbf{C}(v)) \|\mathbf{C}_v(v)\| dv \quad (3.13)$$

Minimization of this energy will move the model towards the central axis of the vessel. Note that all terms in Equation (3.2) are normalized with respect to the length of the vessel axis. This avoids a decrease in the bending and stretching energies which would result in an artifactual shrinkage.

To investigate the effects of vessel curvature on the response of the filter, we analyzed a toroidal vessel model (Figure 3.2) with width $2s$, radius R , and a Gaussian cross-sectional luminance profile

$$I(\mathbf{x}) \triangleq \mathcal{G}(\mathbf{x}, s) = \frac{1}{\sqrt{(2\pi s^2)^3}} e^{-\frac{D^2(\mathbf{x})}{2s^2}} \quad (3.14)$$

where $D(\mathbf{x})$ is the distance between the point \mathbf{x} and the axis of the torus. The Hessian matrix for this model and its eigen-decomposition were computed analytically by Krissian *et al.* [167]. We summarize the relevant results in Appendix 3.A. By using the analytic expressions for the different eigenvalues, λ_k , it is possible to analytically evaluate the response of the filter for this vessel model.

Figure 3.3 shows the response of the filter in the radial direction. This radius was computed in the XZ plane. From this figure we conclude that curved vessels will only be distorted when the radius of curvature is of the order of their width (which only occurs in extremely tortuous vessel paths). For vessels with a radius of curvature larger than twice the vessel width the filter response is still maximum at the central vessel axis.

As noticed in Chapter 2, the proposed filter is not well suited for vessel segmentation on its own, since width estimation is only possible if a model of the cross-sectional luminance profile is known, which varies depending on the acquisition technique and owing to the large variation in patient anatomy.

However, the filter is useful for localization of the central vessel axis since it represents an image feature which smoothly decays from the central vessel axis towards the vessel wall. This image feature provides a long range potential map which also avoids inter-vessel response interference given its zero value beyond vessel boundaries. The response of the filter is only marginally dependent on the curvature of the vessel which makes it even suited for finding tortuous segments. Finally, as shown in Chapter 2, the filter provides excellent noise suppression which will improve the convergence properties of the central vessel axis model. Noise reduction is both a consequence of the multi-scale nature of the filter and the discriminant function (specially the factor containing \mathcal{S}).

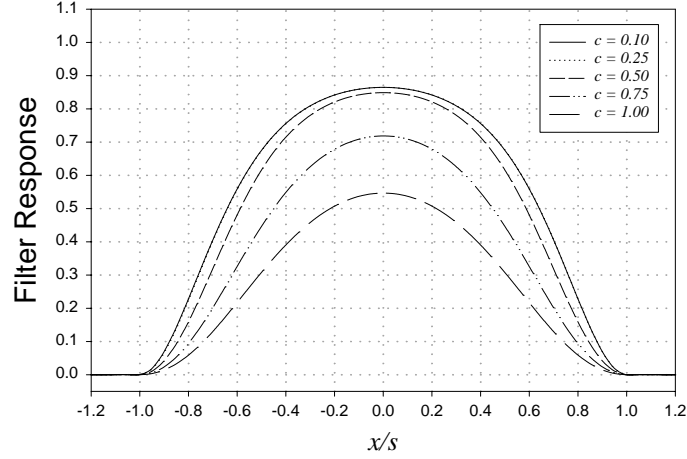


Figure 3.1. Typical filter response at single scale. The parameter c controls the influence of the image contrast and represents the sensitivity of the filter as a percentage of the maximum grey-level value at the center of the vessel. Parameters α and β control the sensitivity to the vessel radial asymmetry and similarity with a blob-like structure respectively. In all experiments we use $\alpha = \beta = 0.5$ and $c = 0.25 \cdot I_{max}$, where I_{max} is the maximum luminance value in a region-of-interest inside the vessel [106]. This filter creates a long range potential which assures that the maximum is found even if the initialization of the vessel axis is significantly off.

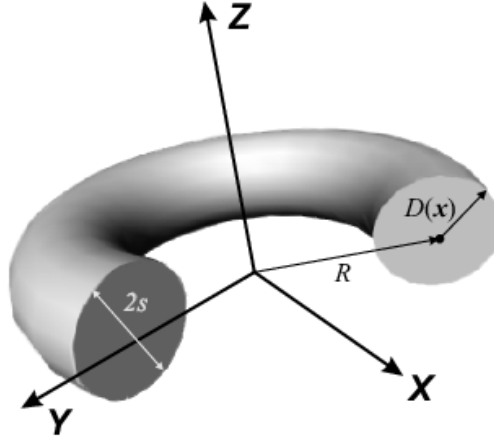


Figure 3.2. Toroidal vessel model with outer radius R and a Gaussian luminance profile of width $2s$. $D(\mathbf{x})$ is the distance between the central axis of the torus and a point \mathbf{x} in the orthogonal plane.

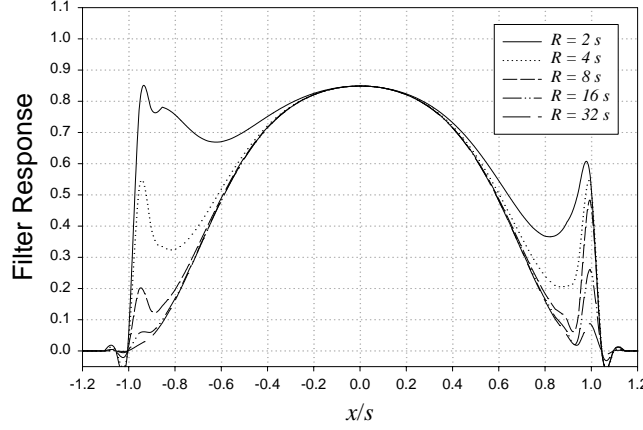


Figure 3.3. Simulation of the influence of vessel curvature on filter response at a single scale. For very small radii of curvature, the response of the filter increases towards the boundaries of the vessel, the strongest effect being observed in the direction of the center of curvature. Simulation performed when $\sigma \rightarrow 0$. In general, replace $s \mapsto \sqrt{s^2 + \sigma^2}$.

Bifurcations are not incorporated in our local vessel model (a tubular structure). For instance, in bifurcations lying in a plane (Υ) there is signal loss, in the filtered image, around the joint. Such bifurcation behaves halfway between a plate and a tubular structure. The eigenvector with the highest magnitude eigenvalue is directed across the plane defined by the bifurcation. The other two eigenvectors point in the same direction as the branches of the bifurcation but form an angle of 90° regardless of the bifurcation angle. The magnitude of these two eigenvalues depends on the symmetry of the bifurcation, the bifurcation angle, etc. In the case of a symmetric bifurcation the magnitude of these eigenvalues will not be zero (as in a plate) but similar to each other and smaller than the third eigenvalue. In this situation, the factors in Equation (3.9) will only differ from the tubular case in that the term in \mathcal{R}_B will be smaller. Despite this fact, in the experiments reported in this chapter we have not seen that this effect imposes a severe obstacle for a reasonable detection of the vessel axis at the joint.

3.2.2 Diameter criterion for MRA

Once the central vessel axis is estimated we proceed to capture the boundary of the vessel and, therefore, its width. To this end *a priori* knowledge of the MRA image acquisition is exploited. In a previous work by Hoogeveen *et al.* [140], the factors that can hamper accurate vessel width assessment from MRA were identified. Intrinsic limitations in the image formation/reconstruction process, finite spatial resolution, gridding artifacts and interpolation determine the achievable accuracy. If the acquisition process is accurately modeled, it is possible to find precise diameter criteria for

the three MRA types most frequently used for stenosis grading and/or flow quantification, namely Time-Of-Flight (TOF), Phase-Contrast (PC) and Contrast Enhanced (CE) MRA. The boundary criteria are defined as a percentage roll-off factor with respect to the maximum luminal MR signal.² For TOF and CE MRA the full-width-half-maximum (FWHM) criteria is applied while for PC MRA the criteria used is the full-width-10%-maximum (FWTM).

These criteria can provide accurate diameter estimates for TOF, PC and CE MRA if the acquisition meets a number of requirements [140]: *i*) resolution is sufficiently high (at least 3 pixels/diameter), *ii*) saturation due to slow inflow at the borders is limited (only for TOF MRA), and *iii*) flow artifacts are negligible.

For smaller vessels, diameter quantification is still possible but a more complex model of the acquisition is required which also incorporates tissue properties and parameters of the MR imaging sequence [141].

3.2.3 Vessel wall model

The vessel wall is modeled using a tensor product B-spline surface [236]

$$\mathbf{W}(v, u) = \sum_{j=0}^q \sum_{k=0}^r N_{jl}(u) N_{km}(v) \mathbf{P}_{jk} \quad (3.15)$$

where \mathbf{P}_{jk} are $((q+1) \times (r+1))$ control points, $N_{jl}(u)$ is the j -th B-spline periodic basis function of order l and $u \in [0, 2\pi)$, $N_{km}(v)$ is the k -th B-spline non-periodic basis function of order m and $v \in [0, 1]$. The parameters u and v traverse the surface in the circumferential and longitudinal directions respectively.³ We have deliberately coupled the longitudinal parameter (v) of the vessel wall and central vessel axis since both span the vessel in the longitudinal direction. This coupling makes it possible to relate central vessel axis points with the corresponding boundary points.

The model can be initialized using a standard CAD technique known as *swept surfaces* [236]. A prototype cross-section (*viz.* a circle with a radius equal to the expected average vessel width) is swept along the central vessel axis, and orthogonal to the curve at every point. In this way, the model is initialized as a flexible cylinder.

To fit the vessel wall model in a smooth fashion we use an approach similar to the one applied in Section 3.2.1, extending the concept from curves to surfaces. The wall model is deformed in a way that maximizes the following integral criterion

$$\mathcal{E}^W = \mathcal{E}_{external}^W + \tilde{\gamma}_s^W \cdot \mathcal{E}_{stretching}^W + \tilde{\gamma}_b^W \cdot \mathcal{E}_{bending}^W \quad (3.16)$$

where

$$\mathcal{E}_{stretching}^W = \frac{1}{S} \int_0^1 \int_0^{2\pi} \left(\frac{\|\mathbf{W}_v\|^2}{\|\mathbf{W}_u\|^2} \right) \|\mathbf{W}_v \times \mathbf{W}_u\| dv du \quad (3.17)$$

²Compared to [140] the criterion has been made more robust to noise by using as a reference the average of the MR signal in a small neighborhood along the central vessel axis. Although the derivation of the FWHM in [140] was done only for TOF MRA, the same criterion is valid for CE MRA since it is based on assuming a step-like intensity function. This function corresponds to full inflow, an assumption also valid in CE MRA.

³For the sake of simplicity, the arguments of the vessel wall model will be henceforth omitted, *i.e.* $\mathbf{W} \triangleq \mathbf{W}(v, u)$.

$$\bar{\mathcal{E}}_{bending}^W = \frac{1}{S} \int_0^1 \int_0^{2\pi} \left(\frac{\|\mathbf{W}_{vv}\|^2}{2\|\mathbf{W}_{vu}\|^2} \right) \|\mathbf{W}_v \times \mathbf{W}_u\| dv du \quad (3.18)$$

$$S = \int_0^1 \int_0^{2\pi} \|\mathbf{W}_v \times \mathbf{W}_u\| dv du \quad (3.19)$$

$$\vec{\gamma}_s^W = (\gamma_{s_v}^W, \gamma_{s_u}^W) \quad (3.20)$$

$$\vec{\gamma}_b^W = (\gamma_{b_{vv}}^W, \gamma_{b_{vu}}^W, \gamma_{b_{uu}}^W) \quad (3.21)$$

where $\vec{\gamma}_s^W$ and $\vec{\gamma}_b^W$ are vectors of weight factors for the internal energy terms. The stretching energy term can be physically interpreted as an approximation to the energy of a thin plate under tension while the bending energy is related to the rigidity of the deformable surface [313].

So far the vessel wall model is purely geometric. To further incorporate prior knowledge of the acquisition, let us assume that the maximum MR signal intensity is attained at the central vessel axis. Although this assumption might be violated in certain cases, it provides a simplified formulation of the problem that leads to accurate results in most situations. Under this assumption we can cast the diameter criteria of Section 3.2.2 into the external energy term of the deformable wall as follows

$$\mathcal{E}_{external}^W = \frac{1}{S} \int_0^1 \int_0^{2\pi} \left| \tau_{acq} - \frac{I(\mathbf{W}(v, u))}{I(\mathbf{C}(v))} \right| \|\mathbf{W}_v \times \mathbf{W}_u\| dv du \quad (3.22)$$

where τ_{acq} is a threshold that introduces the knowledge about the type of MRA imaging technique. This constant equals 0.5 for TOF and CE MRA, and 0.1 for PC MRA (cf. Section 3.2.2).

3.3 Implementation issues

3.3.1 Image resampling

In order to reduce the effect of gridding artifacts due to the MR image reconstruction, the original image was interpolated to a two-fold larger reconstruction matrix. Based on the properties of the MR image formation process, Du *et al.* [85] showed that partial volume effect in MR can be reduced with *sinc interpolation*. They also suggested an efficient implementation based on zero-filled interpolation. We have used an approximation to *sinc* interpolation based on cubic convolution which is computationally more efficient than zero-filled interpolation and has extremely good *sinc* approximating properties [201].

3.3.2 Scenario for 3-D interaction

Although deformable models have been shown to be useful in a variety of 3-D applications, it has been recognized that initialization and interaction in 3-D is, in general, an open problem. On the other hand, it has also been acknowledged that

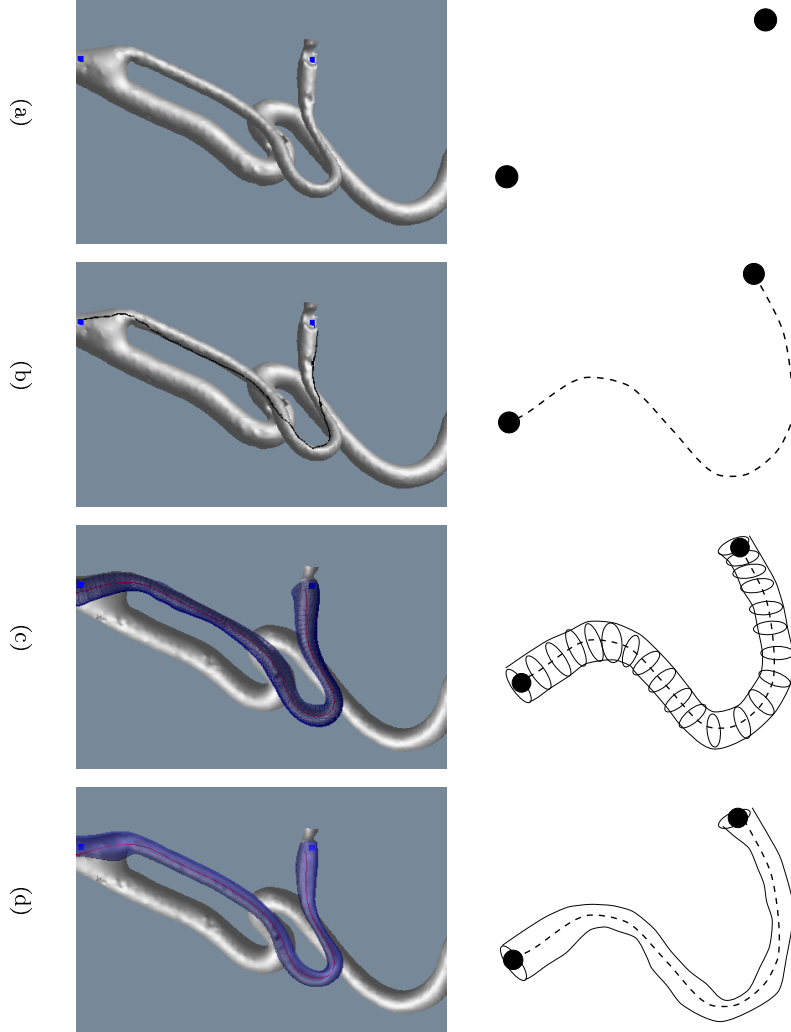


Figure 3.4. Interaction scenario. *a)* A user initializes two (or more) points on the iso-surface generated from the original image. *b)* From these seeds, a geodesic path is computed. *c)* The geodesic path is deformed until the central vessel axis is determined. Using the distance between the newly obtained vessel axis and the original geodesic, a circular cross-section is swept along the axis to generate an initialization of the vessel wall model. *d)* Vessel wall (after deformation) and central vessel axis. Note that each model deforms using a different external energy (cf. Equations (3.13) and (3.22)).

proper initialization is a requirement for good convergence of most deformable model approaches.

We suggest the use of an iso-surface rendering for interactively inspecting the vascular anatomy and for selecting the target segment in which the quantitative analysis will be performed. In Figure 3.4 the steps of the procedure are highlighted. Firstly, an iso-surface rendering of the original angiogram is generated – Figure 3.4(a). This is accomplished using *marching cubes* [183]. We are aware that this step implies the selection of a threshold. However, we recall that the *only* purpose of this step is to provide a support for visual interaction. Secondly, the operator defines a vessel segment by clicking two points on the iso-surface which define the end-points of a geodesic path.⁴ This path is used for initializing the central vessel axis after it has been converted into B-spline form using a least squares approximation – Figure 3.4(b). Thirdly, once the central vessel axis has been determined, the vessel wall has to be initialized. This can be accomplished with *no extra* user interaction by computing a radius function as the distance between the central vessel axis and the geodesic path. Since the geodesic path lies somewhere close to the vessel boundary, its distance to the vessel axis provides a rough approximation of the vessel radius at every point along the center line. This function is subsequently used to modulate the radius while sweeping a circular cross-section along the vessel axis – Figure 3.4(c). Figure 3.4(d) shows the final result of the fitting procedure. Once the model is obtained, a report can be generated indicating cross-sectional area as well as minimum, maximum and average vessel diameter along the vessel axis.

3.3.3 Model optimization

Having specified the energy functionals for the central vessel axis and vessel wall, we have to choose how to optimize the degrees of freedom of these geometric models (the control points of the B-curve/surface).

The optimization is performed in two steps. First the central vessel axis is deformed according to Equation (3.2). Once it converges, the initial guess of the vessel wall is generated by sweeping along the central vessel axis. Subsequently, the model of the vessel wall is deformed to reach the vessel boundary following Equation (3.16). The deformation process of both the central vessel axis and vessel wall is performed using the *conjugate gradient* [241] algorithm with *analytical derivatives* (Appendix 3.B). The energy integrals involved in Equations (3.2) and (3.16) were computed numerically using *Gauss-Legendre quadrature* formulas [241].

To avoid surface self-intersections during the deformation process of the wall model, we constrain the movement of the control points. Each subset of control points sharing the same column index (*i.e.* affecting the same circumferential wall strip) are constrained to move in a plane perpendicular to the central vessel axis (Figure 3.5). Mathematically

$$\mathbf{P}_{jk_o} = \mathbf{C}(v_{k_o}) + r_{jk_o} \cos \theta_{jk_o} \mathbf{N}(v_{k_o}) + r_{jk_o} \sin \theta_{jk_o} \mathbf{B}(v_{k_o}) \quad (3.23)$$

⁴Given two points on a surface, a *geodesic* is defined as the shortest path on the surface connecting them.

where \mathbf{C} , \mathbf{N} and \mathbf{B} are the central vessel axis coordinates, and the central vessel axis normal and binormal vectors of its Frenet frame at parameter value v_{k_o} .⁵ In this expression (r_{jk}, θ_{jk}) represents the location of the control point \mathbf{P}_{jk} in polar coordinates of the local cross-sectional plane. By restricting $r_{jk} \geq 0$ and $\theta_{j-1,k} \leq \theta_{j,k} \leq \theta_{j+1,k}$,⁶ the central vessel axis is enforced to lie inside the boundaries of the vessel wall.

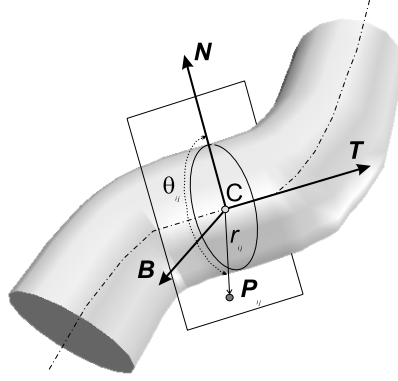


Figure 3.5. The control points of the vessel wall model are restricted to move in a plane orthogonal to the vessel axis.

3.3.4 Geometric modeling

In Table 3.3 the parameters of the vessel model for the carotid bifurcation segment are summarized. Note that the internal energy weights are small (the external energy range typically from 0 to 1) such that, unless the model is subjected to large stretching or bending deformations, it will be mainly guided by the external energy term. Problems often attributed to deformable models are the *ad hoc* nature of the selection of weights, and the fact that they have to be tuned for each application (which most of the times means “each image”). In our implementation we chose to normalize each internal energy term with respect to its value in the initialization. By proceeding in this way, we obtain internal energy terms that are dimensionless and that were suited for all the experiments we carried out (Table 3.3). Moreover, internal energy terms and the external energy are now commensurable, and it is possible to incorporate an extra coefficient in the weights that represents their relative contribution to the total energy. Note that using such normalization factors is justified if the initial shape of the models is representative of their final shape which is ensured by our initialization procedure.

⁵Here, v_{k_o} is the parametric value, v , where the basis function $N_{k_o m}(v)$ is maximal. This corresponds to the parameter value for which \mathbf{P}_{jk_o} have maximum influence on the curve, for all j .

⁶In this expression j denotes a cyclic index with period q .

Table 3.3. Geometric Model Parameters

Vessel Axis		
n	B-spline curve order	3
$s + 1$	Number of control points	15
γ_s^C	Stretching weight	$0.1/E_s^C$
γ_b^C	Bending weight	$0.05/E_b^C$
Vessel Wall		
l	B-spline surface order (circ.)	3
$q + 1$	Number of control points (circ.)	5
m	B-spline surface order (long.)	2
$r + 1$	Number of control points (long.)	25
$\gamma_{s_u}^W$	Stretching weight (circ.)	$0.1/E_{s_u}^W$
$\gamma_{s_v}^W$	Stretching weight (long.)	$0.1/E_{s_v}^W$
$\gamma_{b_{uu}}^W$	Bending weight (circ.)	$0.05/E_{b_{uu}}^W$
$\gamma_{b_{vu}}^W$	Bending weight (mixed)	$0.05/E_{b_{vu}}^W$
$\gamma_{b_{vv}}^W$	Bending weight (long.)	$0.05/E_{b_{vv}}^W$

3.4 In vitro evaluation

3.4.1 Phantom and image acquisition

In order to assess the performance of the algorithm we addressed the problem of diameter measurements for stenosis grading in an MR compatible, carotid bifurcation phantom with an asymmetric stenosis (R.G. Shelley Ltd., North York, Ontario, Canada). A photograph of this phantom is shown in Figure 3.6. The phantom is embedded in a rigid, transparent acrylic and manufactured to reproduce normal dimensions in the human vasculature [275].

Images were acquired on a 1.5 Tesla MR imaging system (Philips Gyroscan ACS-NT, PowerTrak 6000 gradients, Philips Medical Systems, Best, The Netherlands) with a quadrature head-neck receiver coil. Imaging parameters for experiments on the carotid bifurcation phantom were as follows. Three-dimensional TOF MRA acquisition: echo time (TE) 1.9 ms, repetition time (TR) 25.0 ms and flip angle (α) 15° , slice thickness 1.0 mm. CE MRA acquisition: TE 2.0 ms, TR 6.6 ms, α 40° , slice thickness 1.0 mm. Both acquisitions: FOV 256 mm, scan matrix 256×256 . First order flow compensation was applied in the TOF MRA acquisition. The flow was regulated by a computer-controlled pump (Quest Image Inc., London, Ontario, Canada). Water was guided through the phantom with constant velocity (5 ml/s) and a long inlet length was taken to assure that laminar flow was established. For CE MRA acquisitions a 5-mM solution of gadopentetate dimeglumine (Magnevist, Schering, Berlin, Germany) was used under the same flow conditions as the TOF MRA acquisition.

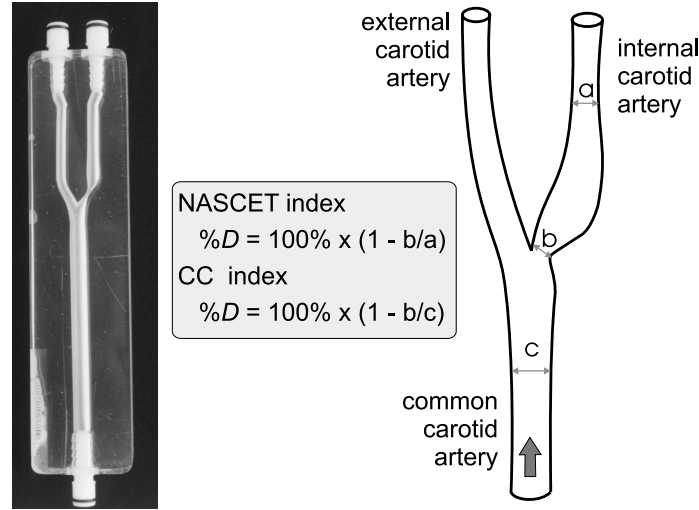


Figure 3.6. Carotid bifurcation phantom with a 70% asymmetric stenosis. Two indexes (NASCET and CC) are usually used to quantify stenosis in the carotids with different reference diameters.

3.4.2 Performance assessment

We assessed the performance of the algorithm in comparison with a human operator and the ground truth as gold standard. To this end, the stenosis in the carotid phantom was graded by two experts following a manual procedure. This is based on visual inspection of vessel dimensions on a Multi Planar Reformatted (MPR) image. The reformatting was generated by manually drawing a central vessel axis and subsequently computing the plane perpendicular to it. This procedure was performed on a clinical workstation (EasyVision, Philips Medical Systems, Best, The Netherlands).

In order to compare the measurements provided by the experts and the results obtained with our algorithm, a measurement protocol was established. The degree of stenosis was computed using the NASCET index [216]. A second measure of stenosis, taken relative to the *common carotid artery* (CC index), was also computed for comparison.⁷ To incorporate the variability inherent to the definition of the stenosis diameter, our protocol required that the experts measured the distal diameter at $D = 15$ mm from the center of the stenosis and repeated the measurements for two other successive planes separated by $d = 5$ mm. For each plane, the minimum and maximum observed diameters were recorded. All measurements were done twice by the same expert with enough delay to disregard any possible bias in the second measurement. The average stenosis grade and the 99% confidence interval (CI) were computed for each observer, for both observers and for the proposed algorithm. The statistics of stenosis grading with the model-based approach were computed based on all possible values of the degree of stenosis for a region of 2 mm around the stenosis

⁷The definition of the two indexes can be found in the inset of Figure 3.6.

and a region of $2d = 10$ mm centered at a distance $D + d = 20$ mm from the stenosis. This yields a measure of stability of the model-based measurements in the region where the operators performed the manual analysis.

3.5 Results

3.5.1 Carotid bifurcation phantom

In Figure 3.7 the average diameter measurements are shown (the average diameter in the orthogonal plane, at a given location along the central vessel axis). For comparison purposes, it also includes, at three points, diameter values from the specifications of the phantom [275]. From this figure it is apparent that manual assessment suffers from a large variability. This can be attributed to factors such as the window leveling settings of the MR console and the subjective criterion that each radiologist uses to define the “boundaries” of the vessel. This is further aggravated by the fact that even circular vessels will show different apparent cross-sections [140] depending on the effective resolution (the number of pixels per diameter).

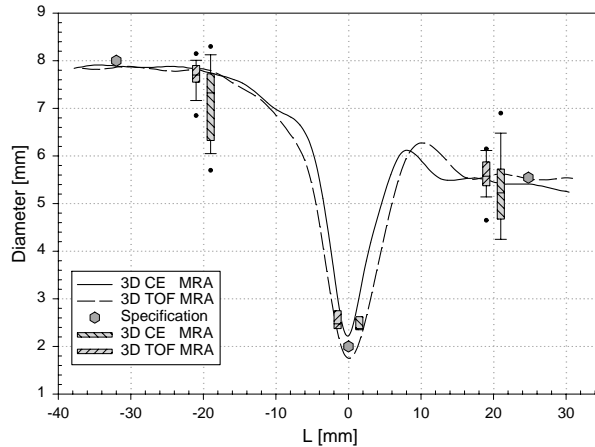


Figure 3.7. Average diameter of the carotid bifurcation phantom. The average is performed over all pairs of antipodal points at a given point along the vessel axis. The diameter of the phantom (estimated from phantom specifications [275]) and the box-and-whisker plots corresponding to the measurements performed by two experts are also included (average between min and max diameter). For the sake of clarity, the average abscissa of each pair of boxes corresponds to the place where the measurements were carried out.

In Table 3.4, the statistics of the stenosis grading are summarized. The phantom we used has a stenosis index of 69.2% according to NASCET and 78.5% according to CC [275]. The table shows that the method improves stenosis grading, with an absolute error smaller than 3.3% for both criteria. Moreover reproducibility is much

Table 3.4. Stenosis Grading Summary: carotid bifurcation phantom with asymmetric stenosis⁸. Within (WO_1 , WO_2) and between observer (BO_{12}) statistics of two experts compared to the model-based approach (MB).

Criterion	Acquisition	WO_1	WO_2	BO_{12}	MB
		% $D \pm CI_{99\%}$	% $D \pm CI_{99\%}$	% $D \pm CI_{99\%}$	% $D \pm CI_{99\%}$
CC	3-D TOF MRA	69.8 ± 3.5	62.8 ± 5.3	66.3 ± 3.2	76.7 ± 0.2
(78.5% $\pm 0.6\%$)	3-D CE MRA	68.4 ± 1.4	62.8 ± 4.1	65.6 ± 2.3	76.0 ± 0.2
NASCET	3-D TOF MRA	55.2 ± 4.1	39.1 ± 7.5	47.2 ± 5.2	67.6 ± 0.1
(69.2% $\pm 0.9\%$)	3-D CE MRA	55.8 ± 3.3	48.3 ± 5.2	52.1 ± 3.4	65.9 ± 0.2

⁸ Stenosis indexes according to CC and NASCET criterion.
True values are indicated in the first column.

better in the model-based approach.

3.5.2 Illustration of the algorithm on patient data

In Figure 3.8, results of the algorithm on patient data are shown. Figure 3.8(a) and 3.8(b) show MIPs of 3-D TOF angiograms of the left (mild stenosis) and right (severe stenosis) carotids of the same patient, respectively. Figure 3.8(c) shows the left carotids of a second patient with a mild stenosis. The datasets are part of an on-going trial in our hospital to compare several imaging techniques for stenosis grading [90]. The parameters of the 3-D TOF MRA sequence were as follows: TR 30.6 ms, TE 6.8 ms, α 15°, with a pixel size of 0.5 mm, slice thickness of 1.0 mm and a slice gap of 0.5 mm.

A summary of quantitative results for stenosis grading of these data is given in Table 3.5. In the same table, stenosis grades assessed by a radiologist from MIPs of 3-D TOF MRA images and 2-D DSA projections are also included for comparison. To illustrate that in our model there is no assumption of circularity, we show in Figure 3.9 several shape characteristics such as the minimum, maximum and average diameter, and cross-sectional area measurements for the examples of Figure 3.8(a) and 3.8(c). Our model-based method correlates better with DSA, which is the gold standard in many radiological studies [6, 67, 134], than the manual assessment from 3-D TOF.

Flow artifacts were small in the *in vitro* experiments. In patient data, however, the algorithm performs well for non-severe stenosis and/or when flow artifacts are negligible. This was one of the assumptions for the validity of the FWHM criterion. In Figure 3.8(b) an example of a severe stenosis is shown. Post-stenotic flow artifacts hampered good fit of the model at the stenosis and distal to it. At the stenosis, the luminal intensity has a cloudy appearance and the vessel axis in this region is mainly guided by the internal energy term which forces the axis model to extrapolate the non-stenosed vessel axis. Even when the degree of stenosis, occasionally, agrees with the expert's grading based on DSA, if the vessel axis falls outside the vessel lumen, the vessel wall determination cannot be accurate. We therefore considered this as a failure case (noted between parenthesis). When images contain large flow artifacts,

manual assessment of the degree of stenosis is also difficult and more susceptible to intra observer variability.

Table 3.5. *In-Vivo* Stenosis Grading of the Carotids Manual (3-D TOF and DSA) and Model-Based (3-D TOF)

Patient	3-D TOF %D	DSA %D	3-D TOF (MB) %D
A – L ICA (Figure 3.8(a))	28%	36%	38%
A – R ICA (Figure 3.8(b))	90%	53%	(48%)
B – L ICA (Figure 3.8(c))	53%	34%	28%
B – R ICA	74%	53%	49%

The stenosis index follows the NASCET criterion. L = left R = right

3.6 Discussion

We devised a method to perform quantitative diameter assessment with sub-voxel precision. The method shares some features with multi-scale vessel enhancement algorithms based on eigenvalue analysis of the Hessian originally proposed by Koller and co-workers [163] and further modified by Sato *et al.* [260, 261] and Lorenz *et al.* [184]. However in these approaches a segmentation of the vasculature was obtained by estimating the vessel width as a function of the scale of maximum response. The accuracy of these algorithms is therefore *a priori* limited by the discretization of the scale parameter. This limits the applicability of these methods to give a general overview of the vasculature; for stenosis grading a more accurate approach is required.

Our method performs quantitative analysis based on the original three-dimensional images. It is known from the literature [6, 67, 134] that assessment of stenosis based on MIPs tends to overestimate the degree of stenosis. Table 3.5 nicely exemplifies this fact. This artifact is not only attributed to flow related signal loss but also to the image processing involved in generating the MIPs [7, 53, 263]. In order to avoid this artifact, some authors have argued in favor of methods that avoid the MIP operation. Anderson *et al.* [6], for instance, have suggested to grade stenoses based on the source images. De Marco *et al.* [67] resourced to MPR images which allow for better visualization of the vessel lumen in a plane orthogonal to the vessel axis. De Marco *et al.* [67] compared stenosis grading based on MIPs and MPR images of 3-D TOF MR angiograms, and used intra-arterial angiography (DSA) as standard of reference. They reported a statistically significant difference between MIPs and DSA scores with an average absolute error $\sim 9\%$ ($SD \sim 14\%$). MPR images provided a better agreement with DSA, and a negligible bias. Although this study suggests the potential benefit of MPR-based diagnosis, generation and inspection of MPRs is relatively time consuming. Our method shares the basic idea behind MPR-based measurements. We apply an objective vessel diameter criterion in planes orthogonal to the vessel axis and, therefore, similarly to the radiologists when analyzing MPR images. On the other hand, the method is objective (does not depend on window leveling settings)

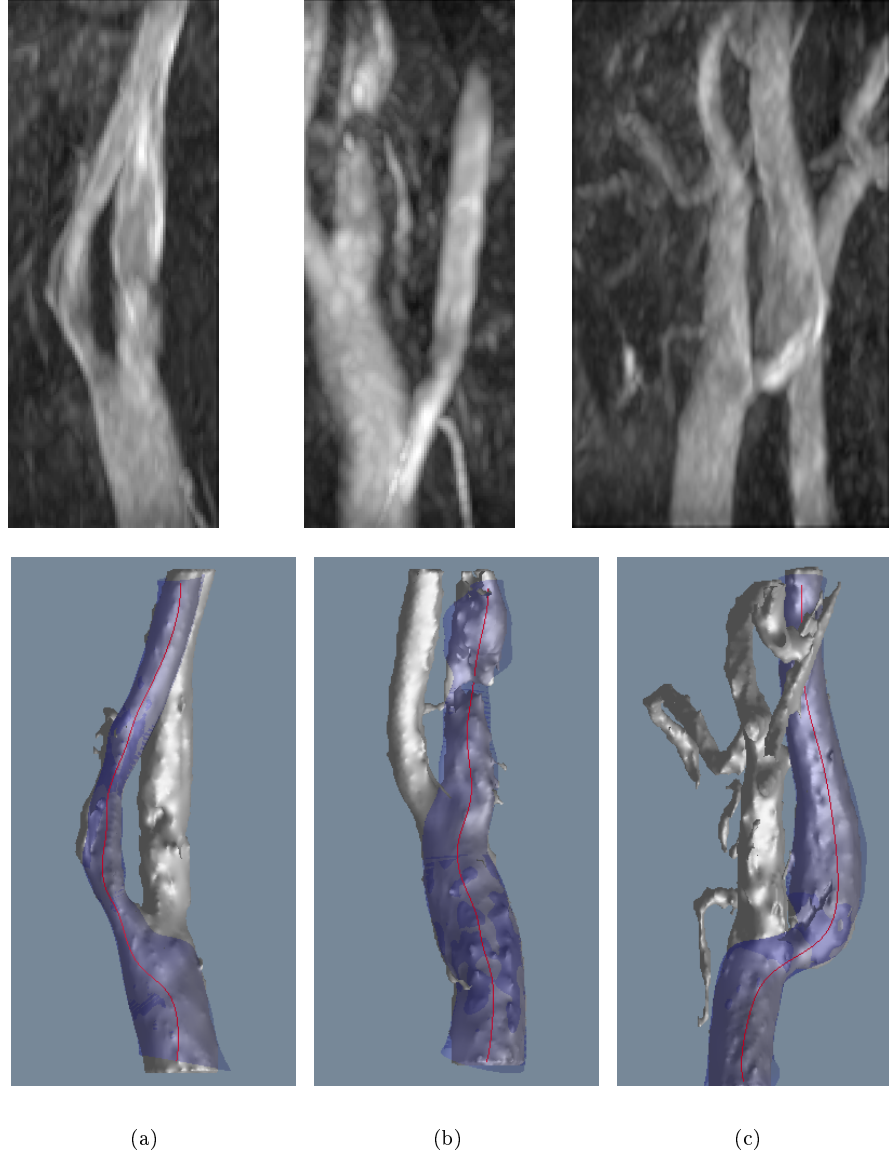


Figure 3.8. Stenosed left *internal carotid arteries* (ICA). The top row shows MIPs of 3-D TOF datasets of the ICA. *a)* and *b)* correspond to the left and right ICA of the same patient and *c)* corresponds to the left ICA of a second patient. In the lower row we show the corresponding vessel models. The models are quite accurate for the two left ICA cases shown. For the right ICA, however, the presence of flow artifacts close to the severe stenosis (90% graded on MRA and 53% on DSA according to NASCET) precluded following the vessel axis.

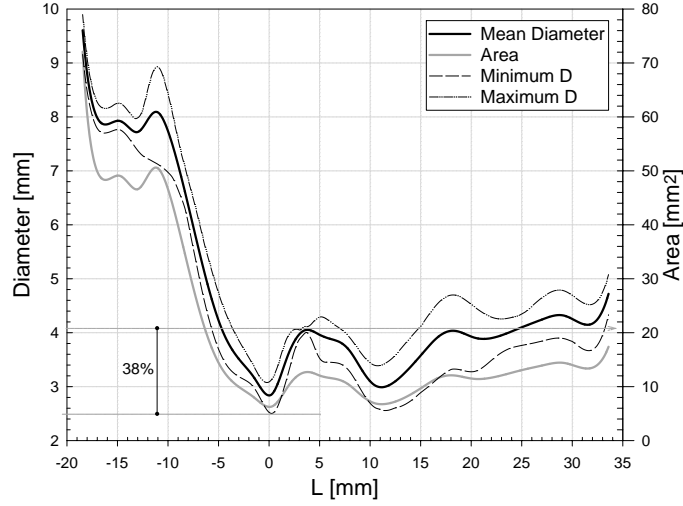


Figure 3.9. Stenosed ICA. Area and (min/max/average) diameter measurements of the left ICA long the vessel axis, for the patient in Figure 3.8(a). Stenosis index computed based on the maximal vessel narrowing and the average distal diameter.

and requires little interaction. We hypothesize that this correspondence between our method and MPR-based diagnosis is responsible for the smaller bias in our method (vs DSA) compared to manual assessment based on MIPs (vs DSA). This hypothesis, however, has to be further evaluated on a larger number of patients. The differences observed between our model-based method and DSA are close to the figures reported in the literature for intra-observer differences using DSA. Anderson *et al.* [6], for instance, reported intra-observer absolute differences of 5% but they can be as high as 30% [34]. Therefore, the difference between the model-based method and DSA may not be statistically significant. Compared to measurements based on DSA, our method avoids the difficulties of selecting a suitable projection angle [258] by providing true three-dimensional measurements.

We have applied an algorithm which estimates the boundaries of the vessels using knowledge of the MRA image acquisition technique. This is a distinguishing property of our method compared to other previously published multi-scale techniques [13, 106, 163, 167, 168, 184, 239, 260, 261]. Whereas the algorithm contains a scale selection procedure in the determination of the central vessel axis, this does not influence the diameter assessment. Moreover, our model based on splines can model non-circular vessel cross-sections. Although often it is assumed that vessels have a circular cross-section, *ex vivo* measurements [227] have shown that this assumption is rather simplistic and, especially at the stenosis, a wide variety of geometric shapes can be observed. Elgersma and co-workers [90] have supported this idea based on *in vivo* measurements from multiple projections of 3-D rotational angiography (RA) images and concluded that this imposes a severe limitation to measurements performed

on (only two or three) 2-D projections. Three dimensional approaches, as the one presented in this work, provide a basis for both the description of the actual cross-sectional shape and its quantification. They also allow definition of stenosis indexes based on cross-sectional area reduction (cf. Figure 3.9) which are more robust than those based on diameter reduction.

The method has been illustrated on phantom and patient data. In the phantom data the method obtained diameter and stenosis measurements with an accuracy which was considerably better than the experts. Although the results on the clinical data are promising, a thorough validation is still required.

Other aspects of the methodology need further research. The influence of vessel bifurcations in the deformation of the model has to be better understood. Apparently, if the stenosis is reasonably away from the flow divider, stenosis assessment can be performed with good accuracy. This was observed, for instance, in the carotid bifurcation phantom and in the patient data of Figure 3.8(a). However, it is clear that with a tubular model there will always be a region where “diameter” measurements will be an extrapolation of the diameters before and after the bifurcation (see Figure 3.8(c)). Note, however, that in such situations a radiologist would also have to mentally perform such an extrapolation.

The method performed poorly in the presence of large flow artifacts (see Figure 3.8(b)). This is a potential limitation of the methodology when applied to 3-D TOF MRA since stenoses are usually regions of disturbed flow. In such situations, however, manual assessment of stenosis is also delicate. Our method is in principle applicable to other techniques like CE or blood pool agent (BPA) MRA, which are less sensitive to disturbed flow. In the next chapter we will evaluate our methodology in a larger set of CE MRA images.

Finally, it would be interesting to analyze a large set of vascular segments and study the influence of the number of control points of the B-spline representation on the accuracy of the measurements. This analysis will probably give a basis for building a database of models tailored to different applications (carotids, aorta, etc.). Each model would consist not only on the optimum number of degrees of freedom of the geometric model but also suitable weights for the energy terms. It is known that the weighting factors present in the formulation of deformable models are generally chosen in an *ad hoc* fashion. However, for a given application suitable values can be found based on the analysis of a representative set of data. This is especially feasible in medical applications where images are acquired according to strict protocols.

3.A Appendix: Analytical model of a toroidal vessel

Krissian *et al.* [167] proposed a vessel model with a Gaussian luminance profile. Although this is a simplification, it allows us to carry out some analytical simulations that would be otherwise quite cumbersome, if at all possible. In this appendix we summarize the results for a toroidal model. An analogous formulation can be derived for a cylindrical model [167].

The vessel is modeled by a torus whose outer circle is parallel to the plane XY and has radius R . The small circle has radius s (Figure 3.2). For the toroidal model

of Equation (3.14), the distance from a point $\mathbf{x} = (x, y, z)$ to the axis of the torus is

$$D(\mathbf{x}) = \sqrt{\left(R - \sqrt{x^2 + y^2}\right)^2 + z^2} \quad (3.24)$$

From the circular symmetry around the Z axis we can choose $y = 0$ and $x > 0$. The Hessian matrix can be expressed as

$$\mathcal{H} = \frac{I(\mathbf{x})}{s^4} \begin{bmatrix} (R-x)^2 - s^2 & 0 & -z(R-x) \\ 0 & \frac{(R-x)s^2}{x} & 0 \\ -z(R-x) & 0 & z^2 - s^2 \end{bmatrix} \quad (3.25)$$

Eigenvalue analysis of Equation (3.25) results in

$$\lambda_1 = -\frac{I(\mathbf{x})}{s^2} \left(\frac{x-R}{x} \right) \quad \vec{\mathbf{u}}_1 = (0, 1, 0) \quad (3.26)$$

$$\lambda_2 = -\frac{I(\mathbf{x})}{s^2} \left[1 - \left(\frac{D(\mathbf{x})}{s} \right)^2 \right] \quad \vec{\mathbf{u}}_2 = (x-R, 0, z) \quad (3.27)$$

$$\lambda_3 = -\frac{I(\mathbf{x})}{s^2} \quad \vec{\mathbf{u}}_3 = (z, 0, R-x) \quad (3.28)$$

where λ_i and $\vec{\mathbf{u}}_i$ denote eigenvalues and eigenvectors, respectively.

3.B Appendix: Analytical expression for the gradient of Equation (3.16)

In this appendix an analytic expression for the gradient of Equation (3.16) is derived. This expression can be used to speed-up the deformation of the vessel model when using optimization techniques that employ the gradient of the energy function. In our case we have used Conjugate Gradient [241] as optimization technique. Conjugate Gradient is a good choice in terms of convergence speed. Schemes that do not use gradient information require much more function evaluations to find a local minimum. If the evaluation time of the function is comparable to the evaluation of the gradient, use of the later can avoid many useless function evaluations. Explicit gradient-descent algorithms are more efficient than algorithms like Powel or Simplex that only rely on function evaluations.

In summary, the gradient of \mathcal{E}^W with respect to each of the $(q+1) \times (r+1)$ 3-D control points, \mathbf{P}_{jk} , has to be computed. Once this is computed, it is trivial to apply the chain rule and to find the gradient of the energy function with respect to the radial and angular degrees of freedom of Equation (3.23).

Before deriving the expression of the analytic gradient, it is convenient to estimate the achievable computational speed-up. Let us assume that we have a control point mesh of 5×15 ($q = 4$, $r = 14$). The easiest way to estimate the gradient of the energy function is to approximate it numerically. A simple calculation will rule out

this alternative. Assume that evaluation of the energy functional takes T_f seconds.⁸ Centered finite difference approximation of the gradient would take roughly $2 \times 3 \times (q + 1) \times (r + 1)T_f = 450T_f$ seconds. If the number of control points in the circumferential direction, $q + 1$, is fixed, and the number of control points in the longitudinal direction is proportional to the vessel length, the computational burden involved in estimating the gradient grows linearly with the length of the vessel. Notice that this is even aggravated by the fact that T_f itself grows linearly.⁹ If, however, we could compute the gradient analytically in a time, T_g , comparable to T_f , a considerable speed-up would be obtained. In our application it was empirically observed that $T_g \approx 4T_f$. Moreover, the complexity of computing the energy gradient and the energy function (in T_f units) will not depend on the vessel length.

In the following, we derive the analytic expression for the gradient of \mathcal{E}^W . Knowing how to compute the whole gradient boils down to know the derivative of the energy function for an arbitrary control point \mathbf{P}_{jk}

$$\frac{\partial \mathcal{E}^W}{\partial \mathbf{P}_{jk}} = \frac{\partial}{\partial \mathbf{P}_{jk}} \left\{ \frac{\mathcal{E}_{external}^W + \tilde{\gamma}_s^W \cdot \tilde{\mathcal{E}}_{stretching}^W + \tilde{\gamma}_b^W \cdot \tilde{\mathcal{E}}_{bending}^W}{S} \right\} \quad (3.29)$$

$$= \frac{1}{S^2} \left\{ S \frac{\partial \mathcal{E}_{external}^W}{\partial \mathbf{P}_{jk}} + S \frac{\partial \mathcal{E}_{internal}^W}{\partial \mathbf{P}_{jk}} \right\} - \frac{1}{S^2} \left\{ (\mathcal{E}_{external}^W + \mathcal{E}_{internal}^W) \frac{\partial S}{\partial \mathbf{P}_{jk}} \right\} \quad (3.30)$$

$$\text{where } \mathcal{E}_{internal}^W = \tilde{\gamma}_s^W \cdot \tilde{\mathcal{E}}_{stretching}^W + \tilde{\gamma}_b^W \cdot \tilde{\mathcal{E}}_{bending}^W.$$

Let us start by computing the derivatives of the total area of the vessel wall, S , of Equation (3.19)

$$\frac{\partial S}{\partial \mathbf{P}_{jk}} = \iint \frac{\partial}{\partial \mathbf{P}_{jk}} |\mathbf{W}_v \times \mathbf{W}_u| dv du \quad (3.31)$$

$$= \iint \frac{\partial}{\partial \mathbf{P}_{jk}} \sqrt{\mathbf{a} \cdot \mathbf{a}} dv du \quad (3.32)$$

$$= \iint \frac{\mathbf{a}^T}{|\mathbf{a}|} \frac{\partial \mathbf{a}}{\partial \mathbf{P}_{jk}} dv du \quad (3.33)$$

where¹⁰

⁸The exact value of T_f depends on the order of the employed numerical integration scheme and on the computer architecture. In a typical vessel model using a 3×5 Gauss-Legendre quadrature scheme per B-spline knot span, $T_f \approx 0.2$ s in a SUN Ultra 60.

⁹The integral in Equation (3.16) has to be integrated numerically. It can be shown that, for a fixed number of circumferential control points, the number of samples to integrate the energy function is proportional to the number of control points in the longitudinal direction.

¹⁰In the reminder of this appendix, superscripts letters will indicate the components (x, y, z) of the corresponding vectors, a prime as superscript will indicate parametric derivatives of the B-spline basis functions, and bold letters with tilde a matrix. Note that in an abuse of notation we will mostly omit the arguments in $\mathbf{W}(u, v)$, $N_j(u)$ and $N_k(v)$. For the sake of parsimony, we will also omit the order of the B-spline basis functions, *i.e.*, $N_j = N_{jl}$ and $N_k = N_{km}$.

$$\mathbf{a} \equiv \mathbf{W}_v \times \mathbf{W}_u = \begin{pmatrix} \mathbf{W}_u^y \mathbf{W}_v^z - \mathbf{W}_v^y \mathbf{W}_u^z \\ \mathbf{W}_v^x \mathbf{W}_u^z - \mathbf{W}_u^x \mathbf{W}_v^z \\ \mathbf{W}_u^x \mathbf{W}_v^y - \mathbf{W}_v^x \mathbf{W}_u^y \end{pmatrix} \quad (3.34)$$

and

$$\tilde{\mathbf{A}}_{jk} \equiv \frac{\partial \mathbf{a}}{\partial \mathbf{P}_{jk}} = \begin{pmatrix} 0 & N'_j \mathbf{W}_v^z - N'_k \mathbf{W}_u^z & N'_k \mathbf{W}_u^y - N'_j \mathbf{W}_v^y \\ N'_k \mathbf{W}_u^z - N'_j \mathbf{W}_v^z & 0 & N'_j \mathbf{W}_v^x - N'_k \mathbf{W}_u^x \\ N'_j \mathbf{W}_v^y - N'_k \mathbf{W}_u^y & N'_k \mathbf{W}_u^x - N'_j \mathbf{W}_v^x & 0 \end{pmatrix} \quad (3.35)$$

Finally, the gradient of the wall surface is,

$$\frac{\partial S}{\partial \mathbf{P}_{jk}} = \iint \frac{\mathbf{a}^T}{|\mathbf{a}|} \tilde{\mathbf{A}}_{jk} dvdu \quad (3.36)$$

Before deriving the gradient of the internal (stretching and bending) energy terms, let us compute the following gradient

$$\frac{\partial |\mathbf{W}_{\alpha\beta}|^2}{\partial \mathbf{P}_{jk}} = \frac{\partial}{\partial \mathbf{P}_{jk}} (\mathbf{W}_{\alpha\beta} \cdot \mathbf{W}_{\alpha\beta}) = 2 \mathbf{W}_{\alpha\beta} \cdot \frac{\partial \mathbf{W}_{\alpha\beta}}{\partial \mathbf{P}_{jk}} = 2 \mathbf{W}_{\alpha\beta} N_j^{(\alpha)}(u) N_k^{(\beta)}(v) \quad (3.37)$$

where α and β stand for the order of parametric derivatives in the u and v direction, respectively.

Using the result from Equations (3.34) and (3.37), we can now write the expression for the gradient of the stretching and bending terms (total internal energy)

$$\begin{aligned} \frac{\partial \mathcal{E}_{internal}^W}{\partial \mathbf{P}_{jk}} = & 2 \iint \{ \gamma_{s_v}^W \mathbf{W}_v N_j N'_k + \gamma_{s_u}^W \mathbf{W}_u N'_j N_k \} |\mathbf{W}_v \times \mathbf{W}_u| dvdu + \\ & 2 \iint \{ \gamma_{b_{vv}}^W \mathbf{W}_{vv} N_j N''_k + 2 \gamma_{b_{vu}}^W \mathbf{W}_{vu} N'_j N'_k + \gamma_{b_{uu}}^W \mathbf{W}_{uu} N''_j N_k \} |\mathbf{W}_v \times \mathbf{W}_u| dvdu + \\ & \iint \{ \gamma_{s_v}^W |\mathbf{W}_v|^2 + \gamma_{s_u}^W |\mathbf{W}_u|^2 + \gamma_{b_{vv}}^W |\mathbf{W}_{vv}|^2 + 2 \gamma_{b_{vu}}^W |\mathbf{W}_{vu}|^2 + \gamma_{b_{uu}}^W |\mathbf{W}_{uu}|^2 \} \frac{\mathbf{a}^T}{|\mathbf{a}|} \tilde{\mathbf{A}}_{jk} dvdu \end{aligned} \quad (3.38)$$

Finally, the gradient of the external energy term is

$$\begin{aligned} \frac{\partial \mathcal{E}_{external}^W}{\partial \mathbf{P}_{jk}} &= \frac{\partial}{\partial \mathbf{P}_{jk}} \iint F(\mathbf{W}) |\mathbf{W}_v \times \mathbf{W}_u| dvdu \\ &= \iint \left\{ \frac{\partial F(\mathbf{W})}{\partial \mathbf{P}_{jk}} |\mathbf{a}| + F(\mathbf{W}) \frac{\mathbf{a}^T}{|\mathbf{a}|} \tilde{\mathbf{A}}_{jk} \right\} dvdu \end{aligned} \quad (3.39)$$

where

$$F(\mathbf{W}) = \left| \tau_{acq} - \frac{I(\mathbf{W}(v, u))}{I(\mathbf{C}(v))} \right| \quad (3.40)$$

and

$$\frac{\partial F(\mathbf{W})}{\partial \mathbf{P}_{jk}} = -\text{sign} \left\{ \tau_{acq} - \frac{I(\mathbf{W})}{I(\mathbf{C})} \right\} \frac{\nabla I(\mathbf{W})}{I(\mathbf{C})} \quad (3.41)$$

Here, $\nabla I(\mathbf{W})$ stands for the gradient of the original image evaluated at the surface point. This term can be evaluated either using finite differences or by precomputing the image gradient using, *i.e.*, Gaussian derivatives.

To summarize, by replacing Equations (3.35), (3.36) (3.38), and (3.39) into (3.30), one is able to compute the analytical gradient of the energy function. Although this derivation might seem cumbersome, it is a mere “advanced” exercise of application of the chain rule and properties of the B-splines. From a computational point of view, evaluation of the gradient is not much more demanding than the function itself once that one realizes that several quantities are shared by most of the terms in the gradient and, therefore, can be used several times after having been computed.

There is a last property of the B-spline basis that can be applied, *viz. local support*: at any given parametric value (u, v) there are at most $(l + 1) \times (m + 1)$ basis functions that are non-zero¹¹, where l and m are the degrees of the B-Spline in the u and v directions respectively. It is possible to show that this is equivalent to say that for any point (u, v) there are only $(l + 1) \times (m + 1)$ control points that contribute to the surface and, thereby, to the gradient. It is not the intention of this appendix to give a detailed account of the implementation of the energy and gradient computation but application of the local support property allows, with minimum bookkeeping, to further speed-up the computations.

Finally, this appendix has shown the derivation of the gradient of Equation (3.16), *i.e.*, the vessel wall energy. However, similar ideas can be applied to compute the gradient of the central vessel axis energy of Equation (3.2).

3.C Appendix: Segmental vessel wall deformation

In this appendix an incremental optimization scheme for the deformation of the vessel wall will be introduced. The basic idea is to subdivide the vessel wall model into vessel wall strips (or segments) that are optimized sequentially. We coin this method *segmental optimization* [104]. Basically, the deformation is started from one end of the vessel wall and it proceeds segment-wise towards the other end.

By taking advantage of the local support property of the B-splines, the deformation of the vessel wall can be broken into several independent optimization problems

¹¹A derivation of this property is beyond the scope of this appendix. For a thorough analysis of this and other B-Spline properties, the interested reader is referred to, *i.e.*, the monograph by Piegel and Tiller [236].

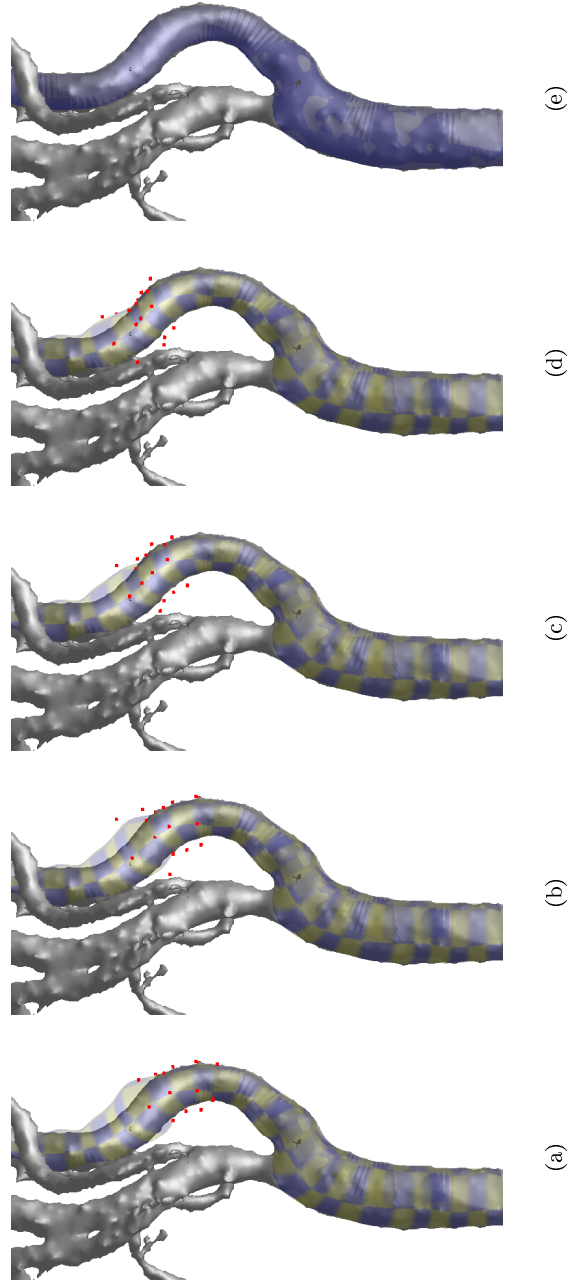


Figure 3.10. Segmental wall deformation. *a)-d)* Four steps in optimizing the vessel wall model segment-wise (from proximal to distal). The surface is tessellated in B-spline patches as indicated by the chess-board pattern. Note how the segment-wise wall fitting progressively attaches to the wall. Therefore, each new optimization starts closer to the final solution than after the sweeping procedure. *e)* Final wall model after all control points have been optimized.

in a lower dimensional space. Although the overall computation load provided by this method is similar to the full-dimensional optimization (all control points simultaneously), this method is able to provide a better local fit. When optimizing all the control points simultaneously, the objective function averages the measure of fit over the whole surface Equation (3.22). Therefore, the effect of small regions of the vessel wall model having a bad local fit would tend to be averaged out. Since in optimizing each vessel strip the objective function only gathers information of a portion of the vessel wall, the segmental optimization yields a better fit along the whole model.

In order to formulate this optimization strategy, let us start off by introducing the parameters that define a B-spline surface model. A B-spline surface of degree l (m) and $q + 1$ ($r + 1$) control points in the u (v) direction, is defined by a bidirectional net of control points, \mathbf{P}_{jk} , two knot vectors, $U = \{u_j; j = 0 \dots q + l + 1\}$ and $V = \{v_k; k = 0 \dots r + m + 1\}$, and the product of univariate B-spline basis functions. This kind of surfaces are also known as *tensor product* surfaces (cf. Equation (3.15)). To break the optimization problem of vessel wall model into wall strips optimized sequentially, the parameter space subdivision has to fulfill the following requirements.¹²

Requirements. *Let a B-spline vessel wall model be defined on the longitudinal parameter $v \in [0, 1]$. A partitioning of this space, $V_i \in [\hat{v}_i, \hat{v}_{l+1})$, suitable for segmental optimization has to fulfill the following requirements*¹³

1. $\bigcup_i V_i = [0, 1]$,
2. $\bigcap_i V_i = \emptyset$,
3. *If \mathcal{P}_i is the subset of control points whose local support influences in V_i , then $\mathcal{P}_i \cap \mathcal{P}_{i+1} = \{\mathbf{P}_{ji}, j = 0 \dots q\}$.*

Condition (1) and (2) simply state that our subdivision of the longitudinal parameter space is complete and non-overlapping. Condition (3) states that after we have optimized the vessel wall in the i -th strip, we can leave $q + 1$ control points fixed. This ensures that after we advance one strip in the segmental optimization, the position of some of the control points can be regarded as optimal. In fact, it is this last condition which ensures that the problem can be broken into small subproblems.

Under clamp-end boundary conditions [236] the knot vector, V , of a B-spline surface has the following form

$$V = \{\underbrace{0, \dots, 0}_{m+1}, v_{m+1}, \dots, v_{r-1}, \underbrace{1, \dots, 1}_{m+1}\} \quad (3.42)$$

If, additionally, multiple knots are not allowed, the following lemma follows from the local support properties of the B-splines [236]

Lemma. *A partition of the parameter space v that exactly fulfill all the above-mentioned requirements is the partition generated by the knot vector V without repeating the begin and end knots, i.e., $\hat{v}_i \equiv v_{m+l}$ with $l = 0 \dots r - m$. Finally, $\mathcal{P}_i \equiv \{\mathbf{P}_{jk}; j = 0 \dots q, k = l \dots l + m\}$.*

¹²In the remainder of the discussion it is assumed that the model will only be chunked in the longitudinal direction, i.e., with respect to the parameter v .

¹³Special care must be taken with the last V_i to also include the value $v = 1$.

In summary, optimizing the energy integral of Equation (3.22) entails solving an optimization problem with $3(q+1) \times (r+1)$ variables. The same problem can be broken into $r-m+1$ subsequent optimizations with $3(q+1) \times (m+1)$ variables. After each subproblem is solved, one row of circumferential control points is frozen, since their values do not influence the subsequent optimization problems. The segmental approach obtains a substantial decrease in dimensionality and, moreover, the dimensionality of each subproblem is independent of the total vessel length. When solving the i -th optimization problem, the support of the double integral in Equation (3.22) can be reduced to the region that is influenced by \mathcal{P}_i . It is possible to show that this corresponds to a surface patch such that $u \in [0, 2\pi)$ and $v \in [v_{\max}(0, i-m), v_{i+1})$.

*True genius resides in the capacity for evaluation of
uncertain, hazardous, and conflicting information.*

— W. Churchill, 1874-1965

Chapter 4

Quantitative analysis of vascular morphology from 3-D MRA: *in vitro* and *in vivo* results

Abstract — A three-dimensional model-based approach for quantification of vascular morphology from several MRA acquisition protocols is evaluated. Accuracy, reproducibility, and influence of the image acquisition technique were studied via *in vitro* experiments with ground truth diameters and the measurements of two expert readers as reference. The performance of the method was similar to or more accurate than the manual assessments and reproducibility also was improved. The methodology was applied to stenosis grading of carotid arteries from CE MRA data. In eleven patients, the approach was compared to manual scores (NASCET criterion) on CE MRA and DSA images, with the result that the model-based technique better correlates with DSA than the manual scores. Spearman's correlation coefficient was 0.91 ($p < 0.001$) for the model-based technique and DSA, versus 0.80 and 0.84 ($p < 0.001$) between the manual scores and DSA. From the results it can be concluded that the approach is a promising objective technique to assess geometrical vascular parameters, including degree of stenosis.

Adapted from: A.F. Frangi, W.J. Niessen, P.J. Nederkoorn, J. Bakker, W.P.Th.M. Mali, and M.A. Viergever (2001). *Quantitative analysis of vessel morphology from 3D MR angiograms: in vitro and in vivo results*. Magnetic Resonance in Medicine, 45(2):311–22, February 2001.

4.1 Introduction

An important prerequisite for planning vascular surgical procedures and for treatment selection of vascular diseases is the quantification of vessel morphology. A relevant application is quantification of the lumen diameter, for instance, to determine the proper dimensions of vascular prostheses, or for accurate stenosis grading. This work, in particular, focuses on the development of a three-dimensional technique to model linear vascular segments and its application to diameter and stenosis quantification.

Treatment selection for patients with carotid artery disease is an example of the need for accurate stenosis grading. The North American Symptomatic Carotid

Endarterectomy Trial (NASCET) [216] and the European Carotid Surgery Trial (ECST) [92], both established that carotid endarterectomy is beneficial for patients with a severe symptomatic (70–99%) carotid artery stenosis.

Two-dimensional DSA has for long time been the gold standard for stenosis grading. Unfortunately, it is a projection technique which introduces problems related to the selection of the optimal projection angle [258], especially in asymmetric stenoses, and to the correction of motion artifacts [200], which is a three-dimensional phenomenon. From projection images, it is generally non-trivial to accurately assess vessel diameter and, especially, cross-sectional area. This last parameter is often derived from the vessel radius [169] under the assumption of a circular cross-section (thus being directly dependent on the vessel radius and not providing additional information).

Although X-ray rotational angiography [298] (RA) can provide a 3-D reconstruction of vessels with high resolution, this technique is still in a research phase and not widely used. Finally, a drawback shared by both DSA and rotational angiography is that they can lead to complications due to invasive catheter manipulations and to the exposure to ionizing radiation. In addition, the contrast agents required for these techniques represent a risk factor themselves [310].

Computed Tomography Angiography (CTA) [253] acquires moderately high resolution images containing high-contrast, artifact-free, vascular signals that are surrounded by a conventional CT scan. The presence of anatomical information, which is not present in the previous techniques, is useful for localizing the vasculature with respect to other organs. A major advantage of CTA with respect to DSA is the ability to retrospectively re-project the information from arbitrary angles. In comparison to MRA, CTA does not suffer from intra-voxel de-phasing and spin saturation which lead to image artifacts. A limitation of CT angiography is the requirement for large quantities of iodinated contrast material. Moreover, the subsequent opacification of all vessels due to the large bolus of contrast prevents a multi-injection/multi-site examination.

Magnetic Resonance Angiography (MRA) is increasingly used [33, 62, 88, 165, 179, 180, 191, 300, 301] to replace DSA in diagnostic procedures. Mistretta [207] has analyzed the relative characteristics of MRA in comparison with other alternative vascular imaging techniques. The advantages of MRA are that it is non-invasive, it does not involve ionizing radiation, and available contrast agents are safer and injected in smaller doses. Whereas the in-plane resolution of MRA is lower than for 2-D DSA, three-dimensional (isotropic) data can be acquired. The introduction of contrast agents, as gadopentetate dimeglumine [243], has considerably improved the clinical applicability of MRA compared to non-enhanced MRA techniques like Time-Of-Flight (TOF) and Phase Contrast (PC) angiography. Contrast-enhanced techniques allow for higher contrast, shorter scan times, arbitrarily positioned imaging planes and reduced flow artifacts. Recent developments with new contrast media such as blood pool agents may further improve image quality.

In clinical practice, analysis of 3-D MRA data sets is mainly performed using Maximum Intensity Projections (MIPs) or Multi Planar Reformatting (MPR) of the three-dimensional volume. The first is known to introduce image artifacts [7, 53, 263] while the second requires precise delineation of a central vessel axis. Although MRA

can provide three-dimensional information, the manual quantification of the vasculature is still tedious and subjective. In Chapter 3, we proposed a scheme for an interactive quantitative analysis of 3-D MR angiograms. The approach uses prior knowledge of the image formation process to accurately define the boundaries of the vessels. In this chapter, this methodology is extended and validated *in vitro* to determine its accuracy and reproducibility, and its dependence on the image acquisition protocol. Moreover, *in vivo* experiments are carried out to determine its potential for clinical use. Ground truth diameters (*in vitro* experiments) and measurements by medical experts (*in vitro* and *in vivo* experiments) are used to validate the method.

The chapter is organized as follows. In Section 4.2 the main ideas underlying the model-based approach to estimate the central axis and width of a vessel are described. Section 4.3 describes the materials and methods involved in the validation of our algorithm. The results of the *in vitro* and *in vivo* validation are presented in Sections 4.4 and 4.5, respectively. Section 4.6 concludes the chapter with a discussion.

4.2 Algorithm overview

Our model-based vascular segmentation procedure consists of two main steps. First, the central vessel axis is computed. Subsequently, a three-dimensional boundary model is initialized and fitted to the image data using a boundary criterion derived from information on the image acquisition technique. The different steps in the algorithm can be summarized as follows (Figure 4.1):

1. Using a rough iso-surface rendering of the vessel(s) of interest, the user selects a couple of points indicating the segment to be measured (Figure 4.1(a)). These points are joined with a geodesic curve that runs *on* the iso-surface and which forms a coarse initialization of the central vessel axis (Figure 4.1(b)). This initialization only requires a simple and intuitive interaction.
2. The central vessel axis, $\mathbf{C}(v)$, is approximated using a B-spline curve of degree n with $s + 1$ control points. This representation enforces the lumen line to be connected

$$\mathbf{C}(v) = \sum_{i=0}^s N_{in}(v) \mathbf{P}_i \quad (4.1)$$

Here \mathbf{P}_i are the control points, $N_{in}(v)$ denotes the i -th B-spline basis function of order n [236], and $v \in [0, 1]$.

3. To fit the vessel axis to the image data, we used a filter based on a local operator that analyzes the eigenvalues of the Hessian matrix computed at each voxel of the image. The filter has the following properties:
 - i. de-enhances non-tubular structures,
 - ii. has maximum response at the center of the vessel,

- iii. analyzes the image at multiple scales to be sensitive to vessels of varying width,
- iv. incorporates directional information.

This filter, as used in this chapter, is an extension of the filter proposed in Chapter 2 and is described in the Appendix 4.A.

4. The vessel wall, $\mathbf{W}(v, u)$, is modeled using a tensor product B-spline surface [236]

$$\mathbf{W}(v, u) = \sum_{j=0}^q \sum_{k=0}^r N_{jl}(u) N_{km}(v) \mathbf{P}_{jk} \quad (4.2)$$

where \mathbf{P}_{jk} are $((q+1) \times (r+1))$ control points, $N_{jl}(u)$ is the j -th B-spline periodic basis function of order l and $u \in [0, 2\pi)$; $N_{km}(v)$ is the k -th B-spline non-periodic basis function of order m and $v \in [0, 1]$. The parameters u and v traverse the surface in the circumferential and longitudinal directions, respectively. The model can be initialized using a standard Computer Assisted Design (CAD) technique known as *swept surfaces* [236]. A circular cross section with a radius equal to the distance between the final central vessel axis and its initialization on the iso-surface is swept along the central vessel axis and orthogonal to the curve at every point (Figure 4.1(c)). This results in a deformable cylinder along the previously computed vascular axis.

5. The vessel wall model is fitted to the boundaries of the underlying vessel (Figure 4.1(d)). Here, the information on the image acquisition is introduced. In an earlier study [140], it was shown that the full-width-half-maximum (FWHM) criterion is a reliable estimate of vessel width in TOF and CE images. For PC, however, the full-width-10%-maximum (FWTM) is preferred. Therefore, we freely deform the vessel wall so the luminance ratio between the voxels on the wall model and on the centerline model fulfills the FWHM or FWTM criterion, respectively. Mathematically, the model is deformed to minimize the function:

$$\mathcal{E}^W = \frac{1}{S} \int_0^1 \int_0^{2\pi} \left| \tau_{acq} - \frac{I(\mathbf{W}(v, u))}{I(\mathbf{C}(v))} \right| dv du + R(\mathbf{W}) \quad (4.3)$$

where $I(\mathbf{x})$ denotes the image gray-level at position \mathbf{x} , S is the total vessel wall area, and τ_{acq} is a threshold that incorporates information on the type of MRA imaging technique. This constant equals 0.5 for TOF and CE, and 0.1 for PC MR angiography. Finally, $R(\mathbf{W})$ is a regularization term that imposes smoothness constraints on the vessel wall surface [103].

The validity of the FWHM and FWTM criteria is dependent on a few assumptions about the image acquisition [103]: *a*) the resolution should be sufficiently high (at least 3 pixels/diameter), *b*) the saturation due to slow inflow at the borders is limited (only for TOF MRA), and *c*) flow artifacts can be neglected. Although it would be

possible to improve on the model of the image acquisition used here (*e.g.*, see [141]), the modeling of signal voids is a more complex issue requiring prior knowledge of the geometry of the vessel, which is precisely what we want to estimate. In practice, this implies that (almost) total occlusions leading to (almost) total signal voids should be interpreted by an expert, whereas accurate estimates should be obtainable in the cases of small to severe stenoses. Evaluation of images in the presence of signal voids usually requires interpretation by an expert. Moreover, in the context of carotid artery disease, clinically, it is only necessary to identify residual lumina smaller than 1 mm. In this case, the stenosis is known to exceed 80% in any event. In other words, the method would be clinically useful if at least can handle moderate voids appearing in non-severe stenoses.

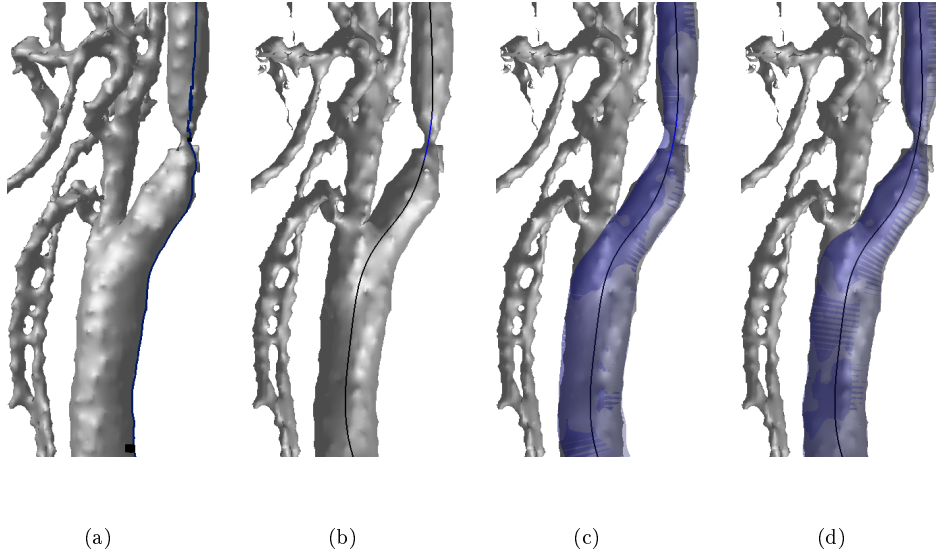


Figure 4.1. Algorithm overview. *a)* The user pinpoints the begin and end position of the segment to be analyzed. From these seeds, a geodesic path is computed. *b)* The geodesic path is deformed until the central vessel axis is determined. *c)* A circular cross section is swept along the axis to generate an initialization of the vessel wall model. *d)* Vessel wall (after deformation) and central vessel axis.

4.3 Materials and methods

4.3.1 Phantoms

To assess the performance of the algorithm, we addressed the problem of diameter measurements which is a prerequisite for stenosis grading. Three phantoms with varying degrees of complexity were analyzed (see Figure 4.2).

The first phantom is a synthetic tube (Elspec Kynar 3/13-X, Aalsmeer, The Netherlands) with a 4.98-mm diameter and a stenosis of 1.73 mm which simulates a stenotic linear vessel (see Figure 4.2(a)). The tube wall thickness (0.1 mm) was small compared to the pixel size (0.5–1.5 mm), so the influence of the wall is expected to be negligible.

The second phantom simulates a carotid bifurcation with an asymmetric stenosis (R.G. Shelley Lt., North York, Ontario, Canada). A photograph of this phantom is shown in Figure 4.2(b). The phantom is embedded in a rigid, transparent acrylic and manufactured to reproduce normal dimensions in the human vasculature [275].

Third, an anthropomorphic phantom of the cerebral vasculature (Instrumentation Department, University Medical Center, Utrecht, The Netherlands) which is embedded within a rigid, transparent acrylic was used. Although it presents a challenging and realistic geometry, no accurate reference dimensions were available from this phantom.

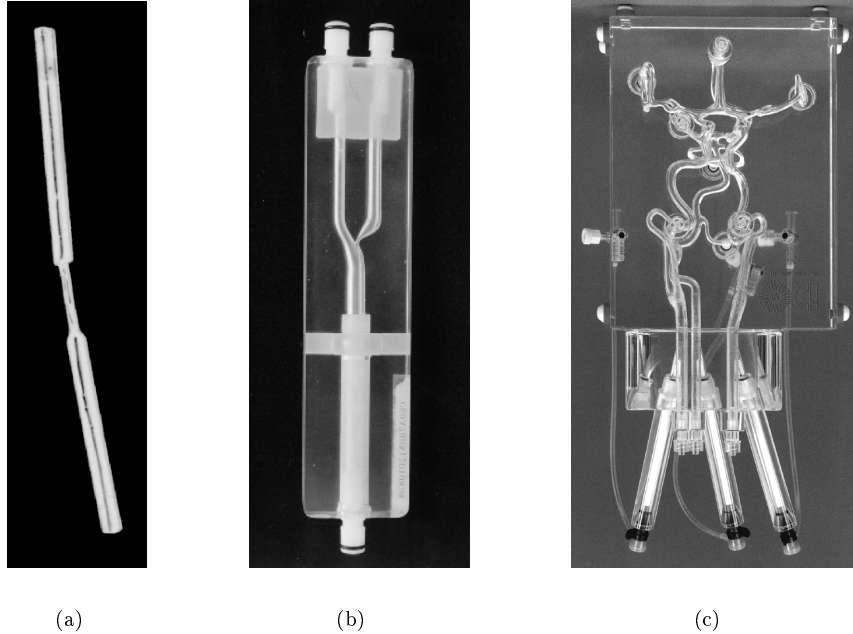


Figure 4.2. Phantoms used in this study. *a)* Linear stenotic phantom. *b)* Carotid bifurcation phantom. *c)* Cerebral vasculature phantom.

4.3.2 Image acquisition

Phantom data

All images were acquired on a 1.5 Tesla MR imaging system (Philips Gyroscan ACS-NT, PowerTrak 6000 gradients, software release 6, Philips Medical Systems, Best, The Netherlands) with a quadrature head-neck receiver coil.

The protocols and imaging parameters used in the experiments with the linear (I), carotid bifurcation (Y), and cerebral vasculature (C) phantoms are summarized in Table 4.1. Multiple 2-D TOF images were acquired at three different pixel sizes (0.5 mm, 1.0 mm and 1.5 mm) to investigate the effect of in-plane resolution. First order flow compensation was applied to all TOF experiments. The flow was regulated by a computer-controlled pump (Quest Image Inc., London, Ontario, Canada). Water was channeled through the tube at a constant velocity (5 ml/s) and a long inlet length was taken to assure that laminar flow was established. The tube was surrounded by the same, but stationary water in all experiments. For CE acquisitions, a 5-mM solution of gadopentetate dimeglumine (Magnevist, Schering, Berlin, Germany) was used under the same flow conditions as the TOF acquisitions.

Reference diameters for the linear and bifurcation phantoms were measured with a Philips Integris V3000 angiographic unit (Philips Medical Systems, Best, The Netherlands), while the phantoms were filled with standard contrast agent (Ultravist, Schering AG, Berlin, Germany). The pixel size was 0.23 mm, and a caliper was available to perform absolute diameter measurements.

Before applying the model-based technique, all images were resampled to have 0.5-mm cubic voxels using *sinc* interpolation. This procedure does not increase the resolution of the acquisition, but reduces partial volume and gridding artifacts [85].

Table 4.1. MRA sequences for the three phantom studies: linear (I), carotid bifurcation (Y) and cerebral (C) phantoms. TE = echo time, TR = repetition time, α = flip-angle, FOV = field-of-view.

<i>Imaging Protocol</i>	<i>Phantom</i>	<i>In-plane Resolution</i> [mm]	<i>TE</i> [ms]	<i>TR</i> [ms]	<i>α</i> [°]	<i>Slice Thickness</i> [mm]	<i>FOV</i> \diamond [mm]
2-D TOF	I/Y	0.5	3.4	18.0	30	4.0	128
2-D TOF	I/Y	1.0	2.7	18.0	30	4.0	256
2-D TOF	I/Y	1.5	2.5	18.0	30	4.0	384
3-D TOF	I/Y	1.0	1.9	25.0	15	1.0	256
3-D PC [▲]	I/Y	1.0	4.0	8.9	15	1.0	256
3-D CE	I/Y	1.0	2.0	6.6	40	1.0	256
3-D CE	C	1.0	3.1	11.0	40	1.0	256

\diamond Matrix size 256×256 in all acquisitions

[▲] $v_{enc} = 200$ cm/s in all directions

Patient data

Eleven patients suspected of carotid artery disease were screened with carotid duplex. All of them had a peak systolic velocity value in the internal carotid artery (ICA) larger than 150 cm/s. Subsequently, each patient underwent a standard clinical MRA protocol including three-dimensional Contrast-Enhanced (CE) MRA. BolusTrak (Philips Medical Systems, Best, The Netherlands) was used to determine the arrival of the contrast bolus. Image acquisition was carried out in the same scanner used for the phantom experiments. The scan parameters were: repetition time, TR 4.4 ms; echo time, TE 1.5 ms; flip angle, α 40°; slice thickness, 1.2 mm; slice gap, -0.6 mm; a 512×280 image matrix, and a 256×140-mm² rectangular field-of-view. The contrast material used was a 5-mM solution of gadopentetate dimeglumine (Magnevist, Schering, Berlin, Germany). Before applying the model-based technique, all images were resampled to have 0.5-mm cubic voxels using *sinc* interpolation.

Each patient also underwent a DSA examination. DSA was performed with a Philips Integris V3000 angiographic unit (Philips Medical Systems, Best, The Netherlands) with an image intensifier matrix of 1024×1024. Using the Seldinger technique, the tip of a 5-F catheter was guided from the femoral artery to the ascending aorta and positioned in the right and subsequently in the left common carotid arteries. Two or three projections (posteroanterior, oblique and possibly lateral) were acquired for each carotid bifurcation. For each projection 6 ml of a contrast agent (Ultravist, 300 mg I/ml, Schering AG, Berlin, Germany) was injected at a constant flow of 3 ml/s.

From the total of twenty-two carotid arteries, three arteries were excluded from the quantitative analysis because of total occlusion. The remaining nineteen vessels ranged from normal/mild to severe stenoses. Manual measurements on MRA and DSA were taken from printed hard copies using a digital display caliper (PAV Electronic, 0.01-mm resolution).

4.3.3 Geometric modeling

In the B-spline representation of the vessel model a few parameters have to be specified – Equations (4.1) and (4.2). In our experiments, third-order (cubic) B-spline curves and surfaces were used ($l = m = n = 3$). The number of control points for the central vessel axis ($s+1$) and the vessel wall ($r+1$) models were determined from their length. A control point was placed every 2.0–2.5 mm in the central vessel axis. For the vessel wall model, a ring of five control points was placed every 5.0 mm orthogonal to the central vessel axis. By means of preliminary experiments with a different number of control points, it was observed that these densities yielded a good trade-off between ability to capture the shape of the *in vivo* carotids and model complexity. Similar parameters were used in the *in vitro* experiments.

4.4 In vitro results

Phantom experiments of varying geometrical complexity were used to assess the performance of the proposed method. First, the accuracy in diameter quantification and the dependence on the image acquisition parameters were studied in simple geometries

where ground truth diameters were available (Section 4.4.1). Finally, experiments were conducted on more complex geometries, with the manual measurements as reference, to assess the robustness to user initialization and the accuracy in diameter measurements (Section 4.4.2).

4.4.1 Linear and carotid bifurcation phantoms

Two experts performed diameter measurements at different points of the linear and carotid bifurcation phantoms. The measurements were taken from Multi Planar Reformatted (MPR) images which were generated by manually drawing a central vessel axis and subsequently computing perpendicular planes along this axis at each measurement point. This procedure was done using the facilities of a clinical workstation (EasyVision, Philips Medical Systems, Best, The Netherlands).

To compare the measurements provided by the experts and the results obtained with our algorithm, a measurement protocol was defined as indicated in Figure 4.3. The location of the stenosis (maximum vessel narrowing) was used as a reference point. Distal and proximal diameter measurements were carried out on both phantoms at 20 mm and 25 mm from the stenosis center. For each cross-sectional plane, the minimum and maximum observed diameters were recorded. For the carotid bifurcation phantom, two extra planes were analyzed and these were placed 5 mm at both sides of the stenosis center. All measurements were done twice by the same expert with enough delay between the sessions to consider the measurements independent.

The semi-automated method was run twice with different initializations of the central vessel axis. For each run, we recorded the minimum and maximum diameter at the same points where the observers performed their measurements.

For each session (run) and observer (semi-automated method) the absolute error in the vessel diameter was computed. Average error and its standard deviation (SD) were calculated to analyze the precision and accuracy of the manual and semi-automated procedures. Since the images of the linear and carotid phantoms were acquired simultaneously (same field-of-view), errors for both phantoms were averaged to have an overall error assessment for each modality.

Diameter quantification: influence of imaging protocol

Table 4.2 summarizes the statistics of the measurement error for a fixed resolution (1 mm) and different acquisition protocols. This table compares the results for the two expert readers (Obs I and II) and for the model-based technique (MB). In the case of multiple 2-D TOF, 3-D TOF and CE MRA, the model-based method performs similarly to or better than the observers. In all three modalities, our method slightly overestimates the diameter (0.08–0.34 mm) but the bias, when compared between sessions, is more systematic than for the observers. Precision of the measurements was 0.42–0.67 mm for the model-based method and 0.29–1.13 mm for the observers.

Phase contrast angiography is the only technique that uses a different criterion for boundary definition, namely, the FWTM [140]. In our experience, this criterion is not very robust when there are large variations in blood velocity along the selected vascular segment. This occurs, for instance, in the presence of a severe stenosis. In

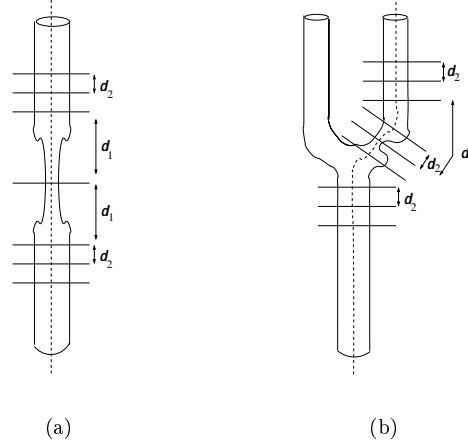


Figure 4.3. Manual measurement protocols: $d_1 = 15$ mm and $d_2 = 5$ mm. *a)* Tube phantom. *b)* Carotid bifurcation phantom.

this case, the velocity encoding is tuned to the highest velocity, which is achieved near the minimum lumen diameter. Therefore, in low velocity regions, the FWTM will indicate boundary points with very low luminance and small signal-to-noise ratio. As a consequence, the model-based technique is prone to becoming trapped in local minima during the fitting procedure. Finally, the bias is smaller with the model-based technique and has an opposite sign. The latter indicates that the visually perceived “boundary” corresponds to a roll-off factor higher than 10%.

Diameter quantification: influence of in-plane resolution (2-D TOF MRA)

Table 4.3 summarizes the mean error in diameter estimation for the linear phantom (I) for the three different in-plane resolutions (0.5, 1.0 and 1.5 mm) of the multi-slice 2-D TOF protocol (cf. Table 4.1). Both accuracy (mean error) and precision (SD) for the two observers and the model-based technique are reported in millimeters. The results show that the model-based technique performs similar to the manual assessment. However, the difference in bias between sessions (or runs) is smaller for the model-based technique, indicating a higher reproducibility of the results.

As expected, increasing voxel size tends to overestimate the vessel width (increased positive bias). This effect is mainly observed at the place of the stenosis where the diameter becomes in the order of the voxel size. This can be appreciated from Figure 4.4 where the average diameter profile for the three resolutions is shown. Box plots summarizing the measurements of all sessions and of the two observers in the planes that are distal and proximal to the stenosis and at the stenosis itself, are overlaid for comparison. The degradation of the model-based measurements with a decrease in voxel size is consistent with the measurements of the experts.

Table 4.2. Luminal diameter absolute error for four imaging protocols. True phantom diameters ranged from 1.18 mm to 7.37 mm. Here, n denotes the total number of measurements per session.

Imaging protocol	Phantom	Session	n	Obs I	Obs II	MB
				$mean (SD)$	$mean (SD)$	$mean (SD)$
2-D TOF 1.0 mm	I	1	14	-0.24 ± 0.51	$+0.44 \pm 0.29$	$+0.25 \pm 0.42$
	I	2	14	-0.76 ± 0.98	$+0.11 \pm 0.36$	$+0.20 \pm 0.42$
3-D TOF 1.0 mm	I/Y	1	32	$+0.10 \pm 0.83$	$+0.58 \pm 0.53$	$+0.08 \pm 0.67$
	I/Y	2	32	$+0.00 \pm 0.80$	$+0.35 \pm 0.50$	$+0.09 \pm 0.62$
3-D PCA 1.0 mm	I/Y	1	32	-0.68 ± 1.08	-0.52 ± 1.25	$+0.37 \pm 1.32$
	I/Y	2	32	-1.29 ± 1.51	-1.08 ± 1.40	$+0.21 \pm 1.18$
3-D CEA 1.0 mm	I/Y	1	32	-0.30 ± 1.13	$+0.63 \pm 0.49$	$+0.34 \pm 0.46$
	I/Y	2	32	-0.26 ± 0.82	$+0.70 \pm 0.61$	$+0.22 \pm 0.42$

Table 4.3. Luminal absolute diameter error for three in-plane resolutions using 2-D TOF acquisition. True phantom diameters ranged from 1.73-mm to 4.98-mm. Here, n denotes the total number of measurements per session.

Imaging protocol	Phantom	Session	n	Obs I	Obs II	MB
				$mean (SD)$	$mean (SD)$	$mean (SD)$
2-D TOF 0.5 mm	I	1	14	-0.11 ± 0.64	$+0.27 \pm 0.26$	$+0.17 \pm 0.45$
	I	2	14	-0.23 ± 0.48	$+0.14 \pm 0.30$	$+0.21 \pm 0.41$
2-D TOF 1.0 mm	I	1	14	-0.24 ± 0.51	$+0.44 \pm 0.29$	$+0.25 \pm 0.42$
	I	2	14	-0.76 ± 0.98	$+0.11 \pm 0.36$	$+0.20 \pm 0.42$
2-D TOF 1.5 mm	I	1	14	$+0.26 \pm 0.92$	$+0.92 \pm 0.74$	$+0.32 \pm 0.46$
	I	2	14	$+0.13 \pm 0.69$	$+0.83 \pm 0.70$	$+0.73 \pm 0.42$

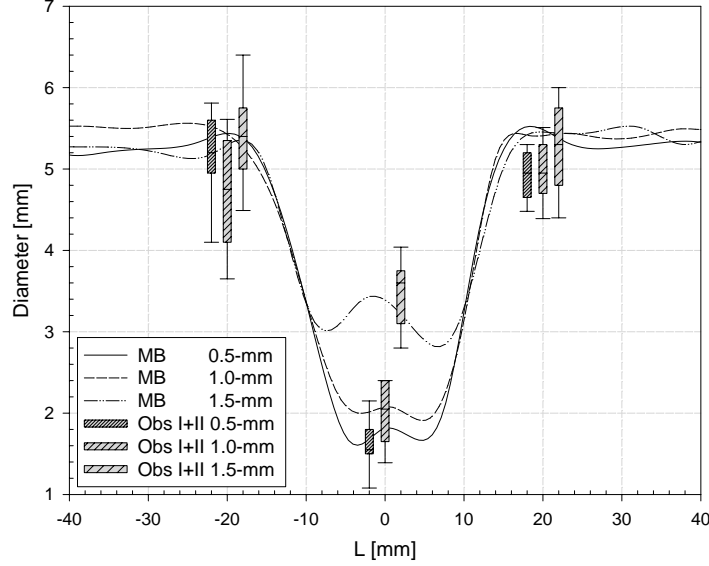


Figure 4.4. Diameter-vs-length (L) plots for the linear stenotic phantom images acquired with the 2-D TOF protocol at three in-plane resolutions: 0.5 mm, 1.0 mm and 1.5 mm. All images were resampled to 0.5 mm cubic voxels using *sinc* interpolation prior to applying the model-based algorithm. For the sake of clarity, the average abscissa of each triad of boxes corresponds to the place where the measurements were carried out.

4.4.2 Cerebral vasculature phantom

Robustness to user initialization

The cerebral vasculature phantom was used to analyze the robustness of the algorithm to different initializations. Figure 4.5(a) shows an iso-surface rendering of the *anterior cerebral artery* (ACA) segment of the cerebral vasculature phantom. Three observers were asked to initialize the central vessel axis by drawing a geodesic path on the iso-surface. The only guide they were provided with was the four landmarks included in the figure, and the remark that the initialization should be close to, but not necessarily through the landmarks. This ensures that they all select the same target vessels and thus allows the assessment of variability caused by initialization of the model for a predefined task. Figure 4.5(b) shows the mean luminal diameter along the central vessel axis averaged over the three initializations. The 95% confidence interval is represented as a needle plot. In the regions where lateral vessels connect into the target segment, the variability is higher. This can be attributed to the fact that at these points the “boundaries” are ill-defined.

Eight centerline points were selected to compare the variability in vessel dimensions caused by different model initializations to the variation caused by multiple readings of the experts. Two observers performed measurements on the source im-

ages using the MPR facility of a clinical workstation (EasyVision, Philips Medical Systems, Best, The Netherlands) and they read the minimum and maximum vessel diameter at each location twice. The average vessel diameter was then estimated with the mean of the minimum and maximum diameters. In Figure 4.5(b), box plots summarizing the four measurements per location are overlaid for comparison. The measurements close to the branch at *B* show a large variability partially because the observers had to extrapolate diameter measurements at the branch. Although the model-based method does not explicitly model the bifurcation, it provides an approximation of the extrapolated diameter at these points. Finally, the overall diameter variability of the expert readings is larger than the variability related to multiple initializations of the model-based method.

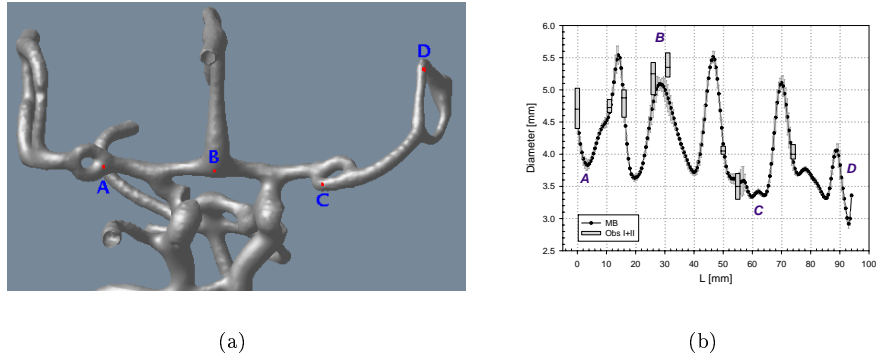


Figure 4.5. Influence of user initialization. *a)* Iso-surface rendering of the *anterior cerebral artery* segment of the cerebral vasculature phantom (CE MRA protocol). *b)* Diameter-vs-length (*L*) plot showing the average value (dots, solid line) and 95% confidence interval (needles) of the mean cross-sectional diameter for three different initializations of the algorithm described in Section 4.2. The initializations were performed by three observers guided only by the four markers indicated in the rendering (*a*) to unambiguously specify a common portion of the vessel. Box plots indicating the overall variability of the observers for some sample points are overlaid for comparison.

Diameter quantification

Two segments of the cerebral vasculature phantom were used to estimate the performance of the method in a complex geometry. The central vessel axis (as computed with our algorithm) was given to the experts to ensure that the measurements of vessel diameter were compared at the same location and that only the variability arising from boundary determination was analyzed. A few sample points along the central vessel axis were selected and each observer performed diameter and area measurements at those locations. The observers did the measurements twice with enough delay between observations to consider them independent.

Figure 4.6 contains diameter (D) and area (A) measurements in the left *external carotid artery* (ECA) segment of the anthropomorphic cerebral phantom. Box plots summarizing the measurements of the two sessions of the two observers at each position are overlaid. Notice that for the measurements inside the *common carotid artery* and close to the flow divider (shaded zone of Figure 4.6) there is limited agreement between our method and the observers. If the segment to be measured contains one branch, positioned very close to one of the ends of the model, the fitting close to the short end tends to be poor. This leads to incorrect extrapolation of the diameter values around the branch.

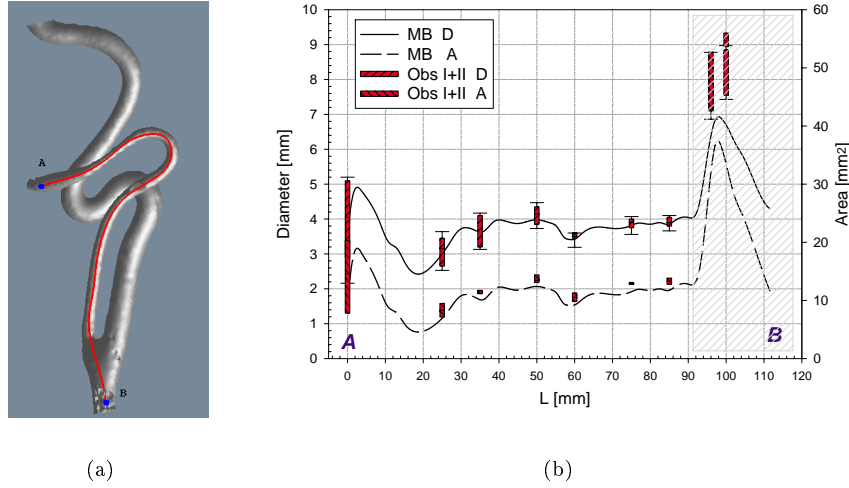


Figure 4.6. Cerebral vasculature phantom: left *external carotid artery* segment. Comparison of average diameter and cross-sectional area along the vessel (L) as assessed by a human observer and with the model-based approach. The shaded region on the graph corresponds to the measurements that are inside the bifurcation.

Since no ground truth diameters were available for the cerebral vasculature phantom, we compared the average diameters measured by observers with those of the model-based approach. Figure 4.7 gives plots as proposed by Bland and Altman [32] indicating repeatability for each “method”, ObsI, ObsII and MB (Figure 4.7(a)), and the agreement between pairs of methods (Figure 4.7(b)). We have excluded from the analysis the two measurements in the shaded zone of Figure 4.6 which can be regarded as outliers. In general, the model should be initialized such that the region of interest is not close to the end points. In this case the method is accurate even if a stenosis is close to a branch. The measurements of Section 4.4.2 were also included in Figure 4.7.

Following Bland and Altman [32], repeatability is defined as $\pm 1.96 \cdot \text{SD}$ of the relative diameter difference between two sessions. This gives a measurement of the inter-observer variability, or to the variability related to multiple initializations of

the model-based technique. The repeatability for the three methods was comparable, ObsI/ObsII/MB = 8.6%/10.7%/8.9% with a bias (average of relative diameter differences between sessions) of +1.6%/+0.98%/-0.3%, respectively. To compare two alternative measurement methods, Bland and Altman define an agreement coefficient as $\pm 1.96 \cdot \text{SD}$ of the relative diameter difference provided by the two methods with a correction for repeated measurements [32]. The agreement coefficient was 18.3% between the two experts, against 16.9% and 17% between each observer and the model-based method. Repeatability was particularly low in the measurements of the *anterior cerebral artery* (ACA) compared to those of the ECA segment. The former had a number of locations at which the diameters had to be extrapolated due to the presence of side branches, and where repeatability was poorer. If only the measurements at the ECA are considered, the repeatability improves (ObsI/ObsII/MB = 4.5%/5.1%/1.7%) and this indicates that where no extrapolation is needed the repeatability is higher with our method, and that otherwise the repeatability is similar to that of the experts.

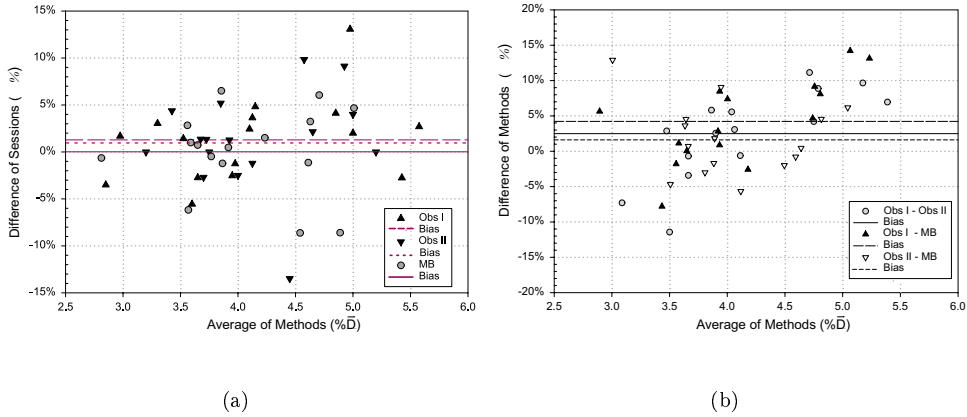


Figure 4.7. Performance in complex geometries. *a)* Repeatability plot indicating the relative diameter differences between the two sessions ($\% \varepsilon = 100\% \times (\%D_1 - \%D_2) / \% \overline{D}$) against the corresponding mean value ($\% \overline{D} = (\%D_1 + \%D_2) / 2$). *b)* Agreement plot indicating the relative diameter differences between pairs of “methods” ($\% \varepsilon = 100\% \times (\%D_A - \%D_B) / \% \overline{D}$) against their mean value ($\% \overline{D} = (\%D_A + \%D_B) / 2$). The measurements compared in the agreement plot are the average of the measurements of the two sessions used for the repeatability plot [32].

4.5 In vivo results

Nineteen internal carotid arteries were analyzed by two experts independently. Stenoses were quantified according to the NASCET index [216]. This index quantifies the percentage of vessel diameter narrowing as $\%D = 100\% \times (1 - b/a)$, where b

and a stand respectively for the vessel diameters at the stenosis, and distal to it, after the post-stenotic bulb (Figure 3.6). Grading of DSA images was performed by averaging the scores from all the available projections without vessel over-projection. Quantification of CE MR angiograms was done by averaging the degree of stenosis computed from maximum intensity projections in the posteroanterior, oblique and lateral views without vessel over-projection. The same arteries were graded with the model-based technique using the NASCET criterion reading the diameters from the diameter-vs-length plots. Figure 4.8 illustrates the results of the *internal carotid artery* (ICA) models that were fitted to several patients. Figures 4.8(a) and 4.8(b) exemplify the models of normal and mildly stenotic ICAs, respectively. Figures 4.8(c) to 4.8(f) are examples of stenotic ICAs with Figs. 4.8(e) and 4.8(f) showing examples of models fitted in the presence of signal loss at the stenosis and distal to the stenosis, respectively. In the latter case, signal voids are present due to poor synchronization between the acquisition and the contrast bolus arrival.

Figure 4.9 shows the linear regression between the DSA and the CE MRA scores of the nineteen carotid arteries included in this study. The scores obtained from the model-based technique were compared against the average of the DSA scores of the two observers for the same artery. In the same figure, the 95% confidence intervals and the 95% prediction intervals for the linear regressions are included. From this analysis, it is concluded that the model-based technique presents tighter confidence bounds than those of the two observers. The slopes of the linear regressions (cf. Table 4.4) indicate that the model-based technique consistently underestimates the degree of stenosis compared to DSA, although this is also the case for one of the observers.

Table 4.4 shows the quantitative comparison between DSA and CE MRA for the two observers and the model-based technique. Spearman's coefficient indicates a good correlation between the model-based technique and DSA. The Wilcoxon test indicates no statistically significant difference in the latter case, nor for the observers at a 5% confidence level. We also computed the Bland and Altman [32] plots to establish the bias between the DSA and CE MRA scores and the 95% agreement intervals for the two observers and the model-based technique. The results are summarized in the third column of Table 4.4, and they agree with the prediction intervals of the linear regression, namely, the model-based technique has a smaller dispersion compared to the manual assessment.

Table 4.4. DSA vs CE MRA results for both observers (I and II) and the model-based (MB) technique. Bias and 95% bounds of agreement are in units of % D .

DSA vs CE MRA	Slope	% D : Bias ($\pm 1.96SD$)	Spearman's r_s (p)	Wilcoxon p
Obs I	0.981	+6.3 (± 28.5)	0.80 (< 0.001)	0.13
Obs II	0.860	+7.2 (± 31.1)	0.84 (< 0.001)	0.09
MB	0.846	-5.0 (± 19.9)	0.91 (< 0.001)	0.97

4.6 Discussion and conclusion

A technique for semi-automated three-dimensional quantitative analysis of vascular morphology from MRA has been presented and evaluated. The method incorporates prior knowledge of the image formation process and can handle irregular vascular cross sections. The method has the additional advantage that it yields a complete description of vascular morphology. Thus, next to vessel diameter, vascular cross-sectional area and vessel wall shape irregularity can be quantified.

The method may replace and supplement manual stenosis assessments which are subject to inter and intra-observer variability. Both accuracy and reproducibility of the method were tested in phantom studies. With no gold standard available, the accuracy of the model-based diameter measurements was compared to the expert readings. The results of the *in vitro* experiments showed that the semi-automated method performed similar to or more accurately than the experts. Moreover, reproducibility of the measurements is improved. Tests showed that the results were not very sensitive to different user initializations.

In Section 4.4.1, it was shown that there is a small bias in the diameters obtained with the model-based technique. This indicates that the FWHM criteria introduce a systematic error. Hoogeveen *et al.* [140] have demonstrated that this is indeed the case in vessels with a resolution of less than 3 pixels/diameter. For vessels in the range 1–3 pixels/diameter there is a maximum systematic underestimation of 20% and for vessels smaller than 1 pixel/diameter the FWHM overestimates the diameter by a maximum of 20%. For vessels larger than 3 pixels/diameter, the bias is negligible ($< 5\%$). This last result is also in agreement with the bias obtained in the experiments with the phantom of the cerebral vasculature where all the measurements corresponded to diameters in the latter range.

In the *in vitro* experiments, the method was compared with those made by the experts who measured the diameter in cross-sectional planes orthogonal to the vessel. In most clinical situations, stenoses are graded from MIP images, as in our *in vivo* study. Our method uses a three-dimensional model which operates directly on the three-dimensional data, and thus no errors owing to projections are introduced [7, 53, 263].

In general, it is assumed that the vessel wall has a circular cross section. *Ex vivo* measurements [227] have shown that this assumption is simplistic and, especially at the stenosis, a wide variety of geometric shapes can be observed. Elgersma and co-workers [90] have supported this idea based on *in vivo* measurements from multiple projections of three-dimensional reconstructions obtained with a rotational angiography system, and concluded that this imposes a severe limitation on the measurements done from (a limited number of) 2-D projections. Three-dimensional approaches, like the one presented in this work, provide a basis for both the description of the actual cross-sectional shape and its quantification. They also allow the definition of stenosis indexes based on cross-sectional area reduction which are more representative of flow obstruction than those only based on diameter narrowing.

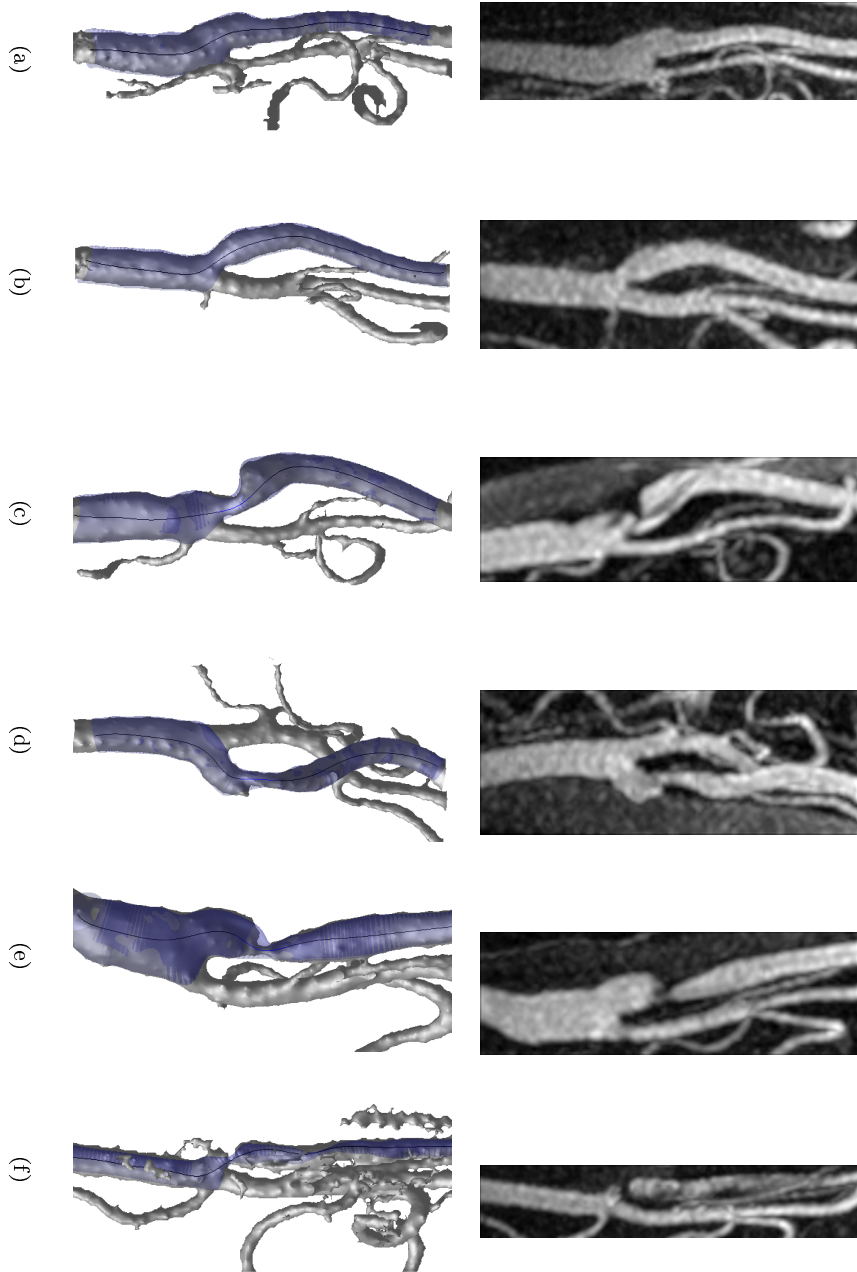


Figure 4.8. Examples of internal ICA models. The top row shows maximum intensity projections of 3-D CE MR angiograms of the ICA. The bottom row shows the three-dimensional models fitted to the source images. Cases (a) and (b) are normal ICAs. Cases (c) and (d) are stenotic ICAs. Cases (e) and (f) correspond to models fitted in the presence of a signal void at the stenosis and distal to the stenosis, respectively. In the latter examples, signal voids are caused by poor synchronization between the acquisition start and the contrast bolus arrival.

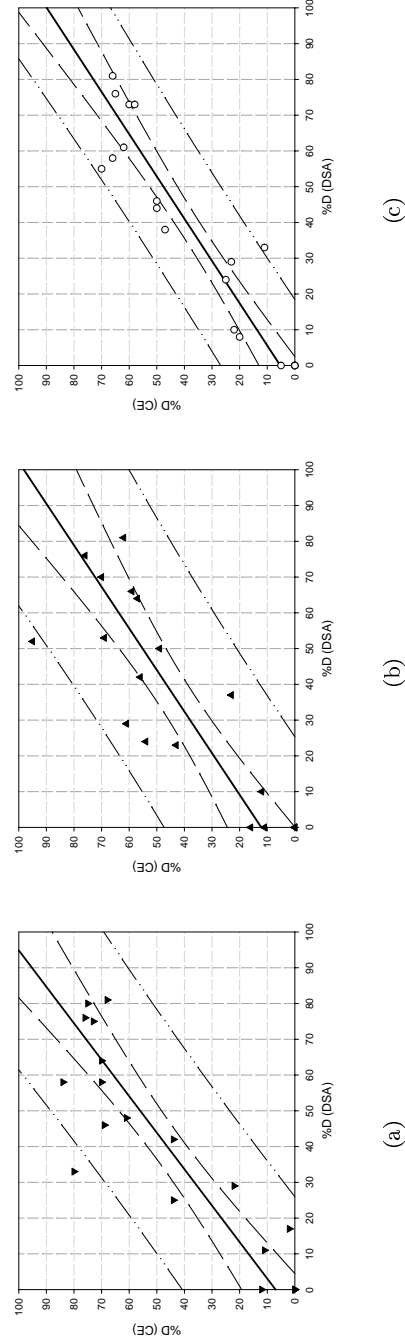


Figure 4.9. CE MRA vs DSA. Degree of stenosis measured in $n = 19$ carotid arteries. Linear regressions (solid line) Obs I (a), Obs II (b), and MB (c), and 95% confidence and prediction intervals (dashed and dash-dot lines, respectively). Note: Observers I and II scored the CE MRA using MIPs. Scores from CE MRA are compared to those of DSA of the same observer. The model-based measurements were compared against the average DSA scores of the two observers for the same artery. All scores were computed using the NASCET criterion [216].

The *in vivo* experiments indicate the potential of the proposed method in a clinical setting. In the previous chapter, a few examples on 3-D TOF MR angiograms were presented. As we had pointed out, applicability of the method is limited to TOF MRA data sets without significant flow artifacts. In this chapter we analyzed 3-D CE MRA data sets which, in principle, are less sensitive to flow-induced artifacts. An analysis of a series of CE MRA clinical data sets was presented with promising results. Although CE MRA reduces the problems related to flow voids, difficulties in triggering the acquisition start can still influence the results. Premature triggering can yield a turbulent appearance in the luminal intensity because of an inhomogeneous mixture of blood and contrast medium. Although the validity of our boundary criterion and the accuracy of the measurements can be influenced, the results presented indicate that the model-based technique correlates better with DSA than manual measurements. Spearman's correlation coefficient was 0.91 ($p < 0.001$) for the model-based technique against 0.80 ($p < 0.001$) and 0.84 ($p < 0.001$) for the two experts. We expect that future improvements in acquisitions that use contrast agents will eventually lead to more accurate measurements.

From the geometric modeling standpoint, a possible improvement of the method is to introduce spatially varying model flexibility (control points of the B-spline model). In the present formulation, the control points of the vessel wall model are evenly distributed along the vessel. This distribution was adequate for the phantom experiments and, to an extent, for the patient data presented in this chapter. This situation, however, is not optimal since some vessel parts have an almost constant diameter while other parts, *viz.* around the stenosis, have abrupt diameter changes over very short distances. An adaptive mechanism to adjust the density of control points as a function of the local diameter changes would be preferred. This would allow for more accurate modeling of shape variations in the stenotic region while capturing the average diameter of the distal portion where the diameter variations are smaller.

4.A Appendix: Central vessel axis image feature

In this appendix we describe the image feature used to guide the fitting of the central vessel axis, which is based on the eigenvectors and eigenvalues of the image Hessian matrix.

Let $I(\mathbf{x})$ and $\mathcal{H}_\sigma(\mathbf{x})$ be the intensity function (Figure 4.10(a)) and the associated Hessian matrix at a given voxel \mathbf{x}

$$\mathcal{H}_\sigma(\mathbf{x}) = \begin{bmatrix} \mathcal{I}_{xx}(\mathbf{x}) & \mathcal{I}_{xy}(\mathbf{x}) & \mathcal{I}_{xz}(\mathbf{x}) \\ \mathcal{I}_{yx}(\mathbf{x}) & \mathcal{I}_{yy}(\mathbf{x}) & \mathcal{I}_{yz}(\mathbf{x}) \\ \mathcal{I}_{zx}(\mathbf{x}) & \mathcal{I}_{zy}(\mathbf{x}) & \mathcal{I}_{zz}(\mathbf{x}) \end{bmatrix} \quad (4.4)$$

where $\mathcal{I}_{\xi_1\xi_2}(\mathbf{x})$ denote regularized derivatives of the image $I(\mathbf{x})$, which are obtained by convolving the image with the derivatives of the Gaussian kernel at scale σ [160]

$$\mathcal{I}_{\xi_1 \xi_2}(\mathbf{x}) = \sigma^2 \frac{\partial^2 G(\mathbf{x}, \sigma)}{\partial \xi_1 \partial \xi_2} * I(\mathbf{x}) \quad (4.5)$$

$$G(\mathbf{x}, \sigma) = \frac{1}{\sqrt{(2\pi\sigma^2)^3}} e^{-\frac{\|\mathbf{x}\|^2}{2\sigma^2}} \quad (4.6)$$

Here λ_k will denote the eigenvalue with the k -th smallest magnitude ($|\lambda_1| \leq |\lambda_2| \leq |\lambda_3|$). A pixel belonging to a vascular region will be signaled by λ_1 being small (ideally zero), and λ_2 and λ_3 being large and of equal sign (the sign is an indicator of brightness/darkness). The respective eigenvectors correspond to singular orientations: $\hat{\mathbf{u}}_1$ indicates the orientation of the vessel (minimum intensity variation) and $\hat{\mathbf{u}}_2$ and $\hat{\mathbf{u}}_3$ form a basis for the orthogonal plane.

To enhance bright vessel-like structures we have proposed in Chapter 2 the following discriminant function. This function performs a non-linear combination of the eigenvalues of the Hessian matrix in such a way that linear structures are enhanced while noise and non-tubular structures are smoothed out.

$$\mathcal{V}(\mathbf{x}, \sigma) = \begin{cases} 0 & \text{if } \lambda_2 > 0 \text{ or } \lambda_3 > 0, \\ \left[1 - \exp\left(-\frac{\mathcal{R}_A^2}{2\alpha^2}\right)\right] \exp\left(-\frac{\mathcal{R}_B^2}{2\beta^2}\right) \left[1 - \exp\left(-\frac{\mathcal{S}^2}{2c^2}\right)\right], & \text{otherwise} \end{cases} \quad (4.7)$$

$$\mathcal{R}_A = \frac{|\lambda_2|}{|\lambda_3|}, \quad (4.8)$$

$$\mathcal{R}_B = \frac{|\lambda_1|}{\sqrt{|\lambda_2 \lambda_3|}} \quad (4.9)$$

$$\mathcal{S} = \|\mathcal{H}_\sigma\| = \sqrt{\sum_j \lambda_j^2} \quad (4.10)$$

Here \mathcal{R}_A , \mathcal{R}_B and \mathcal{S} correspond to local measures of cross-sectional asymmetry, local sphericity and degree of image structure [106]. The parameters α , β and c tune the sensitivity of the filter to deviations in \mathcal{R}_A , \mathcal{R}_B and \mathcal{S} relative to the ideal behavior for a line structure.

Equation (4.7) explicitly states that the filter response is a function of the scale at which the Gaussian derivatives are computed. The filter is applied at multiple scales that span the range of expected vessel widths according to the imaged anatomy. To provide a unique filter output for each pixel, the multiple scale outputs undergo a *scale selection* procedure [182]. This amounts to computing the maximum filter response across scales

$$V(\mathbf{x}) = \max_{\sigma_{min} \leq \sigma \leq \sigma_{max}} \mathcal{V}(\mathbf{x}, \sigma) \quad (4.11)$$

In this way, different vessel sizes will be detected at their corresponding scales and both small and large vessels will be captured with the same scheme (Figure 4.10(b)).

Compared to the original implementation of Chapter 3, improved results have been obtained in experiments by incorporating directional information. The orientation of the vessel at voxel \mathbf{x} corresponds to that of the smallest-magnitude eigenvalue at that location, $\hat{\mathbf{u}}_1(\mathbf{x})$. This orientation is computed at the same scale at which the filter output yielded maximum response –Equation (4.11).

If $\hat{\mathbf{t}}(v)$ is the tangent vector to the B-spline central vessel axis model at parameter value v , the centerline will be obtained by optimizing the following criterion

$$\mathcal{E}^C = -\frac{1}{\ell} \int_0^1 V(\mathbf{C}(v)) |\langle \hat{\mathbf{t}}(v), \hat{\mathbf{u}}_1(\mathbf{C}(v)) \rangle| dv + Q(\mathbf{C}) \quad (4.12)$$

where ℓ is the centerline length, and $Q(\mathbf{C})$ is a regularization term depending only on the central vessel axis model (cf. Chapter 3), and $\langle \cdot, \cdot \rangle$ stands for the scalar product. The extra factor, $\langle \hat{\mathbf{t}}(v), \hat{\mathbf{u}}_1(\mathbf{C}(v)) \rangle$, enforces that the tangent to the central vessel axis model is parallel to the vessel orientation as inferred from the image. Since the eigenvectors of the Hessian matrix only provide an orientation (not a direction) only the magnitude of the scalar product is relevant. Therefore, the model will not only go through the voxels of maximum filter output, but will smoothly vary in orientation according to the variations of the underlying vasculature (Figure 4.10(c)). In particular, we have observed that the addition of this factor improves the fit of the model extremes which will be enforced to end with the same orientation of the vessel.

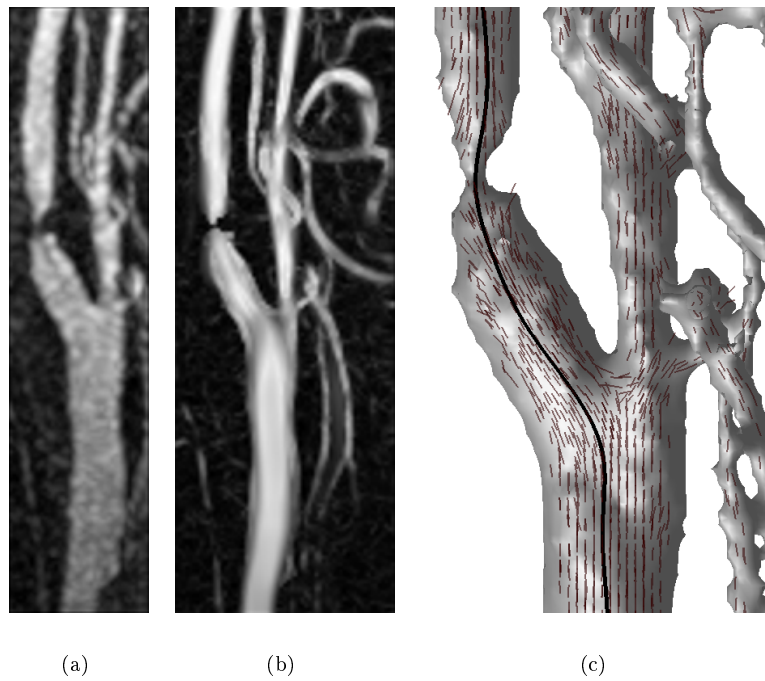


Figure 4.10. Filter performance at a severe stenosis. *a)* MIP of the original CE MRA data set of the carotid arteries. *b)* MIP of the amplitude of the filter output. *c)* Three-dimensional rendering of the vasculature near the stenosis with small needles indicating the local orientation inferred from the Hessian matrix. The centerline, nicely conforming to the orientation field, is also indicated for comparison.

*When possible make the decisions now, even if action is in the future.
A reviewed decision usually is better than one reached at the last
moment.*

— Anonymous

Chapter 5

Three-dimensional modeling for functional analysis of cardiac images – A review

Abstract — Three-dimensional (3-D) imaging of the heart is a rapidly developing area of research in medical imaging. Advances in hardware and methods for fast spatio-temporal cardiac imaging are extending the frontiers of clinical diagnosis and research on cardiovascular diseases.

In the last few years, many approaches have been proposed to analyze images and extract parameters of cardiac shape and function from a variety of cardiac imaging modalities. In particular, techniques based on spatio-temporal geometric models have received considerable attention. This paper surveys the literature of two decades of research on cardiac modeling. The contribution of the paper is three-fold: 1) to serve as a tutorial of the field for both clinicians and technologists, 2) to provide an extensive account of modeling techniques in a comprehensive and systematic manner, and 3) to critically review these approaches in terms of their performance and degree of clinical evaluation with respect to the final goal of cardiac functional analysis. From this review it is concluded that whereas three-dimensional model-based approaches have the capability to improve the diagnostic value of cardiac images, issues as robustness, 3-D interaction, computational complexity and clinical validation still require significant attention.

Adapted from: A.F. Frangi, W.J. Niessen, and M.A. Viergever (2001). *Three-dimensional modeling for functional analysis of cardiac images: A review*. IEEE Trans Med Imaging, in press.

5.1 Introduction

Cardiovascular disease (CVD) has been the number one cause of death in the United States since 1900 in every year but one (1918). More than 2,600 Americans die each day of CVD; an average of one death every 33 seconds [3]. CVD claims more lives each year than the next seven leading causes of death combined. According to the most recent computations of the Centers for Disease Control and Prevention of the National Center for Health Statistics (CDC/NCHS), if all forms of

major CVD were eliminated, life expectancy would rise by almost 10 years while with elimination of all forms of cancer the gain would be 3 years [3].¹

Nowadays, there is a multitude of techniques available for cardiac imaging which provide qualitative and quantitative information about morphology and function of the heart and great vessels (Figure 5.1). Use of these technologies can help in guiding clinical diagnosis, treatment, and follow-up of cardiac diseases. Spatio-temporal imaging is a valuable research tool to understand cardiac motion and perfusion, and their relationship with stages of disease.

Technological advances in cardiac imaging techniques provide 3-D information with continuously increasing spatial and temporal resolution. Therefore, a single cardiac examination can result in a large amount of data (particularly in multi-phase 3-D studies). These advances have led to an increasing need for efficient algorithms to plan 3-D acquisitions, automate the extraction of clinically relevant parameters, and provide tools for their visualization.

Segmentation of cardiac chambers is an invariable prerequisite for quantitative functional analysis. Although many clinical studies still rely on manual delineation of chamber boundaries, this procedure is time-consuming and prone to intra- and inter-observer variability. Therefore, many researchers have addressed the problem of automatic left (LV) and right (RV) ventricle segmentation. Since the shape of the cardiac ventricles is approximately known, it seems natural to incorporate prior shape knowledge into the segmentation process. Such *model-driven* techniques have received ample attention in medical image analysis in the last decade [197, 274]. A few advantages over model-free approaches are: a) the model itself can constrain the segmentation process that is ill-posed in nature owing to noise and image artifacts; b) segmentation, image analysis and shape modeling are simultaneously addressed in a common framework; c) models can be coarse or detailed depending on the desired degree of abstraction; d) in some approaches, most of the chamber's shape can be explained with a few comprehensible parameters which can subsequently be used as cardiac indices (cf. [20, 218, 219, 232, 233] among others).

Use of geometric models is not completely new to the analysis of cardiac images. As a matter of fact, traditional methods of obtaining parameters such as left ventricular volume and mass from echo- and angiocardiology were based on (simple) geometrical models [66, 79, 136, 152]. However, their use was mainly motivated by the need of extracting 3-D parameters from two-dimensional (2-D) images and their accuracy was therefore limited [306].

The literature on model-driven segmentation of cardiac images has grown rapidly in the last few years and this trend is likely to continue. To the best of our knowledge no survey is available that reviews this work.² This paper presents a comprehen-

¹At the time of writing, the authors could not find similar statistics for Europe. There is, however, an ongoing European survey on CVDs whose results are expected to appear soon [273].

²After this chapter has been accepted for publication in journal form [105], the authors have found a very recent parallel review paper by Suri [287]. Suri's review is complementary to ours in that it also surveys the literature on two-dimensional and model-free cardiac image analysis. However, it is less extensive in terms of three-dimensional modeling. The main conclusions of that review are similar to ours. Although many approaches have been presented in the literature, most of them are not yet ripe for clinical use. One of the main topics to be addressed in the future is clinical evaluation.

sive and critical review of the state-of-the-art in geometric modeling of the cardiac chambers, notably the LV, and their potential for functional analysis. In order to set reasonable bounds to the extent of this survey, we have confined ourselves to peer-reviewed *archival publications*³ proposing methods for LV (RV) segmentation, shape representation, and functional and/or motion analysis, that fulfill the following selection criteria:

- the technique is model-based,
- the reconstructed model is 3-D,⁴
- illustration on cardiac images is provided.

This chapter is organized as follows. Section 5.2 gives a brief overview of the different acquisition modalities that have been used in imaging the heart. Section 5.3 overviews and defines the most relevant clinical parameters that provide information on cardiac function. Section 5.4 presents a systematic classification of cardiac models by type of geometrical representation/parameterization. Attention is also given to the different types of input data and features for model recovery. This section is summarized in Table 5.1. Section 5.5 discusses cardiac modeling approaches with respect to the functional parameters they provide and the degree of evaluation of these methods. This section leads to Table 5.2 that links the clinical target of obtaining functional information of the heart (Section 5.3) to the various technical approaches presented in Section 5.4. Finally, Section 5.6 closes the survey with conclusions and suggestions for future research.

5.2 Imaging techniques for cardiac examination

The physical properties on the basis of which the imaging device reconstructs an image (*e.g.*, radioactive emission of an isotope) are intimately related to some specific functional aspects of the heart (*e.g.*, its perfusion properties). Each imaging modality presents advantages and limitations that influence the achievable modeling accuracy. This section briefly reviews the techniques most frequently used for 3-D clinical investigation of the heart. More extensive reviews and complementary readings can be found in [38, 137, 194, 214, 244, 248, 252, 315].

5.2.1 Angiocardiology

Angiocardiology is the X-ray imaging of the heart following the injection of a radio-opaque contrast medium. Although 2-D in principle, this technique can provide projections from two angles using a biplane system. Selective enhancement of the lesion to be demonstrated can be accomplished by positioning an intra-vascular

³A few exceptions were made when the approaches were considered relevant and journal versions were not available.

⁴Even if the imaging technique is not 3-D like, for instance, in the reconstruction of 3-D models from multiple non parallel slices or from multiple 2-D projections.

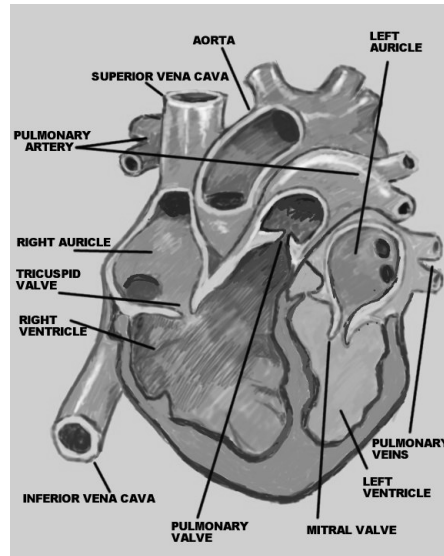


Figure 5.1. Diagram of the heart.

catheter through which the contrast medium is guided and injected. Angiocardiology is usually good at anatomic delineation of lesions but much less satisfactory in determining their severity and the degree of hemodynamic disturbance that they have produced. This technique has been used for a long time to assess ejection fraction and volumes [152] based on simplified geometric models [66, 79, 136] of the LV, but most radiologists use visual assessment based on experience [248].

5.2.2 Cardiac ultrasound

Two-dimensional ultrasonic imaging (US) of the heart or “echocardiography” [194, 244] allows the anatomy and movements of intra-cardiac structures to be studied non-invasively. The application of pulsed and continuous-wave Doppler principles to 2-D echocardiography (2DE) permits blood flow direction and magnitude to be derived and mapped onto a small region-of-interest of the 2DE image. In color flow Doppler mapping (CFM), the pulsed-wave signal with respect to blood velocity and direction of flow throughout the imaging plane is color coded, and produces a color map over the 2DE image. One of the limiting factors of 2DE is the ultrasound window (presence of attenuating tissues in the interface between the US transducer and the organ of interest). To overcome this problem *transesophageal echocardiography* can be used, which allows for high-quality color flow images at the expense of being invasive.

Three-dimensional echocardiography (3DE) [214] is a relatively new development in US that allows 3-D quantitation of organ geometry since the complete organ structure can be imaged. This technique has been used to compute LV volume and mass [8, 59, 120, 174, 283, 294] and to perform wall motion analysis [187].

5.2.3 Isotope imaging

Isotopes have been used to study left ventricular function and myocardial perfusion. Radionuclide techniques for monitoring global and regional ventricular function fall into two major categories: a) *first-pass studies* in which the injected bolus dose is monitored during its first passage through the heart and great vessels; and b) *gated equilibrium studies*, in which the tracer mixes with the blood pool before data collection. First pass acquisitions are typically 2-D, while gated equilibrium studies can be 2-D or 3-D (Single Photon Emission Computed Tomography – SPECT). Isotope imaging can be used to assess parameters like ejection fraction [114] and regional wall motion analysis [93, 96, 114]. It is also used to study myocardial perfusion [115] in cases of ischemia or myocardial infarction, and to assess myocardial viability. The overwhelming majority of radionuclide studies performed for perfusion assessment are SPECT.

5.2.4 Cardiac Computed Tomography

Conventional Computed Tomography (CT) [38] had virtually no place in cardiovascular examinations. Nowadays spiral CT [159, 220] is becoming increasingly popular for cardiac imaging, with image quality rivaling that of magnetic resonance. Dynamical Spatial Reconstruction [252] (DSR) uses multiple X-ray tubes and image intensifier chains to produce “real time” multiple cross-sections with similar acquisition times to ultrafast CT but is not commercially available [248]. Electron Beam Computed Tomography (EBCT) [37] or Ultrafast CT is both relatively inexpensive to perform and capable of providing 3-D information on coronary calcium deposits (plaque) and cardiac cavities’ anatomy and function. A current limitation of this system (relative to DSR) is that the spatial resolution in the transaxial direction is much less than in the in-plane (often transverse) direction.

5.2.5 Magnetic Resonance Imaging

Cardiac Magnetic Resonance Imaging [315] (MRI) is now an established, although still rapidly advancing, technique providing information on morphology and function of the cardiovascular system [138]. Advantages of cardiac MRI include a wide topographical field of view with visualization of the heart and its internal morphology and surrounding mediastinal structures, the capability of multiple imaging planes, and a high soft-tissue contrast discrimination between the flowing blood and myocardium without the need for contrast medium or invasive techniques. Long- and short-axis views of the heart, as used in echocardiography, can be obtained routinely since arbitrary imaging planes can be selected.

Another advantage of MRI is that it can provide both anatomical and functional information about the heart. Several researchers have used MRI to assess global and regional, right and left ventricular function as represented by stroke volume, ejection fraction and LV mass [60, 86, 151, 185, 192, 299], wall-thickening [30], myocardial motion [198], and circumferential shortening of myocardial fibers [51]. Data from MRI is more accurate than that derived from left ventricular angiocardiography, where the

calculation is based on the assumption that the LV is ellipsoidal in shape. Volume measurements by MRI are independent of cavity shape, with the area from contiguous slices integrated over the chamber of interest.

In contrast with other techniques, including 2DE and angiocardiology, anatomic information is easily defined on MRI. The advantages of MRI over 2DE are a wider topographical window and a superior contrast resolution.

A decade ago, MR *tagging* was introduced independently by Zerhouni [326] and Axel [12]. This technique is able to create and track material points (points attached to a fixed location of the myocardium) over time. Myocardial deformations can therefore be studied in a non-invasive manner. SPAtial Modulation of Magnetization (SPAMM) creates two orthogonal sets of parallel planes (sheets) of magnetic saturation, usually orthogonal to the imaging plane. Tissue deformation will be indicated by the displacement of black (saturated) bands in the image that correspond to the intersections of the imaging plane (tag grid). This grid only provides the in-plane motion component (2-D motion). To reconstruct the 3-D motion of the material points, a number of 2-D tagged image sections must be obtained in at least two orientations. Further post-processing is then required to interpolate the displacement field and to eventually perform strain analysis.

5.3 Classical descriptors of cardiac function

Development of models of the cardiac chambers has emerged from different disciplines and with various goals. Cardiac models have been used for deriving functional information, for visualization and animation, for simulation and planning of surgical interventions, and for mesh generation for Finite Element (FE) analysis.

This survey will be confined to the application of modeling techniques for obtaining classical functional analysis. Classical functional analysis can be divided into *global functional analysis* (Section 5.3.1), and *motion/deformation analysis* (Section 5.3.2), from which the most clinically relevant parameters can be obtained.

Model-based methods also allow one to derive new descriptors of cardiac shape and motion. Such advanced descriptors have been mainly presented in the technical literature and their clinical relevance has still to be assessed. Without pretending to be exhaustive, Appendix 5.A summarizes a number of non-classical shape and motion descriptors that demonstrate the extra possibilities provided by some advanced methods.

5.3.1 Global functional analysis

Weber and Hawthorne [311] proposed a classification of cardiac indices according to their intrinsic dimensionality: linear, surface and volumetric descriptors. Linear parameters have been used intensively in the past since they can easily be derived from 2-D imaging techniques like 2DE and X-ray angiocardiology.⁵ However, they

⁵Such parameters are, for instance, left ventricular internal dimension (LVID), relative wall thickness (RWT), and estimates of fractional shortening of the cardiac fibers ($\%\Delta D$) and their velocity (V_{cf}). For a detailed analysis of these parameters the reader is referred to Vuille and Weyman [306].

assume an “idealized” geometry of the LV and strongly depend on external or internal reference and coordinate systems. Besides total ventricular wall area, other surface indices based on curvature and derived parameters have been investigated from 2-D studies [21, 148, 189, 190]. More recently, many image processing approaches to left ventricular modeling have suggested true 3-D global and local shape indices based on surface properties.

In practice, assessment of cardiac function still relies on simple global volumetric measures like left ventricular volume and mass, and ejection fraction. These and other basic parameters will be presented in the following paragraphs.

Left ventricular volume (LVV). *Left ventricular volume* is a basic parameter required to derive other LV indices like, *e.g.*, ejection fraction. Angiocardiology and echocardiography have been traditionally used to assess this quantity. In the latter case, three approaches have been applied: represent the LV volume *a)* as the volume of a single shape (*e.g.*, truncated ellipse); *b)* as the sum of multiple smaller volumes of similar configuration (*e.g.*, Simpson’s method), and *c)* as a combination of different figures [306, p. 585]. The achieved accuracy in the assessment of LVV with echocardiography varies largely with the model used to represent the LV. The best results have been obtained using Simpson’s rule where *in vitro* studies have revealed a relative error ranging from 5.9% to 26.6% depending on the particular implementation and the number of short-axis slices used in the computation [306, p. 588]. It has been shown that echocardiography consistently underestimates ventricular cavity, while angiocardiology consistently overestimates true volumes [306]. In a recent study by Lorenz *et al.* [185] with a canine model and autopsy validation, it has been shown that cine MRI is a suitable and accurate method to estimate right and left ventricular volume. In this study, MR-based and autopsy volumes agreed within 6 ml, yielding no statistically significant differences.

Left ventricular mass (LVM). Left ventricular hypertrophy, as defined by echocardiography, is a predictor of cardiovascular risk and higher mortality [306, p. 599 and references therein]. Anatomically, LV hypertrophy is characterized by an increase in muscle mass or weight.

Left ventricular mass is mainly determined by two factors: chamber volume, and wall thickness. There are two main assumptions in the computation of LVM: *a)* the inter-ventricular septum is assumed to be part of the LV, and *b)* the volume, V_m , of the myocardium is equal to the total volume contained within the epicardial borders of the ventricle, $V_t(epi)$, minus the chamber volume, $V_c(endo)$; LVM is obtained by multiplying V_m by the density of the muscle tissue (1.05 g/cm^3)

$$V_m = V_t(epi) - V_c(endo) \quad (5.1)$$

$$LVM = 1.05 \times V_m \quad (5.2)$$

LVM is usually normalized to total body surface area or weight in order to facilitate inter-patient comparisons. Normal values of LVM normalized to body weight are $2.4 \pm 0.3 \text{ g/kg}$ [185].

Stroke volume (SV). Stroke volume is defined as the volume ejected between the end of diastole and the end of systole.

$$SV = \text{end-diastolic volume (EDV)} - \text{end-systolic volume (ESV)} \quad (5.3)$$

Alternatively, SV can be computed from velocity-encoded MR images of the aortic arch by integrating the flow over a complete cardiac cycle [164]. Similarly to LVM and LVV, SV can be normalized to total body surface. This corrected stroke volume is known as *stroke volume index* (SVI). Healthy subjects have a normal SVI of 45 ± 8 ml/m² [185].

Ejection fraction (EF). *Ejection fraction* is a global index of left ventricular fiber shortening and is generally considered as one of the most meaningful measures of the left ventricular pump function. It is defined as the ratio of the stroke volume to the end-diastolic volume.

$$EF = \frac{SV}{EDV} \times 100\% = \frac{EDV - ESV}{EDV} \times 100\% \quad (5.4)$$

Lorenz *et al.* measured normal values of EF with MR [185]. They found values of $67 \pm 5\%$ (57–78%) for the LV, and $61 \pm 7\%$ (47–76%) for the RV. Similar values were obtained with ultrafast CT, echocardiography and X-ray angiocardiology [185, 306].

Cardiac output (CO). The role of the heart is to deliver an adequate quantity of oxygenated blood to the body. This blood flow is known as the *cardiac output* and is expressed in liters per minute. Since the magnitude of CO is proportional to body surface, one person may be compared to another by means of the *cardiac index* (CI), that is, the CO adjusted for body surface area. Lorenz *et al.* [185] reported normal CI values of 2.9 ± 0.6 l/min/m² and a range of 1.74–4.03 l/min/m².

CO was originally assessed using Fick’s method or the indicator dilution technique [139]. It is also possible to estimate this parameter as the product of the volume of blood ejected within each heart beat (the SV) and the heart rate (HR).

$$CO = SV \times HR \quad (5.5)$$

In patients with mitral or aortic regurgitation, a portion of the blood ejected from the LV regurgitates into the left atrium or ventricle and does not enter the systemic circulation. In these patients, the CO computed with angiocardiology exceeds the forward output. In patients with extensive wall motion abnormalities or misshapen ventricles, the determination of SV from angiocardiology views can be erroneous. Three-dimensional imaging techniques provide a potential solution to this problem since they allow accurate estimation of the irregular left ventricular shape.

5.3.2 Motion and deformation analysis

Motion analysis.⁶ A number of techniques have been used in order to describe and quantify the motion of the heart. They can be divided into three main categories [195]: i) detecting endocardial motion by observing image intensity changes, ii) determining the boundary wall of the ventricle, and subsequently tracking it, and iii) attempting to track anatomical [46, 156, 240, 324], implanted [9, 41, 133, 146, 199, 247, 304] or induced [12, 76, 99, 153, 170, 210, 321, 325, 326] myocardial landmarks. There

⁶At this point it is worth mentioning an excellent on-line bibliographic database maintained by the Special Interest Group on Cardiac Motion Analysis (SigCMA) that can be accessed at <http://www-creatis.insa-lyon.fr/sigcma>. It also provides general bibliographic information on model-based cardiac image analysis.

are a few problems involved with each of these techniques. Assumptions must be made about the motion (motion model) in the first two groups in order to obtain a unique point-wise correspondence between frames. To this end, optic flow methods [2, 74, 75, 81, 242, 293]⁷ and phase contrast MR [121, 205, 277, 278] have been applied for (i), and curvature-based matching [5, 27, 107, 147, 206] has been used to find point correspondences in (ii). Landmark-based methods [9, 12, 41, 46, 76, 99, 133, 146, 153, 156, 170, 199, 210, 240, 247, 304, 321, 324–326] provide information on material point correspondence. However, this information is mostly sparse and, again, assumptions on the type of motion have to be made in order to regularize the problem of finding a dense displacement field. The use of implanted markers adds the extra complication of being invasive, which precludes routine use of this technique in humans. Although implanted markers are usually regarded as the gold standard, there are some concerns in the literature about their influence on both image quality and modification of the motion patterns.

Wall thickening (WT). Azhari *et al.* [17] have compared wall thickening and wall motion in the detection of dysfunctional myocardium. From their study, it was concluded that wall thickening is a more sensitive indicator of dysfunctional contraction [17]. This finding has triggered several researchers to define methods to quantify wall thickness. Azhari *et al.* [17], and Taratorin and Sideman [288] carried out a regional analysis of wall thickness by dividing the myocardium into small cuboid elements. The local wall thickness is then defined as the ratio between the volume of the particular element and the average area of its endocardial and epicardial surfaces [30].

The most widely employed method for wall thickening computation, however, is the *centerline method* [269] and several improvements thereof [35, 36, 42, 299]. Starting with the endo- and epicardial contours at each slice, the centerline method, in its original formulation, measures wall thickening in chords drawn perpendicular to a line that is equidistant to both contours (the centerline). Although more accurate than methods relying on a fixed coordinate system, this method still assumes that the contours are perpendicular to the long axis of the LV. If this is not the case, the myocardial wall thickness is overestimated which invariably occurs, for instance, in slices that are close to the apex. Buller and co-workers [42, 299] introduced an improvement on this method by estimating at each location the angle between the wall and the imaging plane. Recently, Bolson and Sheehan [35, 36] have introduced the *centersurface method* (true 3-D extension of the centerline method) which makes use of a reference medial surface to compute the chords and subsequent wall thickness.

Strain analysis. Strain analysis is a method to describe the internal deformation of a continuum body. It is an appealing tool to study and quantify myocardial deformation. Here we shall briefly introduce some of the concepts related to strain analysis. A comprehensive exposition of this theory can be found in Fung [109].

To describe the deformation of a body the position of any point in the body needs to be known with respect to an initial configuration; this is called the *reference state*. Moreover, to describe position a *reference frame* is needed. In the following a Cartesian reference frame will be assumed. It is also common to use curvilinear coordinates for which some of the expressions simplify.

⁷For a survey of optic flow methods in computer vision see Beauchemin and Barron [26].

A myocardial point, \mathbf{M}_r , has coordinates $\{y_i\}$ and a neighboring point, \mathbf{M}'_r , has coordinates $\{y_i + dy_i\}$. Let \mathbf{M}_r be moved to the coordinates $\{x_i\}$, and its neighbor to $\{x_i + dx_i\}$. The deformation of the body is known completely if we know the relationship

$$x_i = x_i(y_1, y_2, y_3) \quad i=1,2,3 \quad (5.6)$$

or its inverse,

$$y_i = y_i(x_1, x_2, x_3) \quad i=1,2,3 \quad (5.7)$$

For every point in the body we can write

$$x_i = y_i + u_i \quad i=1,2,3 \quad (5.8)$$

where u_i is called the *displacement* of the particle \mathbf{M}_r . In order to characterize the deformation of a neighborhood, the first partial derivatives of Equations (5.6)-(5.8) are computed. These derivatives can be arranged in matrix form to define the *deformation gradient tensor*: $F = [\partial x_i / \partial y_j]$, $(i, j = 1, 2, 3)$. The deformation gradient tensor enables to estimate the change in length between the neighboring points $\{y_i\}$ and $\{y_i + dy_i\}$, when they are deformed into $\{x_i\}$ and $\{x_i + dx_i\}$. Let $d\ell_r$ and $d\ell$ be these lengths before and after deformation. Then

$$d\ell^2 - d\ell_r^2 = 2 \sum_{i=1}^3 \sum_{j=1}^3 E_{ij} dy_i dy_j \quad (5.9)$$

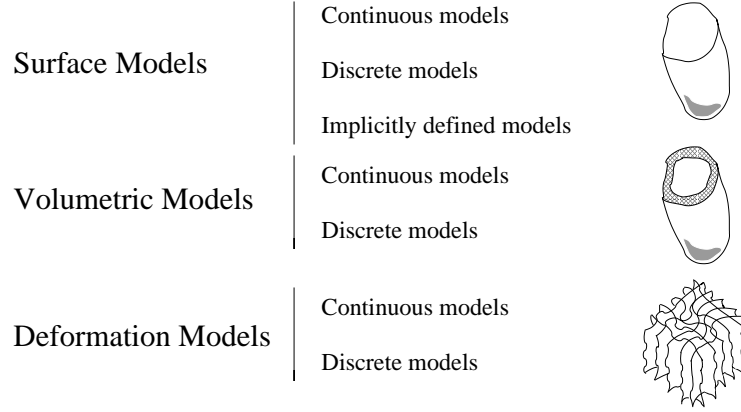
where $E = [E_{ij}]$ is the *Green strain tensor* [109]

$$\begin{aligned} E_{ij} &= \frac{1}{2} \left(\sum_{k=1}^3 \frac{\partial x_k}{\partial y_i} \frac{\partial x_k}{\partial y_j} - \delta_{ij} \right) \\ &= \frac{1}{2} \left(\frac{\partial u_i}{\partial y_j} + \frac{\partial u_j}{\partial y_i} - \sum_{k=1}^3 \frac{\partial u_k}{\partial y_i} \frac{\partial u_k}{\partial y_j} \right) \end{aligned} \quad (5.10)$$

where δ_{ij} is the Kronecker tensor. From the strain tensor it is possible to decompose the strains into two groups: *axial* and *shear* strains. The former correspond to the diagonal elements and represent changes in length aligned with the axes of the reference frame while the latter correspond to off-diagonal terms or deformations where two axes are coupled.

5.4 Overview of modeling techniques

A large effort has been devoted to the analysis and segmentation of cardiac images by methods guided by prior geometric knowledge. When focusing on the way models are geometrically represented, three main categories can be distinguished: 1) surface models, 2) volumetric models, and 3) deformation models. In all cases both discrete and continuous models have been proposed as well as implicitly defined surface models (Figure 5.2).

**Figure 5.2.** Proposed classification of cardiac modeling approaches.

Alternatively, one may classify model-based approaches by considering the information that is used as input for model recovery. This categorization is highly determined by the imaging modality for which the method has been developed. There are a variety of inputs for model recovery: 1) multiple 2-D projection images, 2) multiple oriented 2-D slices, 3) fully 3-D grey-level images, 4) 3-D point sets, 5) phase-contrast velocity fields, and 6) MR tagging information.

In this chapter we will compare the different methods with respect to type of model representation, and types of input data and features that the model is recovered from. Table 5.1, in which the different approaches are grouped according to the type of model representation, summarizes this section.

Keys to Table 5.1:

— *Modality*: BA = Biplane Angiocardiology; US = Ultrasound, MR = Magnetic Resonance; DSR = Dynamic Spatial Reconstructor; CT = Computed Tomography; X = transmission X-ray; SPECT = Single Photon Emission Computed Tomography; Syn = Synthetic images; NS = Non Specific.

— *Recovered from*: M2DP = multiple 2-D projections; MO2DS = multiple oriented 2-D slices; 3DV = 3-D volumetric images/feature maps; PS = point sets; TAG = MR tag intersections, lines or surfaces.

Figure 5.3. Keys to Table 5.1.**5.4.1 Surface models**

Many approaches to cardiac modeling focus on the endocardial (and/or epicardial) wall. Three sub-categories are proposed: a) continuous models with either global,

Table 5.1. Overview of cardiac modeling methods. See Keys in Figure 5.3.

Surface Models					
Reference	Model	Potential	Reported	Input	Feature
<i>Continuous</i> Yettram [316, 317]	Stacked curves	BA	BA	M2DP	manual contours
Young [323, 324]	Bicubic Hermite patches	BA	BA	PS	coronary bifurc. points
Spinale [280] ^{RV}	Stacked hemiellipses	BA	BA	M2DP	manual contours
Pentland [234]	FE and modal analysis	NS	X	M2DP	optic flow
Cauvin [44]	Truncated bullet	NS	SPECT	3DV	thresh. + morph. skel.
Czegledy [63] ^{RV}	Stack of crescentic outlines	NS	CT	3DV	linear measurements
Gustavsson [127]	Cubic B-spline curves' mesh	US	US	MO2DS	manual contours
Sacks [256] ^{RV}	Biquadric surface patches	NS	MR	3DV	manual contours
Chen [47]	Superquad. + spher. harm.	NS	BA	PS	coronary bifurc. points
Denslow [77] ^{RV}	Ellipsoidal shell	NS	MR	3DV	linear measurements
Maehle [187]	Bicubic spline surf. patch.	NS	US	MO2DS	edge detection +
Chen [49]	Voxel repres. / superquadric	NS	DSR	3DV	manual correction
Coppini [59]	Spherical elastic surface	NS	US	MO2DS	shape & intens. prop.
Goshtasby [123]	Rational Gaussian surface	NS	MR	3DV	NN edge detector
Matheny [193]	3-D/4-D harmonic surfaces	NS	DSR/BA	PS	zero-cross Laplacian
Staib [281]	Bayesian Fourier surface	NS	MR/DSR	3DV	iso-surface, coronary bifurc. points
Park [233]	Superquadrics + par. func.	MR ^{tag}	MR ^{tag}	PS	Gaussian gradient
Bardinet [19, 20]	Superquadrics + FFD	NS	DSR/SPECT	PS	motion field [321]
Declerck [69]	Planispheric transformation	NS	SPECT	3DV	iso-surfaces
Sato [259]	B-spline surface	BA	BA	M2DP	norm. radial grad. apparent contours
<i>Discrete</i> Geiser [111, 112]	12-sided stacked polygons	US	US	MO2DS	manual contours
Faber [95]	4-D discrete template	NS	MR/SPECT	3DV	norm. radial grad.
Gopal [120]	Polyhedral mesh	NS	US	MO2DS	manual contours
Friboulet [108]	Triangulated mesh	NS	MR	PS	manual contours
Huang [145]	Adaptive-size mesh	NS	DSR	PS	data-to-node dist. + data curvature
Faber [94]	3D discrete template	SPECT	SPECT	3DV	radioact. distrib. prof.
Germano [116, 117]	Ellipsoid + local refinement	SPECT	SPECT	3DV	radioact. distrib. prof.
McInerney [196]	FE deformable balloon	NS	DSR	3DV	Gauss/Deriche grad.
Ranganath [246]	2D snakes + propagation	MR	MR	3DV	intens. prof. matching
Tu [297]	Spherical template	NS	DSR	3DV	3D+t gradient
Nastar [213]	Mass-spring mesh	NS	DSR	3DV	edge distance map
Rueckert [254]	Geom. Def. Template	NS	MR	3DV	zero-cross Laplacian
Shi [87, 272]	Delaunay triangulation	NS	MR/DSR	PS	bending energy
Legget [174]	Piecewise subdivision surf.	NS	US	MO2DS	manual contours
Montagnat [209]	Simplex meshes	US	US	MO2DS	edges in cylind. coord.
Biedenstein [31]	Bullet-like elastic mesh	SPECT	SPECT	3DV	radioact distrib. prof.
<i>Implicit</i> Yezzi [318, 319]	Implicit snakes	NS	MR	3DV	Gaussian gradient
Teeng [295]	Cont. Dist. Tranf. NN	NS	US	MO2DS	manual contours
Niessen [215]	Implicit snakes	NS	MR/DSR	3DV	Gaussian gradient
Lelieveldt [176]	Fuzzy implicit surfaces	CT/MR	MR	MO2DS	air-tissue transitions
Volume Models					
<i>Continuous</i> Creswell [61, 237]	Approximating NURBS	MR	MR	PS	manual contours
Park [232]	Superellipsoids + par. func.	MR ^{tag}	MR ^{tag}	TAG	tag line intersections + boundary points
Haber [130, 131]	Physics-based FE	MR ^{tag}	MR ^{tag}	TAG	tag line intersections + boundary points
Shi [271]	Biomech. tetrahed. FEM	MR	MR	PS+3DV	bending energy + MR velocity image
<i>Discrete</i> Kuwahara [172]	Voxel representation	MR	MR	MO2DS	manual contours
O'Donnell [218, 219]	Hybrid volum. ventriculoid	MR ^{tag}	MR ^{tag}	TAG	tag line intersections + boundary points
Deformation Models					
<i>Continuous</i> Amini [5]	Local quadric patches	NS	DSR/MR	PS	minimal conf. motion
Young [321]	Bicubic Hermite FE	MR ^{tag}	MR ^{tag}	TAG	tag line intersections
Bartels [23]	Multi-dimensional splines	NS	Syn	3DV	intensity conservation
O'Dell [217]	Affine + prolate spheroidal	MR ^{tag}	MR ^{tag}	TAG	tag lines
Young [325]	Bicubic Hermite FE	MR ^{tag}	MR ^{tag}	TAG	tag lines
Moulton [211]	Higher-order polyn. interp.	MR ^{tag}	MR ^{tag}	TAG	tag surface intersec.
Radeva [245]	Trivariate cubic B-spline	MR ^{tag}	MR ^{tag}	TAG	short axis tag lines
Kerwin [153]	Thin-plate splines	MR ^{tag}	MR ^{tag}	TAG	tag line intersections
Young [320]	"Model tags"	MR ^{tag}	MR ^{tag}	TAG	tag lines
Huang [144]	Four-variated cubic B-spline	MR ^{tag}	MR ^{tag}	TAG	tag surfaces
<i>Discrete</i> Moore [210]	Discrete mesh	MR ^{tag}	MR ^{tag}	TAG	tag line intersections
Denney [76]	Discrete grid	MR ^{tag}	MR ^{tag}	TAG	tag line intersections
Benayoun [27]	Adaptive-size meshes	NS	DSR	3DV	gradient
Papademetris [229–231]	Delaunay triangulation	NS	MR/US	PS	intern. deform. energy

local or hybrid parameterizations, b) discrete models, and c) implicitly defined deformable models.

Continuous models

In the early studies of cardiac images by 2DE and angiocardiology, cardiologists used simplified models of the LV in order to compute functional parameters like ventricular volume and mass from 2-D images. Most of the times, simple ellipsoidal models were considered. See, *e.g.*, Vuille and Weyman [306] and Dulce *et al.* [86] for a comprehensive review of such models and a comparison of their accuracy. In the last decades, however, approaches have appeared that make use of 3-D acquisitions to reconstruct models varying from global parameterizations of the LV surface [44, 59, 69, 123, 193, 232, 235, 281] to hierarchically parameterized models [20, 47, 116, 127, 176].

Global approaches. In this category we will discuss surface representations that are based on simple geometric models. In general they can provide, with a limited number of global parameters, a rough shape approximation. We also include in this category surface representations obtained as series of basis functions with global support.

Cauvin *et al.* [44] model the LV as a *truncated bullet*, a combination of an ellipsoid and a cylinder, that is fitted to the morphological skeleton of the LV. Metaxas and Terzopoulos [204] have proposed superquadrics [22] to model simple objects with a small number of parameters. Since the introduction of superquadrics, several extensions have appeared in the literature. Chen *et al.* [49] apply superquadrics with tapering and bending deformations to model the LV in an integrated approach for image segmentation and shape analysis. The method iterates between a region-based clusterization step [48], using statistics of image intensity and gradient, and a shape-based step that checks the consistency between the current segmentation and a superquadric model. Park, Metaxas and Axel [233] have extended the flexibility of superquadrics by introducing *parameter functions*: radial and longitudinal contraction, twisting and long-axis deformation. These allow for a more detailed representation of the LV while keeping the intrinsic geometrical meaning of the superquadric parameters. LV mid-wall motion is recovered using pre-processed MR tagging data obtained by sampling the LV mid-wall surface from the 3-D Finite Element (FE) model of Young and Axel [321].

Staib and Duncan [281] use sinusoidal basis functions to decompose the endocardial surface of the LV. The overall smoothness of the surface is controlled by adjusting the number of harmonics in the Fourier expansion. Model recovery is cast into a Bayesian framework in which prior statistics of the Fourier coefficients are used to further limit the flexibility of the model. Matheny and Goldgof [193] compare different 3-D and four-dimensional (4-D) surface harmonic descriptions for shape recovery. Time can be incorporated in two ways in the model: a) hyper spherical harmonics, where an event in space-time is converted from Cartesian coordinates to hyper spherical coordinates, and b) “time-normal” coordinates which are formed by including a temporal dependency to each spatial coordinate. Experiments carried out with a 3-D CT data set of a canine heart have indicated that hyper spherical harmonics can represent the beating LV with higher accuracy than direct normal extensions of spherical, prolate spheroidal and oblate spheroidal harmonics. Coppini *et*

al. [59] reconstruct a 3-D model of the LV based on apical views in US images. LV boundaries are obtained by grouping edges with a feed-forward neural network (NN) integrating information about several edge features (position, orientation, strength, length and acquisition angle). This allows discarding many edge points that are not plausible LV boundary points. The 3-D LV geometry is modeled as a spherical elastic surface under the action of radial springs (attracting the model to the edge points); a Hopfield [142] NN is used to solve the minimization problem involved in the reconstruction of this surface. Declerck, Feldmar and Ayache [69] have introduced a spatio-temporal model to segment the LV and to analyze motion from gated SPECT sequences. The model relies on a planispheric transformation that maps endocardial points in one time frame to the corresponding material points in any other frame. First, endocardial edge points are detected in all frames using a Canny-Deriche edge detector [208] in spherical coordinates [70]. Selected points in subsequent frames are matched to the current frame using a modification of the Iterative Closest Point (ICP) algorithm [29, 70, 98]. Based on corresponding point pairs, the parameters of a planispheric transformation are retrieved by least-squares approximation. This transformation allows to describe motion with just a few parameters and to relate them to a canonical decomposition (radial motion, twisting motion around the apico-basal axis, and long-axis shortening).

Hierarchical approaches. Some authors have addressed the problem of building hierarchical representations where a model described with few parameters is complemented with extra deformations that capture finer details.⁸ Gustavsson *et al.* [127], for instance, employ a truncated ellipsoid to obtain a coarse positioning of the left ventricular cavity from contours drawn in two short-axis and three apical echocardiographic views. Further model refinement is achieved using cubic B-spline curves approximating manually segmented contours in multiple views. Chen *et al.* [47] and Bardinet *et al.* [20] use superquadrics [22] to coarsely describe the LV. Their approaches fundamentally differ in the representation of the additional deformation field. Chen *et al.* use spherical harmonics in order to approximate the residual error between the superquadric estimate of the endocardial LV wall and the true wall location. Spherical harmonics have the advantage that fine-tuning can be improved *ad infinitum* with increasing number of harmonics. However, adding a new coefficient influences the shape of the model everywhere (non-local basis functions). Bardinet *et al.* [20] extend the basic superquadric deformations (tapering and bending) through the use of free-form deformations (FFD), a technique introduced in computer graphics by Sederberg and Parry [266]. The superquadric is attached to a flexible, box-like frame, inducing a non-rigid deformation on the superquadric. Bardinet *et al.* use trivariate B-splines to parameterize this deformation field. In a later work, Bardinet *et al.* [19] apply their method to estimate left ventricular wall motion. This is accomplished by deforming the full model (superquadric + FFD) in the first frame, and modifying only the FFD in the subsequent frames. By tracking points with the same parametric coordinates along the cardiac cycle, a number of dynamic parameters like wall thickening and twisting motion are computed. Germano *et al.* [116, 117] have developed a system

⁸Similar approaches have been proposed in computer vision for modeling man-made objects [203, 276, 291, 302, 303] and for elastic matching [18, 98].

for automatic quantification of left ventricular function from gated perfusion SPECT images. An iterative algorithm fits an ellipsoidal model to a semi-automatically obtained segmentation. This iterative algorithm incrementally adapts the ellipsoid's parameters and center of mass so that accurate registration of the model is obtained even in the presence of large perfusion defects. The ellipsoid defines a coordinate system that is used to refine the model. A Gaussian model of the count profiles is used to compute radial offsets corresponding to the endocardial and epicardial walls. Although simple in its formulation, this method has proven very useful in determining most of the classical cardiac functional parameters [115] from SPECT images and has been extensively validated in humans [113, 116, 117].

Local approaches. A number of methods have been reported to provide surface reconstruction using piecewise polynomial surfaces, *e.g.*, B-splines or bicubic Hermite surface patches. These techniques have appeared mainly in the context of surface reconstruction from multiple cross-sections [172, 187] or projections [259, 280, 316, 317, 323]. Given the ill-posed nature of this problem, most of these techniques require extensive user interaction. Usually, a set of land-marks or fiducial points are determined from each cross-section/projection and, using high-level knowledge about the viewpoint and the geometry of the LV, a local surface approximation using surface patches is performed.

A rather different approach is the one by Pentland and Horowitz [234] who applied modal analysis and FE to reconstruct a 3-D model of the LV from X-ray transmission data. Modal analysis offers a principled physically-based strategy for reducing the number of degrees of freedom of the model and to obtain an over-constrained problem for shape recovery. Optic flow is used to derive the deformation of the 3-D model from the 2-D views, and a Kalman filter for tracking the structures over time.

Instead of working with multiple cross-sections or projection images, Goshtasby and Turner [123] segment left and right ventricular endocardial surfaces from 3-D flow-enhanced MR images. In this case, the endocardial surface is modeled as a deformable cylinder using rational Gaussian surfaces [122]. The model is deformed to fit the zero-crossings of the image Laplacian. To avoid attraction by spurious edges, prior to fitting, the feature map is masked by a rough LV region-of-interest obtained by intensity thresholding.

Right ventricle models. Some efforts have also been directed toward geometric modeling of the RV. This chamber has a more complex shape than the LV. Spinale *et al.* [280] fit semi-ellipses to model the crescentic shape of the RV from biplane ventriculograms. Czegledy and Katz [63] model the RV using a crescentic cross-sectional model composed of two intersecting circles of different radii. This 3-D model is parameterized by only a few linear dimensions that can be measured directly from CT, MR or US images. From these dimensions, the RV volume is approximated using analytical expressions. Denslow [77] model the RV as the difference of two ellipsoids (an ellipsoidal shell model). The parameters from this shell are estimated from MR images (a long axis and a four chamber view) and from those, volume estimates can be derived. Sacks *et al.* [256] model the endo- and epicardial walls of the RV by bi-quadratic surface patches (contours were manually traced from MR images), and have studied surface curvature and wall thickness changes along the cardiac cycle using this representation.

Discrete models

An alternative to continuous surface representations is the use of discrete surface models. Several methods have been reported in the literature and they can be grouped in the following way.

Physics-based models. Physics-based modeling has attracted the attention of many computer vision researchers. In this framework, surface recovery is cast into the deformation of a virtual body (the geometric model plus its material properties) under virtual external forces derived from image/point features, or user-defined constraints. In the final (deformed) state, this virtual body reaches an equilibrium between the external forces and internal (regularization) constraints. A good overview of the theory of physics-based deformable models and its applications can be found in the book by Metaxas [202] and in the survey by McInerney and Terzopoulos [197].

McInerney and Terzopoulos [196] have applied this theory to the segmentation and tracking of the LV in DSR image sequences. A FE balloon [54] deformable model is discretized using triangular elements, and deformed according to a first order approximation of the Lagrange equations of motion. User-defined point constraints can be interactively inserted to guide the deformation of the model and to avoid local minima of the potential energy in which the model is embedded. In the Lagrangian formulation, 3-D image sequences can easily be handled by making the potential energy a function of time. Montagnat, Delingette and Malandain [209] apply simplex meshes [72] to reconstruct the LV from multiple views of a rotating US probe. Images are acquired in cylindrical coordinates coaxial with the apico-basal axis. Accordingly, images are filtered in cylindrical coordinates. Boundary points are detected based on a combination of image gradient and intensity profiles normal to the surface. Finally, detected edge points are cast into point attraction-forces deforming the model according to Newton's law of motion. Ranganath [246] reconstructs 3-D models of the LV from MRI images using multiple 2-D *snakes* [149] and devising efficient mechanisms for inter-slice and inter-frame contour propagation. Biedenstein *et al.* [31] have recently published an elastic surface model and applied it to SPECT studies. The elastic surface is deformed according to a second-order partial differential equation. The external (image) forces are derived from the radioactive distribution function and push the elastic surface toward the center surface of the LV wall. Wall thickness can be then computed as the distance between the elastic surface and the mass points of the radioactivity distribution gradient. Huang and Goldgof [145] have presented an adaptive-size mesh model within a physics-based framework for shape recovery and motion tracking. The optimum mesh size is inferred from image data, growing new nodes as the surface undergoes stretching or bending, or destroying old nodes as the surface contracts or becomes less curved. The method is employed to analyze LV motion from a DSR data set. To establish point correspondences, an adaptive-size mesh is generated for the first frame to be analyzed; subsequent frames further deform this mesh while keeping its configuration fixed.

Physics-based modeling frequently makes an assumption that can be problematic: internal constraints are usually represented in the form of *controlled-continuity stabilizers* [290]. It is known that, in the absence of image forces, deformable models tend to shrink. To avoid this, Rueckert and Burger [254] simultaneously model the two

cardiac chambers (RV and LV) using a Geometrically Deformable Template (GDT). The standard stabilizers on the deformed model are replaced by a stabilizer on the deformation field between a rest model and a deformed model. A GDT consists of three parts: a) a set of vertices that defines the rest state (the template), b) a set of vertices that defines a deformed state (an instance of the template), and c) a penalty function that measures the amount of deformation of the template with respect to its equilibrium shape (the stabilizer). Another solution to the above mentioned problem, was proposed by Nastar and Ayache [213] who model a surface as a quadrilateral or triangular mesh of virtual masses. Each mass is attached to its neighbors by perfect identical springs with predefined stiffness and natural length. The system deforms under the laws of dynamics. In addition to elastic and image forces, an “equilibrium force” determines the configuration of the mesh in the absence of external forces.

Spatio-temporal models. Several researchers have developed models that explicitly incorporate spatial *and* temporal variations of LV shape. Faber *et al.* [95] use a discrete 4-D model to segment the LV from SPECT and MR images through a *relaxation labeling* scheme [157]. Endo- and epicardial surfaces are modeled as a discrete template defined in a mixed spherical/cylindrical coordinate system co-axial with the LV long-axis. Each point in the template represents a radius connected to this axis. The model is spatio-temporal since the compatibility functions computed in the relaxation labeling scheme involve neighboring points both in space and time. In this way, surface smoothness and temporal coherence of motion are taken into account. Tu *et al.* [297] have proposed a 4-D model-based LV boundary detector for 3-D CT cardiac sequences. The method first applies a spatio-temporal gradient operator in spherical coordinates with a manually selected origin close to the center of the LV. This operator is only sensitive to moving edges, and less sensitive to noise compared to a static edge detector. An iterative model-based algorithm refines the boundaries by discarding edge points that are far away from the global model. The model is parameterized by spherical harmonics including higher order terms as the refinement proceeds.

Polyhedral models. LV polyhedral representations have been applied by several authors [87, 94, 108, 112, 120, 174, 209, 272] in the literature. The approaches differ either in the type of polygonal primitive (*e.g.*, triangular or quadrilateral meshes) or the details of the shape recovery algorithm (imaging modality, input data or recovery features). Shi *et al.* [87, 272] use a Delaunay triangulation [309] to build a surface description from a stack of 2-D contours obtained with a combined gradient- and region-based algorithm [45]. This representation is subsequently used for motion analysis based on point correspondences. Bending energy under a local thin-plate model is used as a measure of match between models of consecutive frames. Friboulet, Magnin and Revel [108] have developed a polyhedral model to analyze the motion of the LV from 3-D MR image sequences. LV contours are manually outlined using a track-ball. After applying morphological and linear filtering to diminish quantization noise, the contours are radially resampled with constant angular step. Finally, the stack of resampled contours is fed into a triangulation procedure [89] which generates a polyhedral surface with approximately equal-sized triangles. Faber *et al.* [94] use a combination of cylindrical and spherical coordinate systems to build a discrete model of the left ventricle in SPECT perfusion images. A radius function defined in a discrete

(orientation) space of longitudinal and circumferential coordinates describes the LV. For each orientation, the radius is determined by finding the position of maximal perfusion (which is argued to occur in the center of the myocardium). After low-pass filtering to remove outlier radii, the radius function is mapped back to Cartesian space where the surface is represented using triangular or quadrilateral meshes. This approach shares some features of the work described in Faber *et al.* [95] but is purely static. Legget *et al.* [174, 270] use piecewise smooth subdivision surfaces [143] to reconstruct the LV geometry from manually traced contours in 3-D US images. Some elements of the mesh can be labeled so that they allow for sharp edges (*e.g.*, at the mitral annulus and apex) and to define regional surface descriptors. Also from 3-D US images, Gopal *et al.* [120] apply triangulated surfaces to reconstruct the geometry of latex balloons phantoms mimicking the LV. Three-dimensional reconstruction is directly obtained by triangulating the points of manually delineated contours from a stack of quasi-parallel slices.

Implicitly defined deformable models

Either in continuous or discrete form, the models in the two previous paragraphs were characterized by having an explicit surface parameterization. A surface model can also be defined by means of an implicit function. For instance, in the *level-set* approach [267], a model is obtained as the zero level set of a higher-dimensional embedding function. This technique, sometimes referred as *geodesic deformable models* have been introduced independently by Caselles *et al.* [43] and Malladi *et al.* [188] based on the work by Osher and Sethian [222]. Geodesic deformable models have been applied by Yezzi *et al.* [318, 319] to the segmentation of MR cardiac images. Recently, Niessen *et al.* [215] have extended the method to treat multiple-objects and have applied it to the segmentation of 3-D cardiac CT and MR images. Although geodesic models have the ability of handle changes in topology, unwanted and uncontrollable topological changes can occur in images of low-contrast edges or with boundary gaps since this is a purely data driven approach.

There are other types of implicit models not related to level-sets. Tseng, Hwang and Sheehan [296], for instance, use a NN to define a Continuous Distance Transform (CDT) to the LV boundary. A feed-forward NN is trained to learn the distance function to the endocardial and epicardial contours using a few hand-segmented image slices. The surface of the LV is then represented as the zeroes of the distance function. The NN can generalize the boundaries of the LV in the slices not included in the training set, thus serving as an aid to segment a 3-D image for which the user has to provide the segmentation of a few slices only. Under an affine deformation model, the distance transform is used to match different temporal frames and to derive motion parameters. Wall thickness is computed by the centerline method [269] using two CDT NNs for describing the endo- and epicardial surfaces.

A third approach to implicit modeling is the use of surface primitives which are defined in implicit form. Lelieveldt *et al.* [176] segment thoracic 3-D MR images using hierarchical blending of hyperquadrics [132] and concepts of constructive solid geometry (CSG) [251]. The method provides an automatic, coarse segmentation of a multiple-object scene with little sensitivity to its initial placement. The most repre-

sentative organs in the thorax (lungs, heart, liver, spleen, and cardiac ventricles) are incorporated in the model which can be hierarchically registered to the scanner coordinate system using only a few coronal, sagittal and transversal survey slices. Owing to the contextual information present in the model, this sparse information has successfully been used to estimate the orientation of the long-axis of the LV. This allows an observer-independent planning of 3-D long-axis acquisitions in patients [175]. This technique was not designed to estimate accurate cardiac functional parameters but can be used to generate a first initialization for more accurate algorithms.

5.4.2 Volumetric models

As opposed to the plethora of surface representations, the use of volumetric models in the analysis and segmentation of cardiac images has received little attention.

O'Donnell *et al.* [218,219] were the first to suggest a volumetric model to recover myocardial motion from MR tagging. The model, coined *hybrid volumetric ventriculoid*, can be decomposed into three parts: a) a thick-walled superquadric, b) a local offset either in non-parametric [219] or parametric [218] form, and c) a local deformation in the form of a polyhedrization. The thick-walled superquadric represents a high-level abstraction model of the myocardium that is further refined by the local offsets. Altogether, these two parts constitute the *rest model* of the myocardium that is rigidly scaled to the dimensions of a new dataset. The local deformation field is responsible of capturing the detailed shape variability of different data sets. Park *et al.* [232] have extended their LV surface model [233] to a super-ellipsoid model with parameter functions. The model is fitted to tagged MR images providing a compact and comprehensive description of motion. Radial and longitudinal contraction, twisting, long-axis deformation, and global translation and rotation are readily available from the parameter functions. Alternatively, standard strain analysis can be carried out. It is also possible to estimate other volumetric parameters like SV, CO, LVV and LVM. In order to fit the model, a set of boundary points is manually delineated and a set of tags are semi-automatically tracked along the cardiac cycle using the algorithm of Young *et al.* [325]. Therefore, the accuracy of all volumetric measurements depends on the manual outlining.

Haber, Metaxas and Axel [130] have developed a model of biventricular geometry using FEs in a physics-based modeling context. The 3-D motion of the RV is analyzed by defining external forces derived from SPAMM MR tagging data [131]. Creswell *et al.* [61] and Pirolo *et al.* [237] describe a mathematical (biventricular) model of the heart built from 3-D MR scans of a canine specimen. Manual contour delineation of the epicardial, and LV and RV endocardial boundaries provides a set of points that is approximated with cubic non-uniform rational B-splines (NURBS [236]). From this representation, a hexahedral FE model is built in order to generate a realistic geometric model for biomechanical analysis.

Recently, Shi *et al.* [271] have introduced an integrated framework for volumetric motion analysis. This work extends the surface model of Shi *et al.* [272] by combining surface motion, extracted from MR magnitude images, and motion cues derived from MR phase contrast (velocity) images. The latter provide motion information inside the myocardial wall but are known to be less accurate at the boundaries [205].

The two sources of motion evidence (boundary and mid-wall motion) are fused by solving the discretized material constitutive law of the myocardium assuming a linear isotropic elastic material. In this framework, the measured boundary and mid-wall motion estimates at two consecutive frames are used as boundary and initial conditions of a FE element formulation. An advantage of this method with respect to physically-based techniques is that material properties can be set based on experimental knowledge about myocardial mechanical properties, and not on a virtual mechanical analog which usually leads to *ad hoc* parameter settings.

5.4.3 Deformation models

Hitherto, we have focussed on representing either the endocardial (or epicardial) surface, or the volume comprised within the myocardial muscle. Tissue deformation, however, can be modeled without necessarily modeling the ventricular boundaries. To this end, material point correspondences in different temporal frames are required. These correspondences can be obtained by matching certain geometric properties over time (*general techniques*). If images are acquired using MR tagging technology, several other approaches can be applied that exploit the explicit correspondences inferible from tag displacements (*MR tagged-based techniques*).

General techniques

Several techniques have been proposed in the literature for deformation recovery based on shape properties only. These methods are attractive because of their generality. On the other hand, one must reckon with the validity of the underlying assumptions and/or motion models before they are applied to analyze image sequences corresponding to normal and pathological myocardial motion patterns.

a) Continuous models

Amini and Duncan [5] have developed a surface model based on the assumption of *conformal* motion, where angles between curves are preserved but not distances between points. The LV surface is divided into locally quadric patches from which differential properties can be computed. Inter-frame patch correspondences are obtained using a metric that is minimal for conformal motion. An assumption of this model is that the subdivision into surface patches and the number of neighboring patches visited during the matching process are sufficient to accommodate for the largest stretching that can occur between frames. Bartels *et al.* [23, 24] model material deformations with multi-dimensional splines. The method shares properties of optical flow techniques to estimate motion fields. However, those approaches do not return an explicit model of the deformations (only displacements at discrete positions are provided). The main assumption of this technique is that, for a given material point, luminance is a conserved quantity. As in optic flow techniques, with only this assumption the solution remains under-constrained and, therefore, a regularization term must be added. Illustrations of the method on 2-D cardiac X-ray sequences are provided and the formulation readily extends to 3-D sequences. However, it is questionable whether luminance conservation can provide a reliable cue for deformation recovery in regions with homogeneous intensity, or in the presence of imaging

artifacts and noise. For MR tagging, in particular, the approach must be adapted since luminance is not conserved due to the physics of the imaging process [242].

b) Discrete models

Benayoun and Ayache [27] propose an adaptive mesh model to estimate non-rigid motion in 3-D image sequences. The size of the mesh is locally adapted to the magnitude of the gradient, where the most relevant information is supposed to appear (*e.g.*, cardiac walls). Mesh adaptation is carried out at the first frame only; subsequent frames only deform the mesh to recover motion. The underlying hypothesis is that the deformation is small. Meshes at two time instants are registered through an energy-minimizing approach matching differential image properties (curvature and gradient). Recently, Papademetris *et al.* [229–231] have proposed a deformation model inspired by continuum mechanics. The method recovers a dense deformation field using point correspondences obtained with the point-tracking algorithm of Shi *et al.* [272]. Regularization is accomplished by measuring the internal energy of the myocardial tissue assuming a linear elastic body model. This is equivalent to a regularization term on the strain tensor space and not on the displacement field.⁹ Anisotropy of the fibrous structure of the LV is accounted for in the internal energy by making the model stiffer in the fiber direction [125].

MR tagging-based techniques

The introduction of MR tagging has stimulated researchers to develop models of cardiac tissue deformation. Compared to motion recovery based on point correspondences or optic flow, MR tagging has the advantage that, in principle, material point correspondences can be estimated from tag information. In this section, different approaches for modeling the deformation fields are reviewed. Accurate tag localization is a pre-requisite for subsequent deformation recovery and, therefore, it is a closely related topic to deformation models. A brief overview of tag tracking techniques is given in Appendix 5.B.

a) Continuous models

Several approaches have been proposed in which the parameterization of the deformation field is a continuous function. The availability of continuous deformation maps allows the computation of local strains. Young *et al.*, for instance, developed a model-based approach for tracking tag intersections [321] and tag stripes [325]¹⁰ that has been validated using silicone gel phantoms [166]. A deformation field that maps the first (undeformed) frame to a subsequent (deformed) frame is modeled through a piecewise polynomial function. Two fitting steps are involved in this method. First, the material points (tag intersections or stripes) in each deformed frame, $t > 0$, are

⁹Related regularization schemes are the *global* and *body* smoothing terms described in Young and Axel [321] which act on the deformation gradient tensor. However, they are not directly interpretable as an internal deformation energy.

¹⁰Amini *et al.* [4] have compared land-mark based (tag intersections) against curved-based tag (stripes) tracking based on the simulator of Waks *et al.* [307]. It was concluded that as the number of stripes/land-marks increases, the two methods give similar performances. Under large deformations, the degradation of the curve-based techniques is more graceful compared to land-mark based methods.

reconstructed in the coordinate system of the undeformed state, $t = 0$ (*reconstruction fit*). In the latter frame, tag surfaces are arranged in true planes since no motion has occurred yet. In the second step, the material points for $t > 0$, expressed in the reference frame ($t = 0$), are used to reconstruct a displacement field relative to $t = 0$ (*deformation fit*).¹¹

A similar approach is followed by O'Dell *et al.* [217]. One-dimensional displacements are obtained by three independent sets of tag lines: one in the cardiac long-axis, and two orthogonal sets in the short-axis view. Reconstruction of the deformation field is performed in two interpolation steps. The first step assumes a global affine transformation between two time frames. This is done to eliminate global bulk motion, and linear stretches and shear. In a second step, the residual deformation is interpolated using a prolate spheroidal decomposition to describe the curvilinear deformations expected in the heart.

Both Young *et al.* [321,325] and O'Dell *et al.* [217] assume that the reference frame, to which the strain analysis is related, is the undeformed state. This is normally the first frame in the sequence (planar tag surfaces). Although this simplifies the problem by allowing to decouple the motion component normal to the tagging plane, these methods cannot be used to compute strains between two arbitrary frames. The latter can be useful in order to retrospectively select the reference frame to coincide precisely with the diastole or systole, or to compute strains over a subset of the cardiac cycle. To circumvent this limitation, Moulton *et al.* [211] have proposed a Lagrangian approach that explicitly computes the intersection of the tag surfaces in two arbitrary frames. Tag surfaces are obtained by interpolating the tag curves that are stacked in different imaging planes. Surface intersections define a set of material lines for each time frame. These points were used to perform strain calculations employing a p -version of FE basis functions.

Radeva, Amini and Huang [245] use two coupled volumetric models: a tissue deformation field and a model describing the LV geometry. The first model is represented by a cubic trivariate B-spline (coined B-solid by the authors); the second model is represented by two coupled surfaces (endo- and epicardium) fitted to boundary points. It is assumed that the boundaries are either manually delineated or (semi)automatically detected from the tagged images. The B-solid is deformed under thin-plate internal constraints, and under two external forces. The first corresponds to tagging information: the iso-parametric curves of the model are deformed to align with the tag strips. Simultaneously, the B-solid is attracted towards the LV boundaries by integrating a distance function to edge points on the epicardial and endocardial surfaces. Therefore, in this method, boundary and tag information are incorporated in a unified approach. Since this method has been applied in combination with short-axis tagged images only, it yields in-plane 2-D displacements. In a recent paper, Huang *et al.* [144]

¹¹Both fitting steps handle sparse data and, therefore, regularization is needed. Regularization, however, is known to introduce artifactual strains. The effect of three regularization terms has been studied in [321]: i) a *thin-plate spline* stabilizer, ii) a *global smoothing* regularizer minimizing the deformation gradient tensor, F , and iii) a *local body* regularizer minimizing the deformation gradient tensor expressed in some natural local coordinate system (*e.g.*, aligned in circumferential, longitudinal and radial directions). Based on simulations of an axis-symmetric deformation of a thick walled incompressible cylinder, it was shown that all three constraints yield similar results in the strain analysis.

have extended the method to analyze true 3-D deformations using a spatio-temporal model. The method differs from the one of Radeva *et al.* in that no boundary information is now incorporated. On the other hand, a spatio-temporal B-solid is constructed through a 4-D tensor product spline (3-D+t). The fitting process to SPAMM data is governed by a *normal constraint* which enforces the attraction produced by each tag plane to be in its normal direction. Since multiple, orthogonal tag planes are available, this allows a full 3-D reconstruction of the deformation field.

Kerwin and Prince [153] have developed an alternating projection technique to accurately estimate the 3-D location of the intersection points of the tag grid. The deformation field between two frames is recovered using thin-plate-spline interpolation. Myocardial points are distinguished from those in static tissues by checking whether they pass across the imaging plane over time. In points that do not fulfill the previous criterion, a test is performed to check their inclusion within the outlined myocardial borders prior to rejection from the analysis. Such a rejection scheme is important for proper visualization and analysis of myocardial motion.

Recently, Young [320] has introduced the concept of *model tags* that represent the material surfaces within the heart tissue which are tagged with magnetic saturation. Model tags are “attached” to the heart and deform with it. They are embedded within a 3-D FE model describing the geometry of the LV; this model is linear in the transmural direction and employs bicubic Hermite interpolation in the circumferential and longitudinal directions. Instead of finding the 3-D location of the tag plane intersections, this approach finds the intersections of the model tags with the imaging planes (model tag intersections or MTI). The FE model is subsequently deformed so that the MTI match the tag stripes in each image plane. Matching is carried out by a local search algorithm guided by an orientation filter. Additionally mechanisms are incorporated to allow efficient user interaction and to correct for erroneous MTI matches.

b) Discrete models

Moore *et al.* [210] use MR tagging to reconstruct the location of material points through the cardiac cycle by interpolating the positions of the tags from short- and long-axis image planes using an iterative point-tracking algorithm. Discrete tag locations are arranged in cuboid volume elements which are identified in the deformed and reference frames. For each element, a 3-D strain tensor is calculated using the generalized inverse method [82]. Since the strain analysis is performed on a coarse discrete grid, only average strains can be retrieved. The tag tracking procedure of this method compensates for through plane motion. An important conclusion from this work is that strain analysis can be largely influenced by through plane motion if this is not corrected for.

Denney and Prince [76] employ a multidimensional stochastic approach to obtain a dense discrete model of the displacement field from a sparse set of noisy measurements (tag displacements). The displacement field is constrained to be smooth and incompressible (isochoric deformation). This formulation leads to a partial stochastic model of the deformation field that can be solved using Fisher’s estimation framework [265].

Table 5.2. Overview of cardiac modeling methods: reported classical functional parameters and their validation. See Keys and Notes in Figure 5.4

Evaluation	Reference	Modality	Parameters		F	PP	AU	AH	Validation/Illustration		
			Global	Motion					Type	No.	Std. of Ref.
Qualitative or No evaluation	Amini [5]	DSR,MR	–	MF	L	M	+	+	a	1	NA
	Bartels [23, 24]	NS	–	MF	L	N	+	+	m	1	GT
	Benayoun [27]	DSR	–	MF	L	A	+	–	a	1	NA
	Cauvin [44]	SPECT	LVV	–	C	A	+	–	P	NA	NA
	Chen [47]	BA	LVV	SA	H	M	–	–	V	1	NA
	Chen [49]	DSR	LVV	–	C	N	+	–	V	1	NA
	Gustavsson [127]	US	LVV	–	H	M	=	+	V	1	NA
	Huang [145]	DSR	LVV	MF	L	M	+	+	a	1	NA
	Kerwin [153]	MR ¹ tag	–	SA	L	A [†]	+	–	V	1	NA
	Matheny [193]	DSR	LVV	–	G	M	+	–	a	1	NA
	Maehle [187]	US	LVV	WT	L	M	–	–	V/P	NA	NA
	McInerney [196]	DSR	LVV	MF	L	I	–	–	V	1	NA
	Niessen [215]	MR/DSR	LVV	WT	L	I	+	+	a	1/1	NA
	O'Donnell [218, 219]	MR ¹ tag	LVV	WT,SA	H	M	+	+	V	1	NA
	Papademetris [231]	US	–	SA	L	A	+	–	a	3	NA
	Pentland [234]	X	LVV	MF	G	I	+	+	V	1	NA
	Radeva [245]	MR ¹ tag	LVV	MF,SA	L	M	–	+	V	1	NA
	Rueckert [254]	MR	LVV	MF	L	I	+	+	V	1	NA
	Staib [281]	DSR/MR	LVV	–	G	I	+	+	a	1/1	NA
	Yezzi [318, 319]	MR	LVV	WT	L	I	+	+	V	1	NA
	Young [323, 324]	BA	–	SA	L	M	+	+	a	1	NA
	Young [320]	MR ¹ tag	–	SA	L	I	–	+	V	1	NA
Quantitative: synthetic, phantom and animal models	Bardinet [19]	DSR	LVV	MF	H	M	+	–	a/m	1	OB/AS
	Czegledy [63] ^{RV}	CT	RVV	–	C	M	=	–	p	10	AT
	Denney [73, 76]	MR ¹ tag	–	MF	L	A [†]	+	–	m/a	1/1	GT/NA
	Denslow [77] ^{RV}	MR	RVV	–	C	M	=	–	p	13	AT
	Germano [115–117]	SPECT	LVV,EF	–	H	A	+	–	p	1	GT
	Gopal [120]	US	LVV	–	L	M	+	–	p	17	AT
	Kerwin [153]	MR ¹ tag	–	SA [†]	L	A [†]	+	–	m	–	GT
	Haber [130, 131] ^{RV}	MR ¹ tag	–	MF,SA	L	M	+	+	m	1	GT
	Huang [144]	MR ¹ tag	–	MF,SA	L	A	+	–	m/a	–/1	GT/NA
	Legget [174, 177, 212]	US	LVV,LVM	–	L	M	=	–	p/a	6/21+5	GT/AT
	Moore [210]	MR ¹ tag	–	SA	L	A [†]	+	–	m	–	AS
	Moulton [211]	MR ¹ tag	–	SA	L	M [†]	+	–	m/a	–/7	NS/NS
	O'Dell [217]	MR ¹ tag	–	SA	H	M [†]	+	–	m	–	AS
	Papademetris [229, 230]	MR	–	SA	L	A	+	–	a/a	8/3	AT
	Sacks [256] ^{RV}	MR	–	WT	L	M	=	+	p/a	6/1	GT/NA
	Sato [259]	BA	LVV	–	L	M	–	+	m/p	1/1	GT/AT
	Spinale [280] ^{RV}	BA	RVV,SV	WT	L	M	=	+	p/a	22/24	AT/AT
	Shi [272]	MR/DSR	–	WT,MF	L	A	+	+	a	12	AT
	Shi [271]	MR	–	MF,SA	L	A	+	–	a	1	CL
	Tu [297]	DSR	LVV	–	G	M	+	+	a	2	OB
	Yetttram [316, 317]	BA	LVV	–	L	M	=	–	p	8	AT
	Young [321]	MR ¹ tag	–	SA	L	M	+	–	m	–	AS
Quantitative: clinical case studies without standard of reference	Declerck [69]	SPECT	–	MF	G	A	+	+	V/P	3/1	NA
	Kuwahara [172, 257]	BA	LVV,EF,SV	–	L	M	=	–	P	13	NA
	Legget [174, 212]	US	LVV	–	L	M	–	–	V/P	6/2	NA
	Moore [210]	MR ¹ tag	–	SA	L	A [†]	+	–	V	1	NA
	O'Dell [217]	MR ¹ tag	–	SA [†]	H	M [†]	+	–	V	10	NA
	Park [232]	MR ¹ tag	LVV,EF	MF	C	M	+	+	V/P	1/1	NA
	Park [233]	MR ¹ tag	LVV	MF,SA	C	M	+	+	V/P	1/1	NA
	Young [323, 324]	BA	–	SA	L	M	+	+	V	1	NA
	Young [321]	MR ¹ tag	–	SA	L	M	+	–	V	1	NA
Quantitative: clinical case studies with standard of reference	Bardinet [19]	SPECT	LVV	WT,MF	H	M	+	–	V	1	OB
	Biedenstein [31]	SPECT	LVV	–	L	I	+	–	P	42	OB
	Coppini [59]	US	LVV,EF	–	L	N	+	–	V	3	OB
	Faber [95]	SPECT/MR	LVV	WT	L	I	+	+	V/P	22/16	OB
	Faber [94]	SPECT	LVV	–	L	I	+	+	P	10	OB(m)
	Germano [115–117]	SPECT	LVV,EF	WT	H	A	+	–	P	144/65	OB(m)/AT
	Geiser [111, 112]	US	LVV,EF,SV,CO	WT	L	M	=	–	P	4	AT
	Goshdasby [123]	MR	LVV	–	L	I	+	+	V	5	OB
	Legget [174, 177]	US	LVV,SV	–	L	M	–	–	V	5	AT
	Ranganath [246]	MR	LVV,EF	–	L	I	+	+	V	7	OB
	Tseng [296]	US	LVV	WT	G	I	=	–	V	1	OB

5.5 Discussion

Comparison of the performance of different techniques is a difficult task due to the diversity of approaches, the different or complementary information obtained from them, the different imaging modalities and image acquisition protocols, and, last but not least, the lack of a standard way of reporting on performance. In order to draw some comparative conclusions we have classified the existing methodologies according to the degree of their validation (Section 5.5.1). At the same time, we introduce a number of performance criteria (Section 5.5.2). In this comparison we have focussed on techniques leading to traditional cardiac indices, *viz.* global (Sec 5.3.1) and motion parameters (Sec 5.3.2). Table 5.2 summarizes this discussion.

5.5.1 Validation

Three main groups of papers can be distinguished: 1) with no evaluation or only qualitative illustrations, 2) with quantitative evaluation on non-human data sets, and 3) with quantitative evaluation on human data sets. This classification has been used in constructing Table 5.2.

Although there are always exceptions confirming the rule, Table 5.2 indicates several trends. Most papers in the first category correspond to articles presenting technical or methodological aspects of advanced modeling techniques. The result sections in these papers are restricted to either technical aspects or proof-of-concept illustration on realistic images hypothesizing the potential of the technique. Only a few of them have seen follow-up articles confirming those hypotheses in large studies. Further evaluation of these techniques is required in order to determine their usefulness in clinical tasks.

Approaches in the second category are numerous. Methodologies in this category have been evaluated on simulated images or in phantom experiments. These have the advantage of providing ground truth to assess the accuracy and reproducibility of the techniques. Owing to the use of idealized geometries and measurement conditions, extrapolation of the results to *in vivo* human studies remains to be demonstrated. Some papers in this second category have evaluated their techniques on *ex vivo* or *in vivo* animal models. Several researchers have reported experiments with dogs [19, 27, 77, 193, 196, 213, 215, 237, 256, 272, 280, 281], swines [77, 211, 280, 281] or calves [63, 177, 212].¹² Only a few studies have compared measurements, obtained from *ex vivo* [177, 212] or *in vivo* [229, 272, 280] animal studies, against other standard-of-reference techniques. As representative examples we can mention the following evaluation studies. Munt *et al.* [212] employed high-density laser scanning to compute surface area from excised calf hearts. Leotta *et al.* [177] compared *in vivo* stroke volumes in humans computed with their technique against those derived from Doppler measurements. Spinale *et al.* [280] compared cardiac output and stroke volume measurements to those obtained by thermo-dilution. Shi *et al.* [272] validated

¹²Remarkably, a large amount of evaluations involving canine models have been acquired with the dynamic spatial reconstructor. However, the reduced clinical availability of this technique and its specific image properties makes it difficult to extrapolate the results of the evaluation to other clinical imaging techniques.

motion field computations against the trajectories of implanted copper beads filled with gadopentetate-dimeglumine (Gd-DTPA) and lead beads markers for myocardial wall trajectories computed from MR and DSR images, respectively. Papademetris *et al.* [229] evaluated their tissue deformation recovery algorithm against implanted sonomicrometers.

MR tagging techniques for reconstruction of myocardial motion or tissue deformation deserve separate attention. Most *in vivo* animal and human studies have reported on Monte Carlo analysis of sensitivity to errors in tag localization and tracking, and on the ability to recover the location of tags in different frames [73,153,210,211,217].¹³ Several models have been used in the literature to benchmark the accuracy of motion and deformation recovery. These evaluations were based, for instance, on spherical and cylindrical models of cardiac motion [76,210,217,324], FE solutions with realistic geometries [211], artificially generated motion trajectories [19] or synthetic images using the cardiac motion simulator [144,153,155] developed by Waks, Prince and Douglas [307] that builds upon the kinematic model of Arts *et al.* [10]. Recently, a study was carried out by Declerck *et al.* [71] that thoroughly compared four techniques [68,76,217,226] for motion tracking from tagged MR. This paper provides results on normal and pathological subjects. Although the general trends of motion were captured correctly by all methods, this study shows that there are noticeable differences in the displacement and strain computations provided by each technique.

Finally, the third category includes studies that reported application on human volunteers and patients, including quantitative results in terms of cardiac functional parameters. The size of the populations in most of these studies was small. With only three exceptions, all studies were conducted on less than a dozen of volunteers or patients.

5.5.2 Performance criteria

In the following subsections we elaborate on the criteria that we have used to compare the different methods.

Model complexity or flexibility

The complexity or flexibility of a technique has been categorized in four groups according to the number of degrees of freedom¹⁴ (DOF) or parameters involved. 1) *Compact* models with only a few parameters (on the order of a dozen). Prototypical examples are superquadrics. 2) *Flexible* models with large number of DOFs and parameterized with *global*-support basis functions. Representative examples are harmonic parameterizations of several types. 3) *Flexible* models with large number of DOFs and parameterized with *local*-support basis functions. Members of this family are B-spline and polyhedral models. 4) *Flexible hierarchical* models encompassing a reduced set

¹³Validation MR tagging itself for describing tissue deformation has been addressed by Young *et al.* [322] using a silicone gel phantom. Strains derived from MR tagging were compared to the analytic equilibrium strains under a Mooney-Rivlin material law.

¹⁴Here we disregard the obvious rigid transformation parameters to instantiate the model in world coordinates.

Keys to Table 5.2:

— Parameters: **bold** = quantitative results reported; *italic* = computable from the model (but quantitative results not reported). Motion parameters were classified in three categories: WT = wall thickening analysis, MF = wall/tissue motion field (not including strain analysis), SA = strain analysis.

— Flexibility (*F*): C = compact model with small or medium number of degrees of freedom (DOF), G = flexible model with global support basis function and large number of DOF, L = flexible model with local support basis functions and large number of DOF, H = hierarchical models.

— Pre-processing (*PP*) to initialize the model. N = none; M = manual segmentation of contours and/or land-marks; A = (semi) automatic delineation of contours and/or land-marks; I = approximated model initialization or land-mark placement. Pre-computation of feature images (gradient, Laplacian, etc.) was not considered as pre-processing.

— Automation (*AM*) after pre-processing and selection of *ad hoc* parameters: (+) full, (−) interactive guidance may be required to correct/assist intermediate steps, (=) relying on substantial human guidance.

— Ad hoc (*AH*) parameters: (−) none, or robustness demonstrated through sensitivity analysis, (+) yes and no sensitivity analysis was performed.

— Validation/Illustration information. *Type* of evaluation/illustration set: m = mathematical models, p = physical phantoms (mostly balloons or heart casts), a = animal model, V = human volunteers and P = patients. *Standard of reference*: AS = analytic solution, AT = alternative technique, CL = comparison to literature, GT = ground truth, NS = numerical solution, OB(m) = human observer (involving multiple modalities). Papers with several evaluation studies have multiple entries.

— NA = not available / reported

Notes:

[‡]Only the accuracy in determining tag intersections was computed. No quantitative analysis reported on deformation field or strain analysis.

[†]Monte Carlo analysis of sensitivity for this factor is reported.

Figure 5.4. Keys and notes to Table 5.2.

of DOFs coarsely describing shape, plus an extended set of DOFs giving extra flexibility to the model. Representative of this family are superquadrics with free-form deformations. Complexity is, to some extent, related to the computational demand of an algorithm. Highly flexible algorithms are usually related to higher computation time for deforming them to a given image data set.¹⁵ On the other hand it is also a measure of the ability of a modeling technique to accommodate for fine shape details.

Although idealized models of ventricular geometry (mainly ellipsoids or ellipsoidal shells) are appealing for their parsimony and for historical reasons, Table 5.2 shows that no study has quantitatively demonstrated their accuracy in computing simple measurements as LVV and EF. Compact models have developed in two different directions. On one hand, in particular for the RV, some researchers have evaluated combinations of simple models that roughly derive RVV from a small number of linear measurements [63, 77]. The models, however, remain highly constrained and have been tested on *ex vivo* casts experiments only. A second direction has been to trade-off the compactness of the superquadric models and their flexibility without the need of hierarchical decompositions [232, 233]. In this manner, flexibility is added in an elegant way by which each parameter function has an interpretation in terms of local and global shape changes.

Most approaches that reached the stage of quantitative evaluation are based on flexible or hierarchical representations. Both present challenges and advantages. Flexible representations (*e.g.*, polyhedral meshes or harmonic decompositions) are highly versatile and can accommodate detailed shape variations. Most of the quantitative evaluation studies have been reported on local flexible models, most of which are able to cope even with complex topologies. On the other hand, restricting the space of possible shapes is usually difficult or requires substantial manual intervention or guidance [172, 280, 316, 317]. Hierarchical or top-down approaches aim at a reduction in computational time and at improving robustness by incrementally unconstraining the space of allowed shape variation [20, 47, 115, 127, 218, 219]. One weak point in hierarchical approaches is the need for *ad hoc* scheduling mechanisms to determine when one level in the representation hierarchy should be fixed and a new level added, and up to which level the model should be refined. Furthermore, optimization procedures involved in the recovery of hierarchical models have to be designed with particular care. It is unclear how it can be ensured that a succession of optimizations at different modeling levels actually leads to the optimum global deformation. Also the question arises how to link different levels of model detail with the resolution of the underlying image data, and how to interact with the models if, after all, manual editing is required. Still, hierarchical model representations are an active and challenging field in 3-D medical image segmentation research where several investigators have presented encouraging results in cardiac [19, 20, 47, 116, 117, 218, 219] and thorax modeling [176, 186].

¹⁵Actually, it is the conjunction of model parameterization and the recovery strategy which determines the computational load of an approach. It would have been very interesting to report computation time with each technique. Unfortunately, variability in hardware architecture over time and techniques renders any quantitative comparison unrealistic.

Robustness and effective automation

Processing prior to model recovery, automation of the recovery algorithm itself, and the presence of *ad hoc* parameters are factors that determine the *robustness* of a technique and its *effective automation*. By effective automation we refer to the automation of the overall approach, from raw images until the presentation of the functional parameters.

Before a given model can be fitted or deformed to a data set, almost every technique requires some type of *pre-processing* to convert the raw grey-level images into a representation suitable for shape recovery. Section 5.4 has suggested a classification of types of input data. For the sake of simplicity, Table 5.2 only indicates the degree of manual involvement to obtain the corresponding input data. Four categories were considered: (N) no pre-processing required, (I) manual initialization of land-marks/models, (A) (semi) automated initialization of land-marks/models integrated into the technique, and (M) fully manual segmentation of land-marks/contours. Although variability inherent to the pre-processing can have a marked effect on the overall performance of a technique, this factor is usually disregarded in the evaluation of algorithms. A remarkable exception is the evaluation of MR tag tracking algorithms using Monte Carlo analysis to assess the influence of erroneous tag localization in the recovery of tissue deformation [73, 153, 210, 211, 217]. Model initialization is also related to the issue of pre-processing. Although a few techniques make explicit mention of the procedure required to initialize the model [31, 176, 215, 232, 233, 325], model initialization in a 3-D environment can be non-trivial or require expert guidance.

Another factor undermining robustness and reliability of a technique, is the presence of *ad hoc parameters* that have to be set by the user. This can be particularly problematic when such parameters are highly dependent on a given data set. This is a known problem, for instance, of many physics-based deformable models for which several weights must be tuned to balance the smoothing constraints to the external energy terms. However, in the literature, analysis of sensitivity of the result to the weighting parameters is mostly missing. In Table 5.2, we have classified the different techniques into two categories according to the presence of user-defined *ad hoc* parameters: (−) no parameters or parameters with corresponding analysis of sensitivity, and (+) parameters for which no sensitivity analysis was performed. The fact that several methods do not present *ad hoc* parameters (−) does not have to be confounded with overall robustness. Even within the approaches with quantitative evaluation, many papers in the (−) category either require substantial pre-processing [20, 120, 174, 211, 217, 229, 230, 321] or human guidance [63, 77, 111, 112, 296, 316, 317]. Both factors influence the robustness and reproducibility of the derived functional information.

Finally, Table 5.2 also indicates the degree of user guidance (*automation*) of the fitting procedures for given input data (pre-processing) and set of *ad hoc* parameters. Three degrees of automation were used to classify the approaches: (=) relying on substantial human guidance, (−) manual interaction can be necessary for guiding/correcting the deformation, and (+) fully automated. In general terms, the larger the need for human intervention during the fitting procedure, the less robust a technique will become, and the more prone it will be to inter/intra-observer variability of the final results.

5.6 Conclusions and suggested future research

In this chapter we have reviewed techniques for 3-D geometric modeling and analysis of cardiac images. In particular, we have focussed on those techniques leading to traditional indices of cardiac function. We have proposed a systematic classification of the approaches based on the type of representation of the geometric model, and the type of input data required for model recovery (Table 5.1). Furthermore, we have given a critical assessment of these approaches according to the type of functional parameters that they provide, their degree of evaluation, and the performance achieved in terms of modeling flexibility, complexity, and effective automation (Table 5.2).

From the surveyed literature, four main lines of future efforts can be distinguished:

1) *Research on modeling and model deformation techniques.* The last two decades have witnessed an enormous amount of efforts in 3-D models of LV and RV. This holds true for all imaging modalities (cf. Table 5.1). In spite of the large number of attempts, no approach has simultaneously achieved robustness, automation, model flexibility and computational speed. Manual outlining and analysis of cardiac images is still the most popular technique in clinical environments.

Several issues will require more attention in order to integrate the advances of modeling techniques into clinical practice. Accurate 3-D modeling techniques are, in general, computationally intensive. Exploration of flexible modeling techniques that make an efficient use of their degrees of freedom will be worthy of further research. So far the main flow of efforts has been focussed on adopting generic geometrical representations to build cardiac shape models (*e.g.*, superquadrics, B-splines, polyhedral meshes, Fourier descriptors, etc.). As a consequence, in generating a realistic LV shape, the representations are either too restrictive or require a considerable amount of parameters. The question arises of how to infer a compact representation giving rise to realistic shapes, possibly learned from examples.¹⁶ Modeling approaches that go from shape examples to a specific shape representation can reduce computational demands and improve their robustness. A small number of efficiently selected model parameters reduces the dimensionality of the model recovery problem, and naturally constrains its results owing to model specificity.

Further investigation of suitable image features will be needed to improve shape recovery. In particular, incorporation of domain knowledge about the type of image modality (and acquisition protocols) can play an important role in increasing the accuracy of shape recovery techniques.

Most of the modeling techniques presented in this review were either purely geometric or inspired in a *virtual* physical analog (physics-based approaches). Recently, a few papers have introduced known biomechanical properties of the heart in the formulation of models that analyze cardiac images [229–231, 271]. Further development of such approaches, and their application to segmentation tasks, can be a natural way of extending the ideas of physics-based methods and of relating some of the *ad hoc* parameters with experimental evidence provided by biomechanics.

¹⁶ An interesting approach is to extract statistical models from sample shapes [56] and to capture the most representative degrees of freedom via principal component analysis. Although interesting results have been obtained in 2-D applications, more research is needed to solve practical problems in their 3-D extensions.

2) *Research on interactive model-based segmentation.* Table 5.2 supports the idea that model-based cardiac segmentation has not reached the status of being effectively automated since current techniques either require substantial expert guidance, *ad hoc* parameter fine-tuning or non-trivial pre-processing. Although full automation is a desirable end goal, its difficulty has been acknowledged many times in the literature. There is a growing consensus that user interaction is, to some extent, unavoidable, and that it has to be considered as an integrated part of the segmentation procedure. Therefore, development of efficient tools for 3-D interaction will play an important role in the near future. “Efficient” entails that with minimal and intuitive user interaction the operator keeps control over the segmentation process to correct or overrule its results where it has failed, and to guide the algorithm in abnormal situations (*e.g.*, in front of a pathological case). Of course, the issue of reproducibility in case of human intervention needs attention. Where well-defined repetitive tasks are recognized, or where a local user interaction can be extrapolated to a broader area, the process should be automated, thus improving segmentation throughput and repeatability. How to devise such efficient and intuitive mechanisms for 3-D manipulation of models and volumetric data, and how to integrate them into the deformation of the models remain topics of future research.

3) *Research on functional cardiac descriptors.* There are many shape and motion parameters other than traditional indices (cf. Appendix 5.A). Unfortunately, although these new indices seem to provide richer information and/or a more detailed analysis of cardiac function, their clinical evaluation has been very limited. As a consequence, it is difficult to determine their clinical relevance and the extra information provided with respect to traditional indices like LVV, EF, etc. The lack of clinical evaluations may be related to the fact that advanced 3-D modeling techniques, from which these parameters can be derived, are computationally expensive and require considerable user intervention. The need of considerable pre- and post-processing procedures, *ad hoc* parameter settings and technical understanding of the modeling technique itself may explain why most of the described approaches are not available as stand-alone prototypes on which clinical studies can be carried out routinely.

There is certainly place for development of novel shape and motion descriptors. However, there is even a larger need for evaluation of already existing indices on reference data sets and/or large scale clinical studies. It is remarkable that this lack of large evaluation studies is present even in many techniques aiming at the extraction of traditional functional parameters (Table 5.2).

It is unrealistic to expect that every new technique proposed in the future will go through the process of a thorough clinical evaluation study. Unfortunately, many research institutes working on geometric modeling and shape analysis are not located in a clinical environment. Access to state-of-the-art image material and derived parameters for testing and benchmarking purposes is, therefore, difficult. In this respect, a public, common database of a representative set of images from different modalities would be highly beneficial. This database should establish a few standard data sets (both synthetic and clinical study cases) with as much independent measurements as possible of mass, stroke volume, etc. With the current speed of development in the imaging modalities, such a database should be updated regularly to be representative of the state-of-the-art imaging technology.

4) *Multi-disciplinary approaches.* When imaging and modeling techniques get more complex, the interplay of clinicians, medical physicists and technologists in a common environment becomes increasingly important. Several issues have to be addressed in a cooperative fashion: the interrelationship between image acquisition and cardiac modeling, the development of effective visualization techniques of 4-D data sets, realization of intuitive interfaces to interact with geometric models at the various stages of initialization, deformation and eventual correction of results, and concise transfer of clinical information from images/models to the cardiologists.

It is to be expected that approval by clinicians of a model-based technique that provides functional parameters will depend on close collaboration between technicians involved in image acquisition, computer scientists devoted to the development of efficient modeling and model recovery techniques, and cardiologists providing feedback about the desired information and display methods, the validity of the assumptions and the design of evaluation studies.

5.A Appendix: Non-traditional shape and motion descriptors

Three-dimensional model-based analysis of left ventricular shape and motion has the potential of providing rich morphological and functional information. Current clinical assessment of cardiac function is based mainly on global parameters as LVV and EF. However, several researchers have demonstrated in the past the importance of local functional indices as wall thickening and segmental motion analysis [124,228,268,269], and local curvature and shape [21,148,189,190] as potential cardiac indexes. Unfortunately, most of these studies were based on 2-D imaging techniques. Although they can indicate major trends about cardiac shape, a 3-D analysis would be beneficial to better account for the true cardiac geometry. In this section, we briefly summarize several new indices proposed in the literature that describe shape and/or motion. Some of these indices have been presented as a by-product of a specific modeling technique while others are easily computable from any model representation. Therefore, this distinction seems a natural classification.

A. Generic descriptors

Mean and Gaussian curvature. The principal curvatures (k_1 and k_2 , respectively) measure the maximum and minimum bending of a regular surface.¹⁷ Rather than using principal curvatures it is more common to use two derived quantities known as Gaussian ($K = k_1 k_2$) and mean ($H = (k_1 + k_2)/2$) curvatures. By analyzing the signs of the pair (K, H) it is possible to locally distinguish between eight surface types [28].

Friboulet *et al.* [107] have studied the distribution of the Gaussian curvature in the LV at different phases of the cardiac cycle. From this study it was concluded that this distribution remains structurally stable over time. Whereas the LV free wall

¹⁷A subset $M \subset \mathbb{R}^n$ is called a regular surface if for each point $p \in S$, there exists a neighborhood V of p in \mathbb{R}^n and a map $x : U \rightarrow \mathbb{R}^n$ of an open set $U \subset \mathbb{R}^2$ onto $V \cap M$ such that: 1) x is differentiable, 2) $x : U \rightarrow \mathbb{R}^n$ is a homeomorphism, and 3) each map is a regular patch, *i.e.*, it has a full rank Jacobian for any $x \in U$.

provides rich and dense curvature information, the curvature at the septal wall is less suitable to establish point correspondences. Similar findings were made by Sacks *et al.* [256] with respect to the RV free wall: the RV free wall has relatively uniform distribution of principal curvatures, and the surface geometry of the RV free wall does not change significantly from end diastole to end systole.

Shape index and shape spectrum. Although mean and Gaussian curvatures are related to the concept of curvedness, there still remains scale information in these shape descriptors. To overcome this problem, Clarysse *et al.* [52] have used the *shape index* (s) and the *curvedness* (c), two parameters that were introduced by Koenderink and van Doorn [161] and are defined as follows:

$$s = \frac{2}{\pi} \tan^{-1} \left(\frac{k_2 + k_1}{k_2 - k_1} \right) \quad (5.11)$$

$$c = \left(\frac{k_1^2 + k_2^2}{2} \right)^{\frac{1}{2}} \quad (5.12)$$

While c is inversely proportional to the object size, s defines a continuous distribution of surface types ranging from cup-like umbilic ($s = -1$) to peak-like umbilic ($s = 1$) points. It can be shown that while the shape index is invariant by homothecy, the curvedness is not. In this way, shape information and size can be easily decoupled.

The *shape spectrum* [80], $\gamma(h, t)$, is a global shape index defined as the fractional area of the LV with shape index value h , at time t

$$\gamma(h, t) = \frac{1}{A} \iint_S \delta(s(\mathbf{x}) - h) dS \quad (5.13)$$

where $A = \iint_S dS$ is the total area of the surface S , dS is a small region around the point \mathbf{x} , and $\delta(\cdot)$ is the one-dimensional Dirac delta function. Cardiac deformation can be analyzed by tracking the shape index and curvedness of *similar shape patches* (SSP) over time. SSP are connected surface patches whose points have similar shape indices, *i.e.*, the shape index falls within a given range $s \pm \Delta s$. Clarysse *et al.* have shown the potential applicability of these indices by analyzing phantoms of normal and diseased LVs. A LV model of dilated cardiomyopathy, and a model of an ischemic LV (both akinetic and hypokinetic in the left anterior coronary territory) were generated using 4-D spherical harmonics. The curvedness spectrum was significantly altered by both pathologies, even when they were localized (ischemic models). Reduction of the global function in the dilated myocardium had no significant repercussion on the shape index spectra. This could be an indicator that this pathology mostly affects the magnitude of motion only. An alternative to global analysis is to track the curvature parameters in predetermined regions. Clarysse *et al.* have tracked three reference points over time: the apex, a point in the anterior wall, and a point in the cup of the pillar anchor. Using the local temporal variation of the curvedness and shape index, it was possible to distinguish between the normal and diseased model. A potential problem of this techniques is the reliable tracking of SSPs. If local deformations are too large the trace of points might be lost.

Local stretching. Mishra *et al.* [206] have presented a computational scheme to derive local epicardial stretching under conformal motion. In conformal motion, it

is assumed that motion can be described by a spatially-variant but locally isotropic stretching factor. In particular, for any two corresponding patches before and after motion, P and \bar{P} , the *local stretching factor*, τ , can be computed from the change in Gaussian curvature and a polynomial stretching model by means of the relationship

$$\bar{K} = \frac{K}{\tau^2} + \frac{f(E, F, G, \tau, \tau_u, \tau_v, \tau_{uu}, \tau_{vv})}{\tau^2} \quad (5.14)$$

where $f(\cdot)$ is the polynomial stretching model (linear or quadratic in [206]), E , F , and G are here the coefficients of the first fundamental form [78], and (u, v) are coordinates of a local parameterization of the surface patch. Mishra *et al.* [206] present a method to solve for τ in Equation (5.14) and show that the local epicardial stretching factors computed over the cardiac cycle follow a similar evolution to the temporal variation of the principal strains obtained by Young *et al.* [323] using strain analysis techniques.

B. Model-specific shape descriptors

Geometrical cardiogram (GCG). Azhari *et al.* [15] describe a method for classification of normal and abnormal LV geometries by defining a “geometrical cardiogram” (GCG), a helical sampling of the LV geometry from apex to base [16]. The GCG at end systole and at end diastole are subsequently analyzed via a Karhunen-Loeve Transform (KLT) to compress their information. A truncated set of the KLT basis vectors is used to project the GCG of individual patients into a lower-dimensional space, and the mean square error between the projected and original GCG is used to discriminate between normal and abnormal LV [14]. From this vectorial representation LVV and EF [16], and WT [17] can also be computed.

Deformable superquadric and related models. One of the first 3-D primitives used to model the LV was the superquadric. It is a natural extension of the simplified geometric models originally used in 2DE [306] and angiocardiology [66, 79, 136, 152]. Along with three main axes indicating principal dimensions, the superquadric models can be endowed with additional parametric deformations as linear tapering and bending [20, 49], free-form deformations [19], displacement fields [218, 219] or parametric functions providing information about radial and longitudinal contraction, twisting motion, and deformation of the LV long-axis [232, 233] and wall thickness [233]. In particular, Park *et al.* [232, 233] suggest to decompose deformation and motion into a few parametric functions that can be presented to the clinician in the form of simple plots. All these functions are either independent of the total LV volume (*e.g.*, twisting) or can be normalized with respect to the dimensions of the LV (*e.g.*, radial and longitudinal contraction). This allows inter-patient comparisons of contraction and shape change.

Global motion analysis based on departure from an affine model. Friboulet *et al.* [108] modeled the LV using a polyhedral mesh at each frame of the cardiac cycle. The state of the LV was characterized by the center of gravity and the moments of inertia of the polyhedral mesh. The deformation between two frames was hypothesized to follow an affine model. By defining a metric to compare two different polyhedral

representations, the authors were able to quantify the difference between the actual inter-frame deformation and the corresponding deformation derived from an affine motion model. Several parameters of global motion are then derived: the temporal variation of the longitudinal and transversal moments of inertia, and the proportion of total motion explained by the affine model. By means of case studies it was demonstrated that these global indices are able to discriminate between normal ($EF = 0.71$) and highly diseased ($EF = 0.1$) LVs. On the other hand, the global nature of these indices precludes the quantification of localized, inhomogeneous dysfunction of the LV.

Motion decomposition through planispheric transformation. Declerck *et al.* [69] have proposed a canonical decomposition of cardiac motion into three components: radial motion, twisting motion around the apico-basal axis, and long-axis shortening. This decomposition is achieved through a transformation of the Cartesian coordinates of the LV wall to a planispheric space. In this space, a 4-D transformation is defined that regularly and smoothly parameterizes the spatio-temporal variation of the LV wall. Since the canonical decomposition of motion can be directly obtained in the planispheric space, these descriptors also vary smoothly along the cardiac cycle. Finally, by tracking the position of material points over time in the planispheric space and subsequent mapping to Cartesian coordinates, it is possible to reconstruct their 3-D trajectories.

Modal analysis: deformation spectrum. Nastar and Ayache have introduced the concept of *deformation spectrum* [213] which can be applied within the framework of modal analysis [235]. The deformation spectrum is the graph representing the value of the modal amplitudes as a function of mode index. The deformation spectrum corresponding to the deformation between two image frames describes which modes are excited in order to deform one object into another. It also gives an indication of the strain energy [213] of the deformation. As a consequence, a pure rigid deformation has zero strain energy. Two deformations are said to be *similar* when the corresponding deformation fields are equivalent up to a rigid transformation. In order to measure the dissimilarity of two deformation fields, the lower-order modes related to rigid transformation are discarded. The difference of the deformation spectra so computed, can be used to define a metric between shapes (*e.g.*, the LV in two phases of the cardiac cycle) that can be applied to classify them into specific classes (*e.g.*, normal/abnormal motion patterns). Finally, the amplitude of the different modes can be tracked over time. Using Fourier spectral analysis, Nastar and Ayache have shown that these modes concentrate in a few low-frequency coefficients.

5.B Appendix: MR tag localization techniques

Early attempts to model myocardial tissue deformation tracked tag grid intersections manually over time [321]. Other researchers [73, 76, 131, 153, 210, 217] have used semi-automatic tools [11, 128, 129], based on *snakes*, to locate and track tag intersections and to define myocardial contours. Although they still require user interaction, these tools can speed up the manual procedure while reducing inter-observer variability [25].

Young *et al.* [325] propose an interactive scheme for tag tracking. The 2-D tag

grid is modeled as a whole (*active carpet*). Separate manual segmentation of the LV boundaries is required to compute *myocardial* strains only. Tag tracking is performed using a modified *snake* [149] algorithm. Since tags show up in these images as dark lines (intensity valleys), the image intensity is used as external energy. Additionally interactive guidance is supported by introducing user-defined constraints. Only points in the myocardium mask are tracked in each frame while carpet points outside the myocardium (*inactive points*) provide a weak form of continuity. Kraitichman *et al.* [166] have introduced an interactive method for tracking tag intersections. The method shares some features of the *active carpet* model of Young *et al.* [325]. The carpet of tag intersections is modeled as a mass-spring mesh of triangles. Tag intersections are tracked by means of a correlation-based external energy and, eventually, adding interactive constraints. Finally, this technique allows to compute average strains on the triangular patches. Another method for automatic tracking of the SPAMM grid has been presented by Kumar and Goldgof [170]. In the first frame template matching is applied to provide an initial position of the tag grid. In this frame, the tag grid has a high contrast and a regular arrangement. In the subsequent frames, each line of the tag grid is independently tracked using a discrete *thick snake* with a width of two pixels (the typical tag width). The product of the image intensity in the two pixels is used as external energy to attract the snakes to the tag lines. Although these methods for extracting tag intersections can be useful for 3-D deformation analysis, in the original formulations, the methods proposed in [325], [166] and [170] have all been applied to 2-D strain analysis.

There exist other approaches not based on snakes. Zhang *et al.* [327] decouple horizontal and vertical tag tracking via Fourier decomposition and spectral masking. In order to compensate for spectral cross-modulation from perpendicular lines, local histogram equalization is needed prior to spectral analysis. Detection of tag lines is simplified in the pre-processed images and a simple local search can then be used to track local intensity minima (tag lines) over time. Kerwin and Prince [155] have developed a method to simultaneously detect and track tag surfaces without the need for prior 2-D tag tracking. Tag surfaces are modeled using a *kriging update model* [65,154]. This model parameterizes tag surfaces using a global quadratic surface plus a local stochastic displacement. A recursive spatio-temporal scheme is developed that updates the kriging model. Measurements to update the model are obtained through a local search for tag lines. In this search a matched filter is employed modeling the intensity profile across a tag line. Recently, Osman *et al.* [110,224] have introduced and evaluated a method for cardiac motion tracking based on the concept of harmonic phase (HARP). The method uses isolated spectral peaks in the Fourier domain of MR tagged images as a cue for tag tracking. The inverse Fourier transform of a spectral peak is a complex image whose computed angle is called harmonic phase image. In Osman *et al.* [224,225] it is shown how this angle can be treated as a material property that can be related to myocardial strain. This technique has the advantage that is fast, fully automatic and provides dense material properties. So far the method has been applied to 2-D images and thus only provides information about “apparent motion”. In Osman and Prince *et al.* [223], the authors present several visualization techniques that can be used to display the information provided by HARP images.

For we must not misunderstand ourselves; we are as much automatic as intellectual; and hence it comes that the instrument by which conviction is attained is not demonstrated alone. How few things are demonstrated! Proofs only convince the mind. Custom is the source of our strongest and most believed proofs... Who has demonstrated that there will be a tomorrow and that we shall die? And what is more believed?

— B. Pascal, 1623-1662

Chapter 6

Automatic 3-D statistical shape model construction via atlas-based landmarking and volumetric elastic registration

Abstract — A novel method is introduced that allows for the generation of landmarks for three-dimensional shapes and the construction of the corresponding 3-D Active Shape Models (ASM). Landmarking of a set of examples from a class of shapes is achieved by (i) construction of an atlas of the class, (ii) automatic extraction of the landmarks from the atlas, and (iii) subsequent propagation of these landmarks to each example shape via a volumetric elastic registration procedure. This chapter describes in detail the method to generate the atlas, and the landmark extraction and propagation procedures. This technique presents some advantages over previously published methods: it can treat multiple-part structures, and it requires less restrictive assumptions on the structure's topology. The applicability of the developed technique is demonstrated with two examples: CT bone data and MR brain data.

Adapted from: A.F. Frangi, D. Rueckert, J.A. Schnabel, and W.J. Niessen (2001). *Automatic 3-D ASM construction via atlas-based landmarking and volumetric elastic registration. Information Processing in Medical Imaging, IPMI01 (Davis, USA). In press.*

6.1 Introduction

Statistical models of shape variability [57, 58] or Active Shape Models (ASM) have been successfully applied to perform segmentation and recognition tasks in two-dimensional images. In building statistical models, a set of segmentations of a shape of interest is required as well as a set of landmarks that can be defined in each sample shape.

Manual segmentation and determining point correspondences are time consuming and tedious tasks. This is particularly true for three-dimensional applications where the number of slices to analyze and the amount of landmarks required to describe the shape increases dramatically with respect to two-dimensional applications. This work

aims at automating the landmarking procedure while still relying on the existence of a segmentation of the shapes.

Several authors have proposed techniques to find point (landmark) correspondences but only a few of them have indicated or investigated their applicability in the field of statistical shape models. Wang *et al.* [308] use a surface registration technique to find 3D point correspondences based on a metric matching surface-to-surface distance, and surface normals and curvature. The authors suggest that this technique could be used to build 3D ASMs but they do not report any results on statistical model building. Kelemen *et al.* [150] report on the construction of 3D ASMs of neuroradiological anatomical structures. In this method the authors used a correspondence-by-parameterization approach to establish surface landmarks. The landmark correspondence is defined in the parameter domain of an underlying spherical harmonic parameterization. Although this approach has been used to build 3D ASMs, no explicit volumetric or surface registration between shapes takes place.

To our knowledge, little work has been done on the automatic construction of 3D ASM using elastic registration [39, 40, 100, 101]. The frameworks proposed by Brett and Taylor [39, 40] are closely related to this chapter. In these approaches, each shape is first converted into a polyhedral representation. In the first approach [40], shape pairs are matched using a symmetric version of the Iterative Closest Point (ICP) algorithm of Besl and McKay [29]. Using this method, the authors were able to build 3-D ASMs by automatically finding corresponding landmarks between surfaces. Surfaces are represented by means of dense triangulations that are matched via sparse triangulations (obtained by triangle decimation from the dense triangulations). The nodes of this sparse triangulation become the final landmarks. One problem acknowledged by the authors is the possibility of obtaining shape models with surface folding due to some landmark groups (triples) matched in different order between training examples. This is a consequence of the use of the ICP technique which does not incorporate connectivity constraints (purely local registration). In Brett and Taylor [39] this problem is overcome by transforming the surface to a planar domain by means of harmonic maps where connectivity constraints can be explicitly enforced. This technique avoids invalid cross-correspondences but is only applicable to single-part shapes that are topologically isomorphic to a disk. The work by Fleute and Lavallée [100, 101] is also related to our work. They use a multi-resolution elastic registration technique based on octree-splines. This approach is a surface-based technique that registers shapes by minimization of a distance measure.

In this work a technique is introduced that addresses the shortcomings of point-based registration where no overall connectivity constraints are imposed. It uses a free-form elastic registration technique based on maximization of normalized mutual information (volume-based technique). Our method introduces global constraints by modifying the pairwise shape correspondences from a point-based registration technique into a volume-based elastic registration technique. By construction, the deformation field is enforced to be smooth and the regularization term of the deformation will further penalize folding. In addition, our method can be applied to multiple-part shapes.

The chapter is organized as follows. Section 6.2 provides some background on active shape models. In Section 6.3, our approach is described. In Section 6.4, results

are presented that show the applicability of the method to modeling the radius in volumetric Computed Tomography (CT) data and the caudate nucleus in Magnetic Resonance Imaging (MRI); empirical evidence is given on convergence properties and reconstruction errors. Finally, Section 6.5 closes the chapter with some conclusions and directions for future research.

6.2 Active Shape Models

Over the years many approaches have appeared in the field of deformable models [197, 274]. One of the most promising techniques are Active Shape Models (ASMs) [57, 58]. ASMs belong to the group of *generative models* since they allow to synthesize instances of the modeled class of shapes. The model is learned from a set of examples by performing a statistical analysis. Hence ASMs are also referred to as statistical shape models. They have a number of important advantages over other approaches:

- They are *widely applicable* since the same concept can be applied to different problems by presenting different sets of examples.
- It is possible to incorporate *expert knowledge* in the annotation of the examples of the training set.
- The method provides a *compact representation* of the allowed shape variation that is *specific* to model the variation observed in the training set.
- There are *few assumptions* about the nature of the object being modeled other than what is included in the training set.

The technique of ASMs involves two aspects: i) how to build a model from a set of examples, and ii) how to use the models to interpret new images. The first aspect is the focus of this chapter, in particular how to extend the basic theory to three-dimensional models. The remainder of this section will introduce the necessary background theory to put the contributions of this chapter in the perspective of the technique of ASMs. The second aspect involves the application of the models to segmentation or recognition tasks and will not be considered in this chapter. Further details concerning this topic can be found in the report by Cootes and Taylor [57].

6.2.1 Modeling shape variation

Suppose that we have n shapes described as vectors, $\{\mathbf{x}_i; i = 1 \dots n\}$. Each shape consists of l 3-D landmarks, $\{\mathbf{p}_j = (p_{1j}, p_{2j}, p_{3j}); j = 1 \dots l\}$ ¹ that represent, for instance, the nodes of a surface triangulation. Each vector is of dimension $3l$ and is made up of the concatenation of the landmark coordinates, *i.e.*, $\mathbf{x}_i = (p_{11}, p_{21}, p_{31}, p_{12}, p_{22}, p_{32}, \dots, p_{1l}, p_{2l}, p_{3l})$. Moreover, it is assumed that the positions of the landmarks of all shapes are aligned in the same coordinate system. These vectors form a distribution in a

¹How to obtain those three-dimensional landmarks is not a trivial issue and is the aim of this chapter.

3D-dimensional space. If this distribution can be modeled, it would be possible to generate new instances of the same shape class.

In particular, linear ASMs use a parameterized model of the form²

$$\mathbf{x} = \hat{\mathbf{x}} + \mathbf{M}\mathbf{b} \quad (6.1)$$

where $\hat{\mathbf{x}}$ is the average landmark vector, \mathbf{b} is the model parameter vector, and \mathbf{M} is a matrix that transforms the parameter vector into displacements with respect to the mean shape. ASMs use Principal Component Analysis (PCA) to obtain the matrix \mathbf{M} , *i.e.*, to describe the main directions of shape variation in the training set. PCA computes the main axes of the cloud of 3D-dimensional points or landmark vectors. The method can be summarized as follows:

1. Compute the mean landmark vector

$$\hat{\mathbf{x}} = \frac{1}{n} \sum_{i=1}^n \mathbf{x}_i \quad (6.2)$$

2. Compute the covariance of the landmark vectors

$$\mathbf{S} = \frac{1}{n-1} \sum_{i=1}^n (\mathbf{x}_i - \hat{\mathbf{x}})(\mathbf{x}_i - \hat{\mathbf{x}})^T \quad (6.3)$$

3. Compute the eigenvectors, ϕ_i , and corresponding eigenvalues, λ_i , of \mathbf{S} (sorted so that $\lambda_i \geq \lambda_{i+1}$). If Φ contains the t eigenvectors corresponding to the largest eigenvalues, then we can approximate any shape of the training set, \mathbf{x} , using

$$\mathbf{x} \approx \hat{\mathbf{x}} + \Phi \mathbf{b} \quad (6.4)$$

where $\Phi = (\phi_1 | \phi_2 | \dots | \phi_t)$ and \mathbf{b} is a t -dimensional vector given by

$$\mathbf{b} = \Phi^T (\mathbf{x} - \hat{\mathbf{x}}) \quad (6.5)$$

This vector \mathbf{b} provides the parameters of the active shape model that best approximate Equation (6.4) in a least-squares sense. By varying these parameters we can generate different instances of the shape class under analysis using Equation (6.4) (generative model). Under the assumption that the cloud of landmark vectors is drawn from a multi-dimensional Gaussian distribution, the variance of the i -th parameter, b_i , across the training set is given by λ_i . By applying limits to the variation of b_i , for instance $|b_i| \leq \pm 3\sqrt{\lambda_i}$, it can be ensured that the shape generated is similar to the ones in the training shape.

²Linear ASMs assume a multi-dimensional Gaussian distribution as underlying statistical distribution. However, the same landmarking procedure described in this chapter can be applied in conjunction with the non-linear extensions of ASM [57, 279].

6.2.2 Choice of the number of modes

The number of eigenvectors to retain, t , can be chosen in a number of ways. For example, it can be selected in a way that the model explains some proportion (*e.g.* 98%) of the total variance of the data. That is, if the total variance is $V_T = \sum \lambda_i$, then we can choose the t largest eigenvalues such that

$$\sum_{i=1}^t \lambda_i \geq f_v V_T \quad (6.6)$$

where f_v defines the proportion of the total variation one wishes to explain.

If the noise on the measurements of the landmark positions has a variance σ_n^2 , then it is possible to select the largest t such that $\lambda_t \geq \sigma_n^2$, assuming that the eigenvalues are sorted in descending order.

An alternative approach is to choose a sufficient number of modes so that the model can approximate any training example within a given accuracy. This accuracy, however, is not necessarily the same as the reconstruction accuracy calculated for an example not used for building the ASM. Therefore, to gain a better confidence in the required number of modes, t , one can perform a leave-one-out experiment. The smallest t is chosen for the full model such that the models built with t modes from all but one example can approximate the missing example sufficiently well.

6.3 Method

It is apparent from the previous section that in order to apply the concept of ASMs it is fundamental to extract a set of landmarks from each shape of the training set. This is the main aim of the method developed in this chapter.

6.3.1 Overview

Ideally, a landmark is an anatomically characteristic point that can be uniquely identified on a set of shapes. However, anatomical landmarks are usually too sparse to accurately describe a 3-D shape. Therefore, we will consider pseudo-landmarks, *i.e.* landmarks on the shape's surface which determine its geometry.

In our framework, automatic landmarking is carried out by non-rigidly mapping the landmarks of an atlas that is representative of a set of training shapes. Let us assume that n segmented shapes (3-D binary images) are available, $\mathcal{S}_n = \{B_i\}$ where $i = 1 \dots n$. To generate the landmarks for the n shapes, the task is to build an atlas A , landmark it, and propagate its landmarks to the n shapes (Figure 6.1). In the following we will describe these steps in detail.

6.3.2 Atlas building

In the context of this chapter, an *atlas* is an average representation of the shape of a structure inferred from a set of training shapes \mathcal{S}_n . In order to build the atlas, three issues have to be addressed: the selection of a *pairwise corresponder* to match

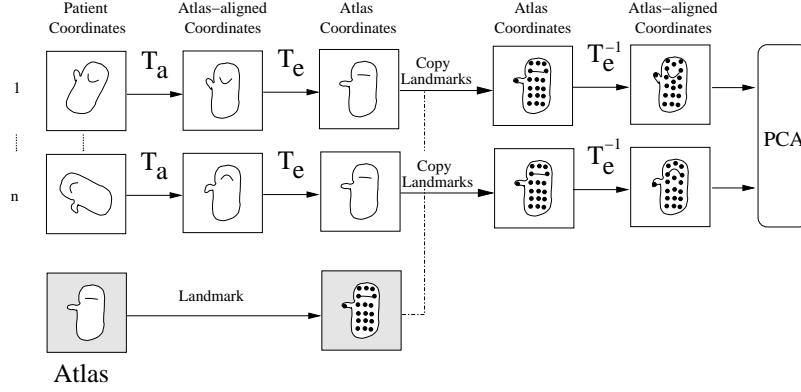


Figure 6.1. Overview of the automatic landmarking framework. All individual data sets are matched to an atlas via a quasi-affine transformation (T_a) and an elastic transformation (T_e). The landmarks in the atlas can then be copied to the individual patients. The elastic deformation is subsequently reversed. Thus, Principal Component Analysis (PCA) is carried out in a space where all shapes are aligned with the atlas (atlas-aligned coordinates). The principal modes of variation will therefore account for elastic deformations and not for pose or size changes.

two different shapes, a strategy to *blend shapes* in a common coordinate frame, and a method to obtain an average or *mean shape* with only marginal bias towards a particular individual.

Pairwise shape corresponder. Given a shape B_i , it is matched to the atlas, A , using a *quasi-affine* registration algorithm with nine degrees of freedom (rigid transformation plus anisotropic scaling) using an algorithm adapted from [284]. This algorithm matches shapes using a criterion based on normalized mutual information [285] (Appendix 6.A). Since the shapes are binary images, we have experimented with several other registration measures (sum of squared differences and cross-correlation) but normalized mutual information was found to be more robust and accurate than any of the other measures tested.

After registration, the shape B_i is expressed in the coordinate system of A . The coordinate system of A will be referred to as the atlas-aligned coordinate system.

Shape blending. Once we have found the quasi-affine transformations that map each of the B_i shapes into atlas-aligned coordinates, these shapes have to be combined to form an average shape (binary image).

Let B'_i and $\mathcal{DT}(B'_i)$ denote the shape in atlas-aligned coordinates and its Euclidean distance transform [64] respectively, with the convention that inner points have a negative distance while outer points have a positive distance. Then, an average shape can be obtained in the distance transformed domain by computing

$\mathcal{DT}(B_{av}) = \frac{1}{n} \sum_{i=1}^n \mathcal{DT}(B'_i)$. A binary representation of the shape B_{av} can be obtained by thresholding the distance transform map to its zero-level set.

Mean shape. To generate the mean shape it is necessary to register all \mathcal{S}_n shapes into a common reference frame (atlas-aligned coordinates). However, the atlas is not initially known. To solve this problem an iterative algorithm was developed. One training shape is randomly selected as the initial atlas, A_0 , and all remaining shapes are registered to it using the pairwise shape corresponder. After this step, all shapes \mathcal{S}_n are expressed in the canonical system of A_0 and can be blended to generate a new atlas A_1 . This procedure is iterated I times to reduce the bias introduced by the initial shape. Any metric of similarity between the atlases of two consecutive iterations can be used to monitor the convergence of the procedure. The final atlas is A_I . This iterative algorithm is summarized in the flow diagram of Figure 6.2. To check for the influence of the randomly selected training shape, atlases with different start shapes have been quantitatively compared.

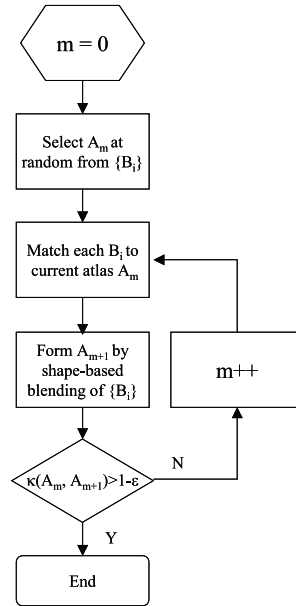


Figure 6.2. Flow diagram of the iterative atlas construction algorithm.

6.3.3 Atlas landmarking

By means of the iterative procedure of the previous subsection a binary atlas, A , has been obtained. The *marching cubes* [183] algorithm is used to generate a dense triangulation of the boundary surface. This triangulation can be decimated to obtain a sparse set of nodes that preserves the geometry of the original triangulation to a

desired degree of accuracy. The nodes in this decimated triangulation correspond to the pseudo-landmarks used to construct the ASM. The use of different triangle densities (decimation ratios) has been investigated to observe their influence in the statistical models generated with our technique (see Section 6.4). The decimation strategy applied in this chapter is the one proposed by Schroeder *et al.* [264]. Note that, as an alternative to marching cubes, an expert could manually localize anatomical landmarks in the atlas. Anatomical landmarks, however, may be too sparse to accurately represent the shape of the structure. By using marching cubes, a dense and approximately even distribution of landmarks is obtained.

6.3.4 Landmark propagation

Once the atlas is constructed and landmarked, its landmarks can be propagated to the individual shapes. This is carried out by warping each sample binary volume into the atlas with a transformation, $\mathbf{T} = \mathbf{T}_a + \mathbf{T}_e$, that is composed of a quasi-affine (\mathbf{T}_a) and an elastic (\mathbf{T}_e) transformation. The transformation \mathbf{T}_a accounts for overall pose and size differences between the atlas and each sample volume while the transformation \mathbf{T}_e accounts for local shape differences.

The quasi-affine transformation is obtained using a registration algorithm adapted from [284] (Appendix 6.A). Registration of binary volumes was carried out using normalized mutual information [285]. The elastic transformation is expressed as a volumetric free-form deformation field using the method of Rueckert *et al.* [255] that also uses normalized mutual information as a registration measure (Appendix 6.A).

Once the global transformation \mathbf{T} has been found, the landmarks of the atlas can be propagated to the atlas-aligned coordinate system by applying the inverse of the elastic transformation (\mathbf{T}_e^{-1}). This process is repeated for each sample shape. As a result, a set of landmarks is obtained that describes shape variations with respect to the atlas. Since these landmarks are now in atlas-aligned coordinates, pose and size variations are explicitly eliminated from the model. These transformed landmarks are subsequently used as the input for Principal Component Analysis (PCA) as indicated in Figure 6.1.

6.4 Results

6.4.1 Data sets

In order to demonstrate the proposed methodology, two case studies were performed. The first case study consists of a set of 14 manual segmentations of the head of the radius, a bone of the wrist, extracted from CT scans (voxel dimensions $1 \times 1 \times 2 \text{ mm}^3$). The second study comprises a set of 20 manual segmentations of the caudate nucleus, a deep structure of the brain, from MR scans (voxel dimensions $1 \times 1 \times 1.2 \text{ mm}^3$).

In building the model of the caudate nucleus each hemisphere of the structure was treated independently. This two-part structure has an almost specular symmetry with respect to the sagittal plane separating the left and right brain hemispheres. Such symmetry is difficult to capture with a single quasi-affine transformation. After

the landmarks of each side (sub-atlas) are extracted and propagated, Principal Component Analysis (PCA) is applied to the set of the landmarks of both sides. In this way, inter-hemispheric relationships are included in the statistical analysis.

6.4.2 Atlas construction

Convergence properties

As a metric to measure convergence of the atlas building procedure, the κ statistic [1] was used. This statistic measures the similarity between two binary images, $\kappa(A_m, A_{m-1})$, in a way that is independent of the structure's volume. Figure 6.3 shows the evolution of the κ statistic, $\kappa(m)$, as a function of the iteration number, m . This statistic ranges between 0.0 and 1.0, and a value above 0.9 is usually regarded as an excellent agreement [1]. The $\kappa(m)$ statistic compares the similarity between the atlases A_m and A_{m-1} . Figure 6.3(a) corresponds to the atlas of the radius. Two curves are shown for two different initial shapes used in the initialization procedure. Similar curves are drawn in Figure 6.3(b) for the left and right caudate nucleus atlases. The atlas of each subpart (left/right caudate nucleus) was obtained independently. The trend of these plots is similar to that observed in the atlas of the radius. Figure 6.3 it indicates that after five iterations the shape of the atlas stabilizes ($\kappa > 0.97$).

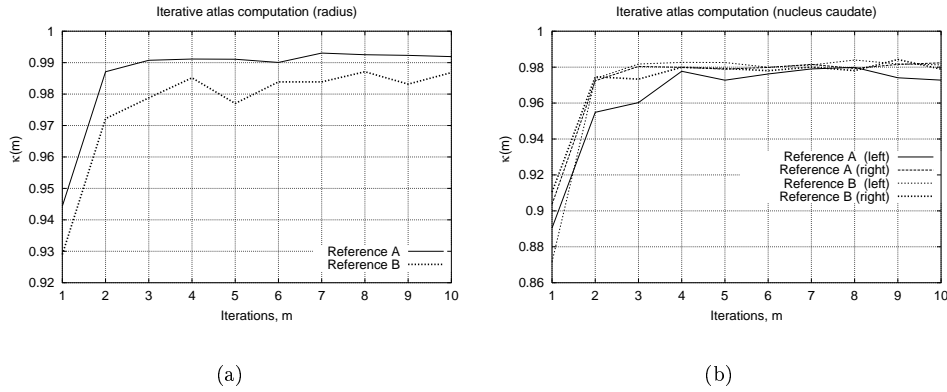


Figure 6.3. Convergence of the atlas construction algorithm. The κ statistic between two consecutive atlases as a function of the iteration number. Iteration zero corresponds to the reference (initial) shape used in the iterative algorithm. The $\kappa(m)$ statistic compares the agreement between the atlases A_m and A_{m-1} . Left and right plots correspond to the atlases of the radius and (left/right) caudate nucleus, respectively. Curves for different initial shapes (A and B) are shown.

Bias introduced by the initial shape

We have investigated whether the atlases generated with the two different initializations are comparable in shape, *i.e.* are similar up to a quasi-affine transformation. Figure 6.4, shows that for each individual shape two quasi-affine transformations can be found that map it to the two different atlases, A and B . Let us call these transformations \mathbf{T}_{A_i} and \mathbf{T}_{B_i} , respectively. Let \mathbf{T}_{AB} be the quasi-affine transformation that maps the atlas A into the atlas B . In this situation, the transformation $\mathbf{T}_i = \mathbf{T}_{B_i}^{-1} \mathbf{T}_{AB} \mathbf{T}_{A_i}$ should yield the identity transformation, \mathbf{T}_I . It is possible now to measure the average and the standard deviation of the difference $\mathbf{T}_i - \mathbf{T}_I$. The statistical analysis is carried out in a parametric domain (translation, rotation and scaling parameters) to quantify the differences between \mathbf{T}_i and \mathbf{T}_I .³ In this way, the bias and dispersion introduced by using two different initial shapes to build the atlas can be studied. The results of this analysis are shown in Table 6.1 for each atlas and each transformation parameter. This table indicates that the deviation from an identity transformation depends on the type of shape. For the very elongated and thin structure of the caudate nucleus the error standard deviations (SDs) are larger compared to the radius. As a consequence, the influence of the initial shape on the final atlas will depend on the shape itself. Translation and rotation error SDs are below 3.3 mm and 0.1° , respectively. Scaling error SDs are below 14.5%. From a practical point of view Table 6.1 indicates that the atlas does indeed depend on the initial shape and that the effect is has to do with the class of shapes being modeled. In the applications presented in this chapter, this effect is not critical. After performing a quasi-affine registration of the atlases generated with two different initializations, the average boundary-to-boundary distance between the two atlases was 1.3 mm and 0.6 mm for the radius and the two caudate nucleus atlases, respectively. These errors are on the order of, and slightly smaller than the voxel dimensions, respectively.

6.4.3 Automatically built statistical shape models

Figures 6.5 and 6.6 show the mean shape models and the first three modes of variation obtained from PCA for the radius and caudate nucleus test cases, respectively. The number of mesh nodes is 2500 for the radius, and 1000 for the caudate nucleus. In both cases there are no visible surface foldings in the mean shape or in the models for $\pm 3\sqrt{\lambda_i}$.

6.4.4 Reconstruction error

Figure 6.7 illustrates the relative shape variance explained with an increasing number of modes for different decimation ratios (number of model triangles). These curves are only marginally dependent on this factor. From ten modes onwards, the model captures more than 90% of the shape variance. Note the steeper slope of the curves corresponding to the caudate nucleus. Over the training set there is less apparent

³For more details on the computation of the transformation parameters from the matrix \mathbf{T}_i refer to Appendix 6.B.

Parameter	Units	Radius	Caudate (L)	Caudate (R)
t_x	[mm]	-0.72 (1.68)	+1.25 (3.28)	+0.62 (1.42)
t_y	[mm]	-1.20 (1.32)	-0.20 (0.71)	-0.14 (0.57)
t_z	[mm]	+0.64 (1.99)	-0.25 (0.54)	+0.06 (0.17)
r_x	[°]	+0.01 (0.02)	-0.01 (0.03)	+0.02 (0.03)
r_y	[°]	-0.01 (0.02)	-0.04 (0.09)	+0.10 (0.05)
r_z	[°]	-0.01 (0.02)	+0.01 (0.08)	-0.02 (0.06)
s_x	[%]	-0.57 (1.99)	+3.45 (14.51)	-5.60 (8.20)
s_y	[%]	-1.48 (1.78)	-2.12 (6.28)	-1.47 (3.92)
s_z	[%]	+1.57 (6.08)	-3.22 (7.23)	-1.98 (4.12)
Γ	[.]	0.992 (0.004)	0.992 (0.005)	0.992 (0.005)
d	[mm]	+1.59 (1.21)	+1.53 (0.98)	+0.87 (0.61)

Table 6.1. Error in each transformation parameter (translation, rotation and scaling) of the transformation \mathbf{T}_i with respect to the identity transformation. Point-to-point transformation error, d , provides information about the average distance between corresponding points before and after transformation. Finally, the parameter Γ provides a figure of merit of the validity of the anisotropic scaling model for the full transformation \mathbf{T}_i . See Appendix 6.B for further details.

variability in the shape of the caudate nucleus than in the shape of the radius. As a consequence, with fewer modes a larger amount of shape variation can be explained.

In order to assess the ability of these models to recover shapes not used in the training set we carried out the following experiment: reconstruction errors were computed by reconstructing the landmarks of one shape of the training set with the ASM built from the remaining shapes (leave-one-out experiment). The errors reported in Figure 6.8 are the average of the reconstruction errors over all shapes taking out one in turn. The same experiment was repeated for different decimation ratios and increasing numbers of modes of shape variation. The reconstruction errors were computed in millimeters. For the caudate nucleus, the reconstruction error is smaller than the voxel dimensions (10 modes). In the case of the radius, the reconstruction error is slightly larger than the slice thickness. One possible explanation to this slightly higher error could be the fact that no image resampling was used during registration. However, in comparison to the shape of the caudate nucleus, the radius represents a more complex structure with larger shape variability in the training set. This could explain the poorer reconstruction performance in the leave-one-out experiments of the radius. The plots of Figure 6.8 also indicate that the reconstruction error is slightly dependent on the decimation ratio and, as expected, decreases as a function of the number of modes of variation.

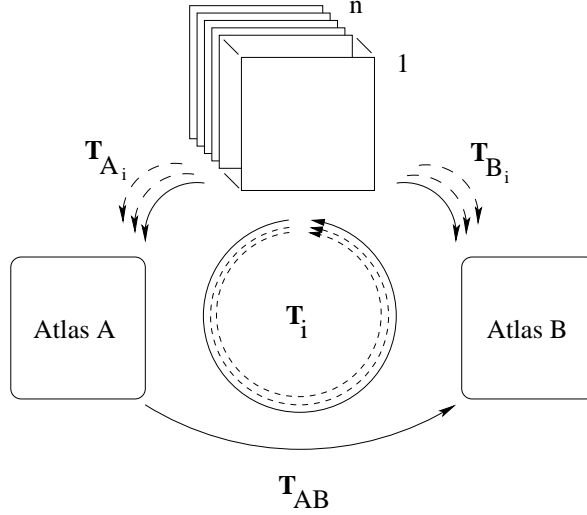


Figure 6.4. Bias introduced by the initial shape in the construction of the atlas. T_{AB} is the transformation between the two atlases, A and B. For each of the n shapes, T_{A_i} and T_{B_i} are the transformations to each atlas A and B, respectively. The similarity of the two atlases can be assessed by computing the deviation of transformation $T_i = T_{B_i}^{-1} T_{AB} T_{A_i}$ from the identity transformation.

6.5 Discussion and conclusion

This chapter has presented a method for the automatic construction of 3-D statistical shape models. The technique is based on the automatic extraction of a dense mesh of landmarks from an atlas constructed from a set of training shapes. The landmarks are subsequently propagated through an elastic deformation field to each shape of the training set. The method is able to treat single and multiple-part shapes.

The first part of the proposed technique involves the building of an atlas from a set of example shapes. In Section 6.4 we showed experimental results suggesting that this procedure is convergent. Moreover, different initial shapes seem to contribute only marginally to the shape of the final atlas. That is, the final atlases are similar up to a quasi-affine transformation. However, we note that the influence of the initial shape depends on the class of shapes being modeled and has to be assessed on a case-by-case basis. In the work by Fleute and Lavallée [100, 101] a similar algorithm was used to build the average model (atlas). However, no experimental evidence was reported with respect to the convergence of the atlas construction algorithm.

An alternative to our iterative method of atlas construction is the tree-based approach presented by Brett and Taylor [40]. This hierarchical strategy is attractive since it gives a unique (non-iterative) way to build an atlas from a given set of examples. However, one problem of Brett's method is that the training shapes have to be ranked according to a pairwise match quality. This requires that all possible pairs have to be matched and scored before the tree is built. Brett presented results

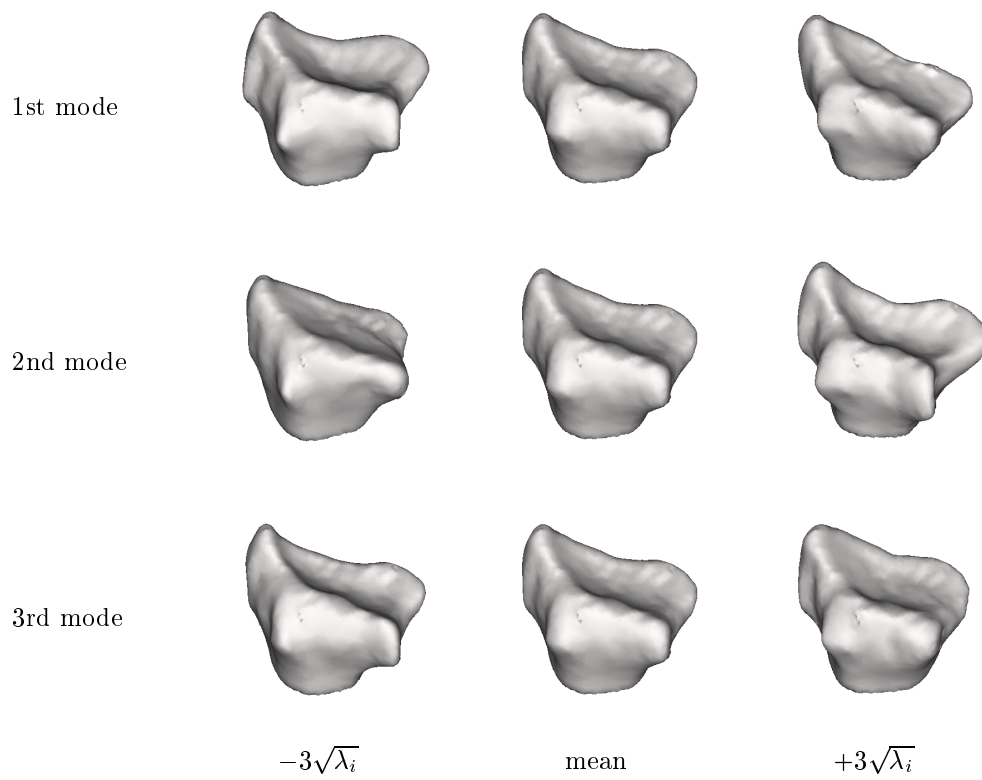


Figure 6.5. Surface renderings of shape instances generated using the 3-D model from 14 data sets of the radius. The instances are generated by varying a single shape parameter, fixing all others constant at zero standard deviations from the mean shape. Each instance of the triangulated model consists of 2500 nodes.

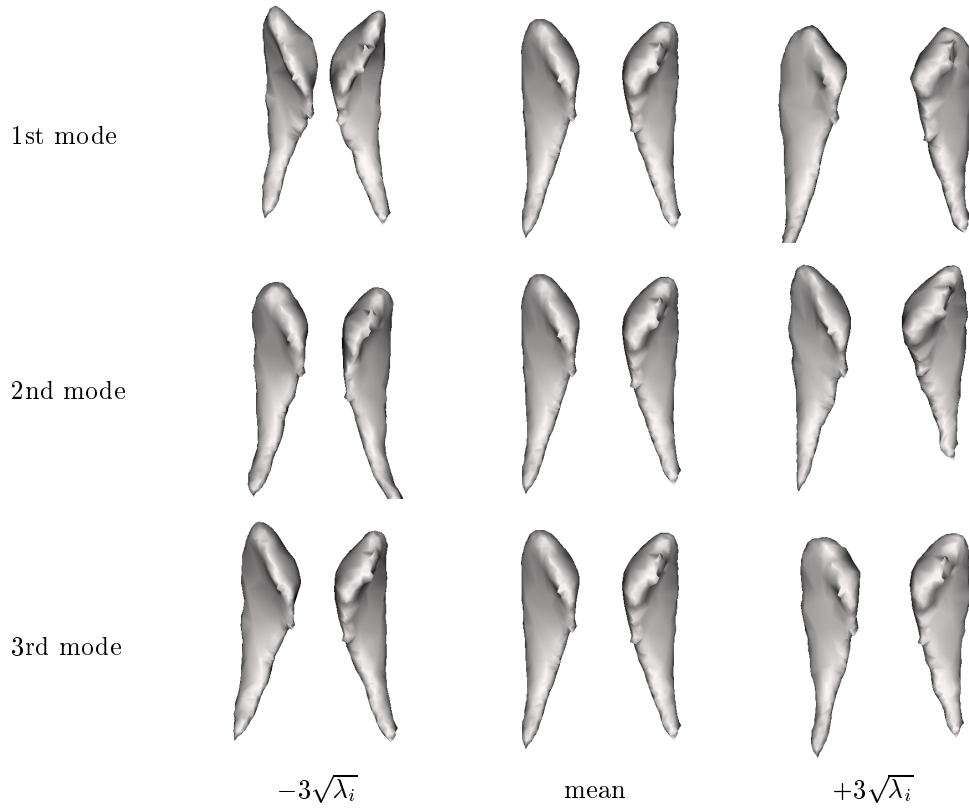


Figure 6.6. Surface renderings of shape instances generated using the 3-D model from 20 data sets of the caudate nucleus. The instances are generated by varying a single shape parameter, fixing all others constant at zero standard deviations from the mean shape. Each instance of the triangulated model consists of 1000 nodes.

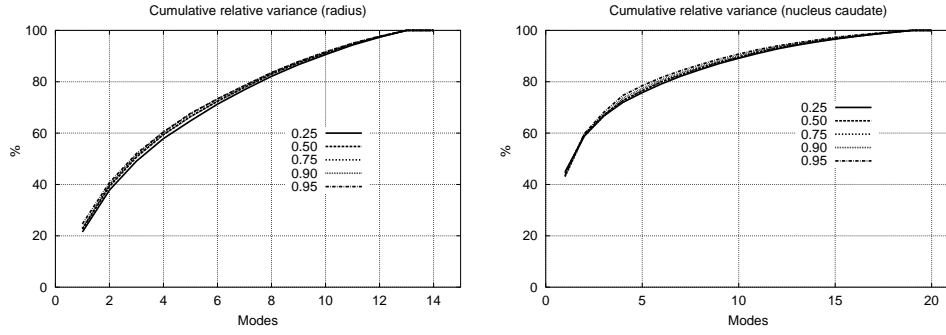


Figure 6.7. Percentage of total shape variance versus the number of modes used in the 3-D ASM. The curves are only marginally dependent on the number of nodes present in the model (decimation ratio). The number of landmarks before decimation was 15519 for the radius, and 2320 for the caudate nucleus. The decimation ratio represents the ratio between the nodes eliminated from the triangulation of the atlas and its initial number.

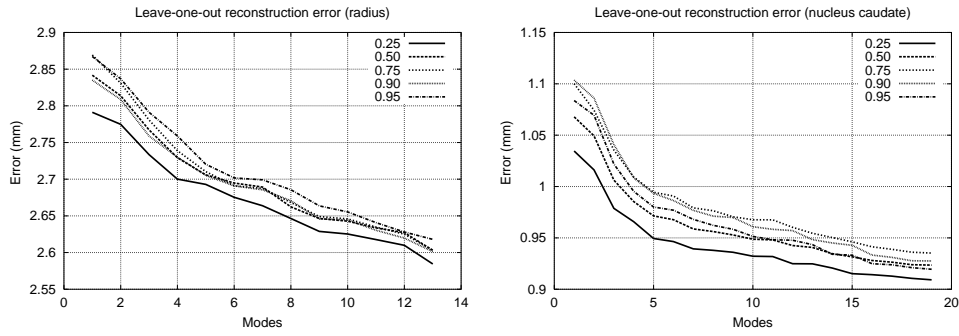


Figure 6.8. Reconstruction error in the leave-one-out experiments. The number of landmarks before decimation was 15519 for the radius, and 2320 for the caudate nucleus. The decimation ratio represents the ratio between the nodes eliminated from the triangulation of the atlas and the original number of modes.

with only eight shapes [40] but ordering the examples according to the matching quality would be cumbersome for a more realistic amount of training shapes. For a total number of n shapes it is necessary to compute $N = (n - 1)^2 \approx \mathcal{O}(n^2)$ pair-wise matches to build the average shape. Our approach obtains the average shape in $N = nI \approx \mathcal{O}(n)$ matches where I is the total number of iterations required for convergence. Section 6.4 shows experimental evidence that after about five iterations the atlas shape stabilizes.

Our method for building the mean shape model is based on averaging shapes in the domain of their distance transforms. A similar strategy was proposed by Leventon *et al.* [178] to incorporate statistical constraints into the level-set approach to image segmentation. However, in that work, PCA is applied on the distance transform domain and not on a surface representation. As a consequence, the number of degrees of freedom is considerably larger than in our method. There is an intrinsic limitation in both our method and that of Leventon *et al.* Averaging distance transforms of several shapes does not necessarily yield a valid mean shape representation. It is easy to show, for instance, that in case of a large misalignment between the averaged shapes, this procedure can introduce topological changes. Although we did not observe this problem in our experiments this can be a potential source of failure of the technique when building models of complex structures.

The proposed technique could be used with any elastic registration algorithm. In this sense, the method is a generic framework open to future research. Currently, the volumetric elastic registration of Rueckert *et al.* [255] is used to match binary images. The use of elastic registration as a method to establish shape correspondences imposes a constraint on the type of shapes that can be handled. It is assumed that the class of shapes has a well-defined topology. If there are sub-structures in one image not represented in the other image to be matched, the transformation would have to destroy those parts. This situation could arise when building a model of normal and abnormal medical structures where some parts in the latter are missing because of a diseased state or surgery. However, establishing correspondences in these mixed models also remains an ill-defined problem with any of the previously published approaches [39, 100, 101].

Results of the model construction for two different anatomical structures, the radius and the caudate nucleus, have been presented. Experiments were carried out to establish the ability of the models to generalize to shapes not present in the training set. The average reconstruction error was below 2.65 mm (radius) and 0.95 mm (caudate nucleus) when the number of nodes used was sufficient to explain 90% of the shape variability. These errors are on the order of, and slightly smaller than the voxel dimensions, respectively. In our experiments we have not observed problems of wrong correspondences leading to flipping of triangles or surface folding. This is an important improvement compared to the initial method of Brett and Taylor [40]. Also, our method is less restrictive in terms of the shapes that can be modeled. This is an important feature with respect to the improved method of Brett and Taylor [39] that is based on harmonic maps and therefore limited to shapes that are isomorphic to a disc.

6.A Appendix: Elastic registration with FFDs

This appendix summarizes the volumetric elastic registration algorithm that is used for landmark propagation. For a more detailed explanation of this technique the reader is referred to Rueckert *et al.* [255]. In this appendix we will refer interchangeably to images and shapes since we are concerned with shapes represented in the form of binary images.

Let $\mathbf{T} : (x, y, z) \mapsto (x', y', z')$ be a transformation that maps any point (x, y, z) in the reference image into the corresponding target image coordinates (x', y', z') . The reference image is also referred to as an *atlas* and defines the coordinate system in which all other images will be expressed. In order to accommodate for non-rigid deformations, \mathbf{T} will consist of a global transformation and an elastic transformation

$$\mathbf{T}(x, y, z) = \mathbf{T}_{global}(x, y, z) + \mathbf{T}_{elastic}(x, y, z) \quad (6.7)$$

6.A.1 Global transformation

The global transformation describes the pose and size of the target shape with respect to the atlas. This can be accomplished with a global transformation in the form of an affine transformation

$$\mathbf{T}_{global}(x, y, z) = \begin{pmatrix} \theta_{11} & \theta_{12} & \theta_{13} \\ \theta_{21} & \theta_{22} & \theta_{23} \\ \theta_{31} & \theta_{32} & \theta_{33} \end{pmatrix} \begin{pmatrix} x \\ y \\ z \end{pmatrix} + \begin{pmatrix} \theta_{14} \\ \theta_{24} \\ \theta_{34} \end{pmatrix} \quad (6.8)$$

where the coefficients Θ parameterize the twelve degrees of freedom of a generic affine transformation. For a quasi-affine transformation, only nine of these parameters are independent (translation, rotation and anisotropic scaling).

6.A.2 Local transformation

The global transformation captures only the pose and size of the shapes. If this transformation is not extended with an elastic deformation field, the PCA would include only nine modes of variation. Moreover, the landmarks would not be correctly propagated from the boundary of the atlas shape to the boundaries of the target shapes. Therefore, an additional local transformation is required. The local deformation field is represented by a free-form deformation (FFD) model based on B-splines. FFDs deform an object by embedding it into a volumetric mesh of control points. The control points are smoothly approximated by a set of B-spline basis functions that define a continuous deformation field.

To define a spline-based FFD, denote the domain of the image volume as $\Omega = \{(x, y, z) | 0 \leq x < X, 0 \leq y < Y, 0 \leq z < Z\}$. Let Φ denote an $n_x \times n_y \times n_z$ mesh of control points $\phi_{i,j,k}$ with uniform spacing δ . Then, the FFD can be written as the 3-D tensor product of the familiar 1-D cubic B-splines [173]

$$\mathbf{T}_{elastic}(x, y, z) = \sum_{l=0}^3 \sum_{m=0}^3 \sum_{n=0}^3 B_l(u) B_m(v) B_n(w) \phi_{i+l, j+m, k+n} \quad (6.9)$$

where $i = \lfloor \frac{x}{n_x} \rfloor - 1$, $j = \lfloor \frac{y}{n_y} \rfloor - 1$, $k = \lfloor \frac{z}{n_z} \rfloor - 1$, $u = \frac{x}{n_x} - \lfloor \frac{x}{n_x} \rfloor$, $v = \frac{y}{n_y} - \lfloor \frac{y}{n_y} \rfloor$, $w = \frac{z}{n_z} - \lfloor \frac{z}{n_z} \rfloor$, and where B_l represents the l -th basis function of the B-spline

$$B_0(u) = (1 - u)^3/6 \quad (6.10)$$

$$B_1(u) = (3u^3 - 6u^2 + 4)/6 \quad (6.11)$$

$$B_2(u) = (-3u^3 + 3u^2 + 3u + 1)/6 \quad (6.12)$$

$$B_3(u) = u^3/6 \quad (6.13)$$

The control points Φ act as parameters of the B-spline FFD, and the degree of local deformation which can be modeled depends on the resolution of the mesh of control points Φ . The smaller the spacing δ the more locally flexible the deformation is allowed to be. The computational complexity of the algorithm is inversely proportional to the spacing parameter. The trade-off between deformation flexibility and computational complexity is mainly an empirical choice which is determined by the accuracy required to deform the atlas into the individual shapes as well as by practical computational issues.

6.A.3 Speed-up of the elastic registration

An implementational detail that can considerably reduce the computational burden is the use of *padding of control points*. Landmark propagation is mainly occurring at the boundaries of the shapes. There is no need to add control points in the middle of or far away from a shape. This observation can be used to freeze all control points of the undeformed mesh that are further than a distance Δ from the atlas boundary (Figure 6.9).

Here it is important to realize that $\delta \ll \Delta$ in order to have enough control points in the region of interest. Moreover, the width of the non-padded area, Δ , should be large enough to accommodate for the maximum displacement needed to elastically register two shapes.

6.A.4 Registration measure

Several voxel-based measures can be used to align two images. In our case, the images are binary. We have experimented with three different measures: sum of squares, correlation and normalized mutual information. After some initial experiments it was observed that the latter yields the best results. Mutual information (MI) is a concept from information theory and expresses the amount of information that one image A contains about a second image B. This similarity measure was independently introduced into medical image registration by Collignon [55] and Viola [305] and is defined as

$$\mathcal{C}_{MI}(A, B) = H(A) + H(B) - H(A, B) \quad (6.14)$$

where $H(A)$ and $H(B)$ are the marginal entropies of A and B , and $H(A, B)$ denotes their joint entropy, which are calculated from the joint histogram of A and

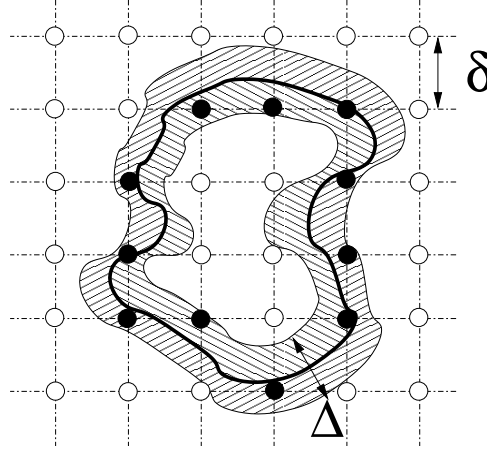


Figure 6.9. Registration speed-up via padding. The bold line represents the boundaries of the atlas for a given cross-section. The shaded regions correspond to the bounds of the non-padded region, a band of width Δ . All filled circles represent active control points located outside the padded area. Empty circles stand for the inactive control points that fall inside the padded area.

B. If both images are fully aligned the mutual information is maximized. It has been shown by Studholme [285] that mutual information itself is not independent of the overlap between two images. To avoid any dependency on the amount of image overlap, Studholme suggested the use of normalized mutual information (NMI) as a measure of image alignment

$$\mathcal{C}_{NMI}(A, B) = \frac{H(A) + H(B)}{H(A, B)} \quad (6.15)$$

This is the similarity measure that we have used in the experiments of this chapter.

6.A.5 Optimization

In order to find the optimal transformation we minimize a cost function associated with the global transformation parameters, Θ , as well as the local transformation parameters, Φ . The cost function consists of two competing goals. The first term represents the cost associated with the image similarity measure of Equation (6.15) while the second term is associated with the smoothness of the transformation

$$\begin{aligned} \mathcal{C}_{smooth} = \frac{1}{V} \iiint & \left(\frac{\partial^2 \mathbf{T}}{\partial x^2} \right)^2 + \left(\frac{\partial^2 \mathbf{T}}{\partial y^2} \right)^2 + \left(\frac{\partial^2 \mathbf{T}}{\partial z^2} \right)^2 + \\ & 2 \left(\frac{\partial^2 \mathbf{T}}{\partial x \partial z} \right)^2 + 2 \left(\frac{\partial^2 \mathbf{T}}{\partial y \partial z} \right)^2 + 2 \left(\frac{\partial^2 \mathbf{T}}{\partial x \partial y} \right)^2 dx dy dz \quad (6.16) \end{aligned}$$

where V denotes the volume of the image domain.

With these definitions, the total cost function that has to be optimized is given by

$$\mathcal{C}(\Theta, \Phi) = -\mathcal{C}_{\text{similarity}}(I, \mathbf{T}(I)) + \lambda \mathcal{C}_{\text{smooth}} \quad (6.17)$$

where λ is the weighting parameter which defines the trade-off between alignment of the two image volumes and the smoothness of the transformation. In the experiments reported in this chapter we have set $\lambda = 0$. This implies that we rely on the intrinsic smoothness of the B-spline deformation fields which has proven sufficient for our application.

6.B Appendix: On the statistical analysis of spatial transformation parameters

In Section 6.4.2 we carried out a statistical analysis of the composition of the three quasi-affine transformations, $\mathbf{T}_i = \mathbf{T}_{Bi}^{-1} \mathbf{T}_{AB} \mathbf{T}_{Ai}$, that ideally should yield the identity transformation. The statistical analysis was carried out in a parametric domain (translation, rotation and scaling parameters) to gain some insight about the sensitivity of the atlas construction algorithm with respect to different initializations. Since the atlas construction procedure involves the computation of the parameters of a quasi-affine transformation (translation, rotation and scaling), it is natural to report the statistical analysis on the basis of the same parameters.

However, a careful look at this problem reveals a fundamental difficulty. Composition is not a closed operation in the set of quasi-affine transformations. Consider two transformations $\mathbf{H}_0 = \langle \mathbf{R}_0 \mathbf{S}_0, \mathbf{T}_0 \rangle$ and $\mathbf{H}_1 = \langle \mathbf{R}_1 \mathbf{S}_1, \mathbf{T}_1 \rangle$, where \mathbf{S}_0 and \mathbf{S}_1 are diagonal scaling matrices, \mathbf{R}_0 and \mathbf{R}_1 are pure rotation matrices, and \mathbf{T}_0 and \mathbf{T}_1 are translation vectors. The composition $\mathbf{H}_3 = \mathbf{H}_1 \mathbf{H}_0 = \langle \mathbf{R}_1 \mathbf{S}_1 \mathbf{R}_0 \mathbf{S}_0, \mathbf{R}_1 \mathbf{S}_1 \mathbf{T}_0 + \mathbf{T}_1 \rangle$ yields, in general, a fully affine transformation.⁴

If the representation of the transformation is carried using homogeneous (4×4) matrices, the extraction of the translation parameters, \mathbf{t}_i , of \mathbf{T}_i is straightforward (upper right 3×1 vector).

In order to extract the orientation and scaling from \mathbf{T}_i , the upper left 3×3 matrix, \mathbf{M}_i , has to be factorized using *polar decomposition* [119]. This produces a factorization $\mathbf{M}_i = \mathbf{R}_i \mathbf{A}_i$ where \mathbf{R}_i is orthogonal and \mathbf{A}_i is positive definite. \mathbf{R}_i represents the rotation and \mathbf{A}_i represents the scaling, but in the coordinate system defined by the eigenvectors of \mathbf{A}_i . The eigenvalues are the scaling factors. In addition, \mathbf{A}_i can be further factorized as $\mathbf{A}_i = \mathbf{O}_i \mathbf{D}_i \mathbf{O}_i^T$ where \mathbf{O}_i is a rotation matrix whose columns are the eigenvectors of \mathbf{A}_i and where \mathbf{D}_i is a diagonal matrix whose diagonal entries are the eigenvalues of \mathbf{A}_i . The matrices $\mathbf{R}_i \mathbf{O}_i$, \mathbf{D}_i and \mathbf{O}_i^T are readily computable from \mathbf{M}_i using *singular value decomposition* [241]. Assuming that a point \mathbf{x} is transformed

⁴Unfortunately, it is in general not possible to invert the rotation and scaling operators $\mathbf{R}_0' \mathbf{S}_1' = \mathbf{S}_1 \mathbf{R}_0$. If that were possible, \mathbf{H}_3 could be written as a quasi-affine transformation $\mathbf{H}_3 = \langle \mathbf{R}_3 \mathbf{S}_3, \mathbf{T}_3 \rangle = \langle (\mathbf{R}_1 \mathbf{R}_0') (\mathbf{S}_1' \mathbf{S}_0), \mathbf{R}_1 \mathbf{S}_1 \mathbf{T}_0 + \mathbf{T}_1 \rangle$. The latter is only valid when isotropic scalings $\mathbf{S} = s \mathbf{I}$ are involved.

to $\mathbf{x}' = \mathbf{M}_i \mathbf{x} + \mathbf{t}_i$, the effective rotation matrix is \mathbf{R}_i . Any suitable rotation parameterization can be used to perform the statistical analysis. We have opted for the Euler angles with respect to the axes of the coordinate system of \mathbf{x} (XYZ permutation of axes).

Finally, a scaling parameterization is required. Strictly speaking one should consider nine parameters (anisotropic scaling *and* shearing coefficients) since in general \mathbf{A}_i is not diagonal. Unfortunately, the statistical analysis cannot be performed on the parameters extracted from the diagonal matrix \mathbf{D}_i since the scaling axes are different for each i (eigenvectors of \mathbf{A}_i). In order to approximately quantify the scaling variability along the axes of the coordinate system in which \mathbf{x} is expressed, let us assume that the matrix \mathbf{A}_i is quasi-diagonal (off-diagonal entries approximately zero). Under this assumption, the shearing is minimal and the scaling factors can be extracted directly from the diagonal of \mathbf{A}_i .

To quantify the quasi-diagonality assumption, we have defined the following quantity whose mean and standard deviation are reported in Table 6.1

$$\Gamma_i = \frac{\sum_{j=1}^3 |a_{jj}^i|}{\sum_{j=1}^3 \sum_{k=1}^3 |a_{jk}^i|} \quad (6.18)$$

where a_{jk}^i are the entries of the matrix \mathbf{A}_i . When no shears are involved, this measure will approach unity.

Finally, as an extra measure of overall consistency, we have computed the mean distance d_i between \mathbf{x}_r and $\mathbf{M}_i \mathbf{x}_r + \mathbf{t}_i$ for all the voxels with world coordinates \mathbf{x}_r in the i -th training shape. Table 6.1 reports the average distance over the training set, d and its standard deviation.

Be not afraid of going slowly, be afraid only of standing still.

— Chinese proverb

Chapter 7

Automatic construction of multiple-object 3-D statistical shape models: Application to cardiac modeling

Abstract — In this chapter we address the problem of building a three-dimensional statistical shape model of the left and right ventricle of the heart from 3-D Magnetic Resonance (MR) images. To this end, a method to construct a statistical shape model using an automatic landmarking procedure has been extended to cope with multiple-part structures with large shape variation. This was accomplished by using a multi-level B-spline free-form registration algorithm and a novel similarity measure to warp label images. Results on a model constructed from 14 cardiac data sets demonstrate the robustness of the method in the presence of large shape variability and multiple objects.

Adapted from: A.F. Frangi, D. Rueckert, J.A. Schnabel, and W.J. Niessen (2001). *Automatic construction of multiple-object three-dimensional statistical shape models: Application to Cardiac Modeling*. Submitted.

7.1 Introduction

Model-based analysis of cardiac images is an active area of research. In Chapter 5, we surveyed the literature on three-dimensional model-based techniques for functional analysis of cardiac images [105]. Model-based approaches have been used for several applications ranging from computation of global cardiac functional parameters, mainly ejection fraction and left ventricular mass [19, 49, 193, 196, 215, 219, 281], to local estimation of cardiac motion [27, 69, 145, 232, 272] and stress [210, 211, 217, 229, 324]. Some authors have applied cardiac models to cardiac scan planning [176] or to derive new descriptors of cardiac function [15, 52, 107, 108, 206, 213, 232, 233]. A common denominator of these methods is that shape description is performed using standard modeling primitives like, for instance, superquadrics [19, 47, 232, 233], series expansions [47, 123, 193], constructive solid geometry [176] or polyhedral representations [108, 120, 145, 209, 281]. Shape con-

straints are either explicitly enforced by the selected primitive (*e.g.* superquadrics) or via *ad hoc* regularization terms in the shape recovery process.

In this chapter we elaborate on the construction of a three-dimensional statistical shape model of the cardiac chambers. Although shape representation is based on standard triangulated meshes, the model contains information of the average location of each node in the mesh, its variability, and the correlation between node locations inferred from a set of training shapes. This information can be used to regularize the problem of model recovery or image segmentation without the need of any *ad hoc* smoothing constraints. This chapter focuses on the automatic construction of statistical shape models and does not address the problem of shape recovery or segmentation, which is a separate research issue.

In order to build a statistical cardiac model, the framework of active shape models (ASM) [57,58] can be utilized. However, prior to applying the methodology of ASMs in 3-D, the problem of extracting landmarks has to be tackled. In Chapter 6 we introduced a method to approach this problem which was suitable for shapes with moderate shape variation. Owing to the large inter-subject variability of cardiac shapes, this method is unsuited for cardiac modeling. This chapter describes two improvements on the framework of the previous chapter that allow the construction of statistical models to describe the shape of multiple-part structures with larger shape variability. The first extension is the use of a hierarchical elastic registration technique [255,262] based on multi-level B-spline free-form deformations (FFDs). The second extension is a novel similarity measure useful for *label images*, *i.e.* images where each voxel is labeled according to the tissue type. With these extensions, a statistical model of the left and right ventricle of the heart was constructed from 14 manually segmented cardiac MR data sets.

This chapter is organized as follows. In Section 7.2, our proposed method for automatic landmarking is described. In Section 7.3, the method is applied to construct statistical models of the left and right ventricle of the heart from 3-D MRI; empirical evidence is given on convergence properties and reconstruction errors. Finally, Section 7.4 closes the chapter with some conclusions and directions for future research.

7.2 Methods

7.2.1 Overview

Ideally, a landmark is a point of correspondence that can be uniquely identified in a set of shapes. Anatomical landmarks fall into this category but, unfortunately, they are usually too sparse to describe a 3-D shape accurately. Therefore, we will consider pseudo-landmarks, *i.e.* a set of densely distributed landmarks lying on the shape's surface which describe its geometry adequately.

In our framework, automatic landmarking is carried out by mapping the landmarks of an atlas that is representative for a set of training shapes. Assume that n segmented shapes are available which constitute the training set, $\mathcal{S}_n = \{L_i\}$ where $i = 1 \cdots n$. Each shape in the training set is represented by a *label image*; in this

image, each voxel value belongs to a label set \mathcal{L} . To generate the landmarks for the n shapes, a shape atlas A can be constructed, landmarked, and these landmarks can be propagated back to the n shapes (Figures 7.1 and 7.2). The following sections describe these steps in detail.

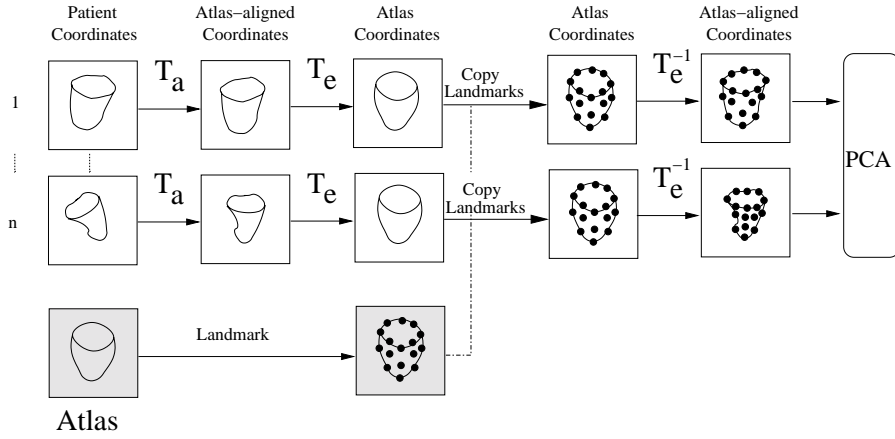


Figure 7.1. Overview of the automatic landmarking framework. All individual data sets are matched to an atlas via an affine transformation (T_a) and an elastic transformation (T_e). The landmarks in the atlas can then be copied to the individual patients. The elastic deformation is subsequently reversed. Thus, Principal Component Analysis (PCA) is carried out in a space where all shapes are aligned with the atlas (atlas-aligned coordinates). The principal modes of variation will therefore account for elastic deformations and not for pose or size changes.

7.2.2 Preprocessing

The automatic landmarking algorithm can be applied to a set of segmented structures. In our application, three main structures of the heart have been segmented from a number of volunteer scans. Each segmentation consists of manual identification of the background (BG), the left ventricular blood pool (LV_{bp}) and myocardium (LV_{myo}), and of the right ventricular blood pool (RV_{bp}) (see Figure 7.3). In the segmentation of the left ventricle, the papillary muscles are considered part of the blood pool as is customary in functional cardiac analysis. Each segmentation is represented as a label image, where each voxel is labeled according to the tissue type to which it belongs ($\mathcal{L} = \{BG, LV_{bp}, LV_{myo}, RV_{bp}\}$).

Owing to the large voxel anisotropy, in MR short-axis acquisitions of functional cardiac data sets, segmentations have significant staircase artifacts in the direction of the long axis of the heart. In order to facilitate image registration and to smooth out those artifacts, shape-based interpolation [135, 249] has been applied to obtain label images of isotropic voxel size without slice gaps.

- **Pre-processing:**
 - Manual segmentation.
 - Shape-based interpolation to cubic voxels.
- **Autolandmarking:**
 - *Input:*
 - $S_n = \{L_i\}$, training set of label images.
 - *Algorithm:*
 1. Build atlas, A , from training set S_n .
 2. Extract landmarks from atlas, A .
 3. Compute the elastic deformations, $\mathcal{D}_n = \{\mathbf{T}_e^i\}$, from each shape in S_n to the atlas A .
 4. Propagate the landmarks from A to each shape in S_n using the inverse of the deformation fields \mathcal{D}_n to produce the set of landmarks $\ell_n = \{l_i\}$.
 - *Output:*
 - A , labeled atlas.
 - $\ell_n = \{l_i\}$, landmarks for each shape in S_n .
- **Post-processing:**
 - Principal Component Analysis (PCA) on the set of landmarks $\ell_n = \{l_i\}$.

Figure 7.2. Algorithmic overview of statistical shape model construction using automatic landmarking.

7.2.3 Atlas construction

Given a set of label images which are instances of an anatomical structure, a shape atlas can be viewed as an average label image representation of the shape under consideration. In the next subsection a method to obtain an atlas for binary images is introduced, which will be subsequently extended to label images containing multiple, and possibly nested, structures.

Atlas construction in single object shapes

Let us assume that a set of n training shapes, S_n , is available and that each shape is represented by a binary image, B_i . That is, the label set contains only two labels corresponding to the object and background segmentations. For the sake of simplicity, we assume that S'_n is the set of shapes S_n after they have been aligned to a reference coordinate system.

Let B'_i and $\mathcal{DT}(B'_i)$ denote the shape in atlas-aligned coordinates and its signed Euclidean distance transform [64] respectively. The signed distance transform of an average shape, B_{av} , can be obtained by computing $\mathcal{DT}(B_{av}) = \frac{1}{n} \sum_{i=1}^n \mathcal{DT}(B'_i)$. A binary representation of the average shape can be retrieved by thresholding the distance transform map to its zero-level set. We coin this averaging procedure *shape-based blending*.

As was mentioned earlier, prior to shape-based blending all shapes have to be

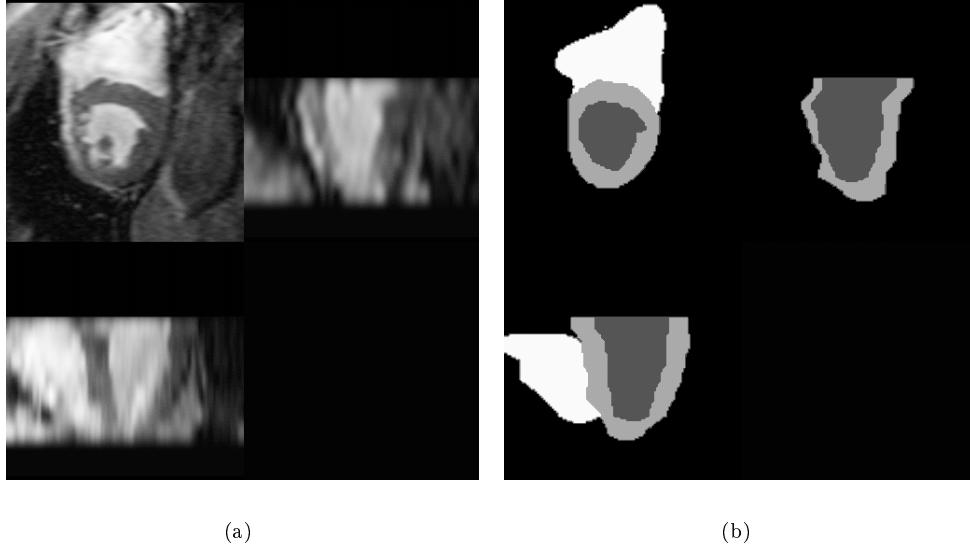


Figure 7.3. Example MR image and manual segmentation from the training set (three orthogonal views). The label images (Figure 7.3(b)) were manually extracted from three dimensional cardiac MR scans (Figure 7.3(a)) and subsequently interpolated using shape-based methods. In each slice the left ventricular blood pool (dark grey), the left ventricular myocardium (light grey), and the right ventricular blood pool (white) were manually outlined. The papillary muscles were included in the segmentation of the blood pool as is customary in clinical practice. The label image shown in Figure 7.3(b) has been resampled using shape-based interpolation. See the text for further details.

aligned into an atlas-aligned coordinate system. As the atlas is yet to be constructed, the initial coordinate system can be chosen arbitrarily to coincide with that of any of the shapes in the training set \mathcal{S}_n . In order to reduce the bias introduced by the selection of the initial reference shape, an iterative algorithm has been developed. In the first iteration, one shape of the training set is randomly selected to be the atlas. Subsequently, all other shapes in the set are registered to the current atlas using a *quasi-affine* transformation (rigid transformation plus anisotropic scaling, but no shearing). This registration is accomplished with a modified version of the method by Studholme *et al.* [284]. After registration, all shapes are blended and a new atlas is generated. This new atlas then becomes the current atlas and the process is iterated until the difference between the current and the new atlas falls below a certain threshold. This can be monitored, for instance, by defining a suitable measure of label agreement between two images. In the results section we shall investigate the convergence properties of this algorithm and the influence of the randomly selected initial reference.

Atlas construction in multiple-part shapes

Let us assume that a set of n training shapes, \mathcal{S}_n , is available and that each shape is represented by a label image, L_i , in which l objects are represented by distinctive labels.

The atlas construction algorithm of the previous subsection applies to binary images for which the distance transform is defined. However, it is possible to generalize the method to multiple-part shapes, which is needed for cardiac modeling. In fact, to extend the method of the previous subsection we only need to specify a method for shape-based blending of multi-valued images. The atlas alignment procedure used in this work readily extends from single-object to multiple-object label images. In the following, we discuss our method for shape-based blending in cardiac label images.

Figure 7.4 schematically represents a typical arrangement of LV_{bp} , LV_{myo} and RV_{bp} as extracted manually from cardiac MR images. This figure also indicates how the cardiac shape can be decomposed into three sub-shapes: the LV_{bp} , the $LV_{bp} \cup LV_{myo}$ and the RV_{bp} . By construction the $LV_{bp} \cup LV_{myo}$ always embeds the LV_{bp} , and both of them are non-overlapping structures with respect to the RV_{bp} . Each one of these sub-shapes can now be represented as a binary image. This casts the problem of shape-based blending of a label image into l problems of shape-based blending of binary images. After the l average sub-shapes have been generated, all of them are combined into a new label image by taking the initial arrangement and labeling into account. An example of shape-based blending with two shapes consisting of three objects is shown in Figure 7.5.

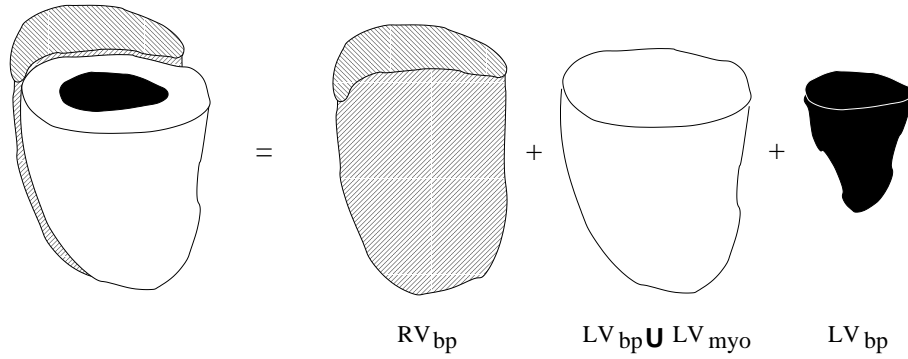


Figure 7.4. Two-chamber model decomposition. In order to apply the shape-based blending, the heart is decomposed into three binary shapes representing, from left to right, the right ventricular blood pool (RV_{bp}), the left ventricular interior ($LV_{bp} \cup LV_{myo}$) and the left ventricular blood-pool (LV_{bp}), respectively.

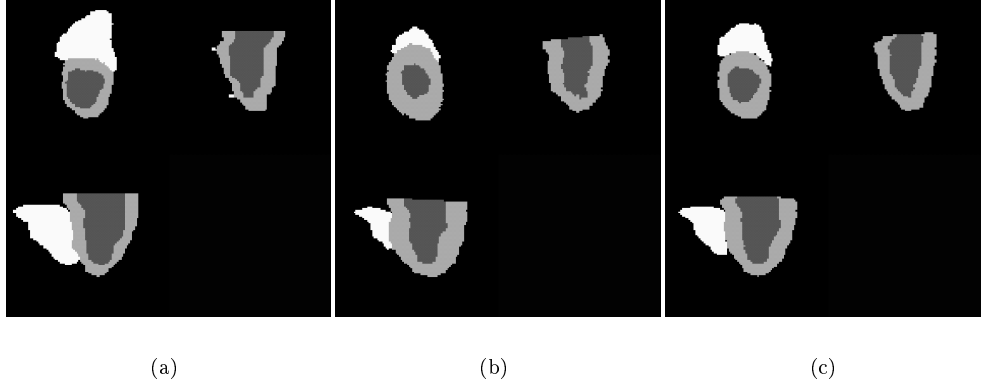


Figure 7.5. Shape-based blending of label images. Figure 7.5(c) illustrates the blending result of the two shapes of Figure 7.5(a) and 7.5(b). All figures contain three equivalent orthogonal views.

7.2.4 Landmark extraction

After an atlas has been constructed, it needs to be landmarked. For cardiac modeling, landmarks for the endocardial and epicardial wall of the left ventricle, and for the endocardial wall of the right ventricle can be extracted. In order to landmark the atlas automatically, the *marching cubes* [183] algorithm was applied. This algorithm generates a dense triangulation of the boundary iso-surfaces that can be further decimated to reduce the amount of triangle nodes. The decimation process can be implemented in such a way that it preserves the accuracy of the surface representation to a desired tolerance [264]. The nodes in the decimated triangulation form the landmarks of the shape. By using marching cubes, a dense and approximately even distribution of landmarks is obtained. Alternatively, any other automatic algorithm for mesh extraction from a binary (label) image can be applied like, for instance, *surface nets* [118] or the *wrapper algorithm* [126]. Note that, as an alternative to these algorithms, an expert could manually localize anatomical landmarks in the atlas. Anatomical landmarks, however, may be too sparse to accurately represent the shape of three-dimensional structures.

7.2.5 Landmark propagation

Subject-to-atlas elastic registration

Once the atlas is constructed and landmarked, its landmarks can be propagated to the individual shapes. This is carried out by warping each sample labeled volume into the atlas with a transformation, $\mathbf{T} = \mathbf{T}_a + \mathbf{T}_e$, that is composed of a quasi-affine (\mathbf{T}_a) and an elastic (\mathbf{T}_e) transformation. The transformation \mathbf{T}_a accounts for overall pose and size differences between the atlas and each sample volume while the transformation \mathbf{T}_e accounts for local shape differences. In the previous chapter, this transformation

was recovered with a free-form elastic registration algorithm. The deformation field was represented with a single-resolution mesh of control points that are interpolated to a continuous field using B-spline basis functions. Pilot experiments revealed that this class of transformations is either too coarse (for coarse mesh resolution) or prone to folding (too fine mesh resolution) to recover the large shape variability present in cardiac shapes.

In order to cope with large shape variations, a multi-level extension [262] of the free-form registration algorithm proposed by Rueckert *et al.* [255] (cf. also Appendix 6.A)) was applied. In this approach, the elastic transformation is decomposed into a hierarchy of FFDs with increasing mesh resolution, $\mathbf{T}_e = \sum_h \mathbf{T}_e^h$. Gross shape warping takes place at the coarsest resolution levels while finer levels take care of more local deformations. Appendix 7.A describes this algorithm in more detail. In the previous chapter binary images were registered with normalized mutual information. In this chapter, the need of registering label images led us to define a novel registration measure that has proven to be more suited. The next subsection elaborates on this issue.

Similarity measure for label image registration

Several measures can be used to recover the transformation \mathbf{T} . In the experiments of the previous chapter we noticed that normalized mutual information [285] had a superior performance over cross-correlation and sum of square differences for the registration of binary images. However, in dealing with label images, we observed that maximization of normalized mutual information can map more than one label in the reference image into a single label in the target image. This was particularly problematic when recovering the elastic transformation.

When applied as a registration function, mutual information tends to maximize the overlap of structures across two images. A particular characteristic of registration algorithms based on mutual information is the fact that structures which are delineated by intensity i in the first image may be mapped to structures which are delineated by intensity j in the second image. It is this characteristic which allows the successful application of mutual information for the registration of images acquired from different imaging modalities. However, for the registration of label images this can lead to misregistrations as structures denoted by label i in the first image may be matched to structures denoted by a different label j in the second image without any consequences for the mutual information of the two images.

Since the correspondences of structures across both images are encoded explicitly in the labeling, we are only interested in maximizing the overlap of structures denoted by the same label in both images. Therefore we have used a registration measure that favors the mapping of identical labels. We have coined this measure *label consistency*. If $P_{AB}(i, j)$ is the joint probability of labels i and j in the reference (A) and target (B) shapes, respectively, the label consistency measure is defined as

$$\mathcal{C}_{LC}(A, B) = \frac{\sum_{i=1}^l P_{AB}(i, i)}{\sum_{i=1}^l \sum_{j=1}^l P_{AB}(i, j)} \quad (7.1)$$

Label consistency is a measure of how many labels of all the labels in the reference shape are correctly mapped into the target shape. When the label consistency measure is zero, none of the reference labels has been correctly mapped into the target shape. If all reference labels are correctly mapped, the label consistency measure yields one.

Landmarking sample shapes

Once the global transformation \mathbf{T} has been found, the landmarks of the atlas can be propagated to the atlas-aligned coordinate system by applying the inverse of the elastic transformation (\mathbf{T}_e^{-1}). This process is repeated for each sample shape. As a result, a set of landmarks is obtained that describes shape variations with respect to the atlas. Since these landmarks are now in atlas-aligned coordinates, pose and size variations are explicitly eliminated from further analysis. These transformed landmarks are subsequently used as the input for Principal Component Analysis (PCA) as indicated in Figure 7.1.

7.3 Results

7.3.1 Data sets and pre-processing

Fourteen adult subjects, free of clinical cardiovascular disease, were scanned on a 1.5 Tesla MR scanner (Philips ACS-NT, PowerTrak 6000 Gradient System, Philips Medical Systems, Best, The Netherlands) using an ECG-triggered Echo Planar Imaging (FFE-EPI) sequence. Cine acquisitions consisting of eight to ten short-axis slices of the heart in eighteen to twenty phases of the cardiac cycle were performed. The most important scan parameters were: repetition time, $TR = 632\text{--}857$ ms; echo time, $TE = 8.9\text{--}9.1$ ms; flip angle, $\alpha = 20^\circ$; slice thickness, 10 mm; slice gap, 0 mm; a 256×256 image matrix, and a $300 \times 300\text{-mm}^2$ field-of-view.

From the acquired temporal sequence of each volunteer, the end diastolic frame was manually segmented as indicated in Section 7.2.2. Subsequently, all segmentations were resampled to isotropic voxels with size equal to the in-plane resolution (1.17 mm) using shape-based interpolation [135, 249].

7.3.2 Comparison of label images

In order to monitor the convergence of the atlas building procedure, a measure to compare two label images is required. For a given voxel, each image can be considered as an observer that provides a class label. Therefore, comparing label images is equivalent to comparing the agreement between two observers. The κ statistic [1] is a statistical measure designed to perform such a comparison

$$\kappa = \frac{p_a - p_c}{1 - p_c} \quad (7.2)$$

where

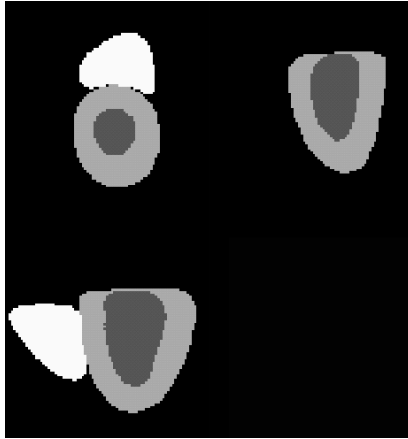
$$p_a = \sum_{i=1}^l P_{AB}(i, i) \quad (7.3)$$

$$p_c = \sum_{i=1}^l P_A(i)P_B(i) \quad (7.4)$$

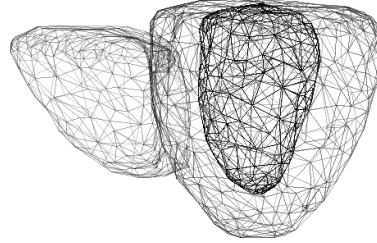
and $P_{AB}(i, j)$, $P_A(i)$, and $P_B(j)$ are the joint probability density and marginal probability densities for the labels in the images A and B . The κ statistic is a measure of agreement between two classifications, p_a , that is corrected for chance agreement p_c [1]. In order to interpret the values of the κ statistic one can refer to standard tables provided in literature [1]. A value below 0.2 indicates poor agreement while values between 0.2 and 1.0 range from fair to perfect agreement.

7.3.3 Atlas construction

Figure 7.6 shows the result of the atlas building process described in Section 7.2.3. The atlas is smooth and the wall thickness is approximately constant everywhere. This result suggests that the shape-based blending procedure captures the global shape of the ventricles without biasing the wall thickness in any particular sector.



(a)



(b)

Figure 7.6. Atlas construction and landmarking. Figures 7.6(a) and 7.6(b) show the result of the iterative atlas construction algorithm as three orthogonal views and as a wire-frame rendering with nodes representing the landmarks. The landmarks have been extracted using marching cubes with subsequent mesh decimation (95% decimation factor).

The convergence of the iterative atlas construction and the effects of different

initial shapes in the generation of the atlas have also been studied. Figure 7.7 plots the κ statistic between two successive iterations of the algorithm of Section 7.2.3. The same curves are plotted for two different initial shapes (A and B). After five iterations the agreement is excellent ($\kappa > 0.94$) and the differences between the atlases of two consecutive iterations are marginal. From these plots one can conclude that most of the changes in the shape of the atlas occur in the first few iterations.

In order to compare the atlas generated with two different initial shapes, we have considered the atlases of the fifth iteration. Since the initial shapes have a different orientation and size, we would like to verify that the atlases generated with different initializations differ by a quasi-affine transformation without intrinsically differing in shape. Accordingly, we have quasi-affinely registered the two atlases and compared their difference after registration. Marching cubes was used to extract iso-surfaces of both atlases prior to registration and the surfaces extracted from the reference image were transformed according to the computed quasi-affine transformation. After transforming the reference surfaces to target coordinates, the average surface-to-surface distance between the two atlases was 0.67 mm, and they were visually indistinguishable. This distance has to be compared to the voxel size which is $1.2 \times 1.2 \times 10 \text{ mm}^3$.

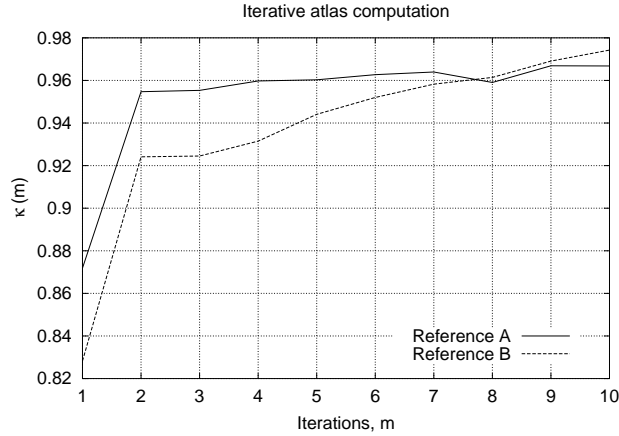


Figure 7.7. Convergence of the atlas construction algorithm. The κ statistic between two consecutive atlases is a function of the iteration number. Iteration zero corresponds to the initial shape used in the iterative algorithm. The $\kappa(m)$ statistic compares the agreement between the atlases A_m and A_{m-1} . Curves for different initial shapes (A and B) are shown.

Another way of assessing the influence of the initial shape is to perform a consistency check. Figure 7.8 shows that for each shape in the training set two quasi-affine transformations can be found that map it to each of the atlases constructed starting with A and B . Let us call these transformations \mathbf{T}_{A_i} and \mathbf{T}_{B_i} , respectively. Let \mathbf{T}_{AB} be the quasi-affine transformation that maps the atlas A into the atlas B . In this situation, the transformation $\mathbf{T}_i = \mathbf{T}_{B_i}^{-1} \mathbf{T}_{AB} \mathbf{T}_{A_i}$, should be equal to the identity transformation, \mathbf{T}_I . By measuring the average and the standard deviation of the

differences $\mathbf{T}_i - \mathbf{T}_I$ it is possible to assess the bias and dispersion introduced by using two different initial shapes to build the atlas. These two initial shapes were chosen randomly from the training set. The statistical analysis is carried out in a parametric domain (translation, rotation and scaling parameters) to quantify the differences between \mathbf{T}_i and \mathbf{T}_I .¹ The results of this analysis for each transformation parameter are shown in Table 7.1. The translation, rotation and scaling error SDs are below 1.4 mm, 0.04° , and 5.1%, respectively.

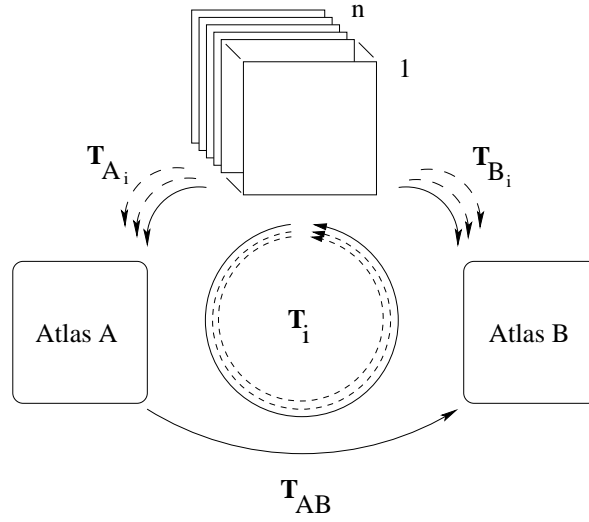


Figure 7.8. Bias introduced by the initial shape in the construction of the atlas. \mathbf{T}_{AB} is the transformation between the two atlases, A and B. For each of the n shapes, \mathbf{T}_{A_i} and \mathbf{T}_{B_i} give the transformations to each atlas A and B, respectively. The similarity of the two atlases can be assessed by computing the deviation of transformation $\mathbf{T}_i = \mathbf{T}_{B_i}^{-1} \mathbf{T}_{AB} \mathbf{T}_{A_i}$ from the identity transformation.

7.3.4 Statistical shape models

To construct a statistical model from the cardiac atlas, landmarks were extracted automatically from the atlas using marching cubes and subsequent mesh decimation (95% decimation ratio). This procedure yielded 215 and 528 landmarks for the left ventricular endo- and epicardial surfaces, respectively, and 372 landmarks for the right ventricular endocardial surface.

After automatic atlas landmarking, Principal Component Analysis (PCA) was performed on the set of propagated landmarks to the 14 shapes. Figure 7.9 and Figure 7.10 show the first five modes of variation of a left ventricle model and a combined left and right ventricle model, respectively. In the former, only the left ventricle

¹For more details on the computation of the transformation parameters from the matrix \mathbf{T}_i refer to Appendix 6.B.

Parameter	Units	Mean	SD
t_x	[mm]	- 1.04	1.05
t_y	[mm]	+ 0.09	0.59
t_z	[mm]	+ 0.27	1.38
r_x	[°]	+ 0.00	0.02
r_y	[°]	- 0.04	0.04
r_z	[°]	- 0.01	0.02
s_x	[%]	- 1.41	4.18
s_y	[%]	- 0.12	1.74
s_z	[%]	- 1.47	5.05
Γ	[.]	0.984	0.009
d	[mm]	+ 1.82	1.49

Table 7.1. Error in each transformation parameter (translation, t_x, t_y, t_z , rotation, r_x, r_y, r_z , and scaling, s_x, s_y, s_z) of the transformation \mathbf{T}_i with respect to the identity transformation. Point-to-point transformation error, d , provides information about the average distance between corresponding points before and after transformation. The parameter Γ provides a measure of the validity of the anisotropic scaling model for the full transformation \mathbf{T}_i . See Appendix 6.B for further details.

segments (LV_{bp} and LV_{myo}) were taken into account in the elastic registration and landmark propagation procedures. In the latter, both the left ventricle (LV_{bp} and LV_{myo}) and the right ventricle (RV_{bp}) were elastically registered to the atlas, and the landmarks were subsequently propagated.

Figure 7.11 indicates the percentage of the total explained variance as a function of the number of modes. Once corresponding landmarks are available, one is free to include or exclude the landmarks corresponding to a certain substructure. The more substructures are incorporated, the larger the required number of modes to explain a given variance since the overall shape variability has been increased.

In order to quantitatively assess the performance of the built models we have analyzed the reconstruction error by performing several leave-one-out experiments. The landmarks of all but one data set were used to build a statistical model. This model was subsequently used to reconstruct the set of landmarks not included in the PCA. The same experiment was repeated by taking out from the PCA, one in turn, each of the sets of landmarks. Finally, the average reconstruction error over the leave-one-out experiments was computed. This error was calculated as the root mean square error between the reconstructed and the true landmark position. Figure 7.12 shows the root mean square reconstruction error as a function of the number of modes used in shape reconstruction. For ten modes of variation (95% shape variability), the mean reconstruction error is 3.6 mm. This error is three times the in-plane voxel dimension and approximately one-third of the slice thickness. Since our training set is relatively small and the shape variability is quite large, these experiments do not reveal much information on the generalization ability of the models. However, they provide a first estimate that could be refined by enlarging the database of shapes.

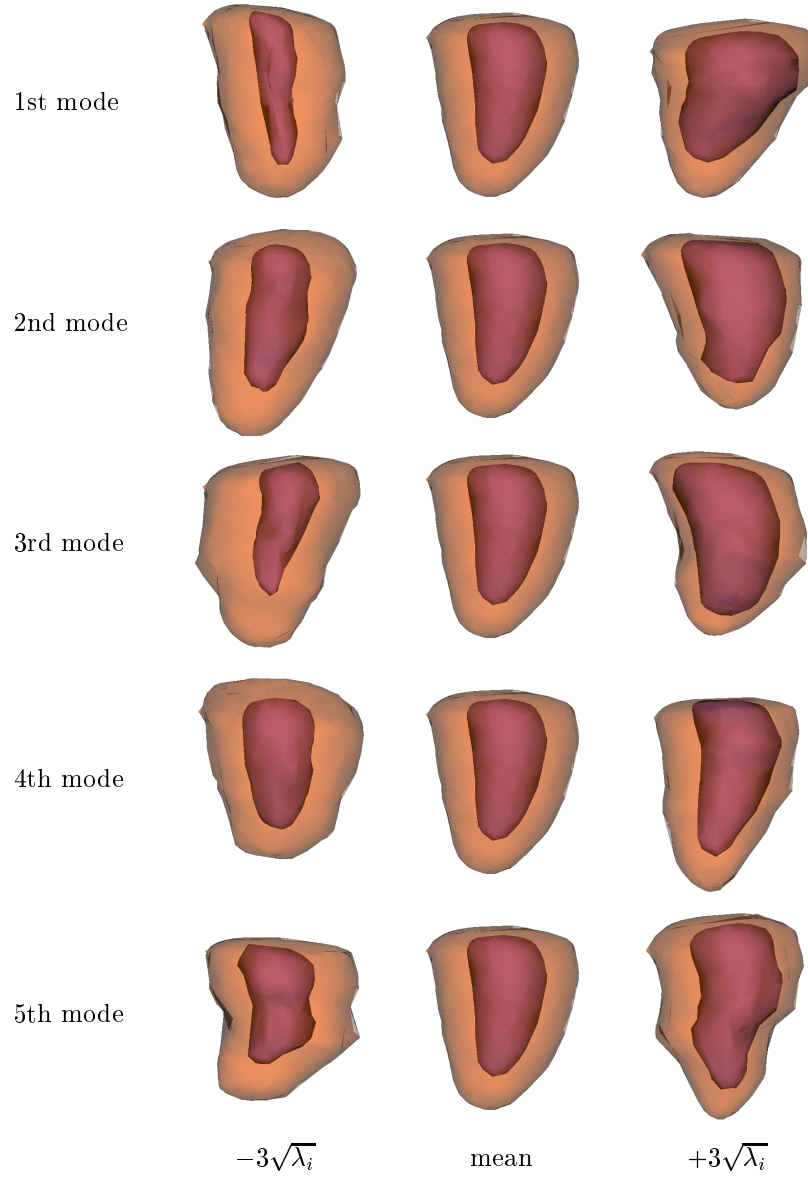


Figure 7.9. Shape instances generated using the 3-D one-chamber (LV) model from 14 cardiac data sets. The instances are generated by varying a single shape parameter, fixing all others at zero standard deviations from the mean shape. The one-chamber model consists of 215 endocardial nodes and 528 epicardial nodes.

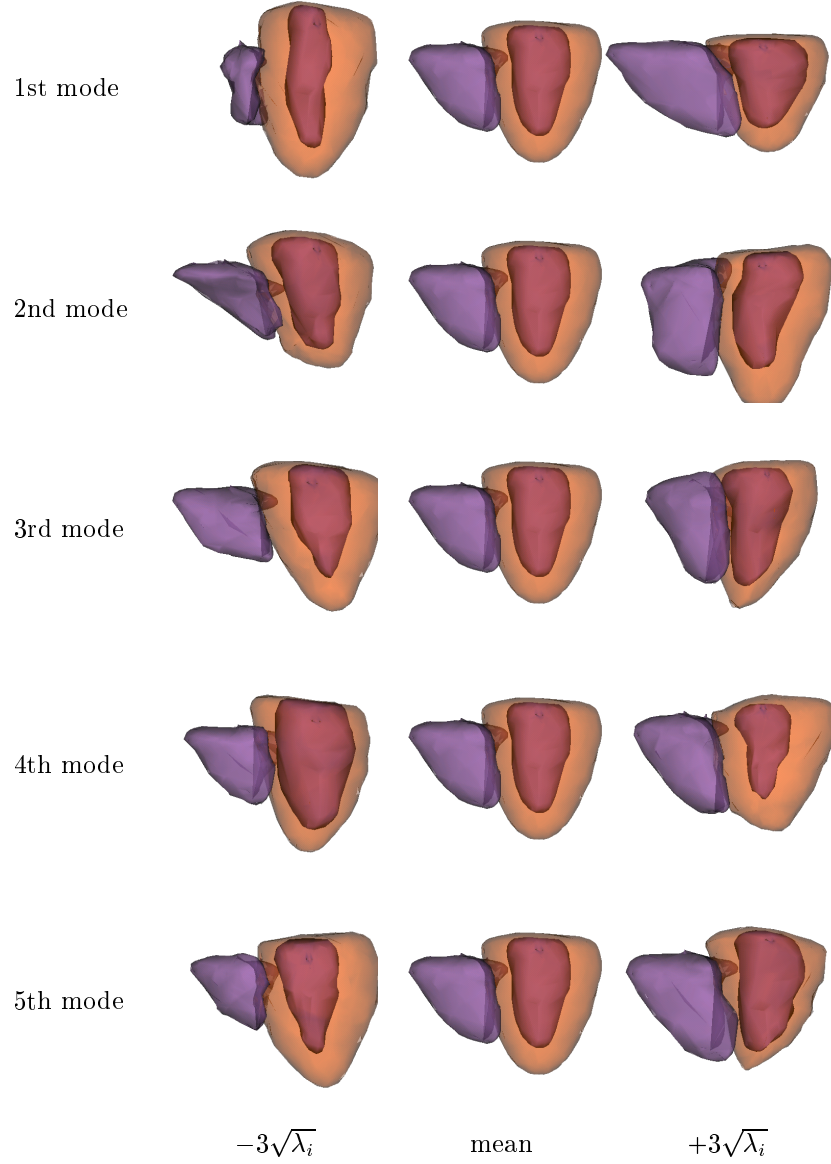


Figure 7.10. Shape instances generated using the 3-D two-chamber model from 14 cardiac data sets of the heart. The instances are generated by varying a single shape parameter, fixing all others at zero standard deviations from the mean shape. The two-chamber model consists of 215 LV endocardial nodes, 528 LV epicardial nodes, and 318 RV endocardial nodes.

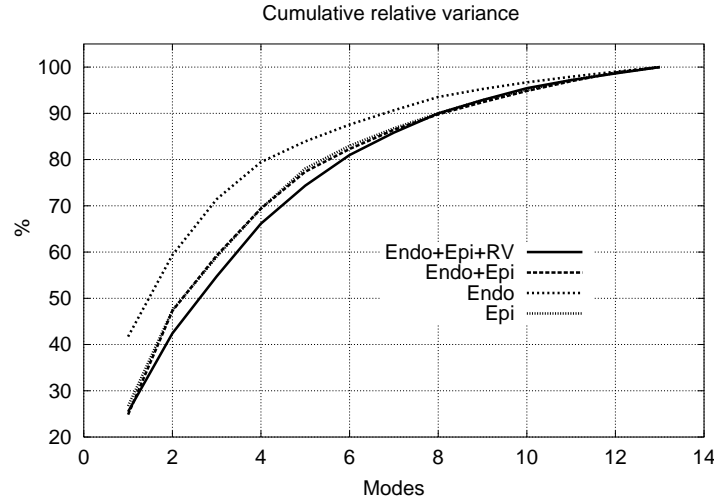


Figure 7.11. Percentage of total shape variance versus the number of modes used in the 3-D statistical shape model. The total number of landmarks was 1061 for the two-chamber heart model (Epi+Endo+RV), 743 for the left ventricular model (Epi+Endo), and 215 and 528 for the left ventricular endocardial (Endo) and epicardial (Epi) models, respectively.



Figure 7.12. Root mean square of landmark position (reconstruction error) in the leave-one-out experiments. The different curves correspond to statistical shape models constructed on the basis of all the landmarks or anatomical subsets. Endo = LV endocardial surface landmarks, Epi = LV epicardial surface landmarks, and RV = RV endocardial surface landmarks.

7.4 Discussion and conclusions

This chapter has presented a method for the automatic construction of 3-D statistical shape models. The technique is based on the automatic extraction of a dense mesh of landmarks in an atlas constructed from the training shapes. These landmarks are subsequently propagated through an elastic deformation field to each shape of the training set. The method is able to treat single- and multiple-part shapes. Results of the construction of a one- and two-chamber cardiac model have been presented. Experiments were carried out to establish the ability of the models to generalize to shapes not present in the training set. The root mean square reconstruction error in landmark position of the two-chamber model was below 3.8 mm when the number of nodes was sufficient to explain 95% of the shape variability.

This work has shown that the combination of our atlas generation method and the multi-level FFD elastic registration algorithm are able to cope with the large deformations involved in inter-patient matching of cardiac shapes. To the best of our knowledge, this work is the first one in suggesting the use of three-dimensional statistical shape models to describe the left and right ventricle of the heart. All the shapes in our training set were acquired at end diastole. However, the fact that the elastic registration algorithm can cope with large inter-patient deformations suggests that the same experiments could be repeated for different phases of the cardiac cycle to build a statistical spatio-temporal model of the heart.

Our model can be classified as a statistical surface model. One of the main differences between our approach and the work by Brett and Taylor [39,40] and Fleute and Lavallée [100,101] is that we use a volume-based elastic registration algorithm as opposed to their surface-based approaches. As a consequence, after elastic registration we are able to recover a dense volumetric displacement field. This could be used to propagate landmarks located inside of the myocardium or blood pools producing a statistical solid model.

The method presented in this chapter can be applied to model-based cardiac image segmentation and analysis. A significant improvement may be accomplished by enlarging the database of training shapes so as to capture the main modes of shape variation of cardiac chambers for a large population, and not only for those of our reduced training set. Although this chapter provides a proof-of-concept for our automatic landmarking algorithm, it is necessary to improve the statistics of the model to achieve an accurate segmentation.

A second step toward segmentation is to devise a deformation strategy that allows for the adaptation of the model mesh to segment a cardiac MR image. This could be achieved, for instance, by applying a method similar to the two-dimensional deformation procedure of active shape models [58]. For each landmark in the model, a statistical model of the intensity profile (or some other suitable image feature) along the surface normal can be computed. The model mesh could be deformed by moving the nodes along the direction of the normals to the position best matching the intensity with the statistical profile model. This method would provide an image-derived displacement for each node. The displacements applied to update the mesh can be obtained by projecting the suggested displacements onto the sub-space spanned by the main modes of variation. This projection step would naturally incorporate shape

constraints in the mesh deformation.

In conclusion, a method was presented to construct a shape atlas and to derive a statistical model of three-dimensional shape variability. We have demonstrated that this method is applicable to the construction of a statistical shape model of the cardiac chambers. This paves the way toward the application of this model to cardiac image segmentation and analysis.

7.A Appendix: Elastic registration with multi-level FFDs

In order to establish shape correspondences between label images, and to propagate landmarks from the atlas to the individual shapes, a multi-level free-form elastic registration algorithm has been applied which was formulated by Rueckert *et al.* [255] and further developed by Schnabel *et al.* [262]. This algorithm manipulates a shape by embedding it in a hierarchy of volumetric grids which define continuous deformation fields through a set of B-spline basis functions. For each location in the reference shape, a corresponding location in the individual shapes is found to obtain an optimal match. The corresponding optimal deformation field is obtained by maximizing a voxel similarity measure on the basis of the corresponding labels. The registration method and a novel similarity measure for label images are briefly summarized in the following subsection.

7.A.1 Transformation model

Let $\mathbf{T} : (x, y, z) \mapsto (x', y', z')$ be a transformation that maps any point (x, y, z) in the reference image into the corresponding target image coordinates (x', y', z') . In our application the reference image is the *atlas* which defines the coordinate system in which all other images will be expressed.²

In order to accommodate for non-rigid deformations, \mathbf{T} will consist of a global transformation \mathbf{T}_{global} and a coarse-to-fine hierarchy of elastic transformations $\mathbf{T}_{elastic}^h$ at increasing grid resolutions

$$\mathbf{T}(x, y, z) = \mathbf{T}_{global}(x, y, z) + \sum_{h=1}^H \mathbf{T}_{elastic}^h(x, y, z) \quad (7.5)$$

7.A.2 Global transformation

The global transformation describes the pose and size of the transformed shape with respect to the atlas. This can be accomplished with a global transformation in the form of an affine model

²Figure 7.1 suggests that each sample shape is warped to the atlas. In this case, the inverse of the deformation field has to be computed to propagate the landmarks. However, this mapping does not necessarily exist. This was illustrated for the sake of conceptual simplicity only. From a computational point of view it is more convenient to warp the atlas to each sample shape and use the direct deformation field for landmark propagation.

$$\mathbf{T}_{global}(x, y, z) = \begin{pmatrix} \theta_{11} & \theta_{12} & \theta_{13} \\ \theta_{21} & \theta_{22} & \theta_{23} \\ \theta_{31} & \theta_{32} & \theta_{33} \end{pmatrix} \begin{pmatrix} x \\ y \\ z \end{pmatrix} + \begin{pmatrix} \theta_{14} \\ \theta_{24} \\ \theta_{34} \end{pmatrix} \quad (7.6)$$

where the coefficients Θ parameterize the twelve degrees of freedom of a generic affine transformation. For a quasi-affine transformation, only nine parameters are independent (rigid transformation, $\{t_x, t_y, t_z, r_x, r_y, r_z\}$, plus anisotropic scaling, $\{s_x, s_y, s_z\}$).³ The computation of these parameters is accomplished with a modified version of the method by Studholme *et al.* [284]

7.A.3 Local transformation

The global transformation captures only the pose and size of the shapes. In order to accommodate for local shape differences, the global deformation field has to be supplemented with a local deformation model. The local deformation field is represented by a hierarchy of free-form deformation (FFDs) based on B-splines. The basic concept of multi-level FFDs is to deform an object by embedding it into a hierarchy of volumetric meshes of control points and subsequently manipulating the meshes. These meshes form a multi-resolution hierarchy with levels of increasing mesh resolution (or decreasing mesh spacing). The control points of each mesh are smoothly approximated by a set of B-spline basis functions that define a continuous deformation field.

To define multi-level FFDs based on B-splines we denote the domain of the image volume as $\Omega = \{(x, y, z) | 0 \leq x < X, 0 \leq y < Y, 0 \leq z < Z\}$. Let Φ^h denote a $n_x^h \times n_y^h \times n_z^h$ mesh of control points, $\phi_{i,j,k}^h$, at level h and with uniform spacing δ^h . Then, the FFD can be written as the 3-D tensor product of the familiar 1-D cubic B-splines

$$\mathbf{T}_{elastic}^h(x, y, z) = \sum_{l=0}^3 \sum_{m=0}^3 \sum_{n=0}^3 B_l(u) B_m(v) B_n(w) \phi_{i+l, j+m, k+n}^h \quad (7.7)$$

³The relationships between the Θ parameters and those of a quasi-affine transformation are

$$\begin{aligned} \theta_{11} &= s_x \cos r_y \cos r_z \\ \theta_{12} &= s_y \cos r_y \sin r_z \\ \theta_{13} &= -s_z \sin r_y \\ \theta_{21} &= s_x (\sin r_x \sin r_y \cos r_z - \cos r_x \sin r_z) \\ \theta_{22} &= s_y (\sin r_x \sin r_y \sin r_z + \cos r_x \cos r_z) \\ \theta_{23} &= s_z \sin r_x \cos r_y \\ \theta_{31} &= s_x (\cos r_x \sin r_y \cos r_z + \sin r_x \sin r_z) \\ \theta_{32} &= s_y (\cos r_x \sin r_y \sin r_z - \sin r_x \cos r_z) \\ \theta_{33} &= s_z \cos r_x \cos r_y \\ \theta_{14} &= t_x \\ \theta_{24} &= t_y \\ \theta_{34} &= t_z \end{aligned}$$

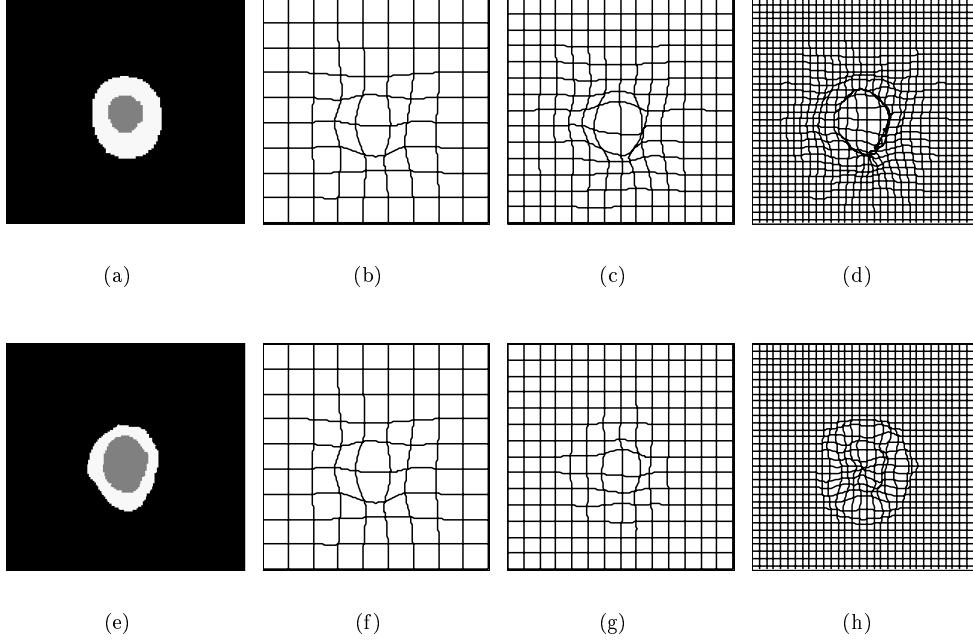


Figure 7.13. Multi-level free-form deformations. The deformation fields for landmark propagation are computed by elastically matching each training shape (Figure 7.13(e)) to the atlas (Figure 7.13(a)). The deformation field is represented as a hierarchy of free-form deformations. Figures 7.13(b)-7.13(d) represent the absolute (cumulative) deformations at 15 mm, 10 mm and 5 mm grid spacing. The relative deformation fields at each level are shown in Figures 7.13(f)-7.13(h).

where $i = \lfloor \frac{x}{n_x^h} \rfloor - 1$, $j = \lfloor \frac{y}{n_y^h} \rfloor - 1$, $k = \lfloor \frac{z}{n_z^h} \rfloor - 1$, $u = \frac{x}{n_x^h} - \lfloor \frac{x}{n_x^h} \rfloor$, $v = \frac{y}{n_y^h} - \lfloor \frac{y}{n_y^h} \rfloor$, $w = \frac{z}{n_z^h} - \lfloor \frac{z}{n_z^h} \rfloor$, and where B_l represents the l -th basis function of the B-spline [173].

The control points Φ^h act as parameters of the B-spline at level h and the degree of non-rigid deformation which can be modeled depends on the resolution level h . The smaller the associated spacing δ^h the more local the deformation is allowed to be. On the other hand, the computational complexity of the algorithm is approximately inversely proportional to the spacing parameter. The trade-off between deformation flexibility and computational complexity is mainly an empirical choice which is determined by the accuracy required to deform the atlas into the individual shapes. In our experiment with cardiac data sets, we have used a deformation field with three mesh levels ($H = 3$) corresponding to grid spacings of 15 mm, 10 mm, and 5 mm (Figure 7.13).

7.A.4 Hierarchical FFD optimization

In order to find the optimal transformation we minimize a cost function with respect to the global transformation parameters, Θ , as well as the local transformation parameters, $\phi_{i,j,k}^h$. In order to perform this registration, a hierarchical optimization algorithm is employed. Initially only the global parameters are optimized. Once the shapes have been aligned with the atlas, the global parameters are frozen and the FFD levels are subsequently optimized one by one in a coarse-to-fine manner using a gradient-descent method, taking the preceding global and local displacements into account. These preceding displacements can be efficiently precomputed to avoid reevaluation during the optimization of a current FFD level.

As an illustration, Figure 7.13 shows a two-dimensional projection of the three-dimensional deformation field for a fixed slice. Figures 7.13(a) and 7.13(e) indicate the reference and target shapes respectively. Figures 7.13(b), 7.13(c) and 7.13(d) indicate the cumulative deformation field of three increasing levels of refinement, while Figures 7.13(f), 7.13(g) and 7.13(h) indicate the relative deformation field of the given level. In our experience, the multi-level approach is less prone to yield grid foldings given that the local flexibility of the deformation is increased only gradually.⁴ This naturally regularizes the FFDs without the need of extra smoothness terms [255].

⁴The apparent “foldings”, especially in Figure 7.13(d), are an artifact of the projection of the three-dimensional deformation field on a two-dimensional planar surface. In this particular plane, the maximal out-of-plane displacement is about 8 mm which occurs close to the region of apparent folding. In this area there is a large gradient in the deformation field. When interactively visualized in 3-D the deformation field is still smooth.

*Books serve to show a man that those original
thoughts of his aren't very new after all.*

— A. Lincoln, 1809-1865

Bibliography

- [1] D.G. Altman, *Practical statistics for medical research*, Chapman & Hall, London, 1991.
- [2] S.C. Amartur & H.J. Vesselle, “A new approach to study cardiac motion: the optical flow of cine MR images”, *Magn Res Med*, vol. 29, no. 1, pp. 59–67, Jan. 1993.
- [3] American Heart Association, *American Heart Association 1999 Heart and Stroke Statistical Update*, Dallas, Tex., 1998. <http://www.americanheart.org>.
- [4] A.A. Amini, Y. Chen, D. Abendschein, “Comparison of land-mark-based and curved-based thin-plate warps for analysis of left-ventricular motion from tagged MRI”, in Taylor and Colchester [289].
- [5] A.A. Amini & J.S. Duncan, “Bending and stretching models for LV wall motion analysis from curves and surfaces”, *Imag Vis Comp*, vol. 10, no. 6, pp. 418–30, July 1992.
- [6] C.M. Anderson, R.E. Lee, D.L. Levin, S. de la Torre Alonso, D. Saloner, “Measurement of internal carotid artery stenosis from source MR angiograms”, *Radiology*, vol. 193, no. 1, pp. 219–26, Oct. 1994.
- [7] C.M. Anderson, D. Saloner, J.S. Tsuruda, L.G. Shapeero, R.E. Lee, “Artifacts in maximum-intensity-projection display of MR angiograms”, *Am J Roentgenol*, vol. 154, no. 3, pp. 623–9, Mar. 1990.
- [8] M. Ariet, E.A. Geiser, S.M. Lupkiewicz, D.A. Conetta, C.R. Conti, “Evaluation of a three-dimensional reconstruction to compute left ventricular volume and mass”, *Am J Cardiol*, vol. 54, no. 3, pp. 415–20, Aug. 1984.
- [9] T. Arts, W.C. Hunter, A.S. Douglas, A.M.M. Muijtjens, J.W. Corsel, R.S. Reneman, “Macroscopic three-dimensional motion patterns of the left ventricle”, *Adv Exp Med Biol*, vol. 346, pp. 383–92, 1993.
- [10] T. Arts, W.C. Hunter, A. Douglas, M.M. Muijtjens, R.S. Reneman, “Description of the deformation of the left ventricle by a kinematic model”, *J Biomech*, vol. 25, no. 10, pp. 1119–27, Oct. 1992.
- [11] L. Axel, D. Bloomgarden, C.N. Chang, D. Kraitchman, A.A. Young, “SPAMMVU: a program for the analysis of dynamic tagged MRI”, in *Proc ISMRM*, p. 724, 1993.
- [12] L. Axel & L. Dougherty, “Heartwall motion: improved method of spatial modulation of magnetization for MR imaging”, *Radiology*, vol. 172, no. 2, pp. 349–50, Aug. 1989.
- [13] S. Aylward, E. Bullit, S. Pizer, D. Eberly, “Intensity ridge and widths for tubular object segmentation and description”, in *Math Meth Biomed Imag Anal*, pp. 131–8, 1996.
- [14] H. Azhari, I. Gath, R. Beyar, M.L. Marcus, S. Sideman, “Discrimination between healthy and diseased hearts by spectral decomposition of their left ventricular 3D geometry”, *IEEE Trans Med Imaging*, vol. 10, no. 2, pp. 207–15, June 1991.
- [15] H. Azhari, E. Grenadier, U. Dinnar, R. Beyar, D.R. Adam, M.L. Marcus, S. Sideman, “Quantitative characterization and sorting of three-dimensional geometries: application to left ventricles in vivo”, *IEEE Trans Med Imaging*, vol. 36, no. 3, pp. 322–32, Mar. 1989.

- [16] H. Azhari, S. Sideman, R. Beyar, E. Grenadier, U. Dinnar, "An analytical descriptor of three-dimensional geometry: application to the analysis of the left ventricle shape and contraction", *IEEE Trans Biomed Eng*, vol. 34, no. 5, pp. 345–55, May 1987.
- [17] H. Azhari, S. Sideman, J.L. Weiss, E.P. Shapiro, M.L. Weisfeldt, W.L. Graves, W.J. Rogers, R. Beyar, "Three-dimensional mapping of acute ischemic regions using MRI : wall thickening versus motion analysis", *Am J Physiol*, vol. 259, no. 5 Pt 2, pp. H1492–503, Nov. 1990.
- [18] R. Bajscy & S. Kovacic, "Multiresolution elastic matching", *Comp Vis Graph & Im Proc*, vol. 46, no. 1, pp. 1–21, Apr. 1989.
- [19] E. Bardinet, N. Ayache, L.D. Cohen, "Tracking and motion analysis of the left ventricle with deformable superquadrics", *Med Image Anal*, vol. 1, no. 2, pp. 129–50, June 1996.
- [20] E. Bardinet, L.D. Cohen, N. Ayache, "A parametric deformable model to fit unstructured 3D data", *Comp Vis Image Underst*, vol. 71, no. 1, pp. 39–54, July 1998.
- [21] G. Barletta, M. Baroni, R. del Bene, A. Toso, F. Fantini, "Regional and temporal nonuniformity of shape and wall movement in the normal left ventricle", *Cardiology*, vol. 90, no. 3, pp. 195–201, Dec. 1998.
- [22] A.H. Barr, "Superquadrics and angle-preserving deformations", *IEEE Comp Graph & Appl*, vol. 1, no. 1, pp. 11–23, Jan. 1981.
- [23] K.A. Bartels, A.C. Bovik, S.J. Aggarwal, K.R. Diller, "The analysis of biological shape change from multi-dimensional dynamic images", *Comp Med Im & Graph*, vol. 17, no. 2, pp. 89–99, Mar. 1993.
- [24] K.A. Bartels, A.C. Bovik, C.E. Griffin, "Spatio-temporal tracking of material shape change via multi-dimensional splines", in *Math Meth Biomed Imag Anal*, Seattle, USA, pp. 110–6, 1994.
- [25] A. Bazille, M.A. Guttman, E.R. McVeigh, E.A. Zerhouni, "Impact of semiautomated versus manual image segmentation errors on myocardial strain calculation by MR tagging", *Inv Rad*, vol. 29, no. 4, pp. 427–33, Apr. 1994.
- [26] S.S. Beauchemin & J.L. Barron, "The computation of optical flow", *ACM Comput Surveys*, vol. 27, no. 3, pp. 444–67, Sept. 1995.
- [27] S. Benayoun & N. Ayache, "Dense and non-rigid motion estimation in sequences of medical images using differential constraints", *Int J Comput Vision*, vol. 26, no. 1, pp. 25–40, Jan. 1998.
- [28] P.J. Besl & R.C. Jain, "Invariant surface characteristics for 3-D object recognition in range images", *Comp Vis Graph & Im Proc*, vol. 33, no. 1, pp. 33–80, Jan. 1986.
- [29] P.J. Besl & N.D. McKay, "A method for registration of 3D shapes", *IEEE Trans Pattern Anal Machine Intell*, vol. 14, no. 2, pp. 239–55, Feb. 1992.
- [30] R. Beyar, E.P. Shapiro, W.L. Graves, W.J. Rogers, Guier W.H., G.A. Carey, R.L. Soulen, E.A. Zerhouni, M.L. Weisfeldt, J.L. Weiss, "Quantification and validation of left ventricular wall thickening by a three-dimensional volume element magnetic resonance imaging approach", *Circulation*, vol. 81, no. 1, pp. 297–307, Jan. 1990.
- [31] S. Biedenstein, M. Schäfers, L. Stegger, T. Kuwert, O. Schober, "Three-dimensional contour detection of left ventricular myocardium using elastic surfaces", *Eur J Nucl Med*, vol. 26, no. 3, pp. 201–7, Mar. 1999.
- [32] J.M. Bland & D.G. Altman, "Statistical methods for assessing agreement between two methods of clinical measurement", *Lancet*, vol. 8476, pp. 307–10, Feb. 1986.
- [33] J.D. Blankensteijn, J. van der Grond, W.P.Th.M. Mali, B.C. Eikelboom, "Flow volume changes in the major cerebral arteries before and after carotid endarterectomy: an MR angiographic study", *Eur J Vasc Endovasc Surg*, vol. 14, no. 6, pp. 446–50, Dec. 1997.
- [34] D.D. Blatter, A.L. Bahr, D.L. Parker, R.O. Robison, J.A. Kimball, D.M. Perry, S. Horn, "Cervical carotid MR angiography with multiple overlapping thin-slab acquisition: comparison with conventional angiography", *Am J Roentgenol*, vol. 161, no. 6, pp. 1269–77, Dec. 1993.

- [35] E.L. Bolson & F.H. Sheehan, "CenterSurface model for 3D analysis of regional left biventricular function", in *IEEE Comput in Cardiol*, IEEE Computer Society Press, London, UK, pp. 735–8, Sept. 1993.
- [36] E.L. Bolson, F.H. Sheehan, Legget M.E., H. Jin, J.A. McDonald, P.D. Sampson, R.W. Martin, G. Bashein, C.M. Otto, "Applying the CenterSurface model to 3-D reconstructions of the left ventricle for regional functional analysis", in *IEEE Comput in Cardiol*, IEEE Computer Society Press, Vienna, Austria, pp. 63–7, Sept. 1995.
- [37] D.P. Boyd & C. Haugland, "Recent progress in electron beam tomography", *Med Imag Tech*, vol. 11, pp. 578–85, 1993.
- [38] D.P. Boyd & M.J. Lipton, "Cardiac computed tomography", *Proc IEEE*, vol. 71, no. 3, pp. 298–307, Mar. 1983. Special Issue on Computed Tomography.
- [39] A.D. Brett & C.J. Taylor, "Automated construction of 3D shape models using harmonic maps", in *Medical Image Understanding and Analysis*, S. Arridge & A. Todd-Pokropek (eds.), London, pp. 175–8, July 2000.
- [40] A.D. Brett & C.J. Taylor, "A method of automated landmark generation for automated 3D PDM construction", *Imag Vis Comp*, vol. 18, no. 9, pp. 739–48, 2000.
- [41] R.W. Brower, H.T. ten Katen, G.J. Meester, "Direct method for determining regional myocardial shortening after bypass surgery from radiopaque markers in man", *Am J Cardiol*, vol. 41, no. 7, pp. 1222–9, June 1978.
- [42] V.G.M. Buller, R.J. van der Geest, M.D. Kool, J.H.C. Reiber, "Accurate three-dimensional wall thickness measurement from multi-slice short-axis MR imaging", in *IEEE Comput in Cardiol*, IEEE Computer Society Press, Maryland, USA, pp. 245–8, Sept. 1994.
- [43] V. Caselles, F. Catté, T. Coll, F. Dibos, "A geometric model for active contours in image processing", *Num Mathematik*, vol. 66, pp. 1–31, 1993.
- [44] J.C. Cauvin, J.Y. Boire, M. Zanca, J.M. Bonny, J. Maublant, A. Veyre, "3D modeling in myocardial 201TL SPECT", *Comp Med Im & Graph*, vol. 17, no. 4–5, pp. 345–50, July 1993.
- [45] A. Chakraborty, L.H. Staib, J.S. Duncan, "Deformable boundary finding in medical images by integrating gradient and region information", *IEEE Trans Med Imaging*, vol. 15, no. 6, pp. 859–70, Dec. 1996.
- [46] C.W. Chen & T.S. Huang, "Epicardial motion and deformation estimation from coronary artery bifurcation points", in *Int Conf Comput Vision*, Osaka, Japan, pp. 456–9, Dec. 1990.
- [47] C.W. Chen, T.S. Huang, M. Arrott, "Modeling, analysis, and visualization of left ventricle shape, and motion by hierarchical decomposition", *IEEE Trans Pattern Anal Machine Intell*, vol. 16, no. 4, pp. 342–56, Apr. 1994.
- [48] C.W. Chen, J.B. Luo, K.J. Parker, "Image segmentation via adaptive K-mean clustering and knowledge-based morphological operations with biomedical applications", *IEEE Trans Imag Proc*, vol. 7, no. 12, pp. 1673–83, Dec. 1998.
- [49] C. W. Chen, J. Luo, K.J. Parker, T.S. Huang, "CT volumetric data-based left ventricle motion estimation : an integrated approach", *Comp Med Im & Graph*, vol. 19, no. 1, pp. 85–100, Jan. 1995.
- [50] H. Chen & J. Hale, "An algorithm for MR angiography image enhancement", *Magn Res Med*, vol. 33, no. 4, pp. 534–40, Apr. 1995.
- [51] N.R. Clark, N. Reichek, P. Bergey, E.A. Hoffman, D. Brownson, L. Palmon, L. Axel, "Circumferential myocardial shortening in the normal human left ventricle. Assessment by magnetic resonance imaging using spatial modulation of magnetization", *Circulation*, vol. 84, no. 1, pp. 67–74, July 1991.
- [52] P. Clarysse, D. Friboulet, I.E. Magnin, "Tracking geometrical descriptors on 3-D deformable surfaces: application to the left-ventricular surface of the heart", *IEEE Trans Med Imaging*, vol. 16, no. 4, pp. 392–404, 1997.
- [53] H.E. Cline, C.L. Dumoulin, W.E. Lorensen, S.P. Souza, W.J. Adams, "Volume rendering and connectivity algorithms for MR angiography", *Magn Res Med*, vol. 18, no. 2, pp. 384–94, Apr. 1991.

- [54] L.D. Cohen, "On active contour models and balloons", *Comp Vis Graph & Im Proc: Imag Underst*, vol. 53, no. 2, pp. 211–8, Mar. 1991.
- [55] A. Collignon, F. Maes, D. Delaere, D. Vandermeulen, P. Suetens, G. Marchal, "Automated multimodality image registration using information theory", in *Inf Proc Med Imag*, pp. 263–74, 1995.
- [56] T.F. Cootes, A. Hill, C.J. Taylor, J. Haslam, "Use of active shape models for locating structures in medical images", *Imag Vis Comp*, vol. 12, no. 6, pp. 355–65, July 1994.
- [57] T.F. Cootes & C.J. Taylor, "Statistical models of appearance for computer vision", Technical Report, Wolfson Image Analysis Unit, University of Manchester, July 2000. <http://www.wiau.man.ac.uk/~bim>.
- [58] T.F. Cootes, C.J. Taylor, D.H. Cooper, J. Graham, "Active Shape Models - Their training and application", *Comp Vis Image Underst*, vol. 61, no. 1, pp. 38–59, 1995.
- [59] G. Coppini, R. Poli, G. Valli, "Recovery of the 3-D shape of the left ventricle from echocardiographic images", *IEEE Trans Med Imaging*, vol. 14, no. 2, pp. 301–17, June 1995.
- [60] G.B. Cranney, C.S. Lotan, L. Dean, W. Baxley, A. Bouchard, G.M. Pohost, "Left ventricular volume measurement using cardiac axis nuclear magnetic resonance imaging", *Circulation*, vol. 82, no. 1, pp. 154–63, July 1990.
- [61] L.L. Creswell, S.G. Wyers, J.S. Pirolo, W.H. Perman, M.W. Vannier, M.K. Pasque, "Mathematical modeling of the heart using magnetic resonance imaging", *IEEE Trans Med Imaging*, vol. 11, no. 4, pp. 581–9, Dec. 1992.
- [62] M. Cronqvist, F. Stahlberg, E.M. Larsson, M. Lonnroft, S. Holtas, "Evaluation of time-of-flight and phase contrast MRA sequences at 1.0-T for diagnosis of carotid artery disease. I. A phantom and volunteer study", *Acta Radiol*, vol. 37, no. 3 Pt 1, pp. 267–77, May 1996.
- [63] F.P. Czegledy & J. Katz, "A new geometric description of the right ventricle", *J Biomed Eng*, vol. 15, no. 5, pp. 387–91, Sept. 1993.
- [64] P.E. Danielsson, "Euclidean distance mapping", *Comp Graph Imag Proc*, vol. 14, pp. 227–48, 1980.
- [65] M. David, *Handbook of applied advanced geostatistical ore reserve estimation*, Elsevier Science Pub., Amsterdam, 1988.
- [66] J.C. Davila & M.E. Sanmarco, "An analysis of the fit of mathematical models applicable to the measurement of left ventricular volume", *Am J Cardiol*, vol. 18, pp. 31–42, July 1966.
- [67] J.K. De Marco, G.M. Nesbit, G.E. Wesbey, D. Richardson, "Prospective evaluation of extracranial carotid stenosis: MR angiography with Maximum-Intensity Projections and Multiplanar Reformation compared with conventional angiography", *Am J Roentgenol*, vol. 163, pp. 1205–12, Nov. 1994.
- [68] J. Declerck, N. Ayache, E.R. McVeigh, "Use of a 4D planispheric transformation for the tracking and the analysis of LV motion with tagged MR images", Tech. Rep. 3535, INRIA, Oct. 1998.
- [69] J. Declerck, J. Feldmar, N. Ayache, "Definition of a four-dimensional continuous planispheric transformation for the tracking and the analysis of the left-ventricle motion", *Med Image Anal*, vol. 2, no. 2, pp. 197–213, June 1998.
- [70] J. Declerck, J. Feldmar, M.L. Goris, F. Betting, "Automatic registration and alignment on a template of cardiac stress and rest SPECT images", *IEEE Trans Med Imaging*, vol. 16, no. 6, pp. 727–37, Dec. 1997.
- [71] J. Declerck, T.S. Denney, C. Öztürk, W. O'Dell, E.R. McVeigh, "Left ventricular motion reconstruction from planar tagged MR images: a comparison", *Phys Med Biol*, vol. 45, no. 6, pp. 1611–32, June 2000.
- [72] H. Delingette, "General object reconstruction based on simplex meshes", *Int J Comput Vision*, vol. 32, no. 2, pp. 111–46, Sept. 1999.

- [73] T.S. Denney & E.R. McVeigh, "Model-free reconstruction of three-dimensional myocardial strain from planar tagged MR images", *J Magn Reson Imaging*, vol. 7, no. 5, pp. 799–810, Sept. 1997.
- [74] T.S. Denney & J.L. Prince, "Optimal brightness functions for optical flow estimation of deformable motion.", *IEEE Trans Imag Proc*, vol. 3, no. 2, pp. 178–91, Mar. 1994.
- [75] T.S. Denney & J.L. Prince, "A frequency domain performance analysis of Horn and Schunck's optical flow algorithm for deformable motion", *IEEE Trans Imag Proc*, vol. 4, no. 9, pp. 1324–7, Sept. 1995.
- [76] T.S. Denney & J.L. Prince, "Reconstruction of 3D left ventricular motion from planar tagged cardiac MR Images : an estimation theoretic approach", *IEEE Trans Med Imaging*, vol. 14, no. 4, pp. 1–11, Dec. 1995.
- [77] S. Denslow, "An ellipsoidal shell model for volume estimation of the right ventricle from magnetic resonance images.", *Acad Radiol*, vol. 1, no. 4, pp. 345–51, Dec. 1994.
- [78] M. Do Carmo, *Differential geometry of curves and surfaces*, Prentice-Hall, Inc., New Jersey, 1976.
- [79] H.T. Dodge, H. Sandler, W.A. Baxley, R.R. Hawley, "Usefulness and limitations of radiographic methods for determining left ventricular volume", *Am J Cardiol*, vol. 18, pp. 10–24, July 1966.
- [80] C. Dorai & A.K. Jain, "Shape spectrum based view grouping and matching of 3D free-form objects", *IEEE Trans Pattern Anal Machine Intell*, vol. 19, no. 10, pp. 1139–46, Oct. 1997.
- [81] L. Dougherty, J.C. Asmuth, A.S. Blom, L. Axel, R. Kumar, "Validation of an optical flow method for tag displacement estimation", *IEEE Trans Med Imaging*, vol. 18, no. 4, pp. 359–63, Apr. 1999.
- [82] A.S. Douglas, W.C. Hunter, M.D. Wiseman, "Inhomogeneous deformation as a source of error in strain measurements derived from implanted markers in the canine left ventricle", *J Biomech*, vol. 23, no. 4, pp. 331–41, 1990.
- [83] Y.P. Du & D.L. Parker, "Vessel enhancement filtering in three-dimensional MR angiography", *J Magn Reson Imaging*, vol. 5, no. 3, pp. 353–9, 1995.
- [84] Y.P. Du & D.L. Parker, "Vessel enhancement filtering in three-dimensional MR angiograms using long-range signal correlation", *J Magn Reson Imaging*, vol. 7, no. 2, pp. 447–50, 1997.
- [85] Y.P. Du, D.L. Parker, W.L. Davis, G.C. Cao, "Reduction of partial volume artifacts with zero-filled interpolation in three-dimensional MR angiography", *J Magn Reson Imaging*, vol. 4, no. 5, pp. 733–41, Sept. 1994.
- [86] M.C. Dulce, G.H. Mostbeck, K.K. Friese, G.R. Caputo, C.B. Higgins, "Quantification of the left ventricular volumes and function with cine MR imaging: comparison of geometric models with three-dimensional data", *Radiology*, vol. 188, no. 2, pp. 371–6, Aug. 1993.
- [87] J.S. Duncan, P. Shi, T. Constable, A. Sinusas, "Physical and geometrical modeling for image-based recovery of left ventricular deformation", *Prog Biophys Mol Biol*, vol. 69, no. 1–2, pp. 333–51, 1998.
- [88] L. Ekelund, L. Sjöqvist, K.A. Thuomas, B. Asberg, "MR angiography of abdominal and peripheral arteries. Techniques and clinical applications", *Acta Radiol*, vol. 37, no. 1, pp. 3–13, Jan. 1996.
- [89] E. Ekoulé, F. Peyrin, C. Odet, "Description d'une procédure de triangulation entièrement automatique", in *Proc COGNITIVA 87*, Paris, France, pp. 88–95, 1987.
- [90] O.E.H. Elgersma, P.C. Buijs, A.F.J. Wüst, Y. van der Graaf, B.C. Eikelboom, W.P.Th.M. Mali, "Assessment of maximum internal carotid artery stenosis: Rotational versus conventional intra arterial digital subtraction angiography", *Radiology*, vol. 213, no. 3, pp. 777–83, Dec. 1999.
- [91] European Carotid Surgery Trialists' Collaborative Group, "Endarterectomy for moderate symptomatic carotid stenosis: Interim results from the MRC European Carotid Surgery Trial", *Lancet*, vol. 347, no. 9015, pp. 1591–3, June 1996.

- [92] European Carotid Surgery Trialists' Collaborative Group, "Randomised trial of endarterectomy for recently symptomatic carotid stenosis: final results of the MRC European Carotid Surgery (ECST)", *Lancet*, vol. 351, no. 9113, pp. 1379–87, May 1998.
- [93] T.L. Faber, M.S. Akers, R.M. Peshock, J.R. Corbett, "Three-dimensional motion and perfusion quantification in gated single-photon emission computed tomograms", *J Nucl Med*, vol. 32, no. 12, pp. 2311–7, Dec. 1991.
- [94] T.L. Faber, C.D. Cooke, J.W. Peifer, R.I. Pettigrew, J.P. Vansant, J.R. Leyendecker, E.V. García, "Three-dimensional displays of left ventricular epicardial surface from standard cardiac SPECT perfusion quantification techniques", *J Nucl Med*, vol. 36, no. 4, pp. 697–703, Apr. 1995.
- [95] T.L. Faber, E.M. Stokely, R.M. Peshock, J.R. Corbett, "A model-based four-dimensional left ventricular surface detector", *IEEE Trans Med Imaging*, vol. 10, no. 3, pp. 321–9, Sept. 1991.
- [96] T.L. Faber, E.M. Stokely, G.H. Templeton, M.S. Akers, R.W. Parkey, J.R. Corbett, "Quantification of three-dimensional left ventricular segmental wall motion and volumes from gated tomographic radionuclide ventriculograms", *J Nucl Med*, vol. 30, no. 5, pp. 638–49, May 1989.
- [97] G. Farin, *Curves and surfaces for computer aided geometric design: a practical guide*, 2nd ed., Academic Press, Inc., 1990.
- [98] J. Feldmar & N. Ayache, "Rigid, affine and locally affine registration of free-form surfaces", *Int J Comput Vision*, vol. 18, no. 2, pp. 99–119, May 1996.
- [99] S.E. Fischer, G.C. McKinnon, M.B. Scheidegger, W. Prins, D. Meier, P. Boesiger, "True myocardial motion tracking", *Magn Res Med*, vol. 31, no. 4, pp. 401–13, Apr. 1994.
- [100] M. Fleute & S. Lavallée, "Building a complete surface model from sparse data using statistical shape models: applications to computer assisted knee surgery", in Wells et al. [312].
- [101] M. Fleute & S. Lavallée, "Incorporating a statistically based shape model into a system for computer-assisted anterior cruciate ligament surgery", *Med Image Anal*, vol. 3, no. 3, pp. 209–22, 1999.
- [102] L.M.J. Florack, B.M. ter Haar Romeny, J.J. Koenderink, M.A. Viergever, "Scale and the differential structure of images", *Imag Vis Comp*, vol. 10, no. 6, pp. 376–88, July 1992.
- [103] A.F. Frangi, W.J. Niessen, R.M. Hoogeveen, Th. van Walsum, M.A. Viergever, "Model-based quantitation of 3D Magnetic Resonance angiographic images", *IEEE Trans Med Imaging*, vol. 18, no. 10, pp. 946–56, Oct. 1999.
- [104] A.F. Frangi, W.J. Niessen, P.J. Nederkoorn, O.E.H. Elgersma, M.A. Viergever, "Three-dimensional model-based stenosis quantification of the carotid arteries from contrast-enhanced MR angiography", *Math Meth Biomed Imag Anal*, pp. 110–18, June 2000.
- [105] A.F. Frangi, W.J. Niessen, M.A. Viergever, "Three-dimensional modeling for functional analysis of cardiac images: a review", *IEEE Trans Med Imaging*, vol. 20, Jan. 2001. In press.
- [106] A.F. Frangi, W.J. Niessen, K.L. Vincken, M.A. Viergever, "Multiscale vessel enhancement filtering", in Wells et al. [312].
- [107] D. Friboulet, I.E. Magnin, C. Mathieu, A. Pommert, K.H. Hoehne, "Assessment and visualization of the curvature of the left ventricle from 3D medical images", *Comp Med Im & Graph*, vol. 17, no. 4–5, pp. 257–62, July 1993.
- [108] D. Friboulet, I.E. Magnin, D. Revel, "Assessment of a model for overall left ventricular three-dimensional motion from MRI data", *Int J Card Imag*, vol. 8, no. 3, pp. 175–90, Sept. 1992.
- [109] Y.C. Fung, *Biomechanics: motion, flow, stress and growth*, Springer Verlag, New York, 1990.
- [110] J. Garot, D.A. Bluemke, N.F. Osman, C.E. Rochitte, E.R. McVeigh, E.A. Zerhouni, J.L. Prince, "Fast determination of regional myocardial strain fields from tagged cardiac images using harmonic phase MRI", *Circulation*, vol. 101, no. 9, pp. 981–8, Mar. 2000.
- [111] E.A. Geiser, M. Ariet, D.A. Conetta, S.M. Lupkiewicz, L.G. Christie, C.R. Conti, "Dynamic three-dimensional echocardiographic reconstruction of the intact human left ventricle: technique and initial observations in patients", *Am Heart J*, vol. 103, no. 6, pp. 1056–65, June 1982.

- [112] E.A. Geiser, S.M. Lupkiewicz, L.G. Christie, M. Ariet, D.A. Conetta, C.R. Conti, "A framework for three-dimensional time-varying reconstruction of the human left ventricle: sources of error and estimation of their magnitude", *Comp Biomed Res*, vol. 13, no. 3, pp. 225–41, June 1980.
- [113] G. Germano & D. Berman, *Clinical gated cardiac SPECT*, Futura Publishing Co, Armonk, NY, 1999, Ch. Quantitative gated perfusion SPECT, pp. 115–46.
- [114] G. Germano, J. Erel, H. Kiat, P.B. Kavanagh, D.S. Berman, "Quantitative LVEF and qualitative regional function from gated 201-Tl perfusion SPECT", *J Nucl Med*, vol. 38, no. 5, pp. 749–54, May 1997.
- [115] G. Germano, P.B. Kavanagh, D.S. Berman, "An automatic approach to the analysis, quantitation and review of perfusion and function from myocardial perfusion SPECT images", *Int J Card Imag*, vol. 13, no. 4, pp. 337–46, Aug. 1997.
- [116] G. Germano, P.B. Kavanagh, J. Chen, P. Waechter, H-T. Su, H. Kiat, D. S. Berman, "Operator-less processing of myocardial perfusion SPECT studies", *J Nucl Med*, vol. 36, no. 6, pp. 2127–32, Nov. 1995.
- [117] G. Germano, H. Kiat, P.B. Kavanagh, M. Moriel, M. Mazzanti, H.-T Su, K.F. van Train, D.S. Berman, "Automatic quantification of ejection fraction from gated myocardial perfusion SPECT", *J Nucl Med*, vol. 36, no. 11, pp. 2138–47, Nov. 1995.
- [118] S. Gibson, "Constrained elastic SurfaceNets: generating smooth surfaces from binary sampled data", in Wells et al. [312].
- [119] G.H. Golub & C.F. van Loan, *Matrix computations*, 3rd ed., Johns Hopkins Series in the Mathematical Sciences, Johns Hopkins University Press, London, 1996.
- [120] A.S. Gopal, D.L. King, J. Katz, L.M. Bost, D.L. King, M.Y. Shao, "Three-dimensional echocardiographic volume computation by polyhedral surface reconstruction: *in vitro* validation and comparison to magnetic resonance imaging", *J Am Soc Echocardiogr*, vol. 5, no. 2, pp. 115–24, Mar. 1992.
- [121] J-M. Gorce, D. Friboulet, I.E. Magnin, "Estimation of three-dimensional cardiac velocity fields: assessment of a differential method and application to three-dimensional CT data", *Med Image Anal*, vol. 1, no. 3, pp. 245–61, Mar. 1996.
- [122] A. Goshtasby, "Design and recovery of 2-D and 3-D shapes using rational Gaussian curves and surfaces", *Int J Comput Vision*, vol. 10, no. 3, pp. 233–56, 1993.
- [123] A. Goshtasby & D.A. Turner, "Segmentation of cardiac cine MR images for extraction of right and left ventricular chambers", *IEEE Trans Med Imaging*, vol. 14, no. 1, pp. 56–64, Mar. 1995.
- [124] R.A. Greenbaum & D.G. Gibson, "Regional non-uniformity of left ventricular wall movement", *Br Heart J*, vol. 45, no. 1, pp. 29–34, Mar. 1981.
- [125] J.M. Guccione & A.D. McCulloch, "Finite element modeling of ventricular mechanics", in *Theory of Heart*, P.J. Hunter, A.D. McCulloch, P. Nielsen (eds.), Springer Verlag, Berlin, pp. 122–44, 1991.
- [126] A. Guéziec & R. Hummel, "Exploiting triangulated surface extraction using tetrahedral decomposition", *IEEE Trans Vis & Comp Graph*, vol. 1, no. 4, pp. 328–42, Dec. 1995.
- [127] T. Gustavsson, R. Pascher, K. Caidahl, "Model based dynamic 3D reconstruction and display of the left ventricle from 2D cross-sectional echocardiograms.", *Comp Med Im & Graph*, vol. 17, no. 4-5, pp. 273–8, July 1993.
- [128] M.A. Guttman, J.L. Prince, E.R. McVeigh, "Tag and contour detection in tagged MR images of the left ventricle", *IEEE Trans Med Imaging*, vol. 13, no. 1, pp. 74–88, Jan. 1994.
- [129] M.A. Guttman, E.A. Zerhouni, E.R. McVeigh, "Analysis and visualization of cardiac function from MR Images", *IEEE Comp Graph & Appl*, vol. 17, no. 1, pp. 55–63, Jan. 1997.
- [130] E. Haber, D.N. Metaxas, L. Axel, "Three-dimensional geometric modeling of cardiac right and left ventricles", in *Biomed Eng Soc An Meeting*, San Diego, USA, 1997.

- [131] E. Haber, D.N. Metaxas, L. Axel, "Motion analysis of the right ventricle from MRI Images", in Wells et al. [312].
- [132] A.J. Hanson, "Hyperquadrics: smoothly deformable shapes with convex polyhedral bounds", *Comp Vis Graph & Im Proc*, vol. 44, no. 2, pp. 191–210, Nov. 1988.
- [133] D.C. Harrison, A. Goldblatt, E. Braunwald, G. Glick, D.T. Mason, "Studies on cardiac dimensions in intact unanesthetized man. I. Description of techniques and their validation", *Circ Res*, vol. 13, pp. 448–55, 1963.
- [134] J.E. Heiserman, B.P. Drayer, P.J. Keller, E.K. Fram, "Intracranial vascular stenosis and occlusion: Evaluation with three-dimensional Time-of-Flight MR angiography", *Radiology*, vol. 185, pp. 667–73, Dec. 1992.
- [135] G.T. Herman, J. Zheng, C.A. Bucholtz, "Shape-based interpolation", *IEEE Comp Graph & Appl*, pp. 69–79, May 1992.
- [136] H.J. Hermann & S.H. Bartle, "Left ventricular volumes by angiocardiology: comparison of methods and simplification of techniques", *Cardiovasc Res*, vol. 2, no. 4, pp. 404–14, Oct. 1968.
- [137] C.B. Higgins, "Overview of MR of the heart–1986", *Am J Roentgenol*, vol. 146, no. 5, pp. 907–18, May 1986.
- [138] C.B. Higgins (ed.), *Special issue: Cardiovascular MRI*, vol. 10(5) of *J Magn Reson Imaging*, Nov. 1999.
- [139] L.D. Hillis, B.G. Firth, M.D. Winniford, "Analysis of factors affecting the variability of Fick versus indicator dilution measurements of cardiac output", *Am J Cardiol*, vol. 56, no. 12, pp. 764–8, Nov. 1986.
- [140] R.M. Hoogeveen, C.J.G. Bakker, M.A. Viergever, "Limits to the accuracy of vessel diameter measurement in MR angiography", *J Magn Reson Imaging*, vol. 8, no. 6, pp. 1228–35, Nov. 1998.
- [141] R.M. Hoogeveen, C.J.G. Bakker, M.A. Viergever, "MR phase-contrast flow measurement with limited spatial resolution in small vessels: value of model-based image analysis", *Magn Res Med*, vol. 41, no. 3, pp. 520–8, Mar. 1999.
- [142] J.J. Hopfield, "Neurons with graded responses have collective computational properties like those of two-state neurons", *Proc Nat Acad Sci*, vol. 81, pp. 3088–92, May 1984.
- [143] H. Hoppe, *Surface reconstruction from unorganized points*, Ph.D. thesis, Washington University, Seattle, US, 1994.
- [144] J. Huang, D. Abendschein, V. Davila, A.A. Amini, "Four-dimensional LV tissue tracking from tagged MRI with a 4D B-spline model", *IEEE Trans Med Imaging*, vol. 18, no. 10, pp. 957–72, Oct. 1999.
- [145] W-C. Huang & D. Goldgof, "Adaptive-size meshes for rigid and non-rigid analysis and synthesis", *IEEE Trans Pattern Anal Machine Intell*, vol. 15, no. 6, pp. 611–6, June 1993.
- [146] N.B. Ingels, G.T. Daughters, E.B. Stinson, E.L. Alderman, "Evaluation of methods for quantitating left ventricular segmental wall motion in man using myocardial markers as a standard", *Circulation*, vol. 61, no. 5, pp. 966–72, May 1980.
- [147] C. Kambhamettu & D.B. Goldgof, "Curvature-based approach to point correspondence recovery in conformal non-rigid motion", *Comp Vis Graph & Im Proc*, vol. 60, no. 1, pp. 26–43, July 1994.
- [148] D.A. Kass, T.A. Traill, M. Keating, P.I. Altieri, W.L. Maughan, "Abnormalities of dynamic ventricular shape change in patients with aortic and mitral valvular regurgitation: assessment by Fourier shape analysis and global geometric indexes", *Circ Res*, vol. 62, no. 1, pp. 127–38, Jan. 1988.
- [149] M. Kass, A. Witkin, D. Terzopoulos, "Snakes: active contour models", *Int J Comput Vision*, vol. 1, no. 4, pp. 321–31, Jan. 1988.
- [150] A. Kelemen, G. Székely, G. Guerig, "Elastic model-based segmentation of 3-D neuroradiological data sets", *IEEE Trans Med Imaging*, vol. 18, no. 10, pp. 828–39, Oct. 1999.

- [151] A.M. Keller, R.M. Peshock, C.R. Malloy, L.M. Buja, R. Nunnally, R.W. Parkey, J.T. Willerson, "In vivo measurement of myocardial mass using nuclear magnetic resonance imaging", *J Am Coll Cardiol*, vol. 8, no. 1, pp. 113–7, July 1986.
- [152] J.W. Kennedy, W.A. Baxley, M.M. Figley, H.T. Dodge, J.R. Blackmon, "Quantitative angiocardiology: I. The normal left ventricle in man", *Circulation*, vol. 34, pp. 272–8, Aug. 1966.
- [153] W.S. Kerwin & J.L. Prince, "Cardiac material markers from tagged MR images", *Med Image Anal*, vol. 2, no. 4, pp. 339–53, Dec. 1998.
- [154] W.S. Kerwin & J.L. Prince, "The Kriging update model and recursive space-time function estimation", *IEEE Trans Sig Proc*, vol. 47, no. 11, pp. 2942–52, Nov. 1999.
- [155] W.S. Kerwin & J.L. Prince, "Tracking MR tag surfaces using a spatiotemporal filter and interpolator", *Int J Image Syst Tech*, vol. 10, pp. 128–42, 1999.
- [156] H.C. Kim, B.G. Min, M.M. Lee, J.D. Seo, Y.W. Lee, M.C. Han, "Estimation of local cardiac wall deformation and regional wall stress from biplane coronary cineangiograms", *IEEE Trans Biomed Eng*, vol. 32, no. 7, pp. 503–12, July 1985.
- [157] J. Kittler & J. Illingworth, "Relaxation labeling algorithms – A review", *Imag Vis Comp*, vol. 3, no. 4, pp. 206–16, Nov. 1985.
- [158] A.K. Klein, F. Lee, A.A. Amini, "Quantitative coronary angiography with deformable spline models", *IEEE Trans Med Imaging*, vol. 16, no. 5, pp. 468–82, Oct. 1997.
- [159] K. Klingenberg-Regn, S. Schaller, T. Flohr, B. Ohnesorge, A.F. Kopp, U. Baum, "Subsecond multi-slice computed tomography: basics and applications", *Eur J Radiol*, vol. 31, no. 2, pp. 110–24, Aug. 1999.
- [160] J.J. Koenderink, "The structure of images", *Biol Cybern*, vol. 50, no. 5, pp. 363–70, 1984.
- [161] J.J. Koenderink & A.J. van Doorn, "Surface shape and curvature scales", *Imag Vis Comp*, vol. 10, no. 8, pp. 557–65, Oct. 1992.
- [162] Th. Koller, *From fata to information: segmentation, description and analysis of the cerebral vascularity*, Diss. ETH no. 11367, Swiss Federal Institute of Technology ETHZ, 1995.
- [163] Th. Koller, G. Gerig, G. Székely, D. Dettwiller, "Multiscale detection of curvilinear structures in 2-D and 3-D image data", in *Eur Conf Comp Vision*, IEEE Computer Society Press, pp. 864–9, June 1995.
- [164] C. Kondo, G.R. Caputo, R. Smelka, E. Foster, A. Shimakawa, C.B. Higgins, "Right and left ventricular stroke volume measurements with velocity-encoded cine MR imaging: *in vitro* and *in vivo* validation", *Am J Roentgenol*, vol. 157, no. 1, pp. 9–16, July 1991.
- [165] Y. Korogi, M. Takahashi, T. Nakagawa, N. Mabuchi, T. Watabe, Y. Shiokawa, H. Shiga, T. O'Uchi, H. Miki, Y. Horikawa, S. Fujiwara, M. Furuse, "Intracranial vascular stenosis and occlusion: MR angiographic findings", *Am J Neuroradiol*, vol. 18, no. 1, pp. 135–43, Jan. 1997.
- [166] D.L. Kraitchman, A.A. Young, C.-N. Chang, L. Axel, "Semiautomatic tracking of myocardial motion in MR tagged images", *IEEE Trans Med Imaging*, vol. 14, no. 3, pp. 422–33, Sept. 1995.
- [167] K. Krissian, G. Malandain, N. Ayache, "Model-based multiscale detection and reconstruction of 3D vessels", RR 3442, INRIA Sophia Antipolis, June 1998.
- [168] K. Krissian, G. Malandain, N. Vaillant, R. Ayache, Y. Troussset, "Model based detection of tubular structures in 3D images", RR 3736, INRIA Sophia Antipolis, July 1999.
- [169] R.A. Kruger, "Estimation of the diameter of an iodine concentration within blood vessels using digital radiography devices", *Med Phys*, vol. 8, no. 5, pp. 652–8, Sept. 1981.
- [170] S. Kumar & D. Goldgof, "Automatic tracking of SPAMM grid and the estimation of deformation parameters from cardiac MR images", *IEEE Trans Med Imaging*, vol. 13, no. 1, pp. 122–32, Mar. 1994.

- [171] R. Kutka & S. Stier, "Extraction of line properties based on direction fields", *IEEE Trans Med Imaging*, vol. 15, pp. 51–8, 1996.
- [172] M. Kuwahara & S. Eiho, "3-D heart image reconstructed from MRI data", *Comp Med Im & Graph*, vol. 15, no. 4, pp. 241–6, July 1991.
- [173] S. Lee, G. Wolberg, S.Y. Shin, "Scattered data interpolation with multilevel B-splines", *IEEE Trans Vis & Comp Graph*, vol. 3, no. 3, pp. 228–44, 1997.
- [174] M.E. Legget, D.F. Leotta, E.L. Bolson, J.A. McDonald, R.W. Martin, X.N. Li, C.M. Otto, F.H. Sheehan, "System for quantitative three dimensional echocardiography of the left ventricle based on magnetic field position and orientation sensing system", *IEEE Trans Biomed Eng*, vol. 45, no. 4, pp. 494–504, Apr. 1998.
- [175] B.P.F. Lelieveldt, *Anatomical Models in Cardiovascular Image Analysis*, Ph.D. thesis, Leiden University Medical Center, The Netherlands, 1999.
- [176] B.P.F. Lelieveldt, R.J. van der Geest, M. Ramze Rezaee, J.G. Bosch, J.H.C. Reiber, "Anatomical model matching with fuzzy implicit surfaces for segmentation of thoracic volume scan", *IEEE Trans Med Imaging*, vol. 18, no. 3, pp. 231–8, Mar. 1999.
- [177] D.F. Leotta, B. Munt, E.L. Bolson, C. Kraft, R.W. Martin, C.M. Otto, F.H. Sheehan, "Quantitative three-dimensional echocardiography by rapid imaging from multiple transthoracic windows: *in vitro* validation and initial *in vivo* studies", *J Am Soc Echocardiogr*, vol. 10, no. 8, pp. 830–9, Oct. 1997.
- [178] M. Leventon, W.E.L. Grimson, O. Faugeras, "Shape-based 3D surface correspondence using geodesics and local geometry", in *Comp Vis Patt Recogn*, vol. 1, IEEE Computer Society, South Carolina, USA, pp. 316–23, June 2000.
- [179] K.C. Li, "MR angiography of abdominal ischemia", *Semin Ultrasound CT MR*, vol. 17, no. 4, pp. 352–9, Aug. 1996.
- [180] K.C. Li, "Mesenteric occlusive disease", *Magn Reson Imaging Clin N Am*, vol. 6, no. 2, pp. 331–50, May 1998.
- [181] T. Lindeberg, "Edge detection and ridge detection with automatic scale selection", in *Comp Vis Patt Recogn*, IEEE Computer Society Press, San Francisco, USA, pp. 465–70, June 1996.
- [182] T. Lindeberg, "Feature detection with automatic scale selection", *Int J Comput Vision*, vol. 30, no. 2, pp. 79–116, Nov. 1998.
- [183] W.E. Lorensen & H.E. Cline, "Marching cubes: a high resolution 3D surface reconstruction algorithm", *Computer Graphics: SIGGRAPH'87 Conference Proceeding*, vol. 21, pp. 163–9, July 1987.
- [184] C. Lorenz, I.-C. Carlsen, T. M. Buzug, C. Fassnacht, J. Weese, "Multi-scale line segmentation with automatic estimation of width, contrast and tangential direction in 2D and 3D medical images", in *Proc CVRMed-MRCAS'97*, J. Troccaz, E. Grimson, R. Mösges (eds.), Lect Notes Comp Science, Springer-Verlag, Berlin, pp. 233–42, 1997.
- [185] C.H. Lorenz, E.S. Walker, V.L. Morgan, S.S. Klein, T.P. Graham, "Normal human right and left ventricular mass, systolic function, and gender differences by cine magnetic resonance imaging", *J Cardiovasc Magn Res*, vol. 1, no. 1, pp. 7–21, 1999.
- [186] J. Lötjönen, P.-J. Reissman, I.E. Magnin, T. Katila, "Model extraction from magnetic resonance volume data using a deformable pyramid", *Med Image Anal*, vol. 3, no. 4, pp. 387–406, Dec. 1999.
- [187] J. Maehle, K. Bjoernstad, S. Aakhus, H.G. Torp, B.A. Angelsen, "Three-dimensional echocardiography for quantitative left ventricular wall motion analysis: a method for reconstruction of endocardial surface and evaluation of regional dysfunction", *Echocardiogr*, vol. 11, no. 4, pp. 397–408, 1994.
- [188] R. Malladi, J. Sethian, B.C. Vemuri, "Shape modeling with front propagation: a level set approach", *IEEE Trans Pattern Anal Machine Intell*, vol. 17, no. 2, pp. 158–74, Feb. 1995.

- [189] G.B. Mancini, S.F. De Boe, E. Anselmo, S.B. Simon, M.T. Le Free, R.A. Vogel, "Quantitative regional curvature analysis: an application of shape determination for the assessment of segmental left ventricular function in man", *Am Heart J*, vol. 113, no. 2 Pt 1, pp. 326–34, Feb. 1987.
- [190] G.B.J. Mancini, S.F. DeBoe, M.J. McGillem, E.R. Bates, "Quantitative regional curvature analysis: a prospective evaluation of ventricular shape and wall motion measurements", *Am Heart J*, vol. 116, no. 6 Pt 1, pp. 1611–21, Dec. 1988.
- [191] W.J. Manning, W. Li, N.G. Boyle, R.R. Edelman, "Fat-suppressed breath-hold magnetic resonance coronary angiography", *Circulation*, vol. 87, no. 1, pp. 94–104, Jan. 1993.
- [192] J.T. Marcus, M.J.W. Götte, L.K. de Waal, M.R. Stam, R.J. van der Geest, R.M. Heethaar, A.C. van Rossum, "The influence of through-plane motion on left ventricular volumes measured by magnetic resonance imaging: implications for image acquisition and analysis", *J Cardiovasc Magn Res*, vol. 1, no. 1, pp. 1–6, 1999.
- [193] A. Matheny & D.M. Goldgof, "The use of three- and four-dimensional surface harmonics for rigid and nonrigid shape recovery and representation", *IEEE Trans Pattern Anal Machine Intell*, vol. 17, no. 10, pp. 967–81, Oct. 1995.
- [194] H.A. McCann, J.C. Sharp, Kinter T.M., C.N. McEwan, C. Barillot, J.F. Greenleaf, "Multi-dimensional ultrasonic imaging for cardiology", *Proc IEEE*, vol. 76, no. 9, pp. 1063–71, Sept. 1988. Special Issue on Emerging Electromedical Systems.
- [195] J. C. McEachen, A. Neohorai, J. S. Duncan, "A recursive filter for temporal analysis of cardiac motion", in *Math Meth Biomed Imag Anal*, Seattle, USA, pp. 124–33, 1994.
- [196] T. McInerney & D. Terzopoulos, "A dynamic finite element surface model for segmentation and tracking in multidimensional medical images with application to 4D image analysis", *Comp Med Im & Graph*, vol. 19, no. 1, pp. 69–83, Jan. 1995.
- [197] T. McInerney & D. Terzopoulos, "Deformable models in medical image analysis: a survey", *Med Image Anal*, vol. 1, no. 2, pp. 91–108, June 1996.
- [198] E.R. McVeigh, "MRI of myocardial function: motion tracking techniques", *Magn Res Img*, vol. 14, no. 2, pp. 137–50, 1996.
- [199] G.D. Meier, A.A. Bove, W.P. Santamore, P.R. Lynch, "Contractile function in canine right ventricle", *Am J Physiol*, vol. 239, no. 6, pp. H794–804, Dec. 1980.
- [200] E.H.W. Meijering, W.J. Niessen, M.A. Viergever, "Retrospective motion correction in digital subtraction angiography: a review", *IEEE Trans Med Imaging*, vol. 18, no. 1, pp. 2–21, Jan. 1999.
- [201] E.H.W. Meijering, K.J. Zuiderveld, M.A. Viergever, "Image reconstruction by convolution with symmetrical piecewise n -th order polynomial kernels", *IEEE Trans Imag Proc*, vol. 8, no. 2, pp. 192–201, Feb. 1999.
- [202] D.N. Metaxas, *Physics-based deformable models: applications to computer vision, graphics and medical imaging*, Kluwer Academic Publisher, Cambridge, 1996.
- [203] D.N. Metaxas, E. Koh, N.I. Badler, "Multi-level shape representation using global deformations and locally adaptive finite elements", *Int J Comput Vision*, vol. 25, no. 1, pp. 49–61, Oct. 1997.
- [204] D.N. Metaxas & D. Terzopoulos, "Shape and nonrigid motion estimation through physics-based synthesis", *IEEE Trans Pattern Anal Machine Intell*, vol. 15, no. 6, pp. 580–91, 1993.
- [205] F.G. Meyer, R.T. Constable, A.J. Sinusas, J.S. Duncan, "Tracking myocardial deformation using phase contrast MR velocity fields : a stochastic approach", *IEEE Trans Med Imaging*, vol. 15, no. 4, pp. 453–65, Aug. 1996.
- [206] S.K. Mishra, D.B. Goldgof, T.S. Huang, C. Kambhamettu, "Curvature-based non-rigid motion analysis from 3D point correspondences", *Int J Image Syst Tech*, vol. 4, pp. 214–25, 1992.
- [207] C.A. Mistretta, "Relative characteristics of MR angiography and competing vascular imaging modalities", *J Magn Reson Imaging*, vol. 3, no. 5, pp. 685–98, Sept. 1993.

- [208] O. Monga, R. Deriche, J.-M. Rocchisani, "3D edge detection using recursive filtering: application to scanner images", *Comp Vis Graph & Im Proc: Imag Underst*, vol. 53, no. 1, pp. 76–87, Jan. 1991.
- [209] J. Montagnat, H. Delingette, G. Malandain, "Cylindrical Echocardiographic Image Segmentation Based on 3D Deformable Models", in Taylor and Colchester [289].
- [210] C.C. Moore, W.G. O'Dell, E.R. McVeigh, E.A. Zerhouni, "Calculation of three-dimensional left ventricular strains from biplanar tagged MR images", *J Magn Reson Imaging*, vol. 2, no. 2, pp. 165–75, Mar. 1992.
- [211] M.J. Moulton, L.L. Creswell, S.W. Downing, R.L. Actis, B.A. Szabo, M.W. Vannier, M.K. Pasque, "Spline surface interpolation for calculating 3-D ventricular strains from MRI tissue tagging", *Am J Physiol*, vol. 270, no. 1 Pt 2, pp. H281–97, Jan. 1996.
- [212] B.I. Munt, D.F. Leotta, E.L. Bolson, K. Coady, R.W. Martin, C.M. Otto, F.H. Sheehan, "Left ventricular shape analysis from three-dimensional echocardiograms", *J Am Soc Echocardiogr*, vol. 11, no. 8, pp. 761–9, Aug. 1998.
- [213] C. Nastar & N. Ayache, "Frequency-based nonrigid motion analysis: application to four dimensional medical images", *IEEE Trans Pattern Anal Machine Intell*, vol. 18, no. 11, pp. 1067–79, Nov. 1996.
- [214] T.R. Nelson, D.B. Downey, D.H. Pretorius, A. Fenster, *Three-dimensional Ultrasound*, Lippincott Williams & Wilkins, Philadelphia, 1999.
- [215] W.J. Niessen, B. M. ter Haar Romeny, M.A. Viergever, "Geodesic deformable models for medical image analysis", *IEEE Trans Med Imaging*, vol. 17, no. 4, pp. 634–41, Aug. 1998.
- [216] North American Symptomatic Carotid Endarterectomy Trial (NASCET) Steering Committee, "North American Symptomatic Carotid Endarterectomy Trial. Methods, patient characteristics, and progress", *Stroke*, vol. 22, no. 6, pp. 711–20, June 1991.
- [217] W.G. O'Dell, C.C. Moore, W.C. Hunter, E.A. Zerhouni, E.R. McVeigh, "Three-dimensional myocardial deformations: calculation with displacement field fitting to tagged MR images", *Radiology*, vol. 195, no. 3, pp. 829–35, June 1995.
- [218] T. O'Donnell, T. Boult, A. Gupta, "Global models with parametric offsets as applied to cardiac motion recovery", in *Comp Vis Patt Recogn*, IEEE Computer Society, San Francisco, USA, pp. 293–9, June 1996.
- [219] T. O'Donnell, A. Gupta, T. Boult, "The hybrid volumetric ventriculoid: new model for MR-SPAMM 3-D analysis", in *IEEE Comput in Cardiol*, IEEE Computer Society Press, Vienna, Austria, pp. 5–8, Sept. 1995.
- [220] B. Ohnesorge, T. Flohr, C. Becker, A. Knez, A.F. Kopp, Fukuda K., M.F. Reiser, "Cardiac imaging with rapid, retrospective ECG synchronized multilevel spiral CT", *Der Radiologe*, vol. 40, no. 2, pp. 111–7, Feb. 2000. In German.
- [221] M.M. Orkisz, C. Bresson, I.E. Magnin, O. Champin, P. C. Douek, "Improved vessel visualization in MR angiography by nonlinear anisotropic filtering", *Magn Res Med*, vol. 37, no. 6, pp. 914–9, June 1997.
- [222] S. Osher & S. Sethian, "Fronts propagating with curvature dependent speed: algorithms based on the Hamilton-Jacobi formalism", *J Computat Phys*, vol. 79, pp. 12–49, 1988.
- [223] N.F. Osman & J.L. Prince, "Visualizing myocardial function using HARP MRI", *Phys Med Biol*, vol. 45, no. 6, pp. 1665–82, June 2000.
- [224] N. F. Osman, W. S. Kerwin, E. R. McVeigh, J. L. Prince, "Cardiac motion tracking using CINE harmonic phase (HARP) magnetic resonance imaging", *Magn Res Med*, vol. 42, no. 6, pp. 1048–60, Dec. 1999.
- [225] N. F. Osman & J. L. Prince, "Motion estimation from tagged MR images using angle images", in *Int Conf Imag Proc*, vol. 1, IEEE Comp Soc Press, Chicago, pp. 704–8, 1998.
- [226] C. Öztürk & E.R. McVeigh, "Four-dimensional B-spline based motion analysis of tagged cardiac MR images", in *SPIE*, vol. 3660, pp. 46–56, 1999.

- [227] X.M. Pan, D. Saloner, L.M. Reilly, J.C. Bowersox, S.P. Murray, C.M. Anderson, G.A. Gooding, J.H. Rapp, "Assessment of carotid artery stenosis by ultrasonography, conventional angiography, and magnetic resonance angiography: correlation with *ex vivo* measurements of plaque stenosis", *J Vasc Surg*, vol. 21, no. 1, pp. 82–9, Jan. 1995.
- [228] N.G. Pandian, D.J. Skorton, S.M. Collins, H.L. Falsetti, E.R. Burke, R.E. Kerber, "Heterogeneity of left ventricular segmental wall thickening and excursion in 2-dimensional echocardiograms of normal human subjects", *Am J Cardiol*, vol. 51, no. 10, pp. 1667–73, June 1983.
- [229] X. Papademetris, P. Shi, D.P. Dione, A.J. Sinusas, R.T. Constable, J.S. Duncan, "Recovery of soft tissue object deformation from 3D image sequences using biomechanical models", in *Inf Proc Med Imag*, A. Kuba, M. Sámal, A. Todd-Pokropek (eds.), vol. 1613 of *Lect Notes Comp Science*, Springer Verlag, pp. 352–7, 1999.
- [230] X. Papademetris, P. Shi, D.P. Dione, A.J. Sinusas, R.T. Constable, J.S. Duncan, "Recovery of soft tissue object deformation from 3D image sequences using biomechanical models", Tech Report 1999-01, Image Processing and Analysis Lab, Dep of Diagnostic Radiology, Yale University, June 1999.
- [231] X. Papademetris, A.J. Sinusas, D.P. Dione, J.S. Duncan, "3D Cardiac deformation from ultrasound images", in Taylor and Colchester [289].
- [232] J. Park, D.N. Metaxas, L. Axel, "Analysis of left ventricular wall motion based on volumetric deformable models and MRI-SPAMM", *Med Image Anal*, vol. 1, no. 1, pp. 53–72, Mar. 1996.
- [233] J. Park, D.N. Metaxas, A.A. Young, L. Axel, "Deformable models with parameter functions for cardiac motion analysis from tagged MRI data", *IEEE Trans Med Imaging*, vol. 15, no. 3, pp. 278–89, June 1996.
- [234] A. Pentland & B. Horowitz, "Recovery of nonrigid motion and structure", *IEEE Trans Pattern Anal Machine Intell*, vol. 13, no. 7, pp. 730–42, July 1991.
- [235] A. Pentland & S. Sclaroff, "Closed-form solutions for physically based shape modeling and recognition", *IEEE Trans Pattern Anal Machine Intell*, vol. 13, no. 7, pp. 703–14, July 1991.
- [236] L. Piegl & W. Tiller, *The NURBS Book*, 2nd ed., Monographs in Visual Communication, Springer Verlag, Berlin, 1996.
- [237] J.S. Pirola, S.J. Bresina, L.L. Creswell, K.W. Myers, B.A. Szabó, M.W. Vannier, M.K. Pasque, "Mathematical three-dimensional solid modeling of biventricular geometry", *Ann Biomed Eng*, vol. 21, no. 3, pp. 199–219, May 1993.
- [238] S.M. Pizer, D. Eberly, B.S. Morse, D.S. Fritsch, "Zoom-invariant vision of figural shape: the mathematics of cores", *Comp Vis Image Underst*, vol. 69, no. 1, pp. 55–71, Jan. 1998.
- [239] R. Poli & G. Valli, "An algorithm for real-time vessel enhancement and detection", *Comput Methods Programs Biomed*, vol. 52, no. 1, pp. 1–22, 1996.
- [240] M.J. Potel, J.M. Rubin, S.A. MacKay, A.M. Aisen, J. Al-Sadir, R.E. Sayre, "Methods for evaluating cardiac wall motion in three dimensions using bifurcation points of the coronary arterial tree.", *Inv Rad*, vol. 18, no. 1, pp. 47–57, Jan. 1983.
- [241] W.H. Press, S.A. Teukolsky, W.T. Vetterling, B.P. Flannery, *Numerical recipes in C: The art of scientific computing*, 2nd ed., Cambridge University Press, Cambridge, 1992.
- [242] J.L. Prince & E.R. McVeigh, "Motion estimation from tagged MR image sequences", *IEEE Trans Med Imaging*, vol. 11, no. 2, pp. 238–49, June 1992.
- [243] M.R. Prince, "Gadolinium-enhanced MR aortography", *Radiology*, vol. 191, no. 1, pp. 155–64, Apr. 1994.
- [244] J.U. Quistgaard, "Signal acquisition and processing in medical diagnostic ultrasound", *IEEE Sign Proc Magazine*, pp. 67–74, Jan. 1997.
- [245] P. Radeva, A.A. Amini, J. Huang, "Deformable B-solids and implicit snakes for 3D localization and tracking of SPAMM MRI data", *Comp Vis Image Underst*, vol. 66, no. 2, pp. 163–78, May 1997.
- [246] S. Ranganath, "Contour extraction from cardiac MRI studies using snakes", *IEEE Trans Med Imaging*, vol. 14, no. 2, pp. 56–64, June 1995.

- [247] J.S. Rankin, P.A. McHale, C.E. Artentzen, D. Ling, J.C. Greenfield, R.W. Anderson, "The three-dimensional dynamic geometry of the left ventricle in the conscious dog", *Circ Res*, vol. 39, no. 3, pp. 304–13, Sept. 1976.
- [248] M.J. Raphael & R.M. Donaldson, "The normal heart: methods of examination", in *Textbook of Radiology and Imaging*, D. Sutton (ed.), 6th ed., Churchill Livingstone, New York, pp. 541–65, 1998.
- [249] S.P. Raya & J.K. Udupa, "Shape-based interpolation of multidimensional objects", *IEEE Trans Med Imaging*, vol. 9, no. 1, pp. 32–42, Jan. 1990.
- [250] J.H.C. Reiber & P.W. Serruys, "Quantitative coronary angiography", in *Cardiac Imaging—A Companion to Braunwald's Heart Disease*, M.L. Marcus & et. al. (eds.), Saunders, Philadelphia, 1991.
- [251] A.A. Requicha & H.B. Voelcker, "Solid modeling: a historical summary and contemporary assessment", *IEEE Comp Graph & Appl*, vol. 2, no. 2, pp. 9–24, Mar. 1982.
- [252] R.A. Robb, E.A. Hoffman, L.J. Sinak, L.D. Harris, E.L. Ritman, "High-speed three-dimensional X-ray computed tomography: the dynamic spatial reconstructor", *Proc IEEE*, vol. 71, no. 3, pp. 308–19, Mar. 1983. Special Issue on Emerging Electromedical Systems.
- [253] G.D. Rubin, M.D. Dake, C.P. Semba, "Current status of three-dimensional spiral CT scanning for imaging the vasculature", *Radiol Clin North Am*, vol. 33, no. 1, pp. 51–70, Jan. 1995.
- [254] D. Rueckert & P. Burger, "Geometrically deformable templates for shape-based segmentation and tracking in cardiac MR image", in *Energy Minim Meth Comput Vision & Patt Recog*, vol. 1223 of *Lect Notes Comp Science*, Springer Verlag, Venice, Italy, 1997.
- [255] D. Rueckert, L.I. Sonoda, C. Hayes, D.L.G. Hill, M.O. Leach, D.J. Hawkes, "Non-rigid registration using free-form deformations: application to breast MR images", *IEEE Trans Med Imaging*, vol. 18, no. 8, pp. 712–21, Aug. 1999.
- [256] M.S. Sacks, C.J. Chuong, G.H. Templeton, R. Peshock, "In vivo 3-D reconstruction and geometric characterization of the right ventricular free wall", *Ann Biomed Eng*, vol. 21, no. 3, pp. 263–75, May 1993.
- [257] S. Sasayama, H. Nonogi, M. Fujita, T. Sakurai, A. Wakabayashi, C. Kawai, S. Eiho, M. Kuwahara, "Three-dimensional analysis of regional myocardial function in response to nitroglycerin in patient with coronary artery disease", *J Am Coll Cardiol*, vol. 3, no. 5, pp. 1187–96, May 1984.
- [258] Y. Sato, T. Araki, M. Hanayama, H. Naito, S. Tamura, "A viewpoint determination system for stenosis diagnosis and quantification in coronary angiographic image acquisition", *IEEE Trans Med Imaging*, vol. 17, no. 1, pp. 121–37, Feb. 1998.
- [259] Y. Sato, M. Moriyama, M. Hanayama, H. Naito, S. Tamura, "Acquiring 3D models of non-rigid moving objects from time and viewpoint varying image sequences: a step toward left ventricle recovery", *IEEE Trans Pattern Anal Machine Intell*, vol. 19, no. 3, pp. 253–9, Mar. 1997.
- [260] Y. Sato, S. Nakajima, H. Atsumi, Th. Koller, G. Gerig, S. Yoshida, R. Kikinis, "3D multi-scale line filter for segmentation and visualization of curvilinear structures in medical images", in *CVRMed-MRCAS'97*, J. Troccaz, E. Grimson, R. Mösges (eds.), Lect Notes Comp Science, Springer Verlag, Berlin, pp. 213–22, 1997.
- [261] Y. Sato, S. Nakajima, N. Shiraga, H. Atsumi, S. Yoshida, Th. Koller, G. Gerig, R. Kikinis, "Three-dimensional multi-scale line filter for segmentation and visualization of curvilinear structures in medical images", *Med Image Anal*, vol. 2, no. 2, pp. 143–68, June 1998.
- [262] J.A. Schnabel, D. Rueckert, V. Knowles, D.L.G. Hill, D.J. Hawkes, "Non-rigid registration using multi-level non-uniform free-form deformations: application to inter-subject registration of brain MRI", 2001. Submitted.
- [263] S. Schreiner, C.B. Paschal, R.L. Galloway, "Comparison of projection algorithms used for the construction of maximum intensity projection images", *J Comput Assist Tomogr*, vol. 20, no. 1, pp. 56–67, Jan. 1996.
- [264] W.J. Schroeder, J.A. Zarge, W.E. Lorensen, "Decimation of triangle meshes", *Comp Graphics*, vol. 26, no. 2, pp. 65–70, 1992.

- [265] F.C. Schweppe, *Uncertain dynamic systems*, Prentice-Hall, Inc., Englewood Cliffs, NJ, 1973.
- [266] T.W. Sederberg & S.R. Parry, "Free-form deformation of solid geometric models", in *SIGGRAPH'86*, vol. 20, ACM, Dallas, USA, pp. 151–60, 1986.
- [267] J.A. Sethian, *Level set methods and fast marching methods: evolving interfaces in computational geometry, fluid mechanics, computer vision, and materials science*, 2nd ed., Cambridge Monographs on Applied and Computational Mathematics, Cambridge University Press, Cambridge, 1999.
- [268] E. Shapiro, D. L. Marier, M. G. St. John Sutton, D. G. Gibson, "Regional non-uniformity of wall dynamics in normal left ventricle", *Br Heart J*, vol. 45, no. 3, pp. 264–70, Mar. 1981.
- [269] F.H. Sheehan, E.L. Bolson, H.T. Dodge, D.G. Mathey, J. Schofer, H.K. Woo, "Advantages and applications of the centerline method for characterizing regional ventricular function", *Circulation*, vol. 74, no. 2, pp. 293–305, Aug. 1986.
- [270] F.H. Sheehan, E.L. Bolson, R.W. Martin, G. Bashein, J. McDonald, "Quantitative three dimensional echocardiography: methodology, validation and clinical applications", in Wells et al. [312].
- [271] P. Shi, A.J. Sinusas, R.T. Constable, J.S. Duncan, "Volumetric deformation analysis using mechanics-based data fusion: application in cardiac motion recovery", *Int J Comput Vision*, vol. 35, no. 1, pp. 87–107, Nov. 1999.
- [272] P. Shi, A.J. Sinusas, R.T. Constable, E. Ritman, J.S. Duncan, "Point-tracked quantitative analysis of left ventricular surface motion from 3D image sequences: algorithms and validation", *IEEE Trans Med Imaging*, vol. 19, no. 1, pp. 36–50, Jan. 2000.
- [273] M.L. Simoons, "The European Heart Survey: inventory of the care of cardiovascular diseases", Presentation of the ESC President Elect at the XXist European Society of Cardiology Congress, Barcelona, 1999.
- [274] A. Singh, D. Goldgof, D. Terzopoulos (eds.), *Deformable models in medical image analysis*, IEEE Computer Society Press, Los Alamitos, CA, 1998.
- [275] R.F. Smith, B.K. Rutt, A.J. Fox, R.N. Rankin, D.W. Holdsworth, "Geometric characterization of stenosed human carotid arteries", *Acad Radiol*, vol. 3, no. 11, pp. 898–911, Nov. 1996.
- [276] F. Solina & R. Bajcsy, "Recovery of parametric models from range images: the case of superquadric with global deformations", *IEEE Trans Pattern Anal Machine Intell*, vol. 12, no. 2, pp. 131–47, Feb. 1990.
- [277] S.M. Song & R.M. Leahy, "Computation of 3D velocity fields from 3D cine CT images of a human heart", *IEEE Trans Med Imaging*, vol. 10, no. 3, pp. 295–306, Sept. 1991.
- [278] S.M. Song, R.M. Leahy, D.P. Boyd, B.H. Brundage, S. Napel, "Determining cardiac velocity fields and intraventricular pressure distribution from a sequence of ultrafast CT cardiac images", *IEEE Trans Med Imaging*, vol. 14, no. 2, pp. 386–97, June 1994.
- [279] P.D. Sozou, T.F. Cootes, C.J. Taylor, E.C. Di Mauro, "Non-linear point distribution modelling using a multi-layer perceptron", *Imag Vis Comp*, vol. 15, no. 6, pp. 457–63, 1997.
- [280] F.G. Spinale, B.A. Carabello, F.A. Crawford, "Right ventricular function and three-dimensional modeling using computer-aided design", *J Appl Physiol*, vol. 68, no. 4, pp. 1707–16, Apr. 1990.
- [281] L.H. Staib & J.S. Duncan, "Model-based deformable surface finding for medical images", *IEEE Trans Med Imaging*, vol. 15, no. 5, pp. 720–31, May 1996.
- [282] C. Steger, "An unbiased detector of curvilinear structures", *IEEE Trans Pattern Anal Machine Intell*, vol. 20, no. 2, pp. 113–25, Feb. 1998.
- [283] G.D. Stetten & S.M. Pizer, "Medial-node models to identify and measure objects in real-time 3-D echocardiography", *IEEE Trans Med Imaging*, vol. 18, no. 10, pp. 1025–34, Oct. 1999.
- [284] C. Studholme, D.L.G. Hill, D.J. Hawkes, "Automated 3D registration of MR and PET brain images by multiresolution optimization of voxel similarity measures", *Med Phys*, vol. 24, no. 1, pp. 25–35, 1997.

- [285] C. Studholme, D.L.G. Hill, D.J. Hawkes, "An overlap invariant entropy measure of 3D medical image alignment", *Pattern Recogn*, vol. 32, no. 1, pp. 71–86, 1998.
- [286] P.E. Summers, A.H. Bhalerao, D.J. Hawkes, "Multiresolution, model-based segmentation of MR angiograms", *J Magn Reson Imaging*, vol. 7, pp. 950–7, 1997.
- [287] J.S. Suri, "Computer vision, pattern recognition and image processing in left ventricle segmentation: the last 50 years", *Pattern Anal & Appl*, vol. 3, no. 3, pp. 209–42, 2000.
- [288] A.M. Taratorin & S. Sideman, "3D functional mapping of left ventricular dynamics", *Comp Med Im & Graph*, vol. 19, no. 1, pp. 113–29, Jan. 1995.
- [289] C.J. Taylor & A. Colchester (eds.), *Med Imag Comput & Comp Assist Intervent* (Cambridge, UK, Oct. 1999), vol. 1679 of *Lect Notes Comp Science*, Springer Verlag.
- [290] D. Terzopoulos, "Regularization of inverse visual problems involving discontinuities", *IEEE Trans Pattern Anal Machine Intell*, vol. 8, no. 4, pp. 413–24, Apr. 1986.
- [291] D. Terzopoulos & D.N. Metaxas, "Dynamic 3D models with local and global deformations: deformable superquadrics", *IEEE Trans Pattern Anal Machine Intell*, vol. 13, no. 7, pp. 703–14, July 1991.
- [292] D. Terzopoulos, A. Witkin, M. Kass, "Constraints on deformable models: recovering 3D shape and nonrigid motion", *Artif Intell*, vol. 36, no. 1, pp. 91–123, 1988.
- [293] M. Tistarelli & G. Marcennaro, "Using optical flow to analyze the motion of human body organs from bioimages", in *Math Meth Biomed Imag Anal*, Seattle, USA, pp. 100–9, 1994.
- [294] G. Treece, R. Prager, A. Gee, L. Berman, "Volume measurements in sequential freehand 3-D ultrasound", in *Inf Proc Med Imag*, A. Kuba, M. Sámal, A. Todd-Pokropek (eds.), vol. 1613 of *Lect Notes Comp Science*, Springer Verlag, pp. 70–83, 1999.
- [295] Y.-H. Tseng, J.-N. Hwang, F.H. Sheehan, "Three-dimensional object representation and invariant recognition using continuous distance transform neural networks", *IEEE Trans Neural Networks*, vol. 8, no. 1, pp. 141–7, Jan. 1997.
- [296] Y.-H. Tseng, J.-N. Hwang, F.H. Sheehan, "3-D heart modeling and motion estimation based on continuous distance transform neural networks and affine transform", *J VLSI Sign Proc Syst for Sign, Imag & Video Technol*, vol. 18, no. 3, pp. 207–18, Apr. 1998.
- [297] H.K. Tu, A. Matheny, D.B. Goldgof, H. Bunke, "Left ventricular boundary detection from spatio-temporal volumetric computed tomography images", *Comp Med Im & Graph*, vol. 19, no. 1, pp. 27–46, Jan. 1995.
- [298] R.K. Tu, W.A. Cohen, K.R. Maravilla, W.H. Bush, N.H. Patel, J. Eskridge, H.R. Winn, "Digital subtraction rotational angiography for aneurysms of the intracranial anterior circulation: injection method and optimization", *Am J Neuroradiol*, vol. 17, no. 6, pp. 1127–36, June 1996.
- [299] R.J. van der Geest, A. de Roos, E.E. van der Wall, J.H.C. Reiber, "Quantitative analysis of cardiovascular MR images", *Int J Card Imag*, vol. 13, no. 3, pp. 247–58, June 1997.
- [300] K.J. van Everdingen, C.J. Klijn, L.J. Kappelle, W.P.Th.M. Mali, J. van der Grond, "MRA flow quantification in patients with symptomatic internal carotid artery occlusion. The Dutch EC-IC Bypass Study Group", *Stroke*, vol. 28, no. 8, pp. 1595–600, Aug. 1997.
- [301] R.L. Vanninen, H.I. Manninen, P.K. Partanen, H. Tulla, P.A. Vainio, "How should we estimate carotid stenosis using magnetic resonance angiography?", *Neuroradiology*, vol. 38, no. 4, pp. 299–305, May 1996.
- [302] B.C. Vemuri, Y. Guo, S.H. Lai, C.M. Leonard, "Fast algorithms for fitting multiresolution hybrid shape models to brain MRI", in *Visualiz Biomed Comput*, K. H. Höhne & R. Kikinis (eds.), vol. 1131 of *Lect Notes Comp Science*, Springer Verlag, pp. 213–28, 1996.
- [303] B.C. Vemuri & A. Radisavljevic, "Multiresolution stochastic hybrid shape models with fractal priors", *ACM Trans Graph*, vol. 13, no. 2, pp. 177–207, Apr. 1994.
- [304] F. L. Villarreal, L. K. Waldman, W. Y. W. Lew, "Technique for measuring regional two-dimensional finite strains in canine left ventricle", *Circ Res*, vol. 62, no. 4, pp. 711–21, Apr. 1988.

- [305] P. Viola, *Alignment by maximization of mutual information*, Ph.D. thesis, AI Lab, Massachusetts Institute of Technology, USA, 1995.
- [306] C. Vuille & A.E. Weyman, "Left ventricle I: general considerations, assessment of chamber size and function", in *Principles and practice of echocardiography*, A. E. Weyman (ed.), 2nd. ed., Lea and Febiger, Philadelphia, 1994.
- [307] E. Waks, J.L. Prince, A. Douglas, "Cardiac motion simulator for tagged MRI", in *Math Meth Biomed Imag Anal*, pp. 182–91, 1996.
- [308] Y. Wang, B.S. Peterson, L.W. Staib, "Shape-based 3D surface correspondence using geodesics and local geometry", in *Comp Vis Patt Recogn*, vol. 2, IEEE Computer Society, South Carolina, USA, pp. 644–51, June 2000.
- [309] D.F. Watson, "Computing the n-dimensional Delaunay tessellation with application to Voronoi polytopes", *The Computer Journal*, vol. 24, no. 2, pp. 167–72, May 1981.
- [310] J.R. Waugh & N. Sacharias, "Arteriographic complications in the DSA era", *Radiology*, vol. 182, no. 1, pp. 243–6, Jan. 1992.
- [311] K.T. Weber & E.W. Hawthorne, "Descriptors and determinants of cardiac shape: an overview", *Fed Proc*, vol. 40, no. 7, pp. 2005–10, May 1981.
- [312] W.M. Wells, A. Colchester, S. Delp (eds.), *Medical Imaging Computing & Computer-Assisted Intervention* (Boston, USA, Sept. 1998), vol. 1496 of *Lect Notes Comp Science*, Springer Verlag.
- [313] W. Wesselink, *Variational modeling of curves and surfaces*, Ph.D. thesis, Computer Science Department, Utrecht University, The Netherlands, 1996.
- [314] D.L. Wilson & J.A. Noble, "Segmentation of cerebral vessels and aneurysms from MR angiography data", in *Inf Proc Med Imag*, J. Duncan & G. Gindi (eds.), Poultney, Vermont, USA, pp. 423–8, June 1997.
- [315] G.A. Wright, "Magnetic resonance imaging", *IEEE Sign Proc Magazine*, pp. 56–66, Jan. 1997.
- [316] A.L. Yettram & C.A. Vinson, "Geometric modeling of the human left ventricle", *J Biomech*, vol. 101, pp. 221–3, 1979.
- [317] A.L. Yettram, C.A. Vinson, D.G. Gibson, "Computer modeling of the human left ventricle", *J Biomech*, vol. 104, no. 2, pp. 148–52, May 1982.
- [318] A. Yezzi, S. Kichenassamy, A. Kumar, P. Olver, A. Tannenbaum, "A geometric snake model for segmentation of medical imagery", *IEEE Trans Med Imaging*, vol. 16, no. 2, pp. 199–209, Apr. 1997.
- [319] A. Yezzi, A. Tannenbaum, S. Kichenassamy, P. Olver, "A gradient surface approach to 3-D segmentation", in *Proc IS&T 49th Ann Conf*, Minneapolis, USA, May 1996.
- [320] A.A. Young, "Model tags: direct 3D tracking of heart wall motion from tagged MR images", *Med Image Anal*, vol. 3, no. 4, pp. 361–72, Dec. 1999.
- [321] A.A. Young & L. Axel, "Three-dimensional motion and deformation of the heart wall: estimation with spatial modulation of magnetization— a model-based approach", *Radiology*, vol. 185, no. 1, pp. 241–47, Oct. 1992.
- [322] A.A. Young, L. Axel, L. Dougherty, D.K. Bogen, C.S. Parenteau, "Validation of tagging with MR imaging to estimate material deformation", *Radiology*, vol. 188, no. 1, pp. 101–8, July 1993.
- [323] A.A. Young, P.J. Hunter, B.H. Smaill, "Epicardial surface estimation from coronary angiograms", *Comp Vis Graph & Im Proc*, vol. 47, no. 1, pp. 111–27, July 1989.
- [324] A.A. Young, P.J. Hunter, B.H. Smaill, "Estimation of epicardial strain using the motions of coronary bifurcations in biplane cineangiography", *IEEE Trans Biomed Eng*, vol. 39, no. 5, pp. 526–31, May 1992.
- [325] A.A. Young, D.L. Kraitchman, L. Dougherty, L. Axel, "Tracking and finite element analysis of stripe deformation in magnetic resonance tagging", *IEEE Trans Med Imaging*, vol. 14, no. 3, pp. 413–21, Sept. 1995.

- [326] E.A. Zerhouni, D.M. Parish, W.J. Rogers, A. Yang, E.P. Shapiro, "Human heart: Tagging with MR imaging - a method for noninvasive assessment of myocardial motion", *Radiology*, vol. 169, no. 1, pp. 59–63, Oct. 1988.
- [327] S. Zhang, M. A. Douglas, L. Yaroslavsky, R. M. Summers, V. Dilsizian, L. Fananapazir, S. L. Bacharach, "A Fourier based algorithm for tracking SPAMM tags in gated magnetic resonance cardiac images", *Med Phys*, vol. 23, no. 8, pp. 1359–69, Aug. 1996.

Samenvatting

Volumetrische beeldvormende technieken zoals Computed Tomography (CT), Magnetic Resonance Imaging (MRI), Positron Emission Tomography (PET), Single Photon Emission Computed Tomography (SPECT) en Ultrasound (US) verschaffen de clinici een grote hoeveelheid anatomische en functionele informatie. Dit heeft er toe geleid dat de vraag naar technieken om zo optimaal mogelijk gebruik te maken van de overvloed aan beschikbare informatie drastisch is toegenomen en medische beeldanalyse met behulp van computers een levendig vakgebied is geworden.

Door de jaren heen is het werkterrein van de medische beeldanalyse uitgebreid. Klassieke problemen die in deze discipline veel aandacht hebben gekregen zijn o.a. beeldregistratie, kwantificatie en visualisatie van volumetrische datasets, rigide en niet-rigide bewegingsanalyse, beeldsegmentatie en patroonherkenning. Recentelijk heeft de introductie van computerondersteunde technieken in de chirurgie tot nieuwe onderzoeksgebieden geleid, zoals de ontwikkeling van technieken voor chirurgische planning, simulatie en intra-operatieve navigatie.

In eerste instantie werd medische beeldanalyse verricht door gebruik te maken van eenvoudige, zogenaamde *low level* operatoren, die vervolgens gecombineerd werden. In de beeldsegmentatie behoren bijvoorbeeld drempeling, *region growing*, statistische pixel-clustering en *relaxation labeling* tot de meest populaire technieken. Deze *bottom-up* benaderingen hadden als doel volledig automatisch te zijn. Hoewel een volledige automatisering vanuit het standpunt van de gebruiker ideaal zou zijn, kan dit over het algemeen slechts bereikt worden indien de te onderzoeken structuren een goed contrast hebben ten opzichte van de achtergrond. Doordat een *bottom-up* aanpak slechts lokale informatie gebruikt, is ze kwetsbaar voor onvolkomenheden in klinische data, waarvan de beeldkwaliteit beperkt wordt vanwege veiligheidsaspecten, beperkte opnametijd en patiëntbewegingen.

In de laatste twee decennia zijn in de literatuur over medische beeldanalyse veel *top-down* benaderingen geïntroduceerd. In deze benaderingen staat de introductie van *a priori* kennis in de modelvorm ter ondersteuning van de medische analysetaak centraal. Een model, in de betekenis van een vereenvoudiging van de fysische werkelijkheid, wordt in de wetenschap vaak gebruikt om een probleem te reduceren tot hanteerbare proporties. Echter, in de medische beeldanalyse zijn de modelgebaseerde strategieën dikwijls geavanceerder dan modelvrije benaderingen. Het gebruik van generieke of *a priori* contextuele kennis is met name aantrekkelijk in medische toepassingen waar de te analyseren structuur (weefsel of orgaan), de beeldvormende modaliteit en het acquisitieprotocol op voorhand bekend zijn.

Er zijn verschillende argumenten ten faveure van modelgestuurde medische beeldanalyse. In sommige gevallen is het gebruik van *a priori* modellen noodzakelijk. Dit is typisch het geval wanneer ten gevolge van beperkte beeldkwaliteit de oplossingsruimte verkleind dient te worden om tot een plausibele oplossing te komen. Een bijkomend voordeel is dat de beeldanalysetaak op een hoger abstractieniveau kan worden uitgevoerd. Ter toelichting volgen enkele voorbeelden. Een model dat de vorm van een orgaan beschrijft, kan worden uitgedrukt in een klein aantal parameters die direct diagnostische informatie geven. Daarnaast kan een geometrisch model worden gebruikt ter ondersteuning van een gebruikersvriendelijke interactie, *i.e.* het manipuleren van krommen of oppervlakken in plaats van interactie met de data op voxelniveau. Een spatio-temporeel model kan een compacte beschrijving geven van een beweging in een beeldreeks, die robuust is voor extreme afwijkingen en rekening houdt met vooraf opgelegde randvoorwaarden zoals de periodiciteit van de beweging. Een andere reden om voor een modelgebaseerde benadering te kiezen is de complexiteit van algoritmen. Een model reduceert het aantal vrijheidsgraden ten opzichte van een modelvrije analyse. Dit is typisch het geval in modellen van objectvormen waar een geschikte geometrische

representatie het aantal benodigde parameters voor de beschrijving van de vorm kan beperken.

Model-gebaseerde benaderingen maken dikwijls gebruik van *a priori* kennis van de vorm van de structuren, het gaat in dit geval om geometrische modellen. Echter, er zijn andere bronnen van *a priori* kennis denkbaar. In de medische beeldanalyse zijn tenminste drie modelleringstypen te onderscheiden:

1. *Modellering van de beeldacquisitie.* Er zijn veel factoren die bijdragen tot het beeldvormingsproces. Het onderliggende fysische principe voor beeldcontrast, de bemonsteringsstrategie, de aanwezigheid van mogelijke beeldartefacten, het beeldvormend systeem en de omgevingsruis beïnvloeden alle de uiteindelijke dataset. Het modelleren van deze informatie kan helpen bij de beslissing hoe de beelddata dienen te worden geïnterpreteerd of hoe de nauwkeurigheid van algoritmen kan worden verbeterd.
2. *Modellering van het af te beelden object.* *A priori* kennis van de anatomie, functie, fysiologie en/of pathologie van de structuren die van belang zijn, kan worden meegenomen in de analyse. Anatomische kennis is waarschijnlijk één van de meest gebruikte vormen van *a priori* kennis. Het inbrengen van deze kennis stelt iemand in staat voorwaarden te stellen die helpen bij het regulariseren van de beeldanalysetaak. Zo kan bijvoorbeeld kennis over de vorm van organen worden geïntroduceerd bij de selectie van de geschikte modelparameterisatie of bij het uitvoeren van een statistische analyse, die leidt tot een beschrijving van een gemiddelde vorm en de variatie over een populatie.

Het modelleren van het af te beelden object behoeft niet noodzakelijkerwijs beperkt te blijven tot het modelleren van de vorm. Soms bestaat de taak uit het relateren van de in de beelddata aanwezige informatie aan een model dat de onderliggende (patho-)fysiologie van het onderzochte object beschrijft.

3. *Modellering van de gebruiker.* Dit type kennis modelleert het effect van de gebruikersinteractie in het klinische beslissingsproces. In de klinische praktijk worden manuele beeldanalyseprocedures soms uitgevoerd volgens vastomlijnde protocollen om de reproduceerbaarheid van de resultaten te maximaliseren. Een nauwkeurige studie van het protocol kan aanwijzingen geven welke stappen geautomatiseerd kunnen worden.

Een ander gerelateerd onderwerp is efficiënte gebruikersinteractie. In de meeste beeldanalysebenaderingen wordt tegenwoordig de gebruiker buiten de *loop* van het algoritme gehouden. De interactie blijft vaak beperkt tot het bewerken van de resultaten van een min of meer automatisch algoritme. Een efficiënt interactiemechanisme zou de gebruiker in staat moeten stellen het proces intuïtief te sturen; idealiter zouden kleine gebruikersacties een groot effect moeten hebben op de uiteindelijke resultaten en een volledig handmatige bewerking moeten voorkomen. Tegelijkertijd dienen de resultaten intuïtief en reproduceerbaar te zijn.

In dit proefschrift word de potentie van het gebruik van de bovengenoemde types *a priori* kennis in driedimensionale modelgestuurde beeldanalyse geëxploreerd, met de nadruk op vasculaire en cardiale MR data.

In de hoofdstukken 2 tot en met 4 worden verschillende aspecten van een modelgebaseerde techniek voor de semi-automatische kwantificatie van lineaire vaatsegmenten in 3-D Magnetische Resonantie Angiografie (MRA) beelden beschreven.

Hoofdstuk 2 handelt over een multi-schaal filter voor de verbeterde visualisatie van bloedvaten in 2-D en 3-D angiogrammen. Hier is de *a priori* kennis aanwezig in de vorm van een lokaal discriminerende functie, die buisvormige structuren versterkt. Deze discriminant is gebaseerd op een geschikte combinatie van de eigenwaarden van de Hessiaan-matrix van een beeld. In de aanwezigheid van een buisvormige structuur voldoen de eigenwaarden van de Hessiaan-matrix aan bepaalde onderlinge eigenschappen. Deze eigenschappen worden in hoofdstuk 2 gebruikt om onderscheid te maken tussen driedimensionale buisvormige structuren en plaat- of blobvormige structuren. Er wordt aangetoond dat het ontwikkelde filter nuttig is als een voorberekingsstap om vaatstructuren te benadrukken ten opzichte van nabijliggende structuren. Deze voorberekingsstap heeft evenwel de neiging om vernauwingen van de vaatstructuren te introduceren. Daarom wordt in het daaropvolgende hoofdstuk een nauwkeuriger methode voor kwantificatie van de vaatmorfologie ontwikkeld.

In hoofdstuk 3 wordt het in hoofdstuk 2 ontwikkelde filter toegepast om de centrale as in een bloedvat in 3-D MRA beelden te berekenen. Deze berekening wordt geïnitieerd door een efficiënte gebruikersinteractie die op natuurlijke wijze de kennis van de gebruiker over het bloedvat

in kwestie incorporeert. Eveneens wordt in dit hoofdstuk een vaatmodel toegepast om de positie van de wand van het bloedvat te bepalen, teneinde een kwantitatieve analyse van de vasculaire morfologie te kunnen verrichten. *A priori* kennis wordt hoofdzakelijk in twee vormen gebruikt: een cilindrisch model introduceert kennis over de vorm, terwijl *a priori* informatie van de beeldacquisitie (type MRA techniek) wordt gebruikt om een criterium voor de bepaling van de positie van de wand van het bloedvat op te stellen. De eerste *in vivo* en *in vitro* resultaten illustreren dat zowel geometrisch als acquisitie gerelateerde kennis succesvol kunnen worden gecombineerd in het raamwerk van deformeerbare modellen.

Voor acceptatie in de klinische praktijk, is een evaluatie van medische beeldverwerkings algoritmen een voorwaarde. Om die reden is in hoofdstuk 4 een uitgebreide *in vitro* en *in vivo* evaluatie van het in hoofdstuk 3 geïntroduceerde algoritme beschreven. *In vitro* experimenten hebben het voordeel dat de werkelijke dimensies (bijvoorbeeld vaatlumens) bekend zijn en zo objectief kunnen worden vergeleken met andere methoden. Aan de andere kant verschaffen *in vivo* experimenten een realistische situatie. Ter evaluatie zijn de resultaten verkregen met de modelgebaseerde techniek vergeleken met manuele metingen van experts. De nauwkeurigheid van de modelgebaseerde techniek in het kwantificeren van vaatstructuren is vergelijkbaar met die van de manuele metingen in de drie belangrijkste MRA technieken (*time-of-flight* (TOF), *phase contrast* (PC) en *contrast-enhanced* (CE) MRA). Echter, in PC MRA kan in gebieden met grote variatie in de bloedstroom (bijvoorbeeld als gevolg van stenoses) het criterium ter bepaling van de wandpositie onnauwkeurig zijn. De eerste experimenten in hoofdstuk 3 gaven aan dat in sterk gestenoseerde vaten de aanwezigheid van bloedstroomartefacten in PC MRA de toepasbaarheid van de modelgestuurde methode beperkte. In hoofdstuk 4 zijn resultaten opgenomen met *state-of-the-art* CE MRA, waar de modelgestuurde techniek de mate van stenoses kan bepalen met een nauwkeurigheid gelijk aan die in de door de experts uitgevoerde manuele metingen. Bovendien zijn bij gebruik van de modelgestuurde methode een aantal andere driedimensionale morfologische parameters direct beschikbaar.

In de hoofdstukken 5 tot en met 7 wordt de nadruk gelegd op de cardiale beeldanalyse, een vakgebied waarbinnen het gebruik van modelkennis intensief onderzocht is.

Spatio-temporele beelden van het hart worden op dit moment verkregen met een variëteit van modaliteiten zoals CT, MRI en US. De beelden worden gewoonlijk gemaakt in een kort tijdsbestek, wat de beeldkwaliteit beperkt. Een functionele hartstudie bestaat daarnaast uit een grote hoeveelheid 4-D data, hetgeen een arbeidsintensieve handmatige nabewerking vereist alvorens de relevante informatie hieruit gedestilleerd kan worden. In de laatste twee decennia is een rijke bibliografie verschenen betreffende hartmodellering, maar tot op heden was er geen kritisch overzichtsartikel beschikbaar.

In hoofdstuk 5 wordt een uitgebreid overzicht, een categorisatie en een kritische bespreking over 3-D hartmodellering gegeven. De belangrijkste gevolgtrekking van dit hoofdstuk is dat ondanks het grote aantal algoritmen dat in de literatuur gepresenteerd is voor het modelleren en extraheren van de morfologie en beweging van het hart, er nog geen succesvol in is gebleken deze doelen te bereiken op een geautomatiseerde wijze. Uit het overzicht kan ook geconcludeerd worden dat de meeste methoden voor hart modellering gebruik maken van standaard geometrische primitieven, zoals *superquadrics*, *B-splines*, of *polygon meshes*, om de vorm van de ventrikels van het hart te bepalen. Het extraheren van de structuren wordt normaliter bereikt door het oplossen van een optimalisatieprobleem. Hierbij worden twee termen, te weten een beeldinformatie-term (bijvoorbeeld intensiteit- of gradiënt-informatie) en een regularisatie-term, die de flexibiliteit van de gekozen geometrische representatie beperkt, afgewogen. De beperkingen op de geometrische vorm zijn gewoonlijk vrij generiek. Het gebruik van statistische vormmodellen is daarom een veelbelovende aanpak om de toegestane vormen te beperken tot die vormen die plausibel een hart voor kunnen stellen. Het gebruik van statistische vormmodellen is tot op heden echter niet beschreven in de literatuur. Dit komt waarschijnlijk door de inherente problemen bij het construeren van een driedimensionaal statistisch model, die het extraheren van een verzameling van corresponderende driedimensionale *landmarks* in een verzameling voorbeeldvormen noodzakelijk maken. Dit probleem is het belangrijkste onderwerp van de laatste twee hoofdstukken.

In hoofdstuk 6 wordt een nieuw algoritme geïntroduceerd om driedimensionale vormmodellen te construeren uit een verzameling voorbeeldvormen. Bestaande benaderingen selecteren eerst in alle datasets de *landmarks*, om vervolgens hun onderlinge correspondentie te bepalen. In onze benadering worden de *landmarks* aan alle voorbeeldvormen toegekend door middel van een volumetrische elastische registratie met een atlas. Deze benadering kent een aantal voordelen ten opzichte van

eerder gepubliceerde methoden. De methode kan worden toegepast op structuren bestaande uit meervoudige vormen, en er zijn minder beperkende aannamen noodzakelijk aangaande de topologie van de structuur. De methode wordt geïllustreerd aan de hand van de constructie van statistische vormmodellen van twee anatomische structuren: een segment van de *radius* in het polsgewricht, en de *nucleus caudatus*, een structuur in het brein.

In hoofdstuk 7 wordt de methode, zoals geïntroduceerd in hoofdstuk 6, uitgebreid om statistische vormmodellen uit cardiale MRI beelden te construeren. Deze modellen bevatten zowel de epi- als de endocardiale wand van het linker ventrikel en de endocardiale wand van het rechter ventrikel. Omdat anatomische variatie van het hart vrij groot is, diende de volumetrische elastische registratie worden aangepast; een hiërarchische benadering is toegepast om de deformatie op een *coarse-to-fine* manier te bepalen. Daarnaast wordt een nieuwe similariteitsmaat, *label consistency*, gebruikt, terwijl in hoofdstuk 6 de maximalisatie van de genormaliseerde mutuele informatie werd toegepast. De nieuwe maat is beter voor structuren waarin meer objecten voorkomen. De combinatie van de hiërarchische representatie van het deformatieveld en de nieuwe similariteitsmaat konden succesvol omgaan met de grote variabiliteit die bestond in de vorm van de hartkamers. De resultaten van hoofdstuk 7 effenen de weg voor segmentatie van 3-D cardiale MR data met gebruik van statistische vormmodellen.

Publications

Publications in International Journals:

- A.F. Frangi, W.J. Niessen, R.M. Hoogeveen, Th. van Walsum, and M.A. Viergever. Model-based quantitation of 3D magnetic resonance angiographic images. *IEEE Transactions on Medical Imaging*, Special Issue on Model-based Medical Image Analysis, 18(10):946–56, October 1999.
- A.F. Frangi, W.J. Niessen, P.J. Nederkoorn, J. Bakker, W.P.Th.M. Mali, and M.A. Viergever. Quantitative analysis of vessel morphology from 3D MR angiograms: *in vitro* and *in vivo* results. *Magnetic Resonance in Medicine*, 45(2):311–22, February 2001.
- A.F. Frangi, M. Egmont-Petersen, W.J. Niessen, J.H.C. Reiber, and M.A. Viergever. Bone tumor segmentation in MR perfusion images with neural networks using multi-scale pharmacokinetic features. *Image and Vision Computing*, Special Issue on Application of Artificial Neural Networks for Image Analysis and Computer Vision. In press.
- A.F. Frangi, W.J. Niessen, and M.A. Viergever. Three-dimensional modeling for functional analysis of cardiac images: A review. *IEEE Transactions on Medical Imaging*. In press.
- A.F. Frangi, D. Rueckert, J.A. Schnabel, and W.J. Niessen. Automatic construction of multiple-object three-dimensional statistical shape models: Application to Cardiac Modeling. Submitted.

Publications in International Conference Proceedings:

- A.F. Frangi, W.J. Niessen, K.L. Vincken, and M.A. Viergever. Multiscale vessel enhancement filtering. *Modelical Image Computing & Computer Assisted Interventions*, MICCAI98, vol 1496 of *Lecture Notes in Computer Science*, pages 130–7, Boston, USA, September 1998. Springer Verlag.
- A.F. Frangi, W.J. Niessen, R.M. Hoogeveen, O. Wink, J.M. Scheffers, J. Bakker, and M.A. Viergever. Automated model-based stenosis grading with 3D MRA: *in vitro* evaluation. In *ISMRM Workshop on Flow and Motion in Cardiovascular MRI*, London, UK, June 1999. In CD-ROM.
- A.F. Frangi, W.J. Niessen, R.M. Hoogeveen, Th. van Walsum, and M.A. Viergever. Quantitation of vessel morphology from 3D MRA. *Modelical Image Computing & Computer Assisted Interventions*, MICCAI99, vol 1679 of *Lecture Notes in Computer Science*, pages 358–67, Cambridge, UK, October 1999. Springer Verlag.

- A.F. Frangi, W.J. Niessen, P.J. Nederkoorn, O.E.H. Elgersma, and M.A. Viergever. Three-dimensional model-based stenosis quantification of the carotid arteries from contrast-enhanced MR angiography. *Mathematical Methods in Biomedical Image Analysis*, pages 110–18, South Carolina, USA, June 2000. IEEE Computer Society Press.
- A.F. Frangi, D. Rueckert, J.A. Schnabel, and W.J. Niessen. Automatic 3-D ASM construction via atlas-based landmarking and volumetric elastic registration. *Information Processing in Medical Imaging*, IPMI01, Davis, USA, June 2001. In press.
- S.A.M. Baert, W.J. Niessen, E.H.W. Meijering, A.F. Frangi, and M.A. Viergever. Guide wire tracking during endovascular interventions. *Modelical Image Computing & Computer Assisted Interventions*, MICCAI00, vol 1935 of *Lecture Notes in Computer Science*, page 727–34, Pittsburgh, USA, October 2000. Springer Verlag.
- S.A.M. Baert, W.J. Niessen, E.H.W. Meijering, A.F. Frangi, and M.A. Viergever. Guide wire tracking in interventional radiology. In H.U. Lemke, M.W. Vannier, K. Inamura, A.G. Farman, and K. Doi, editors, *Computer Assisted Radiology and Surgery—CARS 2000*, no 1214 in International Congress Series, pages 537–542, California, USA, June 2000. Elsevier Science.
- M. Egmont-Petersen, A.F. Frangi, W.J. Niessen, P.C.W. Hogendoorn, J.L. Bloem, M.A. Viergever, and J.H.C. Reiber. Segmentation of bone tumor in MR perfusion images using neural networks and multiscale pharmacokinetic features. In A. Sanfeliu, J.J. Villanueva, M. Vanrell, R. Alquezar, J. Crowley, and Y. Shirai, editors, *International Conference on Pattern Recognition*, vol 4, pages 80–83, Barcelona, Spain, September 2000. IEEE Computer Society.

Curriculum Vitae



The author was born in La Plata, Buenos Aires, Argentina, on 15th November 1972. In the period 1985–1990 he received a technical secondary education at the Escuela Nacional de Educación Técnica No 1 “Albert Thomas” in the branch of Electronics.

In January 1991, he entered university at the Universidad Nacional de La Plata, La Plata, Argentina, where he studied a semester of the undergraduate studies of Electronic Engineering. In September 1991, he moved to Barcelona, Spain, where he completed his M.Sc. studies in Telecommunication Engineering at the Universidad Politécnica de Cataluña (UPC). He graduated in September 1996 with a final project on Electrical Impedance Tomography (EIT). After graduation he worked as research assistant of the División de Bioingeniería of the Departamento de Electrónica (UPC). Over the space of a year he carried out research in the field of EIT under a grant of the Spanish Government.

In September 1997 he started as a Ph.D. student (“AiO”) at the Image Sciences Institute, University Medical Center Utrecht, The Netherlands, in a project entitled “Model-based Analysis of Volumetric Medical Images”. For this period, he received a grant from the Netherlands Ministry of Economic Affairs within the framework of the Innovation Oriented Research Programme (IOP Beeldverwerking, project number IBV97009). The project was carried out in cooperation with EasyVision Advanced Development, Philips Medical Systems B.V. (Best, The Netherlands). The results are described in this thesis. The last two chapters were carried out partly in the Department of Computing at Imperial College, and in Guy’s Hospital at King’s College, over a three-month research stay in London, UK.

